PROGRAMA DE DOCTORADO EN INGENIERÍA DE COSTAS, HIDROBIOLOGÍA Y GESTIÓN DE SISTEMAS ACUÁTICOS (IH2O)

TESIS DOCTORAL

ANÁLISIS NUMÉRICO DE MORFODINÁMICA EN PERFILES DE PLAYA DURANTE EVENTOS EPISÓDICOS CON CFD

PhD THESIS

NUMERICAL ANALYSIS OF CROSS-SHORE MORPHODYNAMICS IN EPISODIC EVENTS USING CFD

AUTOR / AUTORA

JULIO GARCÍA-MARIBONA LÓPEZ-SELA

DIRECTOR / A / ES / AS

JAVIER LÓPEZ LARA

ÍÑIGO LOSADA RODRÍGUEZ

UNIVERSIDAD DE CANTABRIA

Escuela de Doctorado de la Universidad de Cantabria

Santander 2023

Numerical analysis of cross-shore morphodynamics in episodic events using CFD

University of Cantabria

Julio García-Maribona López-Sela

January 2023

Versión resumida en español

Introducción

Las playas constituyen entornos de alto valor que cumplen una serie de funciones económicas, sociales y ambientales. Entre las primeras se encuentran la generación de actividad económica atrayendo turismo o la protección contra daño producido por eventos extremos. Respecto a sus funciones sociales, son espacios muy apreciados por los habitantes de zonas cercanas que pueden albergar actividades de ocio y deportivas. Desde el punto de vista ambiental, las playas son formas de paisaje y hábitats únicos. Una de sus principales características es su capacidad para adaptarse a variaciones del nivel del mar conservando sus funciones.

Gestionar estos entornos es una tarea dificil. Existen una serie de potenciales problemas que pueden degradar su valor, tales como la erosión costera, el desarrollo excesivo de zonas costeras o la contaminación de sus aguas. Por otra parte, se trata se entornos complejos cuyo comportamiento está dictado por la interacción entre hidrodinámica y morfología. Comprender mejor estas interacciones es fundamental para una adecuada toma de decisiones a la hora de proteger las playas.

Una de las principales amenazas para las playas es la erosión costera, la cual puede producir degradaciones severas de su valor. En primer lugar, la reducción de superficie últil conlleva una pérdida de valor económico. Por otra parte, su función como defensa costera también se ve perjudicada, dado que la pérdida de sedimento reduce su capacidad para adaptarse a cambios de nivel del mar y su capacidad de disipar energía del oleaje en condiciones de oleaje extremo. Además, cuando la erosión llega a afectar a infraestructura costera, puede producir importantes daños debidos a la socavación de sus cimientos. Otras posibles consecuencias de la erosión costera son la pérdida de biodiversidad, cambios en los sistemas de corrientes llevando a condiciones peligrosas para el baño o empeoramiento de las condiciones para la práctica de deportes acuáticos.

Para la prevención de erosión costera y la implementación de medidas para remediarla, es indispensable conocer su funcionamiento. El marco de la morfodinámica de playas (Wright & Thom, 1977) establece relaciones entre los principales elementos que regulan este funcionamiento: condiciones ambientales, procesos morfodinámicos y secuencia evolutiva. Las condiciones ambientales incluyen fuentes energéticas (viento, oleaje y nivel del mar fudamentalmente), propiedades del sedimento y estado morfológico (batimetría). Los procesos morfodinámicos son interacciones entre la hidrodinámica y morfología, asociadas al transporte de sedimentos, y que conllevan una modiciación del estado morfológico. La consecución de estados morfológicos, producidos de este modo, a lo largo del tiempo se denomina secuencia evolutiva. Por tanto, de acuerdo con el marco de la morfodinámica de playas, los procesos morfodinámicos juegan un papel fundamental en el comportamiento de las playas

frente a determinadas condiciones ambientales. Los principales elementos del marco de la morfodinámica de playas y las relaciones entre sí se representan en la Figura 1

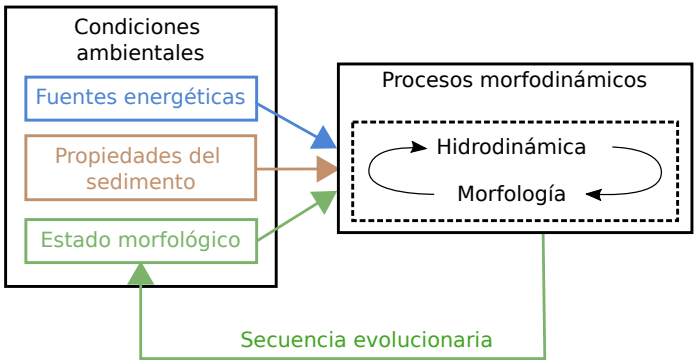

Figura 1: Esquema conceptual del marco morfodinámico propuesto por (Wright & Thom, 1977).

Los procesos morfodinámicos pueden ocurrir en diferentes escalas espacio-temporales. Una de las escalas más importantes para la gestión costera es la de los eventos episódicos, que consisten en la occurencia de condiciones de oleaje altamente energéticas durante periodos de tiempo relativamente cortos, del orden de horas. Durante estos eventos, pueden producirse grandes variaciones de la batimetría y posición de la línea costera. A pesar de su importancia, no está clara la forma en la que las playas responden a este tipo de eventos. Por tanto, comprender los procesos morfodinámicos que rigen la evolución de playas durante eventos episódicos es de gran interés. Por otra parte, los procesos morfodinámicos pueden clasificarse en *cross-shore* y *long-shore*, según ocurran principalmente en un plano perpendicular o paralelo a la línea de costa, respectivamente.

Esta tesis se centra en los procesos *cross-shore*, concretamente en aquellos causados por la acción del oleaje durante eventos episódicos. Éstos están relacionados con una serie de fenómenos hidrodinámicos y de transporte de sedimento complejos, los cuales se describen brevemente a continuación y más en detalle en el Estado del Arte.

En cuanto a los fenómenos hidrodinámicos en perfiles de playas, se puede establer una clasificación basada en las diferentes zonas del perfil donde se producen, que son, desde el mar hacia la costa, las zonas de asomeramiento, surf (exterior e interior) y swash. En la zona de asomeramiento, la hidrodinámica es relativamente sencilla, pudiendo representarse de forma razonablemente precisa a través de teoría de ondas no lineal. Un fenómeno hidrodinámico importante en esta zona es el *steady streaming*, una corriente producida por las ondas progresivas cerca del fondo debido al efecto de la capa límite.

La hidrodinámica en la zona de surf presenta una mayor complejidad debido a la rotura del oleaje. En la misma, se producen multitud de fenómenos hidrodinámicos, tales como la inestabilidad de la onda que lleva al inicio de su rotura o la generación de turbulencia y estructuras coherentes debido a los altos gradientes de velocidad asociados con la rotura. Además, la rotura del oleaje produce un desbalance en los flujos horizontales másico y de cantidad de movimiento, resultando en excesos dirigidos hacia la costa. El exceso de flujo másico se contrarresta con las corrientes de retorno y de resaca, ocurriendo las primeras en el plano *cross-shore* y siendo

las segundas generalmente clasificacas como fenómenos *long-shore*. La corriente de retorno tiene gran relevancia en la evolución de perfiles de playa. Se trata de una corriente dirigida hacia el lado mar que discurre pegada al fondo hasta que, en el llamado punto de separación, se separa del mismo y pasa a discurrir por las capas superiores. Adicionalmente, el desbalance de cantidad de movimiento se compensa con un incremento del nivel medio, denomidado *set-up*.

En la zona de swash, la influencia de la turbulencia y estructuras coherentes resultantes de la rotura combinadas con un mayor efecto de la capa límite y flujo en medio poroso también confieren una gran complejidad a la hidrodinámica. Los principales elementos de la hidrodinámica en el perfil de playa están representados en la Figura 2.

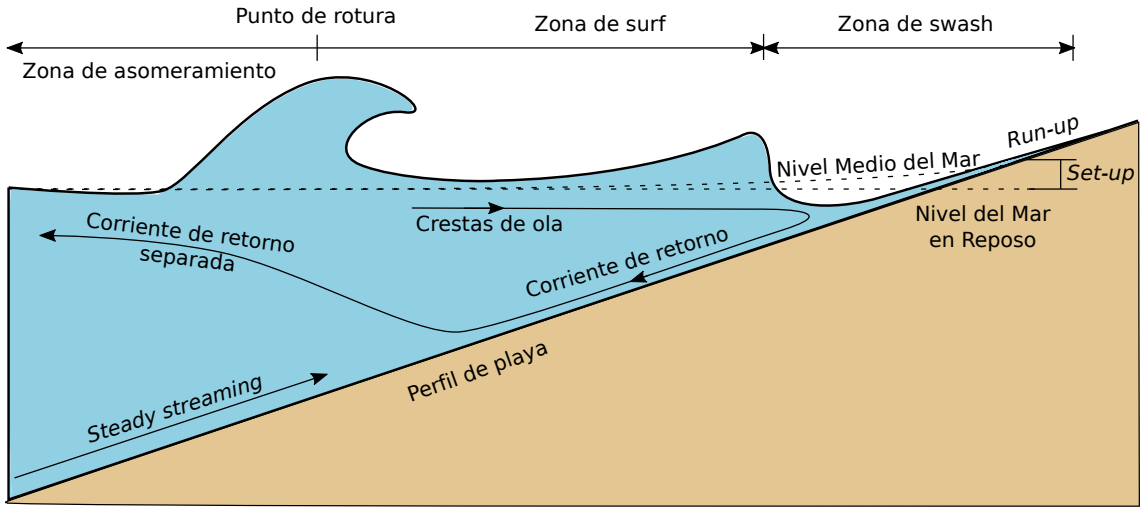

Figura 2: Representación esquemática de los principales fenómenos hidrodinámicos en el perfil de playa.

En cuanto al transporte de sedimentos, generalmente se divide una componente de transporte por fondo y otra de transporte en suspensión. La primera se da en la zona cercana al fondo y está muy condicionada por las interacciones entre partículas de sedimento. El transporte en suspensión sucede más lejos del fondo y está fundamentalmente condicionado por la advección del fluido y por la propia velocidad de caida del sedimento. Además, las interacciones entre partículas son significativas para el transporte en suspensión en zonas donde la concentración de sedimento es alta.

La morfología del perfil de playa incluye diferentes formas de distintas escalas, tales como ondulaciones de pequeña escala, barras de rompientes, senos, bermas y escarpes. Las variaciones de estas formas debidas al transporte de sedimento afectan a la hidrodinámica. Por ejemplo, la generación de una barra de rompientes puede cambiar la posición del punto de rotura y disminuir la energía del oleaje que alcanza las zonas de surf y swash.

Las fuertes interacciones entre hidrodinámica, y morfología (procesos morfodinámicos) añaden una complejidad adicional al estudio de la morfodinámica de playas. Actualmente, estas interacciones no se conocen con suficiente detalle.

Estado del arte

Como se estableció anteriormente, la comprensión del comportamiento de los perfiles de playa durante eventos episódicos es de gran importancia para una adecuada gestión de las costas. En esta sección se proporciona un repaso del conocimiento actual en los los procesos morfodinámicos que rigen dicho comportamiento.

Existen diferentes técnicas para analizar la morfodinámica en perfiles de playas: campañas de campo, ensayos de laboratorio y modelos numéricos. Primeramente, las campañas de campo proporcionan mediciones directas de los fenómenos que se pretende estudiar, sin simplificaciones o distorsiones en las que otras técnicas incurren. Sin embargo, resulta difícil realizar las mediciones con oleaje fuerte y no pueden controlarse las condiciones para las que se obtienen datos. Segundamente, los ensayos de laboratorio son una herramienta clave, ya que proveen datos de gran calidad, pudiendo adaptarse la configuración del experimento a las condiciones de interés en cada caso. Uno de los mayores problemas de los ensayos de laboratorio es el correcto escalado del sedimento. Terceramente, los modelos numéricos tienen un menor coste que las dos técnicas anteriores, pueden reproducir situaciones que no son viables en experimentos de laboratorio debido a su escala y permiten medir simultáneamente múltiples variables de interés.

En las últimas décadas, se ha mejorado significativamente el conocimiento en la evolución de perfiles de playa empleando estas técnicas. Las investigaciones previas suelen analizar determinados procesos morfodinámicos, atentiendo a fenómenos hidrodinámicos y de transporte de sedimento, o bien tratan de establecer una relación directa entre condiciones ambientales y evolución morfológica. A continuación se da una revisión de los principales puntos del Estado del Arte en estas materias.

Procesos morfodinámicos cross-shore

De acuerdo con el marco de la morfodinámica de playas, los procesos morfodinámicos surgen de la interacción entre hidrodinámica y morfología. Dicha interacción está condicionada por las fuentes energéticas, las propiedades del sedimento y el estado morfológico.

La forma en que hidrodinámica y morfología intervienen en la evolución de perfiles de playa se ha estudiado anteriormente. En las secciones siguientes se resumen los avances fundamentales de estas investigaciones.

Hidrodinámica

Algunos fenómenos hidrodinámicos estrechamente relacionados con la morfodinámica en perfiles de playa son la corriente de retorno, el *steady streaming*, los sesgos de velocidad y aceleración debidos a la no-linearidad de las ondas, el proceso de rotura y los movimientos de swash.

La corriente de retorno se indentificó como una de los principales causantes de la evolución de perfiles de playa en (Bagnold, 1940). Dicha corriente está relacionada con el transporte de sedimentos hacia el lado mar. Existen modelos que permiten obtener el perfil de velocidad de la corriente de retorno, como por ejemplo (Deigaard *et al.* , 1991). Estos modelos consideran el balance de cantidad de movimiento horizontal promediado en la vertical y asumen que el perfil de velocidades de la corriente

de retorno debe ser tal que las tensiones tangenciales producidas por el mismo compensen el desequilibrio de cantidad de movimiento, producido por la rotura de olas, junto con el *set-up*.

En cuanto al *steady streaming*, se estudió anteriormente en (Bagnold, 1947) para ondas propagándose sobre un fondo plano. Se observó, mediante la inyección de un tinte en la zona cercana al fondo, que existe una corriente neta en la dirección de propagación de las ondas. El perfil de velocidades asociado al *steady streaming* se representa en la Figura 3. La misma corriente se identificó también en una configuración con fondo inclinado y se observó que la corriente desaparece, aproximadamente, cuando las olas empiezan a romper. En (Longuet-Higgins & Stoneley, 1953), se da una solución analítica para la velocidad del *steady streaming*.

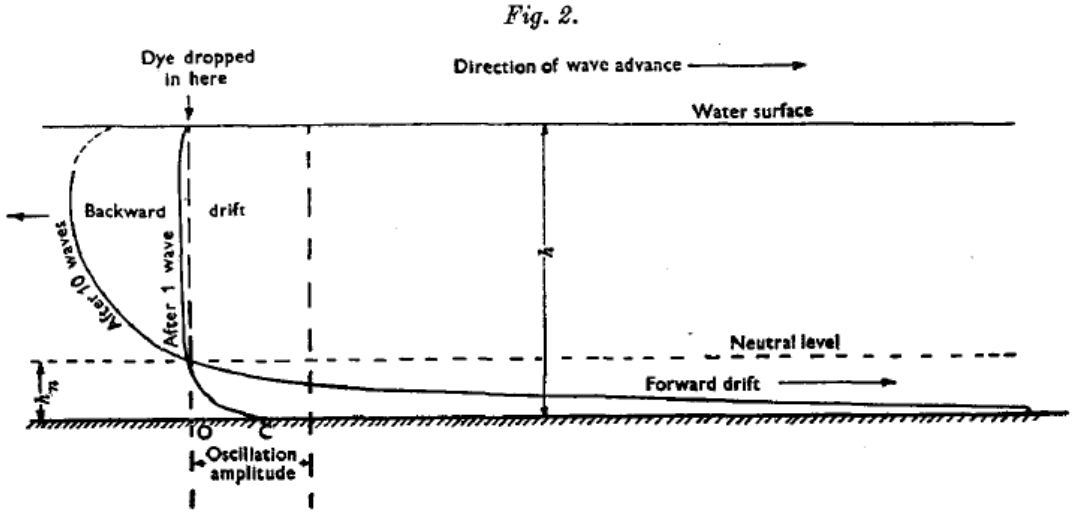

Figura 3: Perfiles de velocidad obtenidos al inyectar tinte en diferentes posiciones a lo largo de la columna de agua. Se puede observar el efecto del *steady streaming* cerca del fondo. Reproducido de (Bagnold, 1947).

La no-linearidad de las ondas en la zona de asomeramiento se manifiesta de dos formas relevantes para el transporte de sedimento: sesgo en la velocidad y sesgo en la aceleración. Estos dos efectos pueden producir transporte de sedimento por sí mismos como se discute en (van Rijn *et al.* , 2013).

La rotura del oleaje se ha estudiado extensamente tanto en ensayos de laboratorio (por ejemplo, (van der A *et al.* , 2017)) como con modelos numéricos ((Watanabe *et al.* , 2005), (Larsen *et al.* , 2020)). Se puede encontrar un sumario de los efectos hidrodinámicos asociados a la rotura del oleaje en (Nadaoka *et al.* , 1989). Estos efectos se pueden dividir en tres componentes: irrotacional, rotacional (con vorticidad media distinta de cero) y turbulencia. La segunda componente es debida a la generación de estructuras coherentes, concretamente vórtices horizontales y vórtices oblicuo-descendentes. Estos dos tipos de estructura coherente se representan en la Figura 4. Se observó que las estructuras coherentes producidas por la rotura tienen una gran capacidad de mezcla vertical, la cual afecta tanto a la masa y cantidad de movimiento como al sedimento en suspensión. Esto, a su vez, influye en los desbalances de flujo másico y de cantidad de movimiento producidos durante la rotura,

afectando a la corriente de retorno y al *set-up*, como se expone en (Ting & Nelson, 2011).

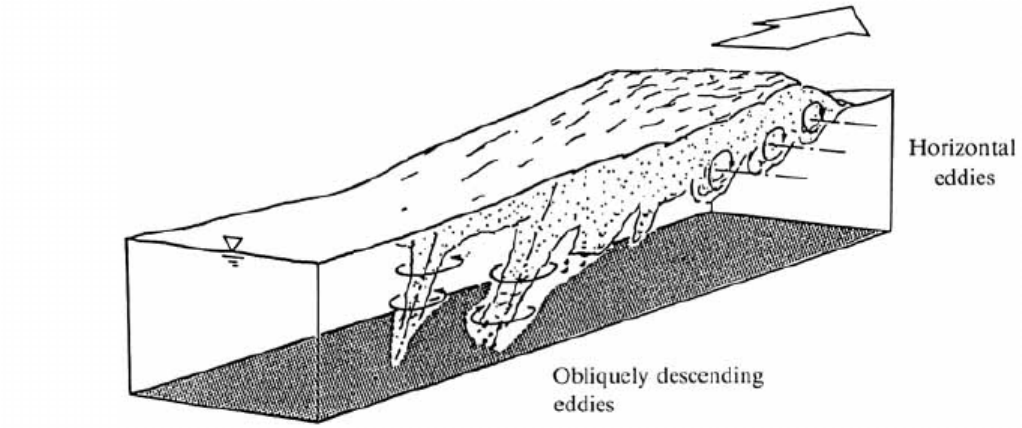

Figure 10. Schematic representation of the large-scale eddy structure under breaking waves.

Figura 4: Estructuras coherentes, vórtices horizontales y oblicuo-descendentes, responsables de la componente rotacional de la hidrodinámca generada por la rotura del oleaje. Reproducido de (Nadaoka *et al.* , 1989).

Finalmente, la hidrodinámica en la zona de swash presenta también una gran complejidad debida a la influencia del flujo poroso, el pequeño espesor del flujo y la alternancia entre condiciones secas y mojdadas. Esto dificulta tanto la obtención de datos en laboratorio y campo como la simulación numérica. En (Elfrink & Baldock, 2002) se puede encontrar un resumen de las principales características de la hidrodinámica en la zona de swash. Éstas se dividen en hidrodinámica debida a las olas y debida a la turbulencia. En cuanto a la causada por las olas, el número de Iribarren resulta ser un parámetro fundamental, dado que determina si el tipo de onda que alcanza la zona de swash rompe nuevamente o si, en cambio, se refleja contra el perfil de playa. En cuanto a la turbulencia, las posibles fuentes en la zona de swash son la turbulencia proviniente de la zona de surf y la generada en el colapso de ondas (durante la fase de ascenso o *run-up*) y los efectos de capa límite (durante la fase de descenso o *backwash*). Éstos efectos de capa límite pueden incrementarse con la aparición de resaltos hidráulicos o interacciones entre el *backwash* y una ola incidente, que pueden llevar a la aparición de vórtices. En (Elfrink & Baldock, 2002) se pone de manifiesto la necesidad de más investigación para establecer condiciones de contorno adecuadas en la zona de swash que representen la turbulencia proviniente de la zona de surf interior.

Transporte de sedimentos

Como se discute en (van Rijn *et al.* , 2013), el conocimento del transporte de sedimento en perfiles de playa ha aumentado significativamente en los últimos años. En la zona de asomeramiento, los principales efectos hidrodinámicos que condicionan el transporte de sedimento son los ya mencionados *steady streaming*, sesgo de la velociad y sesgo de la aceleración. En cuanto al *steady streaming*, el patrón de movimiento de tinte inyectado cerca del fondo que se describe en (Bagnold, 1947) ilustra cómo esta corriente mueve el sedimento erosionado en la zona de asomeramiento

hacia el punto de rotura. Los sesgos de velocidad y aceleración generan transporte por fondo debido a la relación no lineal (típicamente cúbica) entre velociad y transporte por fondo (ver (Meyer-Peter & Müller, 1978) o (Bailard & Inman, 1981)). El transporte en suspensión también se ve afectado por estos sesgos, dado que el máximo de concentración de sedimento a lo largo del periodo de la onda suele darse al mismo tiempo que el de velocidad dirigida hacia la costa, durante el paso de cresta. Esta relación entre velociad y transporte de sedimento es distinta dependiendo del régimen en que se produzca el transporte. Por una parte, el transporte en régimen *sheet-flow* se da para valores altos de velocidad de fricción y se corresponde con una relación aproximadamente cúbica entre velocidad y transporte de sedimento, similar al caso del transporte por fondo (ver, por ejemplo, (Ruessink *et al.* , 2011)). Sin embargo, si el sedimento es de granulometría fina se produce un desfase entre velociad y concentración de sedimento significativo, y el transporte de sedimento no puede asumirse que varía con el cubo de la velocidad. Por otra parte, el régimen *rippled-bed* se corresponde con velociades relativamente bajas y está dominado por una serie de vórtices coherentes que se mueven sobre las ondulaciones del fondo (ver (van der Werf *et al.* , 2007) y (van der Werf *et al.* , 2008)).

En la zona de surf, la corriente de retorno tiene un efecto clave en el transporte de sedimento. Debido a la fuerte advección que produce, el sedimento erosionado en ciertas zonas puede terminar depositándose en lugares muy distantes. Los efectos hidrodinámicos asociados a la rotura del oleaje también influyen en el transporte de sedimento. Por una parte, las estructuras coherentes alteran en transporte en suspensión (ver (van Rijn *et al.* , 2013)). Además, cuando estas estructuras coherentes alcanzan el fondo producen altas tensiones tangenciales y la consecuente erosión (Yoon & Cox, 2012). Por otro lado, la turbulencia contribuye a mantener el sedimento erosionado en suspensión (Ting & Kirby, 1995). En imagenes obtenidas de ensayos de laboratorio, reproducidas en la Figura 5, se puede observar el transporte de sedimento inducido por el proceso de rotura. En cuanto al transporte por fondo, los efectos de la rotura del oleaje se describen en (van der Zanden *et al.* , 2017a).

El transporte de sedimentos en la zona de swash se aborda en (Elfrink & Baldock, 2002). La importancia relativa de los transportes por fondo y en suspensión depdende de la energía del oleaje que alcanza la misma y de las características del sedimento. El transporte por fondo depende de la velocidad de fricción y está, por tanto, influido por los sesgos de velocidad y de aceleración. Éstos resultan en mayor tensión tangencial durante el paso de cresta, lo cual contribuye a un transporte neto hacia la costa. Sin embargo, la pendiente de la playa penaliza el transporte dirigido hacia la costa y favorece el dirigido hacia el mar. Además, la duración en el movimiento de *backwash* es mayor que en el ascenso. Según la importancia relativa de estos factores, el transporte neto en la zona de swash es hacia tierra o mar. El transporte en suspensión es más complejo, dado que le afectan también la interacción del *backwash* con la ola incidente y la separación del flujo. Estos efectos pueden llevar a la generación de vórtices cerca del fondo, que son responsables de la aparición del escarpe que separa las zonas de swash y de surf interior.

Condiciones ambientales y evolución morfodinámica

Las condiciones de equilibrio, bajo las cuales el perfil de playa alcanza una configuración estable para las condiciones ambientales existentes, son de gran interés en

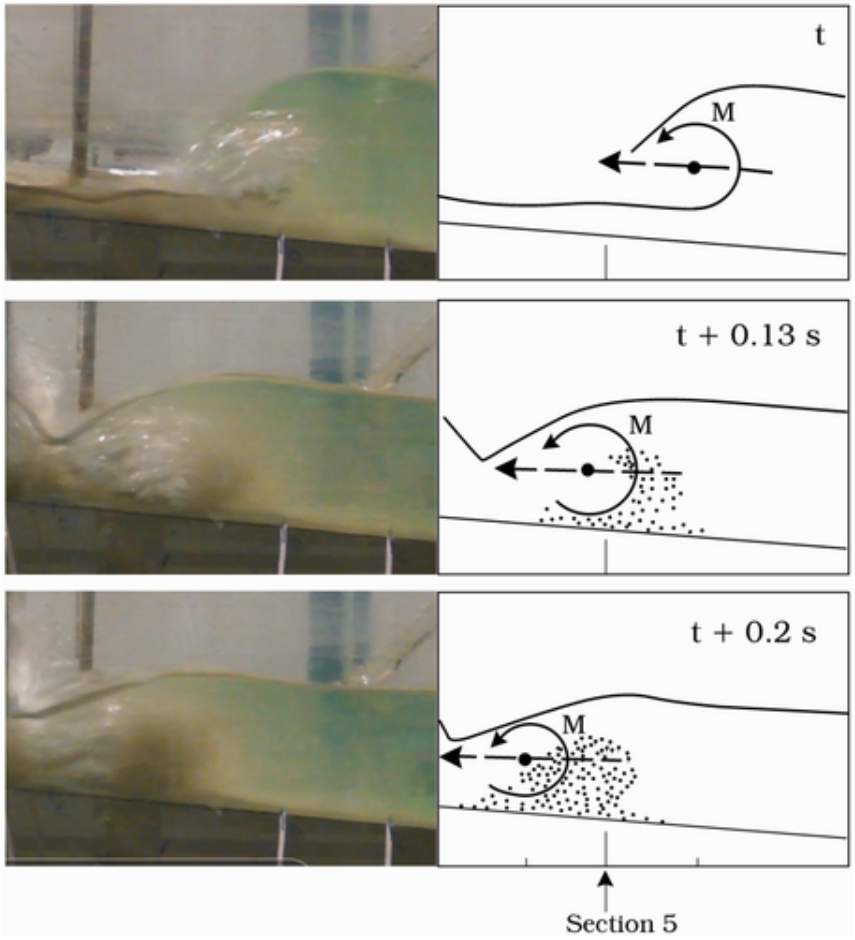

Figura 5: Transporte de sedimento producido por la rotura del oleaje. Se muestran fotografías de ensayos de laboratorio y una representación esquemática de la advección asociada con el denominado vórtice horizontal primario. Reproducida de (Sumer *et al.* , 2013).

aplicaciones de ingeniería. Éstas son comunmente estudiadas directamente a través de las condiciones ambientales, sin entrar a analizar los procesos morfodinámicos que las causan. Uno de los modelos de este tipo más empleados es la regla de Bruun (Bruun, 1962), que establece una relación entre recesión costera y subida del nivel del mar. Otro modelo en esta línea es (Bruun, 1954), donde se propone una ecuación empírica para determinar la forma del perfil de playa en función de las características del sedimento. Sin embargo, el modelo de (Dean, 1977) se utiliza con mayor frecuencia al ser más flexible. En concreto, éste incluye coeficientes de escala y forma dependientes de los parámetros del sedimento y del tipo de fuente energética, respectivamente. El modelo de (Wright *et al.* , 1985) relaciona el estado de la playa con la velociad de caida de grano adimensional, la cual depende de la velocidad de caída del sedimento y de la altura de ola en rotura, considerando tanto el valor actual como las condiciones antecedentes. La dirección de la evolución morfológica (erosión o acreción) depende de la diferencia entre valor actual y de equilibrio de la velocidad de caida de grano adimensional. Otros modelos en esta línea son (Yates *et al.* , 2009), (Davidson *et al.* , 2013) o (Splinter *et al.* , 2014). Debido a que estos modelos están indicados para simular escalas temporales de varios años, se denominan modelos multi-año, y pueden ser a su vez modelos *cross-shore*, *long-shore* o una combinación de ambos dependiendo de los fenómenos que reproduzcan. De cualquier modo, no contar con los efectos morfodinámicos lleva a grados de capacidad predictiva relativamente bajos. Mejorar el conocimiento en procesos morfodinámicos también puede llevar a mejoras en este tipo de modelos.

Modelos numéricos basados en procesos para mordofinámica en perfiles de playa

Los modelos anteriormente comentados son interesantes para simular escalas temporales del orden de varios años, dado su bajo coste computacional. Sin embargo, los modelos basados en procesos son más adecuados para escalas temporales menores, como los eventos episódicos, al resolver hasta cierto punto los procesos morfodinámicos.

Existen varios tipos de modelos basados en procesos. Se puede establecer una clasificación de los mismos atendiendo a los tratamientos de hidrodinámica y transporte de sedimentos. Respecto a la hidrodinámica, se pueden dividir en modelos de flujo promediado y modelos intra-ola. Los primeros no resuleven procesos intra-ola, si no que aproximan sus efectos a través de parametrizaciones y formulaciones semiempíricas. Los segundos sí resuelven este tipo de procesos. Un tipo común de modelos intra-ola son los llamados modelos CFD (*Computational Fluid Dynamics*) que, generalmente, resuelven las ecuaciones RANS (*Reynolds-Averaged Navier-Stokes*). Otro tipo de modelo intra-ola comunmente empeado son los modelos Boussinesq. En la Figura 6 se representa esquemáticamente la clasificación de modelos para evolución de playas atendiendo al tratamiento hidrodinámico.

Los modelos de flujo promediado tienen menor coste computacional que los intra-ola siendo, por tanto, adecuados para simular escalas temporales más largas. Sin embargo, al no resolver algunos procesos de transformación del oleaje (por ejemplo, la rotura) e hidrodinámicos (como las separaciónes de flujo), este tipo de modelo no es suficientemente preciso para el análsis de los procesos morfodinámicos, siendo más indicados los modelos intra-ola. Puesto que esta tesis tiene como objetivo el estudio

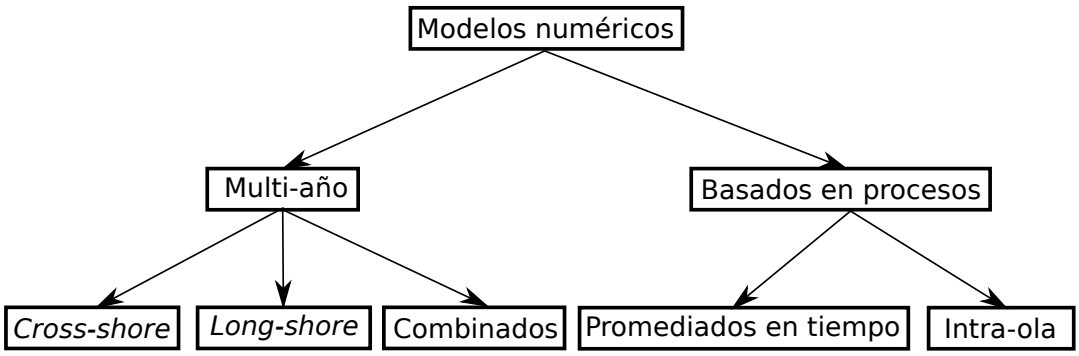

Figura 6: Clasificación de modelos numéricos para la evolución de playas atendiendo al tratamiento de la hidrodinámica. Los modelos multi-año incluyen modelos *cross-shore*, *long-shore* y combinados. Por otra parte, los modelos basados en procesos se dividen en promediados en el tiempo e intra-ola

de los procesos morfodinámicos, lo modelos intra-ola son los más adecuandos y en los que se centra el análisis.

En cuanto al transporte de sedimentos, se puedem dividir los modelos atendiendo a tres criterios. Primero, el tipo de sedimento puede ser granular o cohesivo. El tratamiento de sedimento cohesivo exige considerar físicas adicionales, como la floculación o las interacciones entre flóculos. Segundo, en función de las fases consideradas en las ecuaciones de gobierno de la hidrodinámica. Si el sedimento aparece de forma explícita en dichas ecuaciones, se considera un modelo de dos fases. El caso contrario se considera como modelo de una fase. Tercero, en función del marco de referencia de las ecuaciones de gobierno, que puede ser Lagrangiano o Euleriano.

En la Figura 7 se muestra una clasificación general de los modelos intra-ola basados en procesos para transporte de sedimentos en playas.

Cada uno de los anteriores tipos tiene sus ventajas y desventajas. En general, a mayor cantidad de procesos resueltos, mayor coste computacional. Los modelos CFD tienen un coste computacional alto comparados con los Boussinesq. Entre ellos, sólo los modelos Eulerianos de una fase son actualmente apropiados para simular un perfil de playa completo, mientras que los modelos Lagrangianos o Eulerianos de dos fases están indicados para estudiar fenómenos en escalas espaciales mucho más pequeñas, dado su excesivo coste computacional.

Una de las primeras implementaciones de modelos Eulerianos de una fase para problemas de transporte de sedimento es (Roulund *et al.* , 2005). Este modelo se empleó más adelante en (Fuhrman *et al.* , 2014) y (Li *et al.* , 2020) para analizar la socavación en tuberías submarinas y en (Larsen *et al.* , 2017) para simular la socavación inducida por tsunamis en cimentaciones de mono-pilas. Cabe destacar el trabajo en (Jacobsen *et al.* , 2014) y (Jacobsen & Fredsoe, 2014), donde se demuestra la capacidad de los modelos Eulerianos de una fase para reproducir la evolución de un perfil de playa.

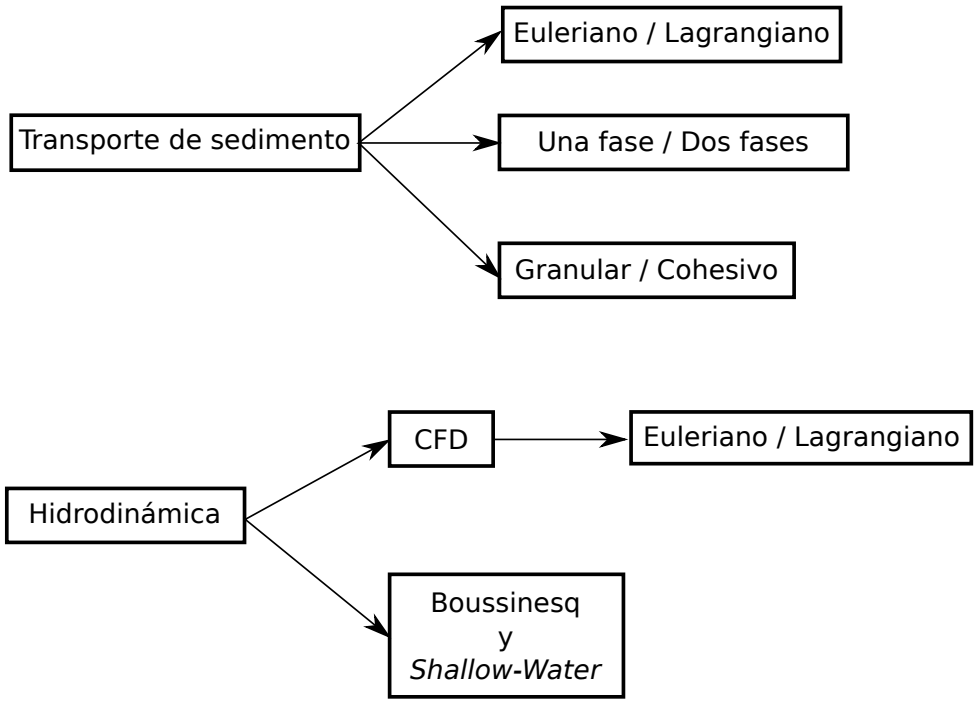

Figura 7: Clasificación de modelos intra-ola en función de los tratamientos de hidrodinámica y transporte de sedimento.

Objetivos

Como se indicaba anteriormente, los procesos morfodinámicos que rigen la evolución de perfiles de playa en las condiciones ambientales asociadas a eventos episódicos no son suficientemente conocidos. Los principales aspectos de la hidrodinámica en perfiles de playa se han tratado en anteriores investigaciones, y algunos aspectos del transporte de sedimento también se han estudiado en detalle. Resta, sin embargo, una visión detallada e integral de las interacciones entre hidrodinámica y morfología asociadas al transporte de sedimentos (procesos morfodinámicos). Como resultado de esta falta de conocimiento, la morfodinámica de playas se aborda comunmente de una manera excesivamente simplificada. Los modelos comunmente empleados para cálculos a largo plazo requieren de un elevado número de parámetros de calibración para compensar este desconocimiento. A su vez, esto lleva a menor eficacia y eficiencia en las soluciones que se plantean para combatir la erosión costera y otros problemas de gestión costera.

Los objetivos de esta tesis se establecen de acuerdo con estas limitaciones del conocimiento en morfodinámica de perfiles de playa.

Objetivo principal El objetivo principal de esta tesis es aumentar el conocimiento en los procesos morfodinámicos que rigen la evolución de perfiles de playa durante eventos episódicos. En particular, se pretende lograr una compresión global de los principales procesos hidrodinámicos y morfológicos, de cómo los mismos dan lugar a procesos morfodinámicos y de cuáles son sus mayores condicionantes.

Objetivos específicos El objetivo principal se articula en tres objetivos específicos, que se afrontan individualmente en los capítulos siguientes. Estos objetivos específicos son:

1. Desarrollar un modelo numérico capaz de simular los principales procesos morfodinámicos en perfiles de playa durante eventos episódicos con un coste computacional razonable.

2. Validar el modelo numérico.

3. Proporcionar un análisis completo de los procesos morfodinámicos que rigen la evolución de perfiles de playa basado en resultados numéricos. En particular:

   (a) Procesos morfodinámicos causantes del crecimiento de una barra de rompientes.

   (b) Procesos morfodinámicos causantes de la migración de la barra de rompientes.

   (c) Procesos morfodinámicos causantes del equilibrio de la barra de rompientes.

De acuerdo con los objetivos específicos, la metodología a seguir para alcanzar el objetivo principal consiste en desarrollar una nueva herramienta numérica para posteriormente emplearla en el análisis. La herramienta numérica se basa en el existente modelo numérico bidimensional IH2VOF, el cual se ha empleado con anterioridad para analizar hidrodinámica costera. Para abordar el transporte de sedimentos, se desarrollará un nuevo módulo acoplado a IH2VOF que incluya tanto el transporte de sedimentos como la gestión de los cambios batimétricos producidos por el mismo. Una vez desarrollado y validado el modelo, se utiliza para el análisis de procesos morfodinámicos como forma de obtener datos detallados. Además, el análisis se complementa con observaciones y conocimientos disponibles en la literatura científica.

Desarrollo del modelo

El desarrollo del modelo numérico da respuesta al primer objetivo específico de la tesis. En esta línea, se ha desarrollado un modelo de transporte de sedimentos Euleriano de una fase para sedimentos no cohesivos y se ha acoplado al modelo hidrodinámico RANS IH2VOF. El nuevo modelo numérico se ha denominado IH2VOF-SED. A continuación, se describen brevemente las ecuaciones de gobierno y algoritmos de resolución empleados en el modelo hidrodinámico y en el de transporte de sedimentos. Puede encontrarse una descripción detallada de los mismos en la versión completa de esta tesis (en inglés).

Modelo hidrodinámico

Las ecuaciones de gobierno del modelo hidrodinámico son las denominadas ecuaciones RANS bidmiensionales en el plano vertical (2DV):

$$\frac{\partial(\vec{U})}{\partial t} + \nabla \cdot (\vec{U} \otimes \vec{U}) = -\frac{\vec{\nabla} p}{\rho} + (\nu + \nu_t)\nabla^2 \vec{U} + \vec{S_M} \tag{1}$$

donde $\vec{U}$ es el vector velocidad, t es el tiempo, p la presión, ρ la densidad del fluido, ν y ν_t las viscosidades cinemáticas molecular y turbulenta y $\vec{S_M}$ el vector de fuerzas volumétricas, que generalmente incluye la gravitatoria en este tipo de aplicaciones.

Las ecuaciones RANS se basan en las ecuaciones de Navier-Stokes, que modelan el comportamiento de los fluidos. Respecto a las ecuaciones de Navier-Stokes, las RANS incluyen simplificaciónes que permite tener en cuenta el efecto de las fluctuaciones turbulentas en el flujo sin necesidad de resolverlas, lo cual resultaría tremendamente costoso. Resolviendo dichas ecuaciones se obtienen los campos de velocidad y presión en el dominio computacional, que en este caso es un perfil de playa. Una vez obtenidos los campos de velocidad y presión, es necesario modelar el transporte de ciertas magnitudes escalares relacionadas con el modelado de la turbulencia y el seguimiento de la posición de la superficie libre. En el caso del modelo de turbulencia, las ecuaciones de transporte son las k-ϵ. Para el seguimiento de la superficie libre se utiliza el método VoF (*Volume of Fluid*) para el cual se emplea una ecuación de transporte advectivo. Una característica distintiva del modelo IH2VOF es el tratamiento de contornos sólidos, que se lleva a cabo mediante el método *cut-cell*. Este método considera el grado de apertura de las caras y volúmen de cada celda (proporción de espacio disponible para el fluido) en el cálculo de flujos. Esto supone incluir ciertas modificaciones a la hora de discretizar las ecuaciones de gobierno.

La solución de las ecuaciones del modelo hidrodinámico se lleva a cabo mediante el denominado *Two-Step Projection Method*. Este método plantea una nueva ecuación, llamada *Poisson Pressure Equation*, o PPE, que debe resolverse para obtener el campo de presiones:

$$\nabla \cdot \left(\frac{\vec{\nabla} p^{\,n+1}}{\rho^n} \right) = \frac{1}{\Delta t} \nabla \cdot \left(\vec{\tilde{U}}^{n+1} \right) \tag{2}$$

donde los superíndices n y $n+1$ representan las variables actuales y las del paso de tiempo siguiente, respectivamente. $\tilde{U}$ es el campo intermedio de velocidades. De nuevo, los detalles de esta ecuación pueden encontrarse en la versión completa de la tesis.

Para resolver la PPE se realiza una discretización espacial empleando el Método de Diferencias Finitas, resultando en un un sistema de ecuaciones algebraico que se resuelve mediante el método de Gradiente Conjugado precondicionado con una factorización incompleta de Cholevsky. Como se indicó anteriormente, el método *cut-cell* para el tratamiento de contornos sólidos conlleva una adaptación de la discretización de la PPE para tener en cuenta el grado de apertura de las caras y el volumen de las celdas. Las ecuaciones de transporte del modelo de turbulencia y VoF se resuelven explícitamente empleando el Método de Diferencias Finitas para su discretización espacial.

Modelo de transporte de sedimentos

El modelo de transporte de sedimentos considera por separado los transportes por fondo y en suspensión, siendo las ecucaciones de gobierno distintas para cada uno.

En primer lugar, para el transporte por fondo se emplea la formulación empírica de (Engelund & Fredsoe, 1976):

$$\vec{Q_{bl}} = \frac{1}{6}\pi d P_{ef} \vec{U_b} \tag{3}$$

en la cual $\vec{Q_{bl}}$ es el vector de transporte por fondo, d el diámetro de partícula, P_{ef} es la proporción de partículas en movimiento y $\vec{U_b}$ es el vector de velocidad de las partículas de sedimento.

Por otra parte, el transporte en suspensión se modela con una ecuación de transporte advectivo-difusivo:

$$\frac{\partial C}{\partial t} = \nabla \cdot \left[(\vec{U} + \vec{w_s})C\right] + \nabla \cdot \left[\left(\frac{\nu + \nu_t}{\sigma_c}\right)\vec{\nabla} C\right] \tag{4}$$

donde C es la concentración de sedimento, $\vec{w_s}$ el vector de velocidad de caida del sedimento y σ_c el número de Schmidt del sedimento.

Además de las ecuaciones de transporte de sedimento, el nuevo módulo incluye la gestión del desplazamiento del fondo marino. Para obtener los desplazamientos del fondo se realiza una balance de volumen de sedimento en cada segmento del mismo. Una vez obtenida la varición del fondo, se modifican los parámetros de apertura de las caras y volumen en las celdas, de modo que el modelo hidrodinámico considere la variación del fondo en la resolución del siguiente paso de tiempo.

La solución de la ecuacuón empírica de transporte por fondo exige conocer la velocidad de fricción, la cual deriva del campo de velocidades proporcionado por el modelo hidrodinámico. En este sentido, se ha implementado un método para obtener dicha velocidad de fricción compatible con el método *cut-cell* de tratamiento de contornos sólidos. Una vez conocida la velocidad de fricción, se pueden obtener directamente las magnitudes de las que depende el transporte por fondo. Posteriormente, el volumen de sedimento acumulado en cada segmento del fondo se obtiene como la divergencia de este transporte.

En cuanto a la solución del transporte en suspensión, se plantea una estrategia explícita que consta de una discretización espacial empleando el Método de Volúmenes Finitos y otra temporal empleando el método Runge-Kutta de cuarto grado. En primer lugar, la discretización espacial conduce a una ecuación diferencial ordinaria que modela la evolución temporal de la concentración de sedimento en cada celda. Posteriormente, para determinar la concentración en un instante determinado, se aplica la discretización temporal para llegar a una ecuación algebraica que se resuelve explícitamente. A lo largo de este procedimiento, se obtienen también los flujos a través de las caras de las celdas que intersectan el fondo marino, los cuales constituyen el intercambio de sedimento entre agua y fondo y permiten obtener el volumen de sedimento ganado (depositado) o perdido (erosionado) en cada segmento del fondo. Cabe destacar que la discretización espacial requiere la implementación de varios esquemas de interpolación para obtener los valores de variables intervinientes en las caras de las celdas sin que se generen inestabilidades. Estos esquemas se detallan en la versión extensa, en inglés, de la tesis.

Una vez conocidas las cantidades de sedimento acumuladas en cada segmento del fondo por los dos mecanismos de transporte considerados, se realiza el balance de sedimento para obtener el desplazamiento del fondo. Esta resolución es relativamente

simple y no requiere de esquemas de discretización complejos. Sin embargo, la modificación de los parámetros de celda parciales requiere derivar relaciones analíticas para asignar cambios en la apertura de las caras partiendo de unos valores iniciales y de la variación en la posición del fondo en los laterales de la celda. Dichas relaciones analíticas son puramente geométricas. Además, para evitar inestabilidades numéricas debidas a valores excesivamente bajos de la apertura de las celdas, se establecen valores mínimos de apertura de celda a partir de los cuales se cierra la celda completamente.

Finalmente, los trabajos de desarrollo realizados incluyen una paralelización del modelo hidrodinámico. En particular, la resolución del sistema de ecuaciones resultante de discretizar la PPE se puede resolver en la nueva versión del modelo empleando varios procesadores en paralelo. Esto ayuda a reducir significativamente el tiempo computacional.

Una vez realizados los desarrollos anteriores, se considera cumplido el primer objetivo específico de la tesis.

Validación del modelo

Con la finalidad de valorar las capacidades del modelo para proporcionar resultados fiables, se realiza una validación frente a datos obtenidos en ensayos de laboratorio. Se han seleccionado tres casos de validación con diferentes escalas espaciales. El primero consiste en un ensayo de rotura de ondas solitarias sobre una pendiente plana de hormigón, y proporciona resultados de superficie libre y tensiones tangenciales ejercidas sobre el fondo. Esto permite verificar que la velocidad de fricción, directamente relacionada con las tensiones tangenciales, es suficientemente precisa. Los otros dos experimentos tratan la evolución de un perfil de playa, proporcionando mediciones de la evolución del fondo, superficie libre, velocidades y concentración de sedimento. Estos dos experimentos sirven para establecer el grado de precisión en las predicciones de evolución morfológica del modelo numérico, además de verificar que los principales procesos morfodinámicos se reproducen adecuadamente.

En el primer caso de validación se reproduce numéricamente el experimento de (Sumer *et al.* , 2011). Se observa que el modelo numérico es capaz de reproducir la evolución de la superficie libre con un alto grado de precisión. En cuanto a las tensiones tangenciales, el modelo proporciona una aproximación que se considera suficientemente precisa para el tipo de estudios que se pretende abordar. Comparado con otros modelos existentes, el modelo desarrollado en esta tesis proporciona resultados de tensiones tangenciales menos precisos pero a un coste computacional mucho menor, que pasa a ser de varios dias a menos de 2 horas. En la Figura 8 se muestra una comparativa entre las tensiones tangenciales inducidas por la rotura de una onda solitaria en el ensayo de laboratorio ((Sumer *et al.* , 2011)), con el modelo numérico OpenFOAM ((Li *et al.* , 2019) y (Larsen & Fuhrman, 2019)) y con IH2VOF-SED.

En el segundo caso de validación, se realiza una comparación con resultados de evolución de un perfil de playa medidos en laboratorio ((Baldock *et al.* , 2011)) y obtenidos con otro modelo numérico similar basado en OpenFOAM ((Jacobsen & Fredsoe, 2014)). La validación se centra en la evolución morfológica del perfil de playa, que se midió cada 24 minutos. La comparativa muestra un alto grado de precisión del modelo numérico desarrollado en esta tesis, incluso superior a la conse-

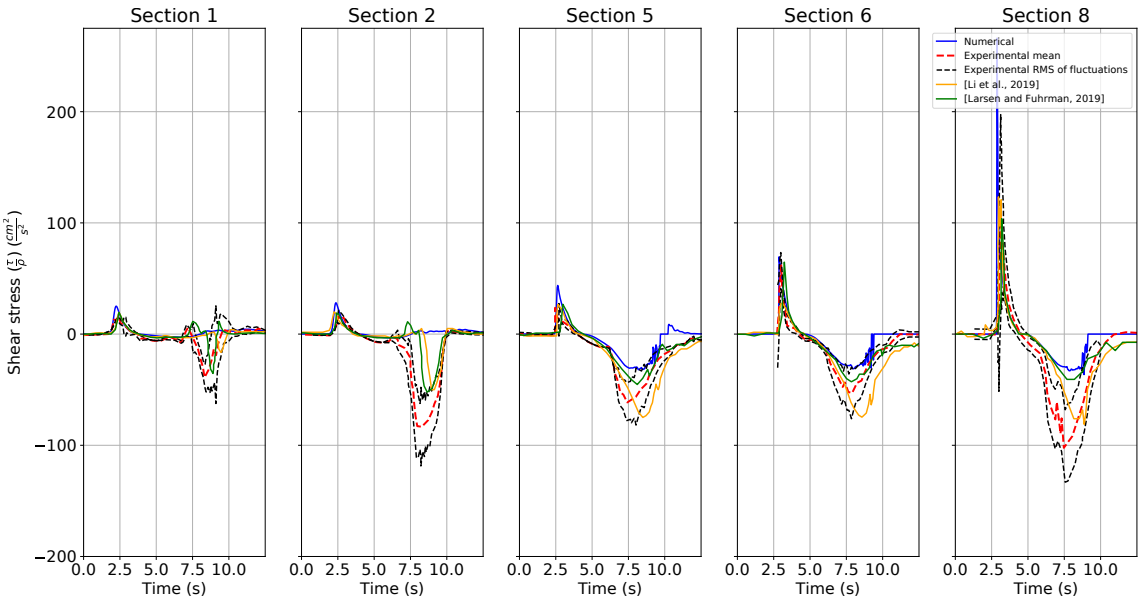

Figura 8: Evolución de la tensión tangencial en el fondo. Curva azul: resultados numéricos de IH2VOF-SED. Curva naranja: resultados de (Li *et al.* , 2019). Curva verde: resultados de (Larsen & Fuhrman, 2019). Curva roja a trazos: media de las tensiones tangenciales obtenidas en (Sumer *et al.* , 2011). Curvas negras a trazos: RMS de las fluctuaciones sumadas y restadas a la media de los resultados de (Sumer *et al.* , 2011).

guida con OpenFOAM. Adicionalmente, el coste computacional es del orden de 10 veces menor utilizando el nuevo modelo. En la Figura 9 se muestra una comparativa entre la batimetría medida en (Baldock *et al.* , 2011) y de simulaciones numéricas con XBeach, OpenFOAM ((Jacobsen & Fredsoe, 2014)) e IH2VOF-SED.

Finalmente, el tercer caso de validación es una comparativa con datos únicamente experimentales obtenidos en (van der A *et al.* , 2017). Se cubren variables adicionales con respecto al caso anterior, inlcuyendo, además de la evolución morfológica, mediciones de velocidad, superficie libre y concentración de sedimento. Las comparativas muestran resultados similares en las variables analizadas, aunque se constata una aproximación pobre de la concentración de sedimento cerca del fondo en el lado mar del punto de rotura. En la Figura 10 se muestra una comparativa entre la batimetría resultante en experimento y modelo numérico.

En definitiva, la validación del nuevo modelo numérico demuestra su capacidad para reproducir los procesos morfodinámicos más significativos en perfiles de playa bajo condiciones erosivas a diferentes escalas. Además, se observa una reducción muy notable del coste computacional. Con esto, se considera completado el segundo objetivo específico de la tesis.

Análisis de processos morfodinámicos

Una vez se cuenta con un modelo numérico capaz de reproducir los principales procesos morfodinámicos a un coste computacional razonable, se emplea el mismo para obtener información detallada que permita su análisis. Se realiza una simulación de la evolución de un perfil inicialmente plano bajo la acción de oleaje regular

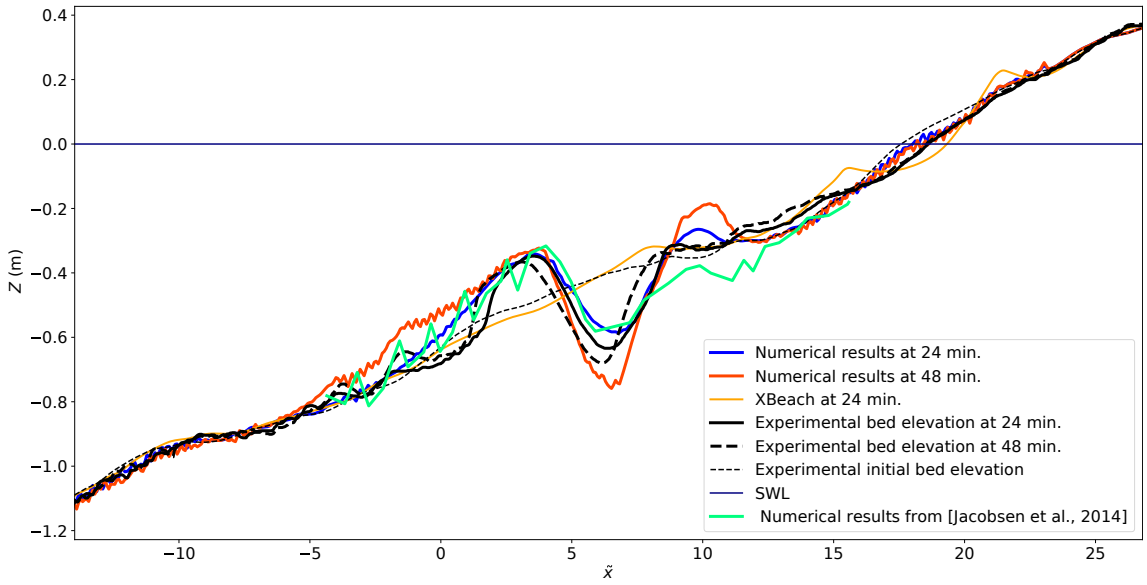

Figura 9: Batimetría resultante tras 24 y 48 minutos de oleaje. Curva azul: IH2VOF-SED tras 24 min. Curva roja: IH2VOF-SED tras 48 min. Curva verde: resultados numéricos de (Jacobsen & Fredsoe, 2014) tras 23 minutos. Curva naranja: XBeach (parámetros por defecto) tras 24 minutos. Curva negra: resultados de (Baldock *et al.* , 2011) tras 24 minutos. Curva negra a trazos, resultados de (Baldock *et al.* , 2011) tras 48 minutos. Curva negra a trazos finos: batimetría inicial.

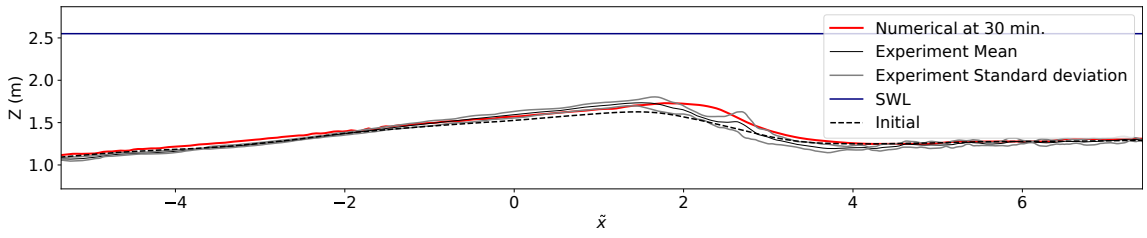

Figura 10: Perfil de playa tras 30 minutos. Curva roja: resultados numéricos. Curva negra: media de los resultados de (van der A *et al.* , 2017). Curvas grises a trazos: desviación estándar de los resultados de (van der A *et al.* , 2017)

suficientemente energético como para producir las condiciones erosivas que se dan en eventos episódicos. Se obtienen a lo largo de la misma variables de interés para el análisis de los procesos morfodinámicos intervinientes, tales como los campos de velocidad y concentración de sedimento o la forma del fondo. Con base en esta información detallada, se plantean una serie de hipótesis sobre el funcionamiento de dichos procesos que se contrastan con los propios resultados numéricos y con observaciones actualmente disponibles en la literatura científica. El análisis se divide en tres fases asociadas a la aparición y evolución de una barra de rompientes en el perfil de playa. Estas fases son: crecimiento, migración y equilibrio. En la Figura 11 se muestra la evolución del perfil de playa a lo largo de la simulación numérica y se indican, en diferentes colores, los inicios de cada una de las fases de la evolución del perfil.

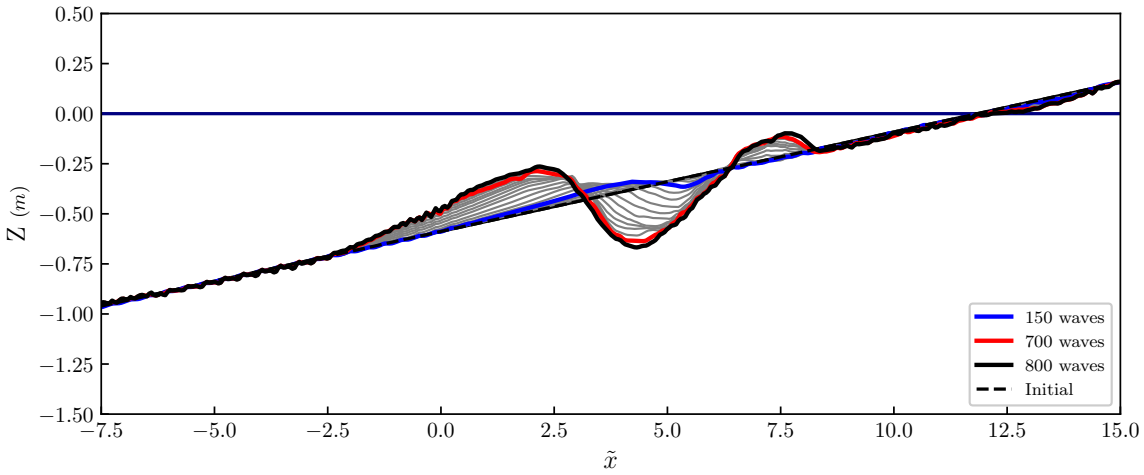

Figura 11: Evolución batimétrica a lo largo de la simulación numérica. Curva negra a trazos, perfil inicial. Curva azul, perfil al final de la fase de crecimiento. Curva roja, perfil al final de la fase de migración. Curva negra, perfil en equilibrio. Curvas grises, perfiles intermedios obtenidos cada 50 olas.

Adicionalmente, se ha realizado una comparación de resultados obtenidos para distintos números de Iribarren con objeto de valorar hasta qué punto las conclusiones de este análisis son aplicables a condiciones ambientales distintas. Los números de Iribarren se corresponden con mecanismos de rotura en decrestamiento, en voluta y con un caso intermedio entre ambos.

Fase de crecimiento

Durante la fase de crecimiento la barra de rompientes se genera en la zona de surf exterior, alrededor del punto de separación de la corriente de retorno. Mientras que el transporte en suspensión tiende a acumular sedimento en toda esta zona, especialmente entre el punto de rotura ($\tilde{x} = 0$) y el de separación ($\tilde{x} = 2{,}85$), el transporte por fondo contribuye al crecimiento únicamente en el lado tierra del punto de separación. Esta distribución de las contribuciones de transporte por fondo y en suspensión se muestran en la Figura 12.

El decalaje entre la posición del punto de separación y la zona en la que el transporte por fondo acumula sedmiento depende del sesgo de la velocidad y de la relación entre el transporte por fondo y velocidad de fricción a lo largo de la fase

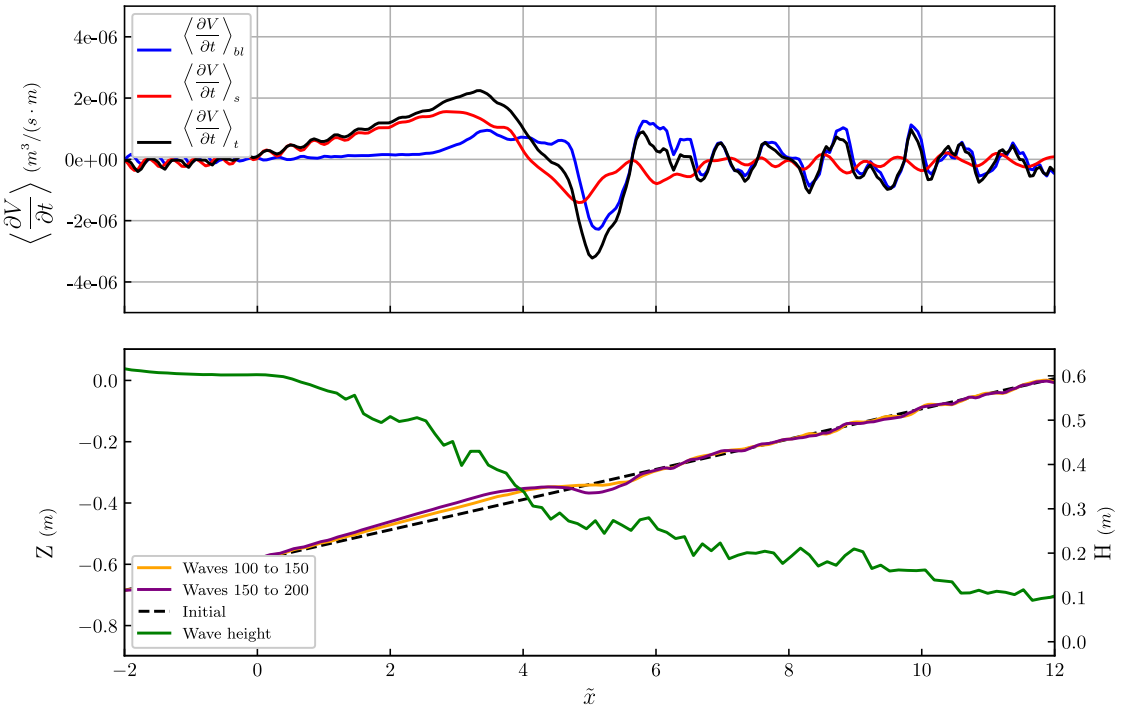

Figura 12: Panel superior (A): ratios de acumulación de sedimento promediados en el tiempo causados por los transportes por fondo y en suspensión entre las olas 100 y 150. Panel inferior (B): perfiles resultantes tras 100 y 150 olas y altura de ola media obtenida entre 150 y 200 olas.

del seno de la onda. Por una parte, la velocidad de fricción promediada en el tiempo es cero en el punto de separación, puesto que está directamente relacionada con la velocidad de corriente. Por otra parte, la velocidad de fricción al cubo promediada tiene un paso por cero hacia el lado onshore del punto de separación debido al sesgo de las velocidades (los picos son más altos que los senos). Sin embargo, el transporte por fondo no siempre es función de la velocidad de fricción cúbica, la relación varía entre lineal y cúbica. En el panel superior de la Figura 13 se representan las oscilaciones medias de superficie libre, velocidad de fricción y transporte por fondo en varias posiciones a lo largo de la zona de surf exterior. Se puede notar que entre $\tilde{x} = 0{,}5$ y $\tilde{x} = 2{,}5$ la velocidad de fricción promediada en el tiempo disminuye debido a una menor velocidad asociada con la cresta. Sin embargo, al avanzar por la zona de surf hacia el punto de plunge, la velocidad en el paso de seno comienza a aumentar ($\tilde{x} = 3{,}5$). En el panel inferior de la Figura 13, se muestra la relación entre transporte por fondo y velocidad de fricción en las mismas posiciones. Como se puede observar, la relación durante el paso del seno está en su mayoría dentro del rango cúbico, mientras que en el paso de cresta es lineal. Esto quiere decir que, una vez la velocidad de fricción durante el paso del seno empieza a aumentar, el transporte por fondo disminuye más rápido, llevando a un mayor gradiente horizontal del mismo y a una mayor tasa de acumulación por transporte por fondo a partir de $\tilde{x} = 3{,}5$. Esto explica el decalaje entre la zona de acumulación del transporte por fondo y el punto de separación de la corriente de retorno.

En cuanto al transporte en suspensión, se identifican dos mecanismos principales: el producido por el *steady streaming* en la zona de asomeramiento y surf exterior,

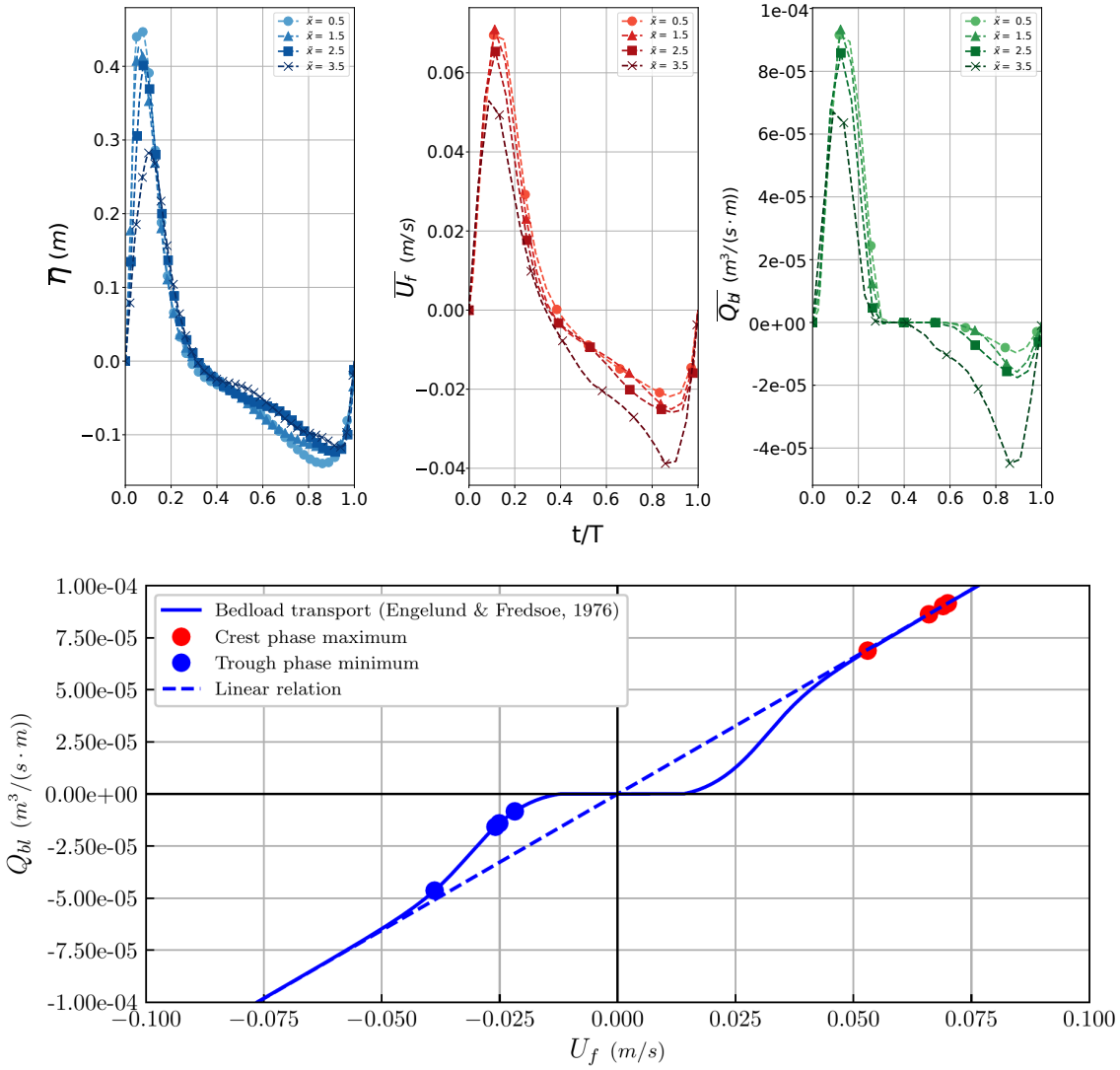

Figura 13: Panel superior (A): oscilaciones medias de superficie libre, velocidad de fricción y transporte por fondo obtenidas en diferentes posiciones a lo largo de la zona de surf exterior. Curvas azules, superficie libre. Curvas rojas, velocidad de fricción. Curvas verdes, transporte por fondo. Panel inferior (B): relación entre velocidad de fricción y transporte por fondo. Curva azul, transporte por fondo, obtenido con (Engelund & Fredsoe, 1976). Curva azul a trazos, relación lineal entre velocidad de fricción y transporte por fondo. Puntos rojos, transporte por fondo correspondiente al paso de cresta en las distintas posiciones del panel (A). Puntos azules, correspondientes al paso del seno. Obtenidas entre las olas 100 y 150.

dirigido hacia la costa, y el producido por la corriente de retorno, en la zona de surf interior y dirigido hacia el mar. Las dos formas de transporte convergen, aproximadamente, en el punto de separación, dando lugar a una acumulación de sedimento a su alrededor. Para comprender mejor el transporte en suspensión, se realiza un análisis bidimensional de los campos promediados de velocidad y concentración de sedimento así como de la covarianza de los mismos.

El campo promedidado de velocidad, mostrado en el panel superior de la Figura 14, evidencia las dos corrientes principales en contacto con el fondo: la corriente de retorno en la zona de surf interior, dirigida hacia el lado mar, y el *steady streaming* en la zona de asomeramiento y de surf exterior, dirigida hacia el lado tierra. Como se indicó anteriormente, las dos corrientes coinciden en el punto de separación de la corriente de retorno. En el panel inferior de la Figura 14 se muestran las oscilaciones de velocidad medias en el punto de despegue ($\tilde{x} = 2{,}85$) y en sus lados mar y tierra ($\tilde{x} = 1{,}5$ y $\tilde{x} = 4{,}5$, respectivamente). Se puede observar también que, aunque la velocidad de fricción promediada en el tiempo tiene un valor relativamente bajo, las velocidades de fricción instantáneas alcanzan valores significativos en estos puntos.

Las principales variables que pueden reforzar o atenuar estas dos corrientes son la asimetría de las ondas, su altura, el flujo másico hacia la costa producido por las crestas de los rompientes y la distribución de tensiones tangenciales del fluido en la vertical. Del análisis de estas variables influyentes se deduce que, en una batimetría plana, el punto de separación se localiza entre el punto de rotura y el de *plunge*, en el que la cresta del rompiente impacta contra la superficie del agua. Por una parte, el *steady streaming* tiene una velocidad máxima en el punto de rotura, y pierde fuerza en la zona de surf exterior al disminuir la altura de ola. Por otra, la corriente de retorno tiene una velocidad máxima en el punto de *plunge*, y disminuye en la zona de surf exterior debido al aumento de la profundidad. En consecuencia, la compensación entre estas dos corrientes sucede en la zona de surf exterior.

En cuanto al campo promediado de concentración de sedmiento, representado en la Figura 15, se observan diferencias en la distribución vertical de la misma debidas a los distintos mecanismos de mezcla vertical que se dan en las zonas del perfil de playa. En la zona de asomeramiento, la concentración de sedimento lejos del fondo es muy baja, dado que no existen mecanismos fuertes de mezcla vertical en la misma. En la zona de surf exterior, las velocidades verticales producidas en el proceso de rotura generan una fuerte advección de sedimento desde las capas inferiores, donde se erosiona, a las superiores. Esto resulta en una distribución de concentración de sedimento más uniforme. En la zona de surf interior, los vórtices inducidos por el proceso de rotura también suponen un efectivo mecanismo de mezcla vertical, que mantiene un perfil de concentración de sedimento más uniforme. Cabe destacar que en el punto de *plunge* se encuentran altos valores de concentración de sedimento relacionados con las altas velocidades de fricción producidas cuando la cresta de la ola penetra en el agua y alcanza el fondo. Este fenómeno está directamente relacionado con la formación del seno alrededor de este punto,

La covarianza entre velocidad y concentración de sedimento da lugar a los llamados efectos intra-ola. Como se puede notar en los perfiles de covarianza en la Figura 16, ésta es alta cerca del fondo en las zonas de asomeramiento y de surf exterior a causa de la alta correlación entre velocidad y concentración de sedimento. En contraste, los efectos intra-ola son menos significativos lejos del fondo y, en general, en la zona de surf interior. Esto permite establecer una distinción entre zonas donde el

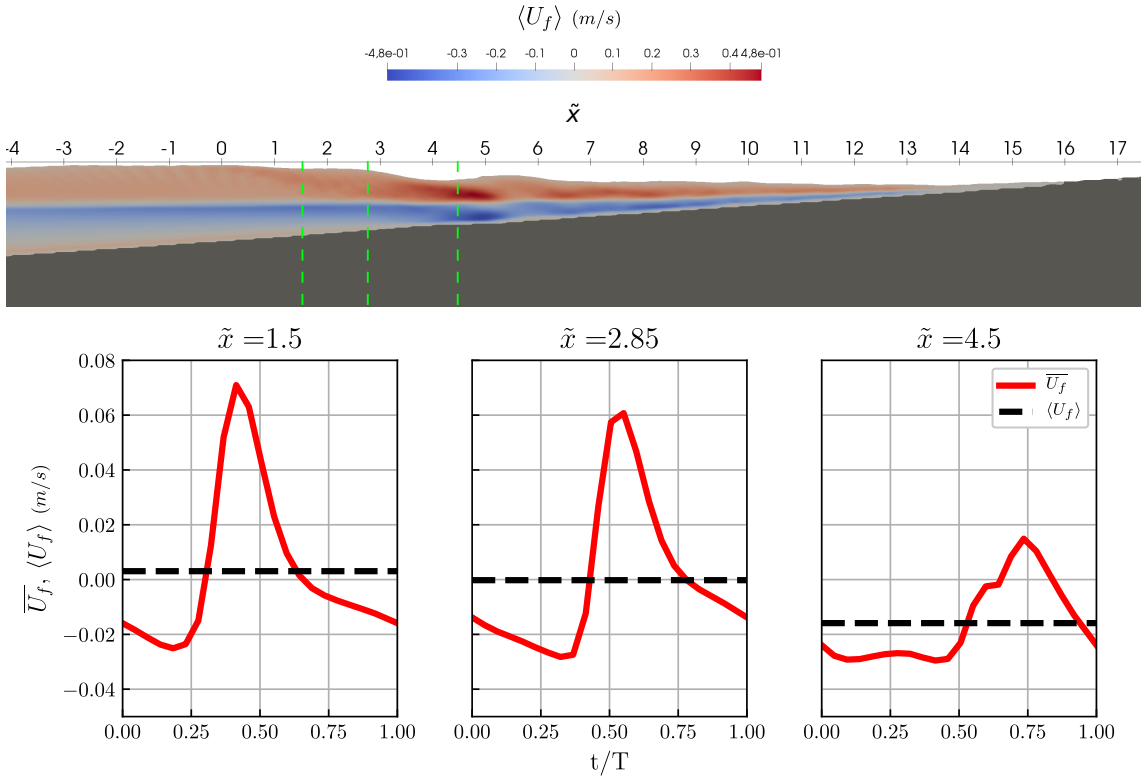

Figura 14: Promediado en el tiempo del campo de velocidades y oscilación media de la velocidad de fricción alrededor del punto de despegue. Panel superior (A): campo de velocidad promediado en el tiempo. Panel inferior (B): oscilaciones medias de velocidad de fricción en el punto de despegue y a su alrededor. Curvas rojas, oscilación media de velocidad de fricción. Curvas negras a trazos, velocidad de fricción promediada en el tiempo. El campo promedio de velocidad se obtuvo entre las olas 100 y 120, las oscilaciones medias entre las olas 100 y 150.

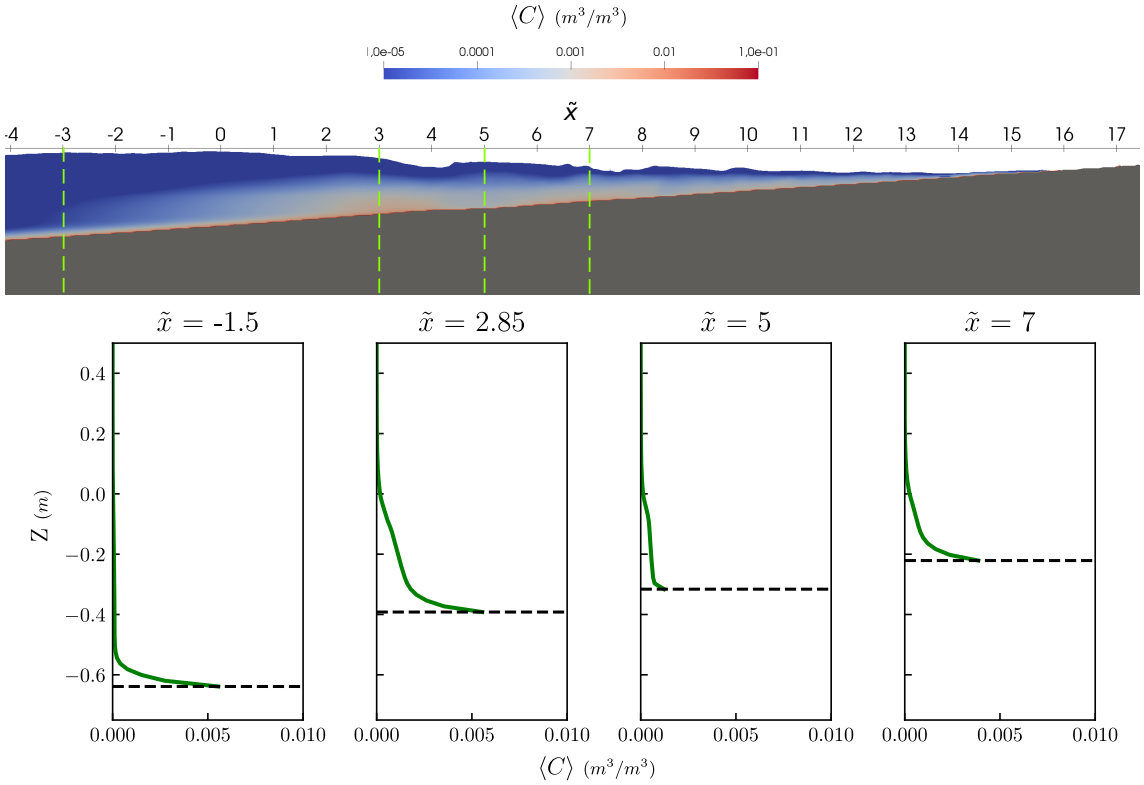

Figura 15: Panel superior (A): promediado en el tiempo del campo de concentración de sedimento. Panel inferior (B): perfiles de concentración de sedimento promediados en el tiempo en distintas posiciones a lo largo del perfil (indicadas en el panel superior). El campo de concentracion de sedimento promediado en el tiempo se obtuvo entre las olas 100 y 120. Los perfiles de concentración de sedimento se obtuvieron entre las olas 100 y 150.

flujo está principalmente condicionado por el sistema de corrientes, siendo aceptable un análisis de procesos morfodinámicos basado en campos promediados, y zonas donde los efectos intra-ola son importantes, en las cuales deben incluir la covarianza entre ambas variables para representar adecuadamente los procesos morfodinámicos relevantes.

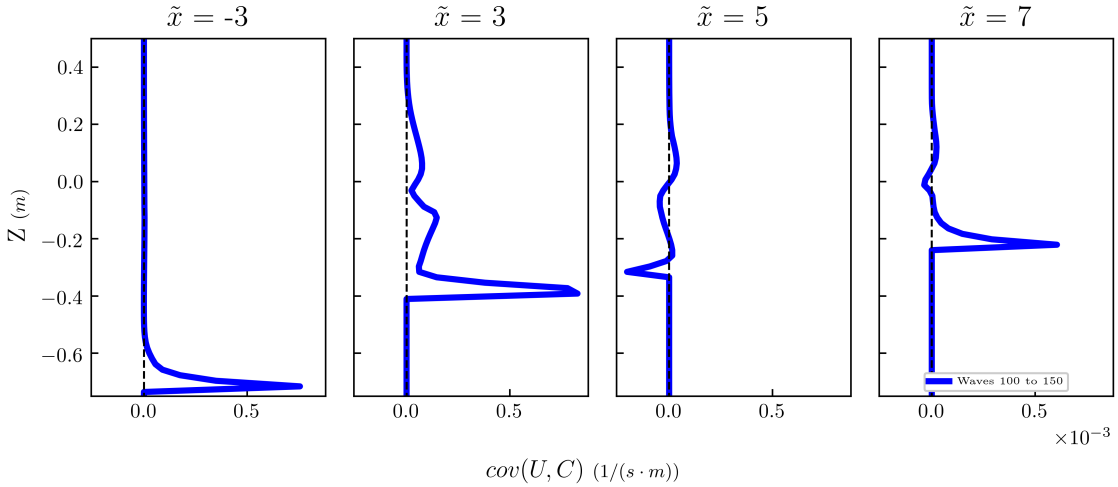

Figura 16: Perfiles verticales de covarianza entre velocidad horizontal y concentración de sedimento en diferentes posiciones a lo largo del perfil de playa. Obtenidos entre las olas 100 y 150.

Finalmente, de la observación del transporte de sedimento en suspensión se puede deducir el patrón de circulación del mismo, representado en la Figura 17. Éste lleva a la anteriormente comentada acumulación de sedimento a lo largo de la zona de surf exterior, entre el punto de rotura y el de separación. El sedimento erosionado en la zona de asomeramiento es llevado por el *steady streaming* hacia la zona de surf exterior. Por otro lado, el sedimento erosionado en las zonas de swash y surf interior es transportado hacia el lado mar por la corriente de retorno. Las dos corrientes coinciden en el punto de separación de la corriente de retorno, donde ésta se despega del fondo y fluye cerca de la superficie. La corriente de retorno separada transporta sedimento por las capas superiores de la zona de surf exterior y de asomeramiento. A medida que la corriente pierde fuerza, el sedimento se va depositando por su propio peso y cae hacia las capas inferiores, donde el *steady streaming* lo transporta nuevamente a la zona de surf exterior.

Fase de migración

En el análisis anterior se establece una relación entre la posición del punto de separación y la zona donde se tiende a acumular el sedimento. Durante la migración de la barra de rompientes, la contribución del transporte por fondo se desplaza hacia el lado mar como resultado de la migración del punto de separación. En la Figura 18 se puede observar este fenómeno.

En el análisis de la fase de migración se establece el motivo por el cual se produce la migración del punto de separación y, consecuentemente, la de la barra de rompientes. Como se puede observar en los resultados de perfiles de velocidad promedios del modelo numérico (Figura 19), se produce un aumento en la velocidad de

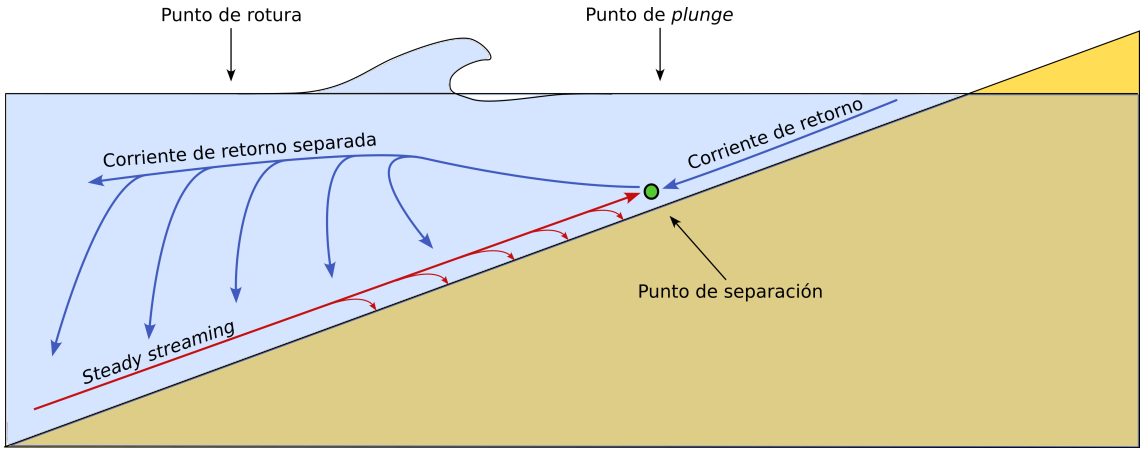

Figura 17: Representación esquemática de los principales flujos de sedimento en el perfil de playa durante la fase de crecimiento de la barra.

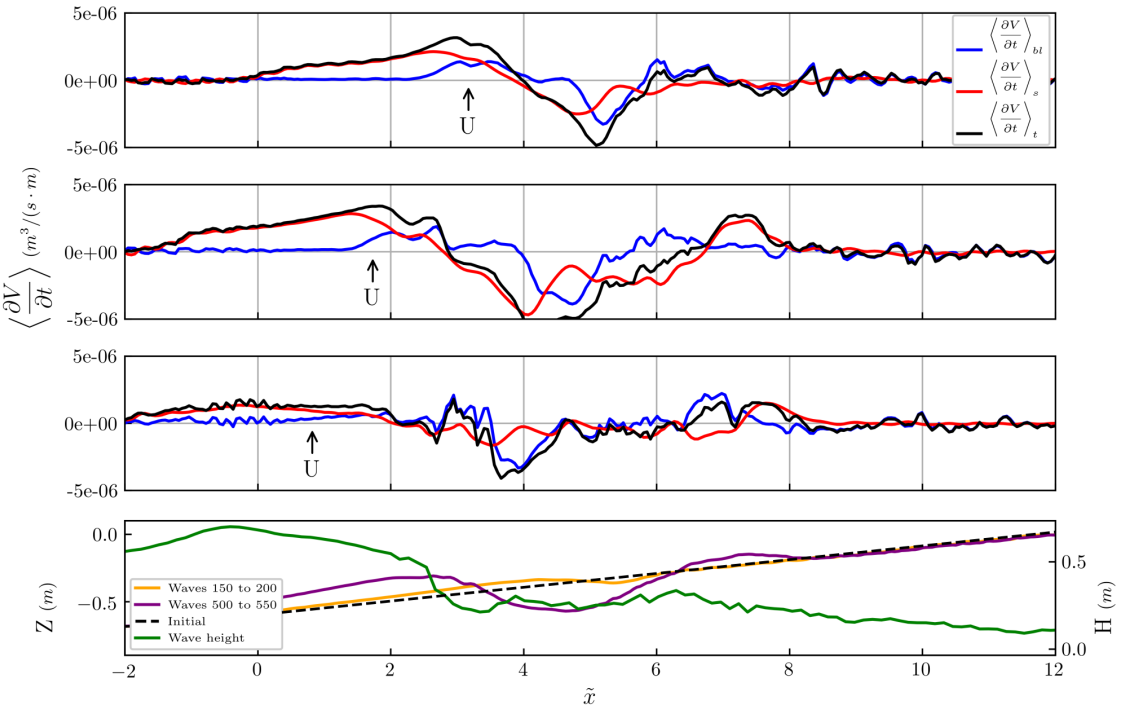

Figura 18: Ratio de acumulación de sedimento debido a los transportes por fondo y en suspensión. Panel superior: olas 100 a 150. Panel central-superior: olas 300 a 350. Panel central-inferior: olas 500 a 550. Panel inferior: Posición del fondo tras 150 y 500 olas y distribución de altura de ola durante la fase de migración. Las flechas negras indican la posición media del punto de despegue en cada intervalo.

la corriente de retorno cerca del fondo en la zona del seno (ver $\tilde{x} = 3{,}5$). Esto causa el desplazamiento hacia el lado mar del punto de separación, dado que la corriente de retorno es capaz de compensar al *steady streaming* en una mayor distancia. Este aumento de la velocidad de la corriente de retorno se debe a una redistribución de los esfuerzos tangenciales en el fluido, que a su vez es consecuencia de la aparición del seno frente a la barra de rompientes.

De acuerdo con lo anteriormente comentado, el desplazamiento del punto de separación implica que la zona en la que el transporte por fondo acumula sedimento también se desplaza hacia el lado mar, contribuyendo a la migración de la barra de rompientes.

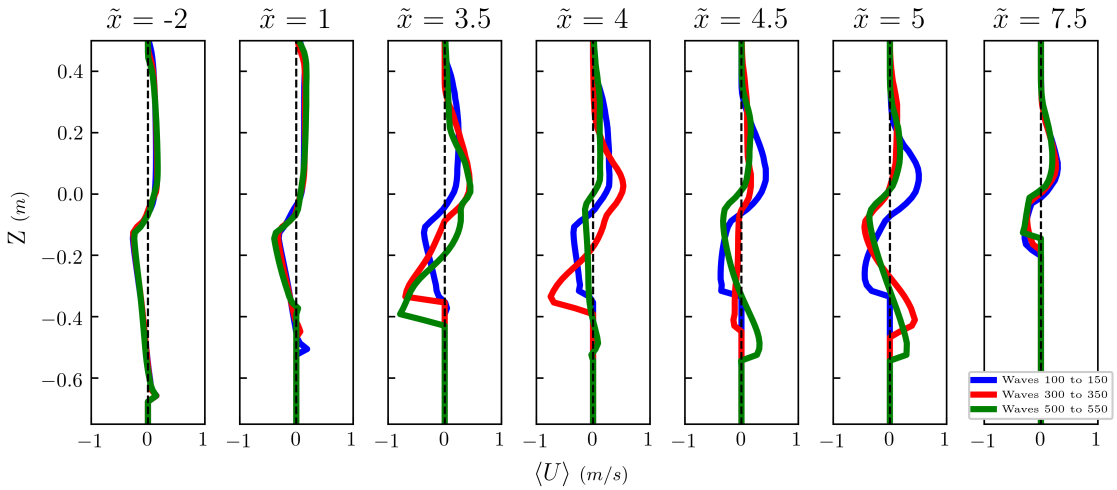

Figura 19: Perfiles de velocidad promediada en el tiempo para diferentes intervalos a lo largo de la simulación y en distintas posiciones del perfil de playa. Curva azul, olas 100 a 150. Curva roja, olas 300 a 350. Curva verde, olas 500 a 550.

En cuanto al transporte en suspensión, los perfiles de flujo de sedimento promediados en el tiempo se representan en la Figura 20. Se observa una reducción del flujo de sedimento cerca del fondo en la zona de surf exterior respecto a la fase de crecimiento ($\tilde{x} = 1$). Además, los resultados muestran un incremento del flujo de sedimento producido por la corriente de retorno separada en esta misma zona. Sin embargo, el flujo de sedimento de la corriente de retorno en la zona de surf interior disminuye ($\tilde{x} = 7{,}5$). El punto en el cual los transportes dirigidos hacia el lado tierra, asociado al *steady streaming*, y hacia el lado mar, asociado a la corriente de retorno, se desplaza también hacia el lado mar siguiendo la migración del punto de separación.

Los perfiles de concentración varían significativamente respecto a la fase de crecimiento. La concentración de sedimento en las capas superiores de la zona de surf exterior aumenta, lo cual explica el mayor flujo de sedimento asociado a la corriente de retorno separada. En el seno de la barra de rompientes, la concentración de sedimento es prácticamente nula al final de la fase de migración ($\tilde{x} = 4$ a $\tilde{x} = 5$).

Para determinar las causas de estas modificaciones de los perfiles promediados de concentración de sedimento, se examina la evolución de la velocidad de fricción, concretamente de sus valores máximos y mínimos, siendo el máximo dirigido hacia la costa y el mínimo hacia el mar. Éstos pueden observarse en la Figura 22. Sobre la barra de rompientes, entorno a $\tilde{x} = 1{,}5$, la velocidad de fricción máxima aumenta

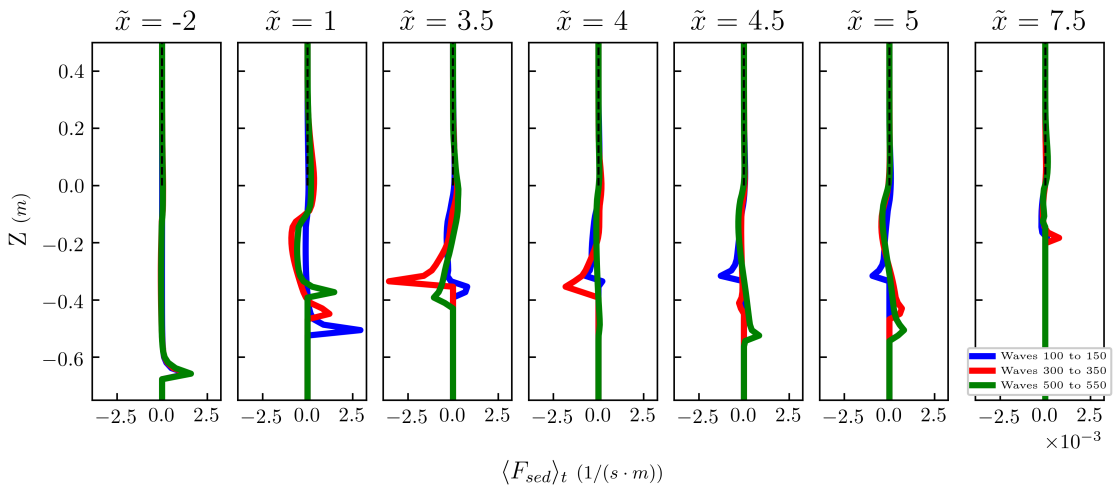

Figura 20: Evolución de los perfiles de flujo advectivo horizontal de sedimento promediado en el tiempo. Curva azul: olas 100 a 150. Curva roja: olas 300 a 350. Curva verde, olas 500 a 550.

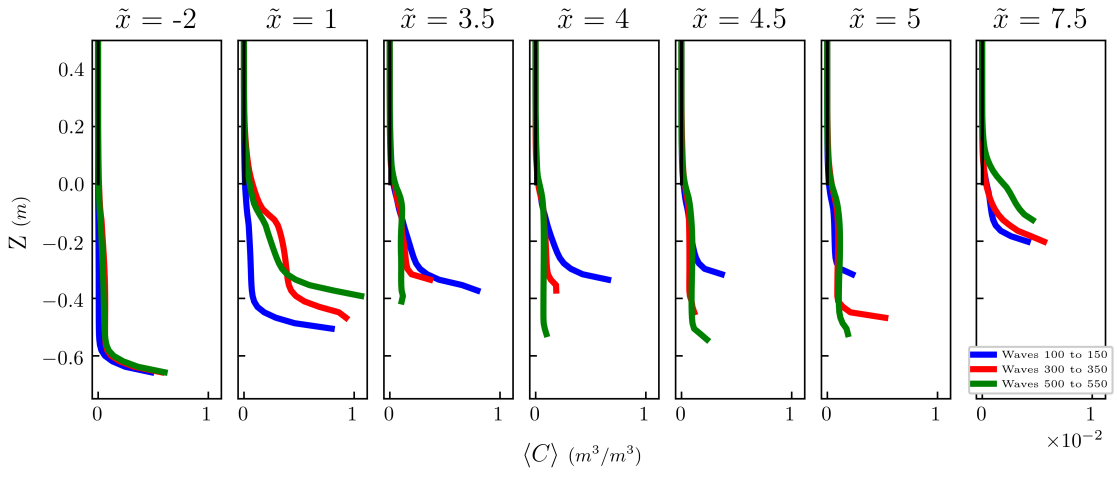

Figura 21: Perfiles de concentración de sedimento promediada en el tiempo para diferentes intervalos a lo largo de la simulación y en distintas posiciones del perfil de playa. Curva azul, olas 100 a 150. Curva roja, olas 300 a 350. Curva verde, olas 500 a 550.

conforme la barra aumenta su tamaño a causa de la menor profundidad. De esta manera, se establece un mecanismo limitante para el crecimiento de la barra: un crecimiento excesivo llevaría a altos valores de velocidad de fricción, que provocarían una rápida erosión de la barra con la consecuente reducción de su tamaño. En cuanto al seno (alrededor de $\tilde{x} = 4$), el valor de velocidad de fricción máxima disminuye debido a la mayor profundiad, dado que las altas velociades producidas por el impacto de la cresta del rompiente se disipan antes de alcanzar la posición del fondo. Sin embargo, el valor mínimo aumenta debido a la mayor fuerza de la corriente de retorno anteriormente comentada.

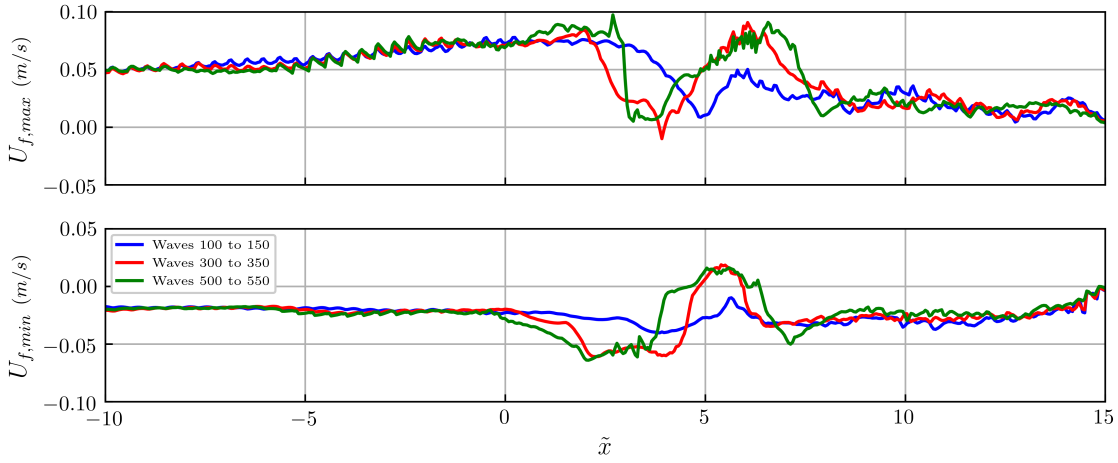

Figura 22: Evolución de la velocidad de fricción máxima y mínima a lo largo del perfil de playa durante varios intervalos. Curva azul, olas 100 a 150. Curva roja, olas 300 a 350. Curva verde, olas 500 a 550.

En cuanto a los efectos intra-ola, éstos se refuerzan en la zona de la barra de rompientes en la segunda mitad de la fase de migración, incrementando el flujo de sedimento dirigido hacia tierra en esta zona a pesar de la disminución de la fuerza del *steady streaming*. Esta tendencia, como se verá, continua durante la fase de equilibrio. En el seno, los efectos intra-ola se reducen hasta ser prácticamente nulos. En la zona de surf interior, éstos generan un transporte hacia la costa que compensa el producido por la corriente de retorno. Ésto puede observarse en la Figura 23.

Los flujos de sedimento durante la fase de migración, resultantes de los fenómenos anteriormente comentados, se representan esquemáticamente en la Figura 24.

Fase de equilibrio

Una vez el perfil de playa alcanza una configuración de equilibrio para las condiciones ambientales existentes, la contribución total de transporte por fondo y en suspensión a la variación del fondo es casi nula. En la barra de rompientes el transporte por fondo tiende a hacer crecer la barra mientras que el de suspensión tiende a erosionarla, de modo que ambos se compensan. En la zona del seno ambos transportes son despreciables. Adicionalmente, se observa que el punto de separación de la corriente de retorno no continúa migrando hacia el lado mar. Estos efectos pueden observarse en la Figura 25.

En lo que respecta al transporte por fondo, como se muestra en la Figura 26 entre $\tilde{x} = 2$ y $\tilde{x} = 6$, se produce una disminución del gradiente horizontal de velocidad

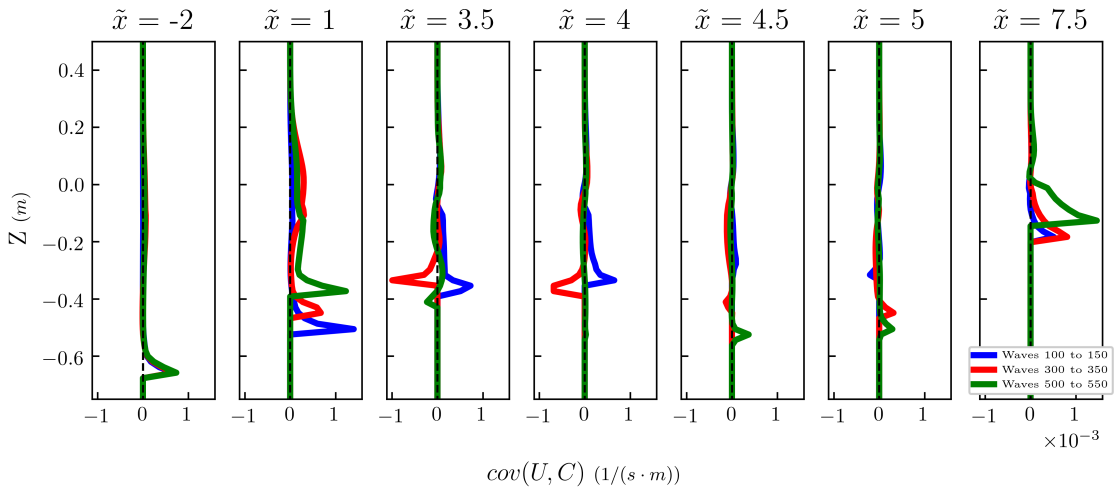

Figura 23: Evolución de la covarianza entre velocidad horizontal y concentración de sedimento. Curva azul, olas 100 a 150. Curva roja, olas 300 a 350. Curva verde, olas 500 a 550.

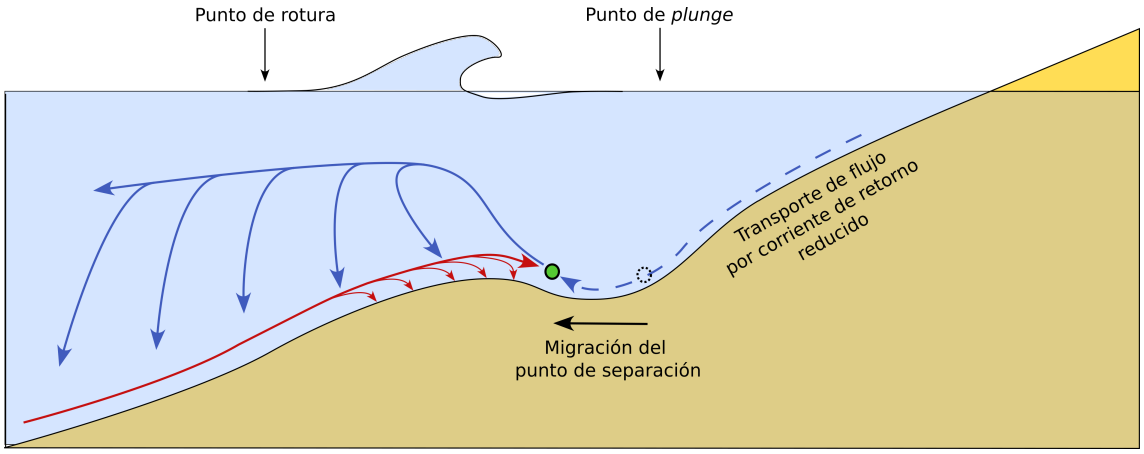

Figura 24: Representación esquemática de los princpiales flujos de sedimento durante la migración de la barra.

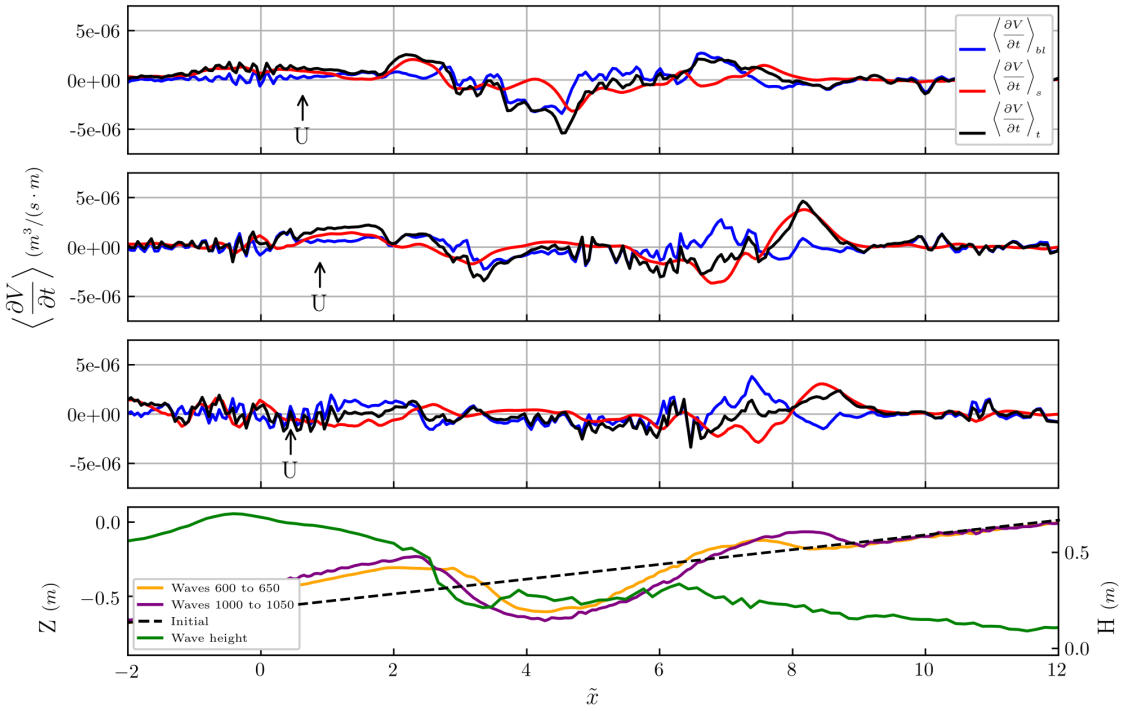

Figura 25: Ratios de acumulación de sedimento debidos a los transportes por fondo y en suspensión una vez alcanzada la configuración de equilibrio. Panel superior: olas 600 a 650. Panel central-superior, olas 800 a 850. Panel central-inferior, olas 1000 a 1050. Panel inferior: posición del fondo tras 650 y 1050 olas y distrbución de la altura de ola en la fase de equilibrio. Las flechas negras indican la posición media del punto de despegue en cada intervalo.

de fricción media que, a su vez, deriva en una disminución del efecto del transporte por fondo. Ésto es causado por una menor velocidad de la corriente de retorno en la region del seno, la cual disminuye como consecuencia de la amplicación del mismo y el consiguiente aumento del área a través de la cual fluye el exceso de agua en la zona de surf producido por la rotura. Tras 800 olas, los cambios en los perfiles medios de velocidad son muy limitados. Esto puede notarse en los perfiles de velocidad promediada en el tiempo, que se muestran en la Figura 27.

No obstante, el gradiente horizontal de velocidad de fricción no puede desaparecer completamente, y siempre tendrá un valor negativo a lo largo de la zona de surf exterior debido a la pérdida de energía en la rotura. Por tanto, siempre que la velocidad de fricción sea suficientemente alta como para movilizar el sedimento, existirá una tendencia por parte del transporte por fondo a acumular sedimento en la barra de rompientes.

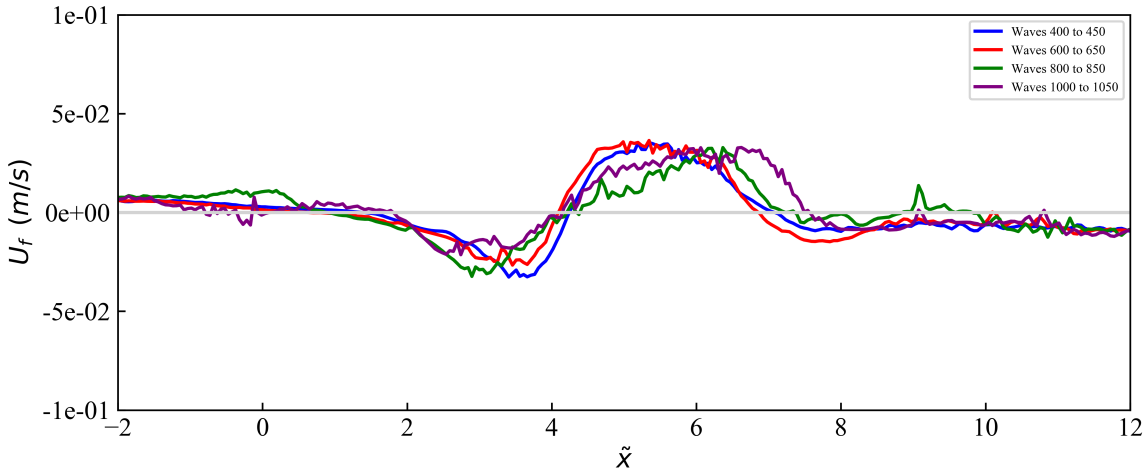

Figura 26: Velocidad de fricción promediada en el tiempo para diferentes intervalos de la fases de migración y equlibrio. Curva azul, olas 400 a 450. Curva roja, olas 600 a 650. Curva verde, olas 800 a 850. Curva morada, olas 1000 a 1050.

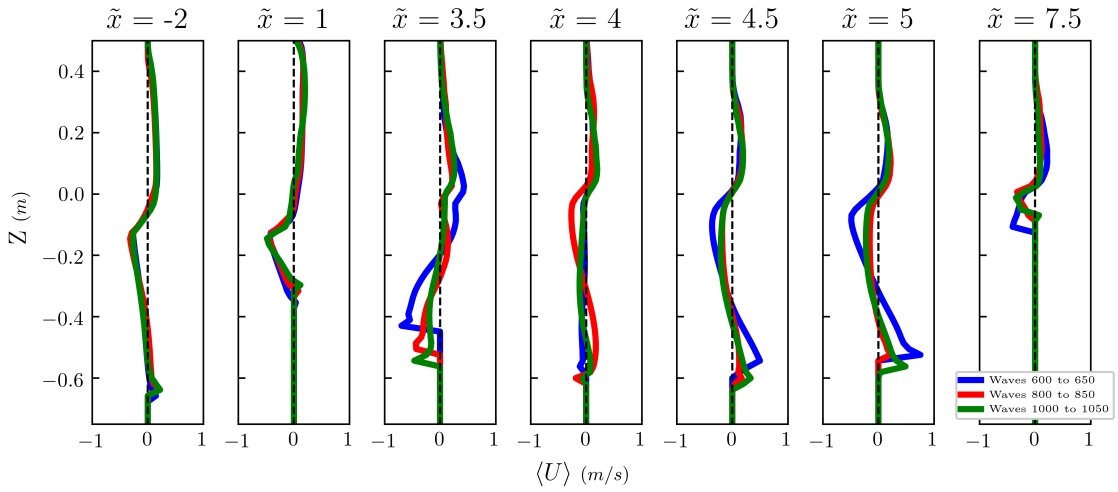

Figura 27: Perfiles de velocidad horizontal promediados en el tiempo. Curva azul, olas 600 a 650. Curva roja, olas 800 a 850. Curva verde, olas 1000 a 1050.

En cuanto a la contribución del transporte en suspensión, la cantidad de concentración de sedimento en el seno es muy baja. Sobre la barra, la concentración sigue incrementándose hasta alcanzar un valor constante. Dicho incremento se debe al aumento de la velocidad de fricción durante el paso de la cresta como resultado del crecimiento de la barra, que lleva a altas cantidades de sedimento erosionado. Por otra parte, la menor concentración en el seno se debe a la reducción de las velocidades en la posición del fondo por el incremento de profundidad. Los flujos de sedimento siguen el mismo patrón que en la fase de migración. Se observa además que la integral del flujo de sedimento medio a lo largo de la columna de agua tiende a cero a lo largo de las zonas de shoaling y surf, como se muestra en la Figura 28.

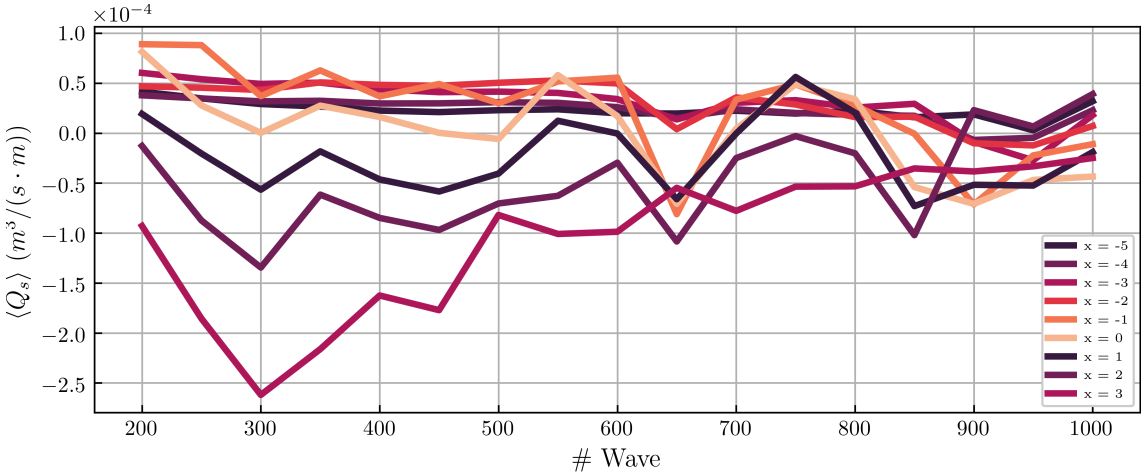

Figura 28: Evolución del flujo de sedimento promediado en el tiempo e integrado en la vertical en varias posiciones a lo largo de las zonas de asomeramiento y surf exterior.

Esto evidencia que el fujo hacia el lado tierra producido por el *steady streaming* se compensa con el flujo hacia el lado mar de la corriente de retorno separada. En la zona de surf interior, los flujos son prácticamente nulos debido a la baja concentración de sedimento. Por tanto, se puede notar que la forma en la que se alcanza el estado de equilibrio en la zona de asomeramiento y surf exterior es distinta a la de la zona de surf interior. En las primeras, se alcanza debido a una compensación entre los flujos asociados al *steady streaming*, a efectos intra-ola y a la corriente de retorno separada que llevan a una pequeña erosión en la zona de la barra que compensa la acumulación debida al transporte por fondo. En la segunda, se debe a la disminución de concentración de sedimento debida a la menor velocidad de fricción en el fondo.

Los efectos intra-ola cobran importancia en la zona de la barra de rompientes, donde son responsables de la mayoría del transporte en suspensión. En la zona del seno, son prácticamente nulos como consecuencia de la baja concentración de sedimento. Esto puede observarse en la Figura 29 en las posiciones $\tilde{x} = 1$ y $\tilde{x} = 3{,}5$, respectivamente.

Examinando la batimetría en la configuración de equilibrio, se observa que la altura de la barra de rompientes se mantiene constante, puesto que está limitada por la máxima reducción de la profundidad que puede mantenerse. Si se se supera esta altura de equlibrio, la erosión producida por el paso de las crestas tiende a reducir la barra hasta alcanzar, nuevamente, su tamaño de equilibrio. Por otra parte, como

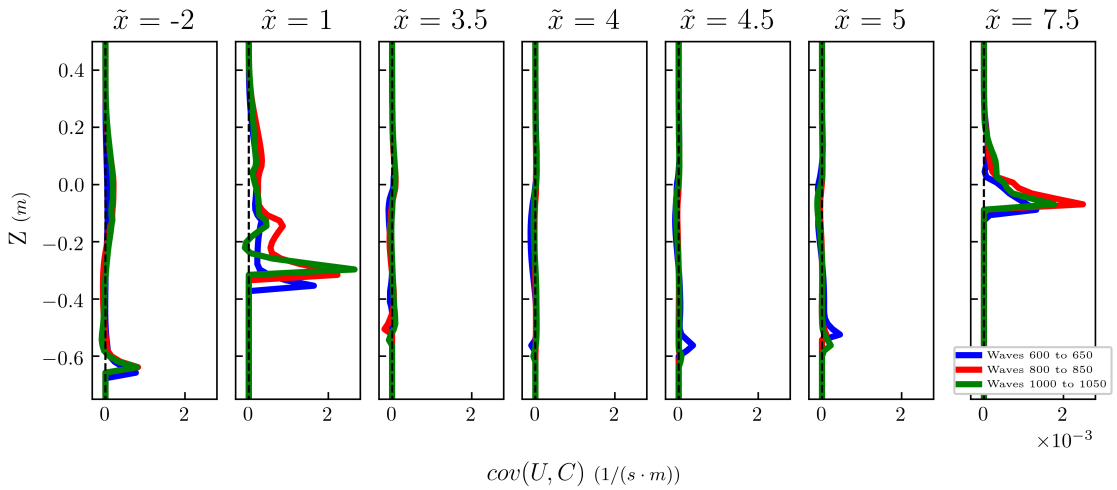

Figura 29: Evolución de la covarianza entre velocidad horizontal y concentración de sedimento. Curva azul, olas 600 a 650. Curva roja, olas 800 a 850. Curva verde, olas 1000 a 1050.

se indicó anteriormente, la profundidad de equilibrio del seno se alcanza cuando las altas velocidades asociadas al impacto de la cresta en el punto de *plunge* se disipan lo suficiente antes de llegar al fondo como para producir tensiones tangenciales por debajo del valor crítico. Cabe destacar, por tanto, que cuanto mayor sea la tensión tangencial crítica del sedimento, o el número de Shields crítico, mayor tamaño podrá alcanzar la barra y menor profundidad tendrá el seno en la situación de equilibrio. En cuanto a la posición de la barra a lo largo del perfil de playa, la situación de equilibrio se alcanza cuando el flujo de sedimento del *steady streaming* se compensa con el de la corriente de retorno separada, una vez estabilizado el punto de separación. A su vez, el punto de separación se estabiliza cuando el seno alcanza la profundidad de equilibrio, dado que la distribución vertical de esfuerzos tangenciales en el fluido también se estabiliza y, en consecuencia, también el perfil de velocidad de la corriente de retorno. Los flujos de sedimento una vez alcanzada la situación de equilibrio en el perfil de playa se muestran esquemáticamente en la Figura 30.

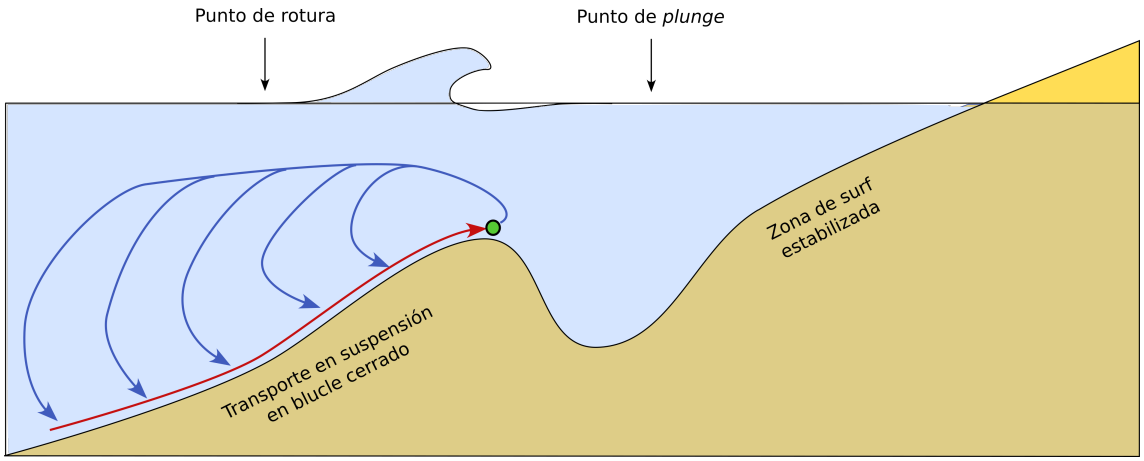

Figura 30: Representación esquemática de los principales flujos de sedimento una vez alcanzado el equilibrio del perfil de playa.

Comparativa de números de Iribarren

La comparación entre ratios de acumulación de sedimento en diferentes números de Iribarren evidencia diferencias en las posiciones de los puntos de rotura, separación de la corriente de retorno y *plunge*. Éstos se muestran en la Figura 31, junto con la forma del perfil de playa tras 150 olas. A medida que el número de Iribarren aumenta, los puntos de rotura, separación de la corriente de retorno y *plunge* se desplazan hacia el lado mar. Consecuentemente, la distribución espacial de la acumulación y erosión de sedimento, y las zonas donde se generan la barra de rompientes y el seno, son diferentes. Además, se observan diferencias importantes en la velocidad con la que se alcanza el estado de equilibrio. El crecimiento y migración de la barra suceden de forma más rápida en condiciones de rotura en voluta, dado que las velociades de fricción son también mayores.

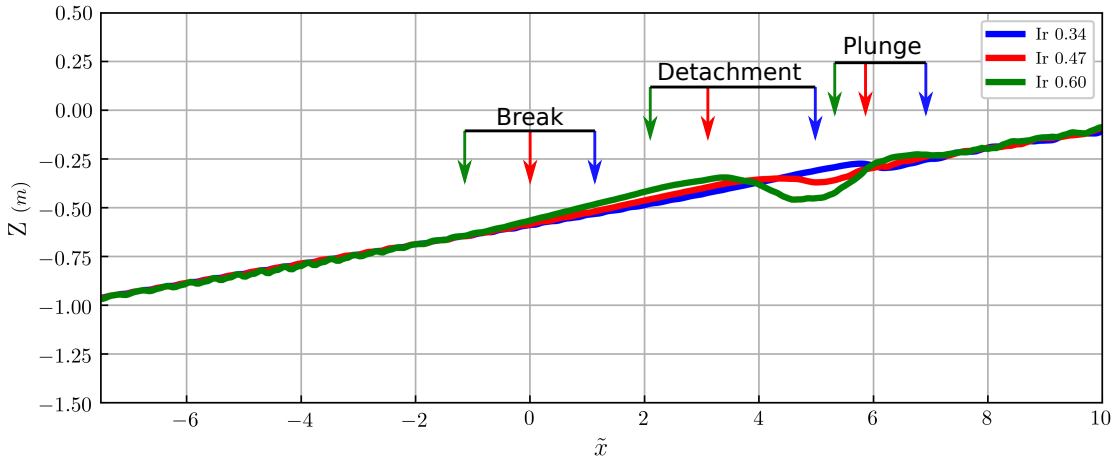

Figura 31: Batimetría tras 150 olas para los tres casos con distintos números de Iribarren. Las flechas muestran la localización de los puntos de rotura, separación de la corriente de retorno y *plunge* en cada caso..

Las diferencias entre los tipos de rompientes son consistentes con las mecánicas descritas en el anterior análisis.

Conclusiones

Se han abordado tanto el objetivo principal de la tesis como los objetivos específicos planteados. En relación a cada uno de los mismos, se pueden extraer las siguientes conclusiones.

Objetivo Específico 1: desarrolo de un modelo numérico para morfodinámica en perfiles de playa. Tras una revisión de los modelos de transporte de sedimento disponibles, se decidió implementar un modelo Euleriano de una fase, puesto que estos modelos combinan una resolución suficiente de los procesos morfodinámicos y un coste computacional razonable. El modelo se ha implementado partiendo del modelo hidrodinámico IH2VOF, previamente existente. Además, se han realizado otras mejoras en la hidrodinámica que permiten abordar mejor el

estudio de los procesos objetivo de esta tesis. Con esto, se consigue completar el Objetivo Específico 1.

Objetivo Específico 2: validación del modelo numérico. Se ha realizado una validación del modelo desarrollado frente a resultados de laboratorio. Las validaciones cubren diferentes escalas espaciales y temporales, siempre dentro del corto plazo y bajo condiciones erosivas. Además de la evolución morfológica, se han abordado otras variables intervinientes, tales como la velocidad, concentración de sedimento o la superficie libre. No se han empleado parámetros de calibración para realizar las validaciones. En general, el modelo es capaz de reproducir los procesos morfodinámicos responsables de la evolución morfológica de perfiles de playa bi-dimensionales. El modelo proporciona resultados que coinciden, tanto cualitativa como cuantitativemente, con los obtenidos en ensayos de laboratorio. Adicionalmente, el coste computacional resulta ser del orden de 10 veces menor al de otros modelos RANS. Por tanto, se considera alcanzado el Objetivo Específico 2.

Objetivo Específico 3: análisis global de los procesos morfodinámicos cross-shore en eventos episódicos. Empleando el modelo desarrollado, se ha simulado la evolución de un perfil de playa en condiciones erosivas, asociadas a eventos episódicos. Se ha examinado la forma en la que las condiciones ambientales (oleaje, propiedades del sedimento y estado morfológico) afectan a los procesos morfodinámicos. Además, se ha investigado la forma en la que los procesos morfodinámicos llevan a la evolución morfológica propia de las condiciones erosivas.

Se han identificado los principales causantes de la generación de la barra de rompientes. Se ha remarcado el papel fundamental del punto de separación de la corriente de retorno, alrededor del cual se forma la barra. Se han discutido los aspectos fundamentales de las contribuciones del transporte por fondo y en suspensión, indicando cómo las condiciones hidrodinámicas causadas por el oleaje influyen en cada uno. Además, se ha proporcionado una descripción detallada del patrón de circulación que sigue el sedimento en suspensión. Con esto, se cumple el Objetivo Específico 3.a.

En cuanto a la migración de la barra de rompientes, se ha establecido que ocurre como consecuencia del desplazamiento del punto de separación de la corriente de retorno. Se ha examinado la forma en que esto afecta a al transporte por fondo y al patrón de circulación del sedimento así como las causas que llevan al desplazamiento del punto de separación. Este análsis da respuesta al Objetivo Específico 3.b.

Finalmente, se ha estudiado la configuración de equilibrio del perfil de playa. Se ha proporcionado una descripción de las codiciones bajo las que se alcanza el equilibrio morfológico del perfil. En la zona de la barra, éste ocurre por la compensación de las acumulaciones producidas por los transportes por fondo y en suspensión, tendiendo el primero a acumular sedimento y el segundo a erosionarlo. En contraste, la zona del seno de la barra alcanza el equilibrio debido a que ambas contribuciones son prácticamente nulas. Se ha observado que el patrón de circulación de sedimento en la zona de asomeramiento y surf exterior evoluciona hacia una configuración en la que el flujo de sedimento integrado en la vertical es, aproximadamente, cero, a pesar de que los flujos de sedimento sean significativos. Con esto, se cumple el Objetivo Específico 3.c.

Objetivo Principal: mejora del conocimiento en morfodinámica costera. Con las conclusiones anteriores, esta tesis contribuye a una mejor comprensión de los procesos morfodinámicos causantes de la secuencia evolutiva de perfiles de playa. Ésto es fundamental para evaluar, prevenir y mitigar problemas de erosión costera por causas tanto naturales como humanas. Más aun, el modelo numérico desarrollado constituye una herramienta útil para investigaciones futuras en morfodinámica de playas y para abordar problemas de erosión en la práctica de la ingeniería costera. Se considera alcanzado, por tanto, el Objetivo Principal de la tesis.

Abstract

Beaches are a highly valuable asset from an economical, social and environmental perspective, and understanding them is fundamental to develop effective strategies for coastal management. The morphodynamic framework highlights the key role of morphodynamic processes, interactions between hydrodynamic and morphology involving sediment transport, in driving the evolution of beaches under given environmental conditions. These morphodynamic processes occur at several temporal scales. Among them, episodic events, which are highly energetic and with temporal scale in the order of hours, can produce significant variations of the coastline in a short time and lead to damage of coastal infrastructure. Therefore, better understanding the morphodynamic processes during episodic events is of great interest.

This thesis is focused on cross-shore morphodynamic processes during episodic events. Current knowledge on these processes includes surf zone hydrodynamics and the sediment transport produced by them. In spite, some knowledge gaps remain. The way in which cross-shore hydrodynamics and sediment transport mechanisms bring about morphodynamic processes is not sufficiently understood. Also, there is a lack of a comprehensive analysis on the combined effect of the different cross-shore morphodynamic processes.

In this thesis, it is aimed to improve our current knowledge on the interplay between hydrodynamics and morphology that bring about morphodynamic processes in episodic events and what are their main drivers. To achieve this, the first step is to develop a numerical model able to reproduce the relevant cross-shore morphodynamic processes with suitable computational cost. Then, the numerical model is validated against laboratory data. Finally, the model is used to gain insight in the morphodynamic processes.

After analysing the available types of numerical models capable of solving the processes intended to be studied, the One-Phase Eulerian RANS models are deemed to be best aligned with the objectives of this research. Consistently, a One-Phase Eulerian sediment transport module is developed and coupled with the previously existing hydrodynamic RANS model IH2VOF. Regarding the hydrodynamic model, it is a 2DV Finite Difference model which uses the Volume of Fluid technique to keep track of the free surface and the cut-cell technique for solid boundary treatment. It also includes a k-ϵ turbulence model. The sediment transport module features a separate treatment of bedload and suspended transport, being the former based on empirical formulae and the latter on solving an advection-diffusion equation for the sediment concentration, The resulting numerical model is validated against three different laboratory experiments, at varying spatial scales. Several magnitudes of relevance for the analysis of sediment transport are covered by these validations, including bathymetric evolution, velocities, free-surface position, sediment concentration and shear stress. Comparisons between experimental and numerical results

show a good agreement. Moreover, the computational cost of simulating the experimental cases is significantly reduced compared to previously existing models with similar capabilities.

Once the numerical model is validated, an in-depth analysis of cross-shore morphodynamic processes under the erosive conditions associated to episodic events is performed. The analysis is divided into three stages attending to the evolution of the breaker bar: growth, migration and equilibrium. Firstly, in the analysis of the growth of the breaker bar, the undertow detachment point, at which undertow and steady streaming compensate each other, is identified as a key feature. The suspended sediment transport trends to accumulate sediment mainly between the break and undertow detachment points, while the bedload transport accumulates sediment on the onshore side of it. Secondly, it is found that the migration of the breaker bar is caused by a migration of the undertow detachment point. The migration of the undertow detachment point is due to a redistribution of the shear stresses in the fluid along the vertical direction as a result of the deepening of the trough. Thirdly, the equilibrium configuration is achieved in different ways for the shoaling and outer surf zones and for the inner surf zone. In the first two, the sediment circulates in a closed loop such that the mean sediment flux is nearly zero. In contrast, in the inner surf zone the equilibrium is achieved when the sediment fluxes are almost zero due to the lack of sediment concentration resulting from the reduction in shear stresses produced on the seabed. The equilibrium depth of the trough is achieved once it is deep enough to dampen the high velocity of the impinging jet below levels that produce erosion. Once the trough is stabilized, the undertow detachment point remains the same, and the breaker bar acquires an equilibrium position. The limiting mechanism for the size of the breaker bar is the shear stress produced by the wave crests, which increases as the water depth is reduced by the growth of the bar.

Dedication

A mis padres. Las actitudes que me transmitieron desde pequeño han sido los recursos más útiles para enfrentarme a la complejidad e incertidumbre tanto en esta tesis como en muchos otros aspectos de mi vida.

Acknowledgements

A mi familia, por su apoyo contínuo y desinteresado.

A mis amigos, Daniel, Bruno, Lucía, Moisés y David. Desde formas de pensar hasta aspectos técnicos, sigo aprendiendo cosas de vosotros que me hacen mejorar como profesional y como persona. A Patrica, que trae mucha felicidad a mi vida. Gracias a todos por los momentos que hemos pasado juntos y por los que vendrán.

A mis supervisores, Javier e Íñigo, por su ayuda, apoyo y contibuciones a los resultados de esta tesis.

A mis compañeros de piso Benedetto y Ottavio, por los buenos momentos que hemos vivido a lo largo de estos años. A mis compañeros de trabajo en IHCantabria: Gabi, María, Enrico, Alberto, Antonio, Juan, Paula, Miguel, Alessandro y muchos otros.

Y a todas aquellas personas que me he encontrado en este camino y que han contribuido a mi desarrollo profesional y personal.

Al Ministerio de Educación, Cultura y Deporte de España (MECD) por la financiación de la beca de Formación del Profesorado Universitario (FPU17/04356)

Contents

Chapter 1

Introduction

Contents

1.1 Motivation

1.1.1 A highly valuable asset

Beaches are highly valuable assets from an economical, social and environmental perspective. They can generate economical activity by attracting tourism and provide protection against extreme events, reducing the cost of coastal infrastructure required to avoid flooding and damage to real property close to the shoreline. Also, beaches are valuable spaces for people living in the area, which can be used for leisure activities and sports, and are important elements of the landscape. From an environmental point of view, beaches are unique landforms and habitats. A distinctive aspect of them is that, due to their ability to migrate seaward and landward, they can adapt to disturbances in the climate, allowing to maintain their functions regardless.

Figure 1.1: El Sardinero beach. Santander, 21st November 2020. Photo by the author.

In 2018, the Coastal Tourism sector was the biggest across the EU Blue Economy in terms of Gross Value Added (GVA) and employment. It generated more than €80 billion GVA, directly employing more than 2.8 million people. This sector was recovering and growing after the financial crisis of 2008 until the COVID-19 pandemic (European Commission *et al.* , 2021). Thus, in the new approach for a sustainable blue economy in the EU (consistent with the European Green Deal and the Recovery Plan for Europe), the proper management of these assets is a fundamental aspect.

Managing these valuable environments is a difficult task. Beaches are threatened by a series of potential problems that can lead to a degradation of their functions (i.e., beach erosion, water pollution and aggressive real state development). Additionally, the natural behaviour of beaches involves many complex interactions between hydrodynamics, sediment transport and bathymetry, and it can be very sensitive to their modification. Further understanding of how these systems behave can help in making better decisions on how to avoid and mitigate some of the problems that can result in a loss of their economical, social and environmental value.

1.1.2 The problem of beach erosion

Beach erosion can produce a severe degradation of their value. The reduction of the available beach width results in less economical revenue from tourism-related businesses (Alexandrakis *et al.* , 2015), (Toimil *et al.* , 2020) and loss of value of nearby property (Gopalakrishnan *et al.* , 2011). The protective function of the beach is also greatly influenced by coastal erosion: if the amount of sediment in the beach decreases, it can loss its ability to adapt to sea level variations and to acquire a dissipative configuration to dampen wave energy, increasing wave loads and overtopping on structures behind. Additionally, excessive erosion can lead to the failure of coastal infrastructure by scouring their foundation (Oumeraci *et al.* , 2001). Changes in the bathymetry can result in further degradation of the recreational uses, such as dangerous conditions for swimming, decrease of available space for leisure activities or loss of surfing spots. Concerning their environmental value, human interventions to address coastal erosion can result in ecological impact and loss of biodiversity (Schlacher *et al.* , 2007).

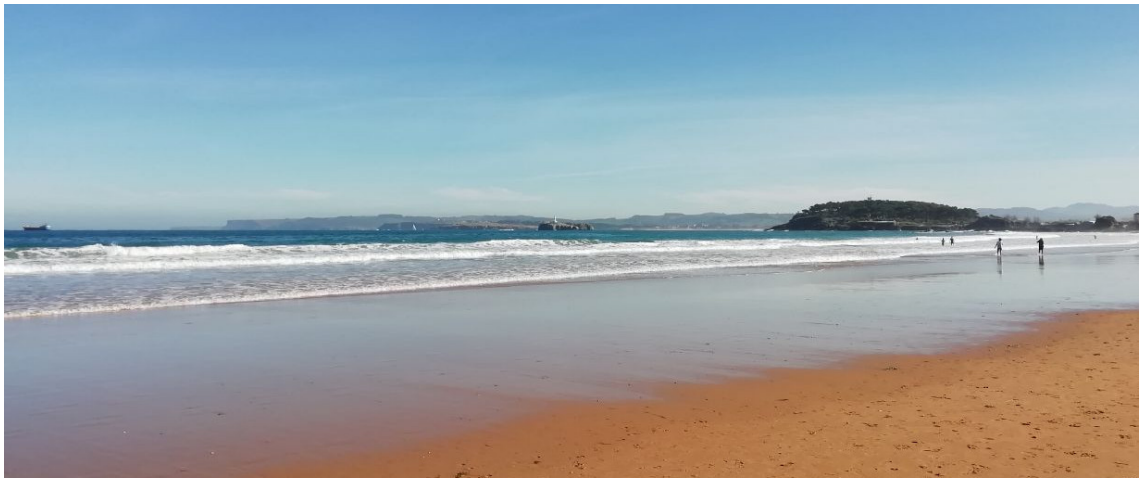

Figure 1.2: El Sardinero beach. Santander, 21st November 2020. Photo by the author.

Preventing coastal erosion annually leads to significant spending of public funds. In the EU, the total expenses in coastal protection for the period between 1998 and 2015 amount to €16.8 billion, from which €10.47 billion correspond to the cost of normal protection (excluding singular "hot-spot" cities and ecosystems), which has been steadily increasing in this period (European Commission & Directorate-General for Maritime Affairs and Fisheries, 2009).

Beach erosion can be caused by natural or human activity. Variations of the wave climate of the beach result in a variation of the shoreline. If the wave climate becomes more energetic, beach erosion with the consequent loss of dry area can occur, as studied in (Wright *et al.* , 1985). Variations of the sea-level lead to displacements of the shoreline as well (following (Bruun, 1962)). Additionally, beach erosion can be due to human interventions, such as constructing seawalls ((Berry *et al.* , 2014)) or interrupting long-shore currents that carry sediment, which can result from the construction of ports, marinas ((Tsoukala *et al.* , 2015)), jetties and other structures perpendicular to the shoreline.

Predicting beach erosion is a difficult task. Beaches are complex, dynamic en-

vironments affected by several variables related to the maritime climate and sediment characteristics. Several, mutually-influencing hydrodynamic, sediment transport and bathymetric processes occur in these environments, with spatial scales ranging from kilometres to millimetres and temporal scales from decades to seconds. Because of the limited knowledge on morphodynamic processes driving the evolution of beaches, models have a limited skill in predicting the implications of changing environmental conditions (Kim *et al.* , 2021). This eventually affects the assessment of consequences of human interventions and climate change on beach erosion. Additionally, policies for coastal management based on inaccurate predictions and incomplete knowledge on how these systems work lead to limited ability to deal with coastal erosion (Stive *et al.* , 2002).

1.1.3 Morphodynamic processes in a beach

The morphodynamic framework proposed by (Wright & Thom, 1977) is useful to explain how the evolution of a beach profile occurs. There are three fundamental participants in this evolution: (1) environmental conditions, (2) morphodynamic processes and (3) evolutionary sequence.

First, environmental conditions include the energy sources, sediment properties and morphologic state. The energy sources include waves, tides, currents and wind. Some relevant sediment properties are the grain size, density and shape. The morphologic state represents the initial bathymetry shape.

Second, morphodynamic processes are defined as the mutual interactions between aero and hydrodynamics and morphology involving sediment transport.

Third, the evolutionary sequence results from the variations that the morphodynamic processes cause in the bathymetry. Thus, it consists of the different bathymetric shapes ordered in time as they occur. The evolutionary sequence is the result of the interaction between the morphologic state and the morphodynamic process, which modify it. This sequence happens as the morphological state and morphodynamic processes are adjusted, trending towards an equilibrium in which they can attain a maximum stability configuration.

This framework is schematically represented in Figure 1.3.

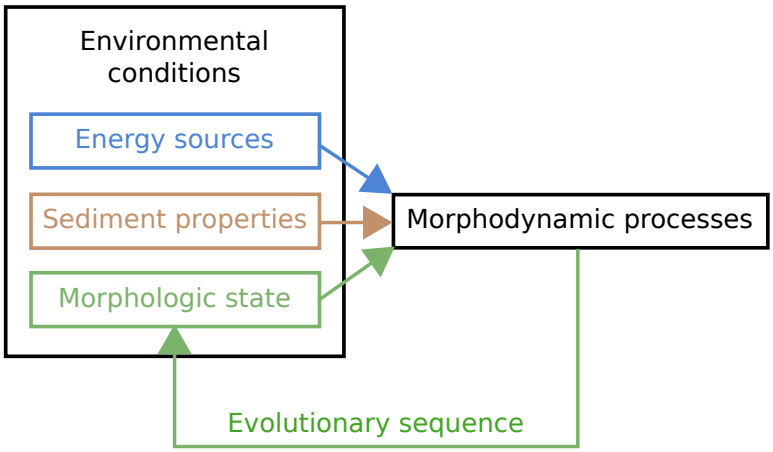

Figure 1.3: Schematic representation of the morphodynamic framework for beach evolution proposed in (Wright & Thom, 1977).

In (Jackson & Short, 2020), morphodynamic processes are defined as the interactions between two opposite effects on sediment and geology; gravity and structure, which stabilize them, and waves, wind and currents, which attempt to mobilize, transport, sort and deposit them. This definition is compatible with that of (Wright & Thom, 1977), although it is more specific regarding the role of each type of environmental condition.

Morphodynamic processes can occur at several temporal and spatial scales. Attending to these scales, they can be classified in very long term, long term, middle term and short term. The approximate temporal and spatial ranges for each scale, according to (Stive *et al.* , 2002), are given in Table 1.1. Notice that hydrodynamic and sediment transport features exist in much smaller temporal (seconds) and spatial (millimetres) scales, and these are relevant to beach morphodynamics (i.e., in-wave effects, vortices induced by wave breaking, turbulence).

Table 1.1: Temporal and spatial ranges for each scale of beach morphodynamic processes.

Denomination	Very long term	Long term	Middle term	Short term
Time scale	100 to 1000 years	10 to 100 years	1 to 10 years	1 hour to 1 year
Spatial scale	100+ km	10 to 100 km	1 to 5 km	10 m to 1 km

Morphodynamic processes in a beach are generally divided in long-shore and cross-shore processes. The formers are approximately parallel to the coast line. An example of a fundamental long-shore morphodynamic process is the long-shore drift, sediment transport parallel to the beach produced by long-shore currents caused by oblique wave breaking. In contrast, cross-shore processes occur in the direction normal to the shoreline. A very distinctive cross-shore morphodynamic process is the accumulation of sediment forming breaker bars under energetic wave conditions.

Long- and cross-shore processes interact with each other in a bi-directional manner. For instance, variations of the cross-shore beach profile may result in modifications of the wave breaking point, affecting the long-shore currents and the resulting long-shore drift. Additionally, long-shore currents can produce erosion or accumulation of sediment that modify the cross-shore beach profile, and rip currents can partially compensate the onshore-directed momentum flux produced by breaking waves, reducing the strength of the undertow and the location of breaker bars. Therefore, the analysis of long-shore features must include a correct treatment of the cross-shore treats and vice-versa.

Consequently, understanding the way in which changes in the energy sources and sediment characteristics affect beach morphodynamic processes, and the resulting evolutionary sequence, is of great interest for many coastal engineering applications. Regarding beach erosion, it would allow for a better assessment of the consequences of building maritime infrastructures, variations of the wave conditions and sea level and dredging. Also, it is fundamental to better evaluate the effectiveness of hard and soft remedies to deal with beach erosion, such as constructing seawalls and jetties, beach nourishment or the use of natural-based solutions to dampen wave energy and retain sediment. Furthermore, other areas of coastal engineering would benefit from better understanding of beach morphodynamic processes, such as assessing the potential damage to coastal infrastructures protected by beaches during extreme events (i.e. seawalls, promenades, pipelines), estimating flooding risk and planning

the maintenance of navigation channels.

Figure 1.4: El Sardinero beach. Santander, 14th November 2020. Photo by the author.

1.1.4 Importance of episodic events

Among the span of temporal scales in which coastal morphodynamic processes can occur, episodic events have great implications on beach erosion. Episodic events are highly energetic wave conditions that last for several hours (short term scale) and that can result in important variations of the bathymetry. Therefore, they can induce significant changes in the position of the shoreline and in the dissipation of wave energy provided by the beach, potentially leading to damage in coastal infrastructure. For instance, storm Gloria produced damages in the Mediterranean coast of Spain in the winter of 2020 which lead to restoration works amounting to €20 million (Europa Press, 2020). Furthermore, in energetic episodic events, the loss of protective effect from the beach can greatly increase the risk of flooding, specially if they coincide with a high tide.

Thus, it is fundamental to understand how beaches behave under such conditions for proper coastal management. However, there is still limited knowledge about this (as explained in (Eichentopf *et al.* , 2019)). For instance, it is not clear why consecutive storms arriving to the same beach can, in some cases, produce larger erosion than if the storms arrive individually (as observed in (Lee *et al.* , 1998)). Furthermore, there are limited studies on the beach recovery in calm periods between storms (i.e. (Morton *et al.* , 1994)), which is of great importance in determining the shoreline retreat after a storm sequence.

1.1.5 Cross-shore morphodynamic processes

The present research is focused on cross-shore morphodynamic processes caused by hydrodynamic effects. These can be studied by looking at the hydrodynamics caused by environmental conditions (i.e., waves, currents, mean sea level changes), the sediment transport produced by such hydrodynamics, and the way in which the beach morphology evolves as a consequence. In the following, a brief review of the main features of these three elements is given. A detailed literature review, covering the main processes, is provided in Chapter 2

Regarding hydrodynamics, the shoaling zone is relatively simple compared to the surf and swash zones. Due to the absence of wave breaking, most of the physics can be represented by non-linear wave theory. An important hydrodynamic feature in this zone is the steady streaming, a current produced by progressive waves close to the seabed due to boundary effects. Surf zone hydrodynamics entail great complexity that arises from the wave breaking process. Wave breaking involves many aspects regarding Fluid Mechanics, like the instability of the wave leading to onset of wave breaking under certain conditions, or the generation of eddies and turbulence due to the high velocity gradients produced in it. Wave breaking can occur in four different ways depending on the relative steepness between wave and seabed: spilling, plunging, collapsing and surging (see Figure 1.5). Also, it produces unbalanced net momentum and mass fluxes towards the coastline, both conditioned by the vertical mixing produced in the breaking process. The excess of mass flux is compensated by the undertow and rip currents. Additionally, the total momentum flux towards the shoreline along the water column (radiation stress) must be compensated, to achieve a dynamic balance, by a gradient of the mean water level (wave set-up). Swash zone hydrodynamics involve considerable complexity as well due to the influence of turbulence and vortices from wave breaking in the velocity profile. The reduced thickness of the flow brings about major importance of boundary layer effects and porous flow. Furthermore, secondary breaking (in collapsing) might occur in the swash zone. A schematic representation of these cross-shore hydrodynamic features is displayed in Figure 1.6.

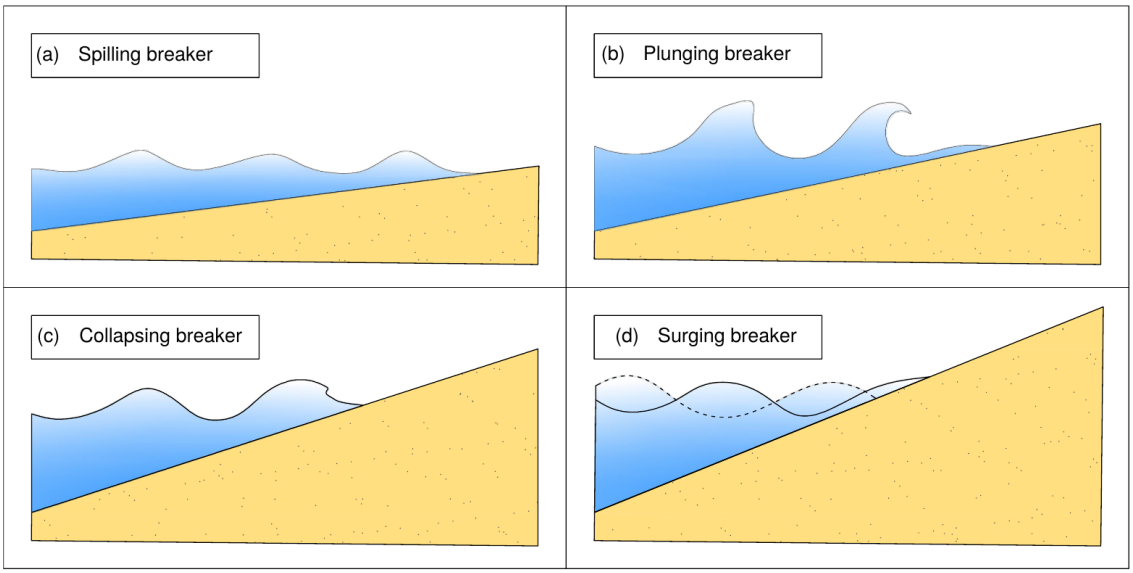

Figure 1.5: Types of wave breaking. Reproduced from (Mares Nasarre, 2021)

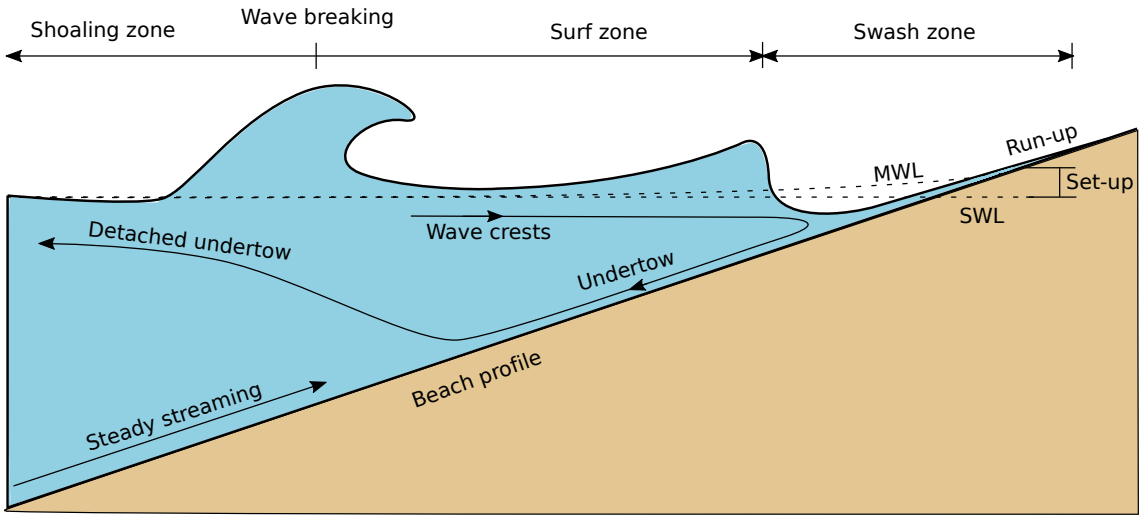

Figure 1.6: Cross-shore hydrodynamic features.

These intricate hydrodynamics produce sediment transport and bring about morphodynamic processes as they interact with the morphology. Sediment transport is fundamentally an advective flux of sediment particles which can interact between them. It is often conceptualized as the combination of two separate mechanisms: bedload and suspended transport. Bedload transport occurs in a thin layer close to the seabed, and consists in particles rolling, sliding and saltating, it is greatly influenced by particle interactions. Suspended transport happens far from the seabed, and it is fundamentally driven by the advection produced by the fluid and the sediment fall velocity. Yet, particle interactions can be significant in zones with high sediment concentration. Note that, to avoid dealing with turbulent motions of sediment particles, the transport produced by them is usually considered as a diffusion with a diffusivity constant related to the turbulent viscosity via the Schmidt number (ratio between kinematic viscosity and mass diffusivity). However, the actual transport of sediment particles is fully advective. In a beach profile, both bedload and suspended transport are important and conditioned by the different hydrodynamic processes occurring in each zone.

The morphological features in a cross-shore profile can include landforms such as small-scale ripples, breaker bars (large deposits of sediment close to the wave breaking point), troughs (depressions that appear on the onshore side of the breaker bar), berms and scarps among others. The variations of these landforms produced by sediment transport result in changes in the hydrodynamics, which in turn modify the sediment transport. For instance, the generation of a breaker bar implies a variation in the local slope of the beach profile, which can lead to earlier wave breaking and the consequent modification of the undertow current and the sediment transport produced by it.

In addition to the complexity of the hydrodynamics, sediment transport and morphological features, the strong interactions between hydrodynamics and morphology add an extra layer of difficulty to the analysis of morphodynamic processes. For this reason, there is a lack of understanding in how they drive the cross-shore beach profile evolution, which also propagates to the long-shore analysis and to the ability to predict changes in the shoreline at different scales (from short to very long term).

1.2 Structure of the thesis

In this section, an brief introduction on beach morphodynamic processes has been provided. In the following, a literature review is performed in Chapter 2, focused on the current knowledge in cross-shore processes and in the available numerical tools to reproduce them. Then, the main objectives of this thesis are presented in Chapter 3. A newly developed numerical model for cross-shore profile evolution is described in Chapter 4 and validated in Chapter 5. Then, this numerical model is applied to research the processes that drive the cross-shore beach profile evolution. An in-depth analysis of cross-shore morphodynamic processes during episodic events, based on the numerical model results, is presented in Chapter 6. The main conclusions extracted from this thesis are given in Chapter 7. Finally, the future lines of research that may derive from this work are given in Chapter 8.

Chapter 2

State of the Art

Contents

2.1 Introduction

As discussed in Chapter 1, understanding the behaviour of beaches in episodic events is fundamental for proper coastal management.

Over the last decades, the knowledge on the morphological evolution of cross-shore beach profiles under different environmental conditions has improved significantly. Among the previous research, some studies are focused on the morphodynamic processes. These examine how different hydrodynamic and morphological features interact. Other works directly address the influence of the environmental conditions (i.e. waves, sea-level, currents, sediment characteristics, initial profile shape) on the morphological evolution, rather than performing an in-depth analysis of the processes that relate them. In this literature review, these two approaches are discussed in Sections 2.2 and 2.3, respectively. According to the aim of this thesis, the literature review is focused on cross-shore features.

In general, studies of morphological evolution of beach profiles involve three different approaches: (1) field campaigns, (2) experimental setups and (3) numerical modelling.

Field campaigns (i.e. (Larson & Kraus, 1994), (Aagaard & Jensen, 2013)) provide highly valuable data, measured directly on the real phenomena intended to be studied, without the simplifications and distortions that other strategies demand (i.e., scaling effects or neglecting 3D effects in laboratory experiments, or assumptions on the behaviour of the drivers in numerical models). However, these data are costly to obtain. Moreover, some instruments cannot be deployed to gather data under highly energetic wave conditions, at the time when the morphodynamic processes of interest are taking place. Also, the conditions under which measurements are obtained cannot be modified at will, as can be done in laboratory experiments and numerical simulations, and can only be anticipated to a certain extent (so that the measuring instruments can be deployed in advance).

Experimental tests (i.e., (Gislason *et al.* , 2009) and (Sumer *et al.* , 2013)) are fundamental to better understand morphodynamic processes. Their major advantage is that they provide good quality results. Additionally, each experiment can be designed for a particular configuration of interest. An important disadvantage is that, in order to attain reliable results, the sediment and wave properties must be correctly scaled. A classic approach to scale sediment properties is to divide the sediment transport mechanisms into bedload and suspended. When both are relevant, each of them must be correctly scaled, and this can lead to the use of expensive materials due to the resulting specifications for particle size and density. Experimental setups have multiple applications, probably the main one is studying the relation between environmental conditions and morphodynamic processes, relating different parameters from wave theory (wave height, period, shape, breaking point, radiation stress tensor), hydrodynamics (velocities, turbulent kinetic energy and other derived results) in both outer and near-bed regions, bedload and suspended sediment transport and the resulting bathymetry. In some cases, the bed shear-stress is used as an intermediate parameter to relate hydrodynamics and sediment transport. Other applications of experimental setups are providing benchmarks for validating numerical models, developing semi-empirical formulae to describe beach morphodynamic processes and to test designs of coastal interventions. In (Sumer *et al.* , 2013), the sediment transport generated by plunging breakers was analysed, relating

the wave properties with hydrodynamics and bed shear stress. Also, a description of the sediment transport during wave breaking was proposed. More recently, in (Cáceres & Alsina, 2016), the beach profile generated under monochromatic and irregular waves was studied, the breaker bar was characterized by its volume, height and other parameters; a spectral analysis of the free-surface, velocity and sediment concentration was performed, too. A detailed analysis of the effects of bedload and suspended transport in the resulting bathymetry was provided in (van der Zanden *et al.* , 2017a). For this experimental set-up, the suspended transport contribution was further analysed in (van der Zanden *et al.* , 2017b). In (Howe *et al.* , 2019) a specific study of the swash zone was presented, relating free surface evolution, velocities and generated bed shear stress.

Numerical modelling has been applied in coastal engineering for a long time. Nowadays, different hydrodynamic models are including sediment transport modules that allow them to solve some of the morphodynamic processes. The main advantages of numerical models are that they are generally cheaper than experimental studies and more flexible to simulate different configurations. Additionally, they can produce data that would be unfeasible to obtain with other strategies (i.e., excessive number of measuring points, limitations to install sensors measuring at the same point and time or survivability of the instruments in field campaigns). The most important drawbacks are the high computational cost of complex models and the lack of precision, for certain applications, of the simpler ones. The available numerical models can offer different compromises between the processes that they can accurately solve and the computational cost of the simulations. Apart from their use in consultancy works, numerical models have also been used in the research of beach morphodynamics, although its use for this purpose is not widely spread because of the difficulties to correctly simulate the complex phenomena involved. For instance, in (Jacobsen *et al.* , 2014) and (**?**), a highly detailed numerical simulation was performed to investigate the hydrodynamics and sediment transport in a cross-shore beach profile, being able to reproduce the generation and development of a breaker bar under different wave conditions. There are numerical modelling studies of beach profiles which only concern hydrodynamic features, without solving sediment transport, such as (Larsen *et al.* , 2020).

In the following review of the State of the Art in cross-shore beach morphodynamics, the knowledge gained in the morphodynamic processes and overall behaviour of the beach is summarized first. Then, the currently available numerical models to simulate them are addressed.

2.2 Cross-shore Morphodynamic processes

According to the morphodynamic framework discussed in Chapter 1, the interaction between hydrodynamics and morphology, involving sediment transport, produces morphodynamic processes. The conditioning factors for these processes are the energy sources, sediment properties and morphological state.

The energy sources are closely related to the hydrodynamic features. Particularly, cross-shore hydrodynamics are mainly produced by waves approaching the beach and breaking at a certain point in the beach profile. This results in a wide range of hydrodynamic features occurring at different time and spatial scales (i.e., currents, intra-wave effects, boundary layer, coherent structures, turbulence, etc.).

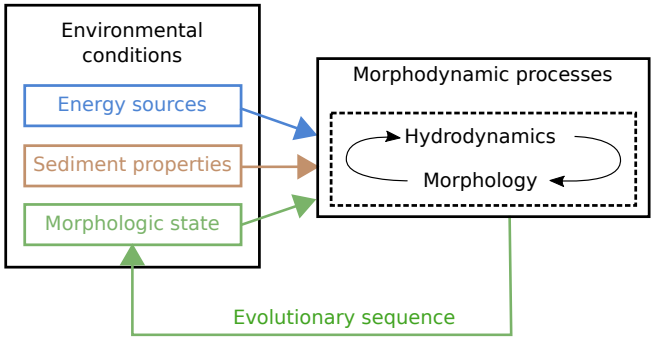

Figure 2.1: Schematic representation of the morphodynamic framework from (Wright & Thom, 1977)

The sediment transport produced by such hydrodynamics is typically divided in bedload and suspended transport. Both are affected by the aforementioned hydrodynamic effects at different scales and depend on sediment properties such as its bulk density and grain size. Finally, the morphological state affects the way in which waves propagate along the shoaling zone, the wave breaking process and, overall, the hydrodynamics.

These interacting hydrodynamics and morphological features condition the cross-shore profile evolution and have been studied for long. The results of such research constitute the basis of the currently available knowledge on how beaches behave under certain wave conditions. In the following, the fundamental advancements in the study of cross-shore hydrodynamics and sediment transport are summarized.

2.2.1 Hydrodynamics

Some of the main hydrodynamic features tightly related to sediment transport, as indicated in (Svendsen, 2006), are the generation of the undertow in the surf zone, the steady streaming due to progressive waves, the velocity and acceleration skewness due to wave asymmetry and the wave breaking process. Another important hydrodynamic effect regarding sediment transport is the swash motion.

The undertow is mentioned as a fundamental driver of beach profile evolution early by (Bagnold, 1940). It is stated that under large wave amplitude relative to the sediment size, corresponding to the episodic events addressed in this thesis, the offshore-directed drift of water close to the seabed displaces the suspended sediment particles towards offshore. In (Longuet-Higgins, 1983), the near-bed currents were investigated by injecting dye. It was found that the near-bed mean flow is directed offshore in the surf zone due the undertow, changing its direction before reaching the break point. The location at which the near-bed current changes its direction was named undertow detachment point. Also, the potential significance of this reversion of the near-bed current regarding the generation of the breaker bar is stated. Later, (Deigaard *et al.* , 1991) developed a model to predict the undertow velocity profile accounting for different sources of stresses in the fluid, arising from the radiation stress gradient, effects of surface rollers, steady streaming and the variation of the mean water level. More experiments have been conducted to investigate the undertow velocity profile, and different models based on experimental and field measurements have been developed aiming to quantify it (i.e., (Rattanapitikon &

Shibayama, 2000) or (Faria *et al.* , 2000)).

The steady streaming produced by waves was addressed experimentally in (Bagnold, 1947) for waves propagating on a plane bed and on a slope. By injecting dye close to the bottom, a forward drift along the bed was detected in the plane bed configuration. Closer to the free surface, a backwards drift was found. Using the same technique, the steady streaming was also detected in the sloped bed configuration, and it was found to increase as the water depth decreases. A schematic representation of the drift profile is shown in Figure 2.2. In this experiment, it was also observed that the dye was suddenly lifted towards the surface on the onshore side of the plunge-line, and then the dye began to drift towards offshore. Finally, when injecting dye at positions between the plunge line and the shore line the dye did not show a tendency to drift outwards across the plunge line. In (Longuet-Higgins & Stoneley, 1953), an analytical solution for the mass transport under progressive waves is derived accounting for viscous effects, in contrast with previous analysis. This resulted in a strong mass flux in the direction of wave propagation due to the boundary layer effect. Later, in the already mentioned publication from (Longuet-Higgins, 1983) where the near-bed current reversal close to the break point was observed, the onshore-directed current on the onshore side of the break point was directly related to this strong mass flux. More recently, the steady streaming was studied by (Holmedal & Myrhaug, 2009) and (Blondeaux *et al.* , 2012), both for a flat bed configuration. They found that the total steady streaming is a combination of two competing mechanisms: the first one due to the near-bed vertical velocities generated by waves, and the second due to the differences in near-bed turbulent viscosity during the wave crest and trough phases that arise from wave skewness. In the case of a cross-shore beach profile, the influence of the sloped seabed, wave breaking, and the effect of mass flux produced by the undertow add extra complexity to finding an analytical solution for the steady streaming.

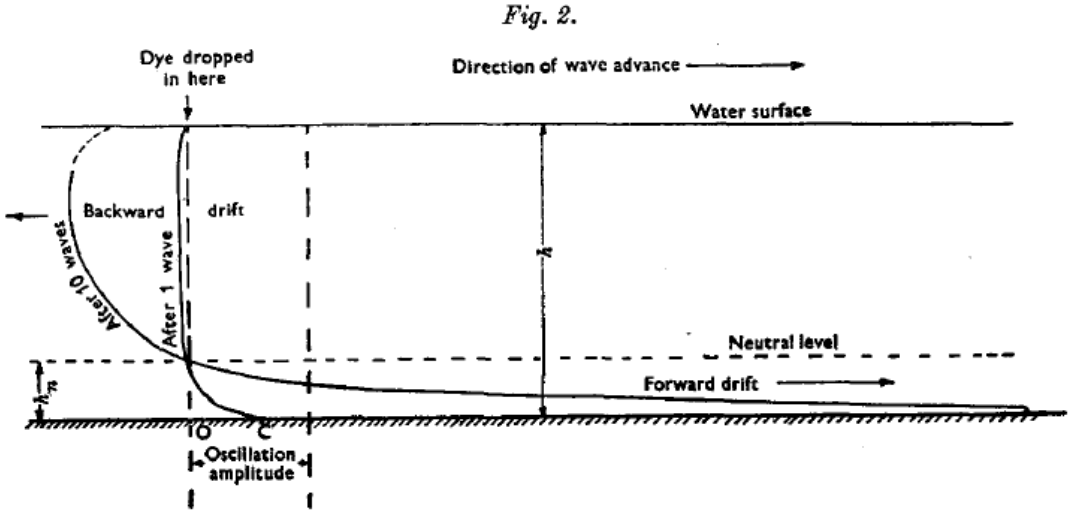

Figure 2.2: Drift profiles, obtaining by injecting dye at different positions along the water column, showing the steady streaming close to the seabed. Reproduced from (Bagnold, 1947).

Wave skewness accounts for the increase in the wave crest height and decrease

in trough depth, which is accompanied by a decrease in wave crest length and an increase of the trough length. Wave asymmetry refers to the increase of the wave front steepness which ultimately results in the sawtooth shape of waves in the inner surf zone. These two features, observed in the free-surface shape, are also reflected in the velocity close to the seabed, resulting in velocity skewness and and acceleration skewness, respectively. The distinction between these two features of the velocity field caused by the direct passage of waves and those caused by streaming and other factors was already introduced in (Bagnold, 1947). Both velocity and acceleration skewness can induce sediment transport per-se, as discussed by (van Rijn *et al.* , 2013).

Wave breaking has been extensively studied as it greatly influences the hydrodynamics in the surf zone. A description of the hydrodynamic features induced by the wave breaking process in the surf zone was given in (Nadaoka *et al.* , 1989). These hydrodynamic features result in a velocity field which can be separated into an irrotational component, a rotational component due to coherent vortical structures (with non-zero average vorticity) and turbulence. The coherent structures consist in horizontal and obliquely descending eddies. A schematic representation of the main coherent structures resulting from wave breaking is given in Figure 2.4. From the analysis of the separated mean flow components (irrotational and rotational), it was found that the coherent structures produces a significant increase in mass and momentum transport respect to that of the irrotational component alone. The mass and momentum flux unbalances, greatly influenced by the aforementioned coherent structures, are responsible for the generation of the undertow and wave set-up. A key aspect is the influence that coherent structures and turbulence resulting from wave breaking have on the undertow velocity profile, as discussed by (Ting & Nelson, 2011). (Ting & Kirby, 1995) and (Ting & Kirby, 1994) presented the differences between plunging and spilling breakers from this perspective, and their implications on momentum exchange between the upper and lower layers of the surf zone. (van der A *et al.* , 2017) measured the velocities generated during wave breaking and the production and transport of turbulent kinetic energy. Other recent studies on wave breaking are based on detailed numerical models instead of laboratory experiments. For instance, (Lubin *et al.* , 2006) used a Large Eddy Simulation (LES) model to provide insight into the breaking process. In (Watanabe *et al.* , 2005), the coherent structures and turbulence resulting from wave breaking are analysed based on the results of a LES model. More recently, (Larsen *et al.* , 2020) simulated waves breaking over a bar to obtain detailed hydrodynamic data of relevant processes (i.e., undertow velocities, turbulence, etc.) using a RANS model. The importance of using stabilized turbulence models for surf zone simulations was also highlighted.

Finally, swash zone hydrodynamics presents particularly complex characteristics, (i.e., alternating wet/dry conditions, influence of porous flow or small water depth) which complicate the measurement of variables of interest in physical modelling and their computation with precise numerical models. (Elfrink & Baldock, 2002) presents a review of the knowledge in swash hydrodynamics and sediment transport. In the swash zone, the main hydrodynamic forcing are the already discussed hydrodynamics of the inner surf zone. In particular, (Elfrink & Baldock, 2002) considers wave characteristics and turbulence. Regarding the wave characteristics, the Iribarren's number was identified as a key parameter as it indicates whether the waves reaching the swash zone are non-breaking waves or bores. Concerning the turbu-

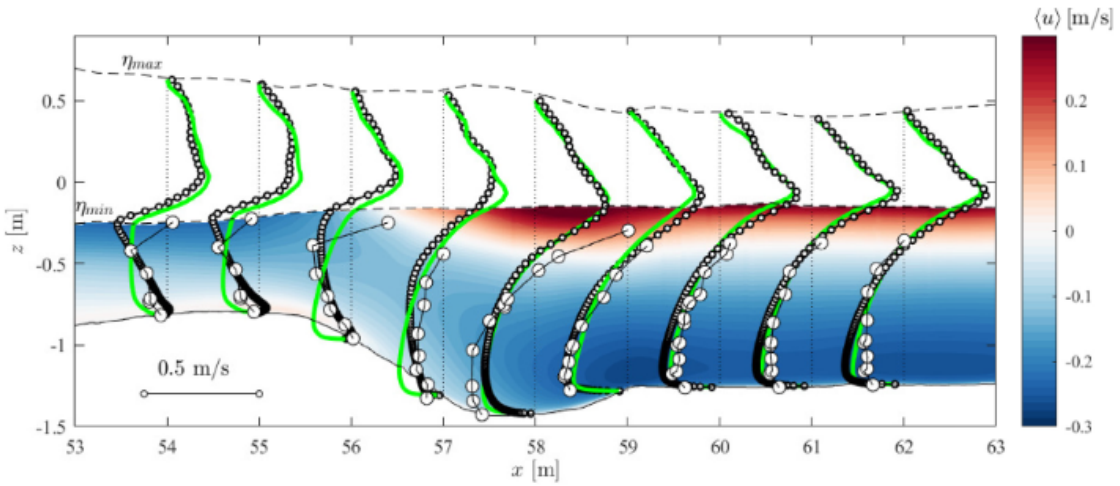

Figure 2.3: Time-averaged cross-shore velocity fields obtained with RANS numerical models. The large circles correspond to experimental measurements. The small circles and colour map are obtained from a stabilized RANS model while the green lines result from a non-stabilized RANS Model. Reproduced from (Larsen *et al.* , 2020).

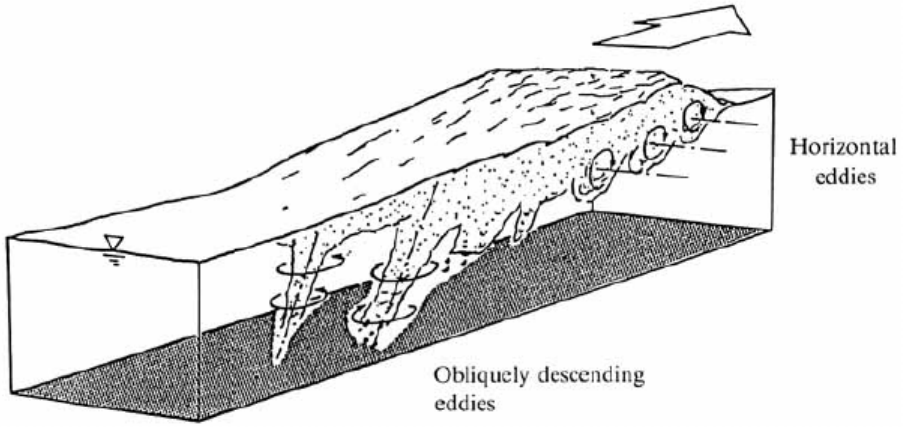

FIGURE 10. Schematic representation of the large-scale eddy structure under breaking waves.

Figure 2.4: Vortical coherent structures, horizontal and obliquely descending eddies, resulting from wave breaking. Reproduced from (Nadaoka *et al.* , 1989).

lence reaching the swash zone, it was stated that more research was required to give an appropriate boundary condition. Two types of swash oscillations were identified depending on whether the waves were non-broken or bores. In both cases, the Iribarren's number was found to be the main conditioning factor in the magnitude of swash motion, together with the wave height. The aforementioned forcing is responsible for the internal flow kinematics, which comprise the dominant free stream velocity and turbulence. The analysis of the free stream velocity from laboratory and field measurements reveals high velocities during both run-up and backwash, which may result in supercritical flow. Another important aspect is the longer duration of the backwash phase compared to the run-up, as observed in (Hughes *et al.* , 1997) from field measurements (i.e., the ones reproduced in Figure 2.5). Regarding turbulence, the potential sources were identified as inner surf zone and bore collapse for the run-up phase, and boundary layer effects for the backwash phase, which can be increased by the appearance of backwash bores and swash-swash interactions at the end of it. These features can lead to the generation of backwash vortices. A visualization of these vortices obtained in a laboratory is given in Figure 2.7.

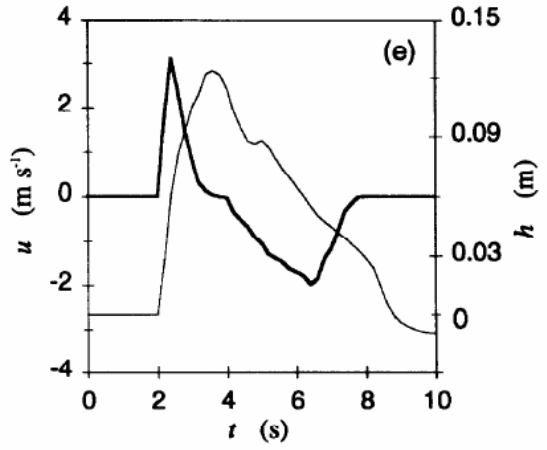

Figure 2.5: Velocity and water depth during a swash event, measured in field. Reproduced from (Hughes *et al.* , 1997).

2.2.2 Sediment transport

The sediment transport mechanisms produced by such complex hydrodynamic effects have also been widely studied. The understanding of the bedload and suspended transport mechanisms has improved significantly during the last years, as explained by (van Rijn *et al.* , 2013).

Regarding the shoaling zone, the main hydrodynamic aspects influencing sediment transport are steady streaming and wave skewness and asymmetry. The drift pattern of dye injected close to the seabed described in (Bagnold, 1947) is very illustrative of how sediment is carried by the steady streaming once it is brought into suspension. Also, importance of steady streaming in sediment transport was highlighted by (Longuet-Higgins & Stoneley, 1953). The effects of wave skewness and asymmetry on bedload transport arises from the non-linear relation between them, typically assumed to be cubic (i.e., in the empirical formulae proposed in (Meyer-Peter & Müller, 1978), (Bailard & Inman, 1981) and (Stive, 1986)). Regarding

suspended transport, the wave-induced oscillations of fluid velocity and suspended sediment concentration result in a net onshore-directed transport close to the seabed along the shoaling zone, since the peak of sediment concentration occurs at the same time as the maximum onshore-directed velocity. The near-bed suspended transport can happen in two regimes which depend on the maximum orbital velocity, sediment size and density. Firstly, the sheet-flow regime occurs for large values of orbital velocity, and the relation between near-bed velocity and sediment concentration is approximately cubic, as in the case of bedload transport. This relation was studied in (Ruessink *et al.* , 2011) based on U-tube measurements. However, for fine sand, the phase lag between velocity and sediment concentration is quite significant, and the relation between near-bed velocity and sediment transport can no longer be assumed cubic. Secondly, the rippled-bed regime corresponds to relatively low maximum orbital velocities, it is dominated by a series of coherent vortices which are advected back and forth from the onshore to the offshore side of each ripple during the flow reversals. This suspended transport regime was studied in (van der Werf *et al.* , 2007) based on laboratory measurements and in (van der Werf *et al.* , 2008) including also results from a 2DV numerical model.

In the surf zone, the undertow is a fundamental feature influencing sediment transport, as concluded in (Gallagher *et al.* , 1998) from the measurements of velocity and observations of sand bar migration in a natural beach. Due to the strong advection that the undertow produces, sediment eroded form a certain area of the beach profile can settle far from it. Additionally, the complex hydrodynamic conditions resulting from wave breaking (i.e., turbulence production, generation of coherent structures or air entrainment) greatly affect the sediment transport mechanisms. Firstly, the coherent structures generated during the breaking process can reach the seabed and alter the near-bed sediment transport mechanisms in both sheet-flow and rippled-bed regimes, described before, as stated in (van Rijn *et al.* , 2013). Furthermore, when these coherent structures reach the seabed they can greatly increase the shear stress and, consistently, the amount of sediment put in suspension. This was studied in (Yoon & Cox, 2012), and it was found that the coherent structures from wave breaking are responsible for a great amount of sediment put in suspension in the surf zone. Also, (Sumer *et al.* , 2013) presented how the shear stress induced by breaking waves can result in a large amount of sediment put into suspension. In Figure 2.6, the distribution of suspended sediment during the wave breaking process is shown. Secondly, the turbulence produced during wave breaking has a fundamental role in keeping sediment in suspension inside the surf zone, as discussed by (Ting & Kirby, 1995) based on laboratory data. This was further observed in a natural beach by (Aagaard & Jensen, 2013) and, more recently, it was experimentally studied in (van der Zanden *et al.* , 2017b) and using a LES numerical model in (Otsuka *et al.* , 2017), respectively. Regarding the bedload transport, the influence of wave breaking was addressed by (van der Zanden *et al.* , 2017a), also addressing the different ways in which bedload and suspended transport contribute to the evolution of the beach profile.

Regarding sediment transport in the swash zone, (Elfrink & Baldock, 2002) also provides a good summary of the current knowledge. Bedload and suspended transport have different relative importance depending on how energetic the swash zone is and the sediment size. The bedload transport depends fundamentally on local conditions, particularly of near-bed velocity. Thus, the bedload transport is influ-

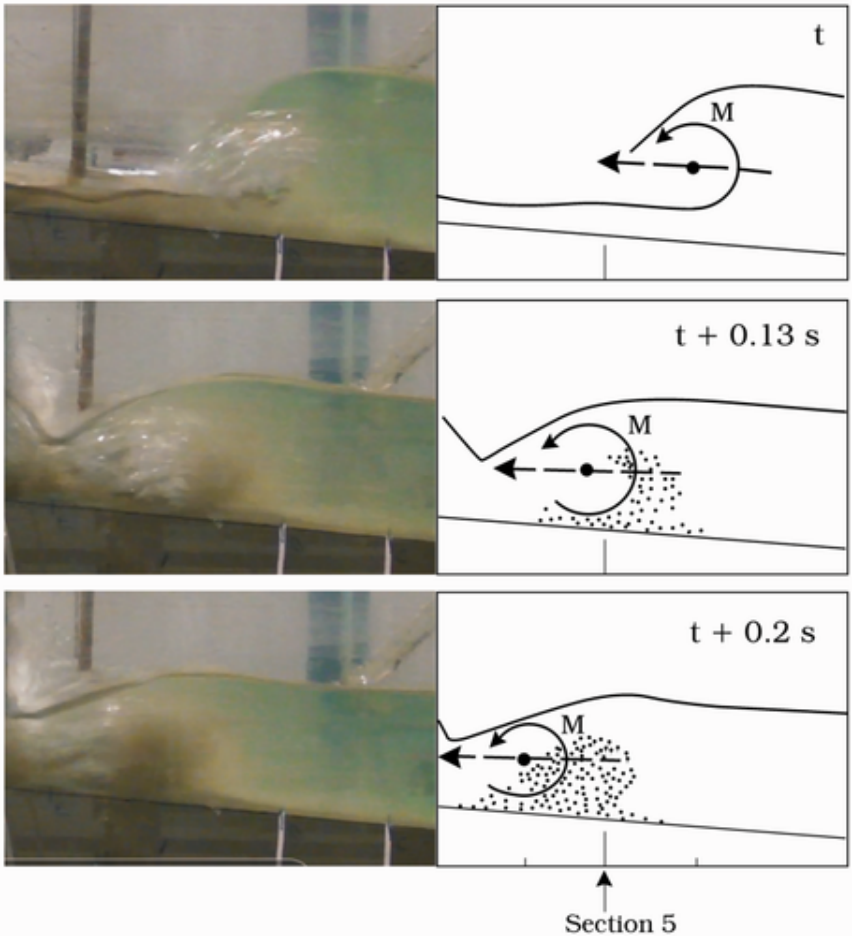

Figure 2.6: Suspended sediment during wave breaking, showing images from laboratory experiments (left) and a schematic view of the effect of the primary vortex resulting from wave breaking in advecting sediment (right). Reproduced from (Sumer *et al.* , 2013).

enced by the velocity and acceleration skewnesses produced by waves. These result in higher shear stress during the rapid increase of velocity in the run-up than in the backwash (i.e., (Howe *et al.* , 2019)). However, the effect of the slope on the stability of sediment grains penalizes bedload transport during run-up respect to that of the backwash. Furthermore, the duration of the backwash motion is larger than that of the run-up. The interplay between duration and excess of shear stresses determines whether the net bedload transport is onshore- or offshore-directed. Another aspect that influences the stability of sediment grains is the change in effective weight produced by infiltration. In contrast with bedload transport, suspended transport cannot be analysed based only on local conditions. Some of the aforementioned hydrodynamic features in the swash zone, such as swash-swash interaction or flow separation if the velocity of the backwash reaches supercritical conditions, result in the generation of strong backwash vortices close to the seabed leading to very high sediment concentration along the water column (i.e., (Larson & Sunamura, 1993), (Matsunaga & Honji, 1980)). Such vortices are responsible for the formation of a beach step separating the swash and inner surf zones. Another literature review of hydrodynamics and sediment transport in the swash zone can be found in (Butt & Russell, 2000), where the lack of suitable instrumentation to gather field measurements is highlighted as a fundamental need to build better models for the swash zone.

2.3 Environmental conditions and cross-shore morphological evolution

Equilibrium conditions of beach profiles, reached once the evolutionary sequence leads to an stable configuration under the current energy sources, is of great interest for engineering applications. The equilibrium beach profile has been often related directly to the environmental conditions (i.e., wave height, period, sea-level, sediment characteristics and initial profile), bypassing the analysis of morphodynamic processes and the evolutionary sequence that leads to it. This approach is schematically illustrated in Figure 2.8, notice the differences with the morphodynamic framework depicted in Figure 1.3. Some of the early equilibrium models developed in this way (i.e., (Bruun, 1954), (Dean, 1977)) are still widely used in several coastal engineering applications due to their simplicity. They are particularly well-suited for long-term calculations due to their low computational cost, and they are commonly referred to as multiyear models.

The Bruun's Rule, (Bruun, 1962), is one of the most commonly used relations of this type. It associates sea level rise and coastal recession considering a perfect balance of sediment mass between near-shore and offshore seabed. A schematic description of this balance is given in Figure 2.9

Also, in (Bruun, 1954), a commonly used empirical equation relating water depth and distance from the shoreline was given (Equation 2.1).

$$h = Ax^{2/3} \tag{2.1}$$

The model from (Dean, 1977) proposes a simple formula (Equation 2.2) for the shape of the beach profile which incorporates two coefficients named scale (A) and shape (m) parameters. The scale parameter is a function of the sediment properties,

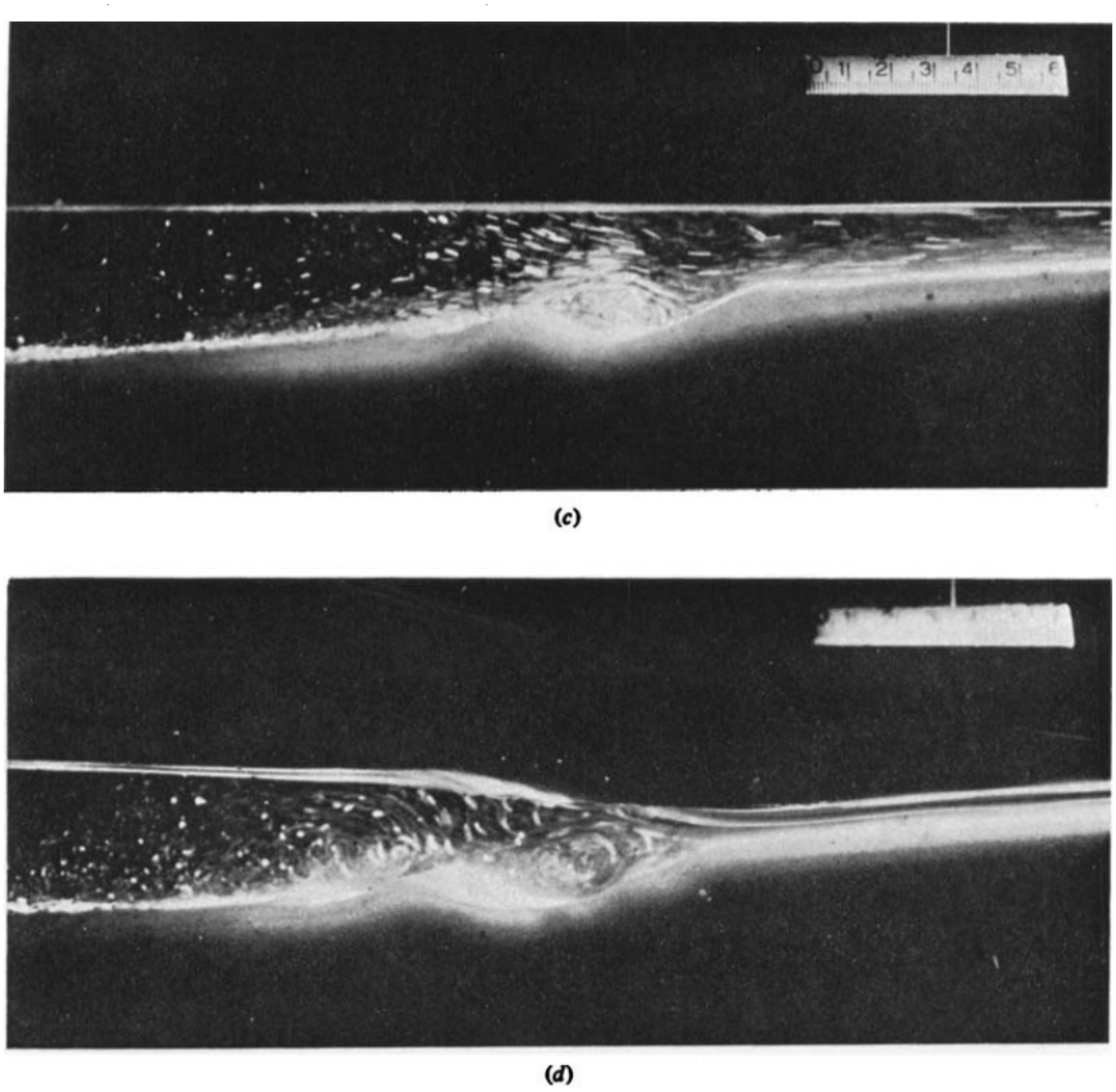

Figure 2.7: Visualization of a backwash vortices in laboratory. Panel C shows a clockwise vortex generated during the run-up . Panel D shows the anticlockwise backwash vortex caused by swash-swash interaction, when the previous backwash encounters the next wave bore. A sawdust bed was used to illustrate the sediment transport induced by it. Reproduced from (Matsunaga & Honji, 1980).

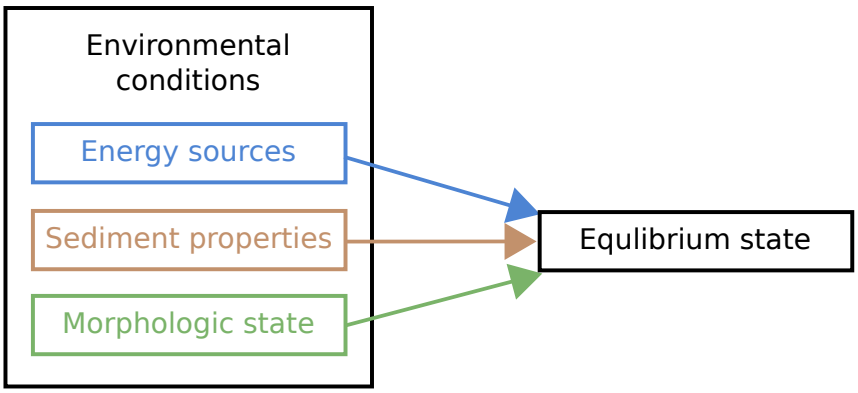

Figure 2.8: Simplified approach directly relating environmental conditions to the equilibrium morphological state.

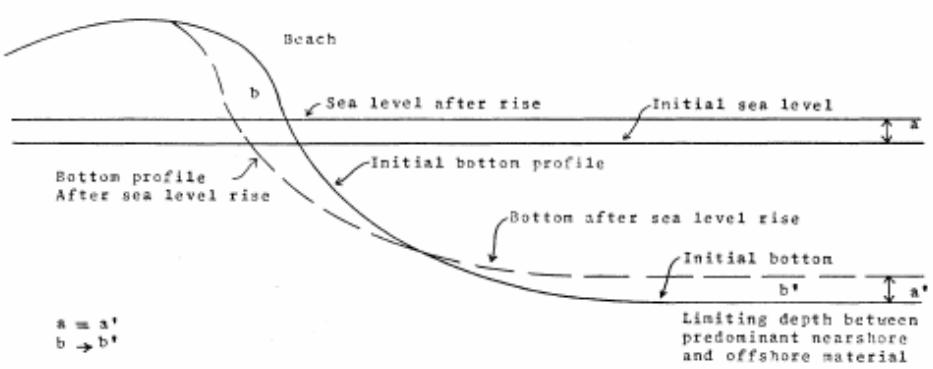

Figure 2.9: Schematic description of variables related by Bruun's law. Reproduced from (Schwartz, 1967).

while the shape parameter depends on the type of energy source and controls the convexity of the profile. This is a widely used expression to approximate the shape of equilibrium beach profiles and assess coastal erosion potential.

$$h = Ax^m \tag{2.2}$$

More information about these developments, validations and limitations can be found in (Bruun, 1988).

(Wright *et al.* , 1985) presents a model to predict the beach state as a function of the dimensionless sediment fall velocity, considering the instantaneous value (obtained from the current environmental conditions and morphological state) and a weighted mean of previous conditions. The antecedent conditions showed a strong relationship with the day-to-day beach state observations. Also, it suggested that the equilibrium status could be determined by setting the time-derivative of dimensionless fall velocity and the sea state to zero. The direction of morphological evolution (erosion or accretion) is predicted based on the difference between equilibrium and instantaneous fall velocity.

(Yates *et al.* , 2009) proposes an equilibrium model which provides the rate of change in mean sea level depending on how far the initial morphology is from the equilibrium configuration and how energetic are the wave conditions. The model incorporates coefficients which control the speed at which the equilibrium is achieved under erosive and accretive conditions.

The model from (Davidson *et al.* , 2013) is also based on the distance between the initial and the equilibrium morphologies, which is calculated based on the dimensionless sediment fall velocities corresponding to initial and equilibrium states, respectively. In this case, the horizontal position of the shoreline is modelled rather than the mean sea level. In this model, the equilibrium status is obtained as a function of the precedent conditions. A parameter controlling the decay of the weighting function for past states is introduced as a calibration parameter.

In (Splinter *et al.* , 2014), another equilibrium model is obtained. The model is pre-calibrated with data obtained globally and then it can be adapted to the specific environmental conditions of the site. The aim of this approach is to reduce the amount of measurements required for the model to provide preliminary results in absence of site-specific calibration and to reduce the size of data sets to perform it. The values of model coefficients were found to systematically depend on the

mean and standard deviation of the dimensionless fall velocity, which relates the significant breaking wave height, sediment settling velocity and spectral peak wave period.

Not accounting for the morphodynamic processes leads to a low level of accuracy in their predictions and, typically, these models give the resulting bathymetry after equilibrium is achieved. This approach, has been refined in more recent studies to account for important morphological features, such as breaker bars, which are not accounted for in earlier models. For example, the dimensions of the breaker bar were related to the incident wave conditions in (Cáceres & Alsina, 2016).

A comprehensive understanding of cross-shore morphodynamic processes can result in better predicting tools for designing and assessing coastal engineering works, leading to more efficient and less intrusive solutions for managing coastal areas.

2.4 Process-based numerical modelling of cross-shore morphodynamics

Numerical models for cross-shore morphodynamics can be designed for multiyear calculations or for shorter time-scales. As explained before, multiyear models are based on semi-empirical formulations and do not solve the morphodynamic processes. In contrast, process-based models solve them to a certain extent and are more suitable for short-term calculations, such as episodic events. In Figure 2.10, a general view of the types of models used to simulate beach morphodynamics are summarized.

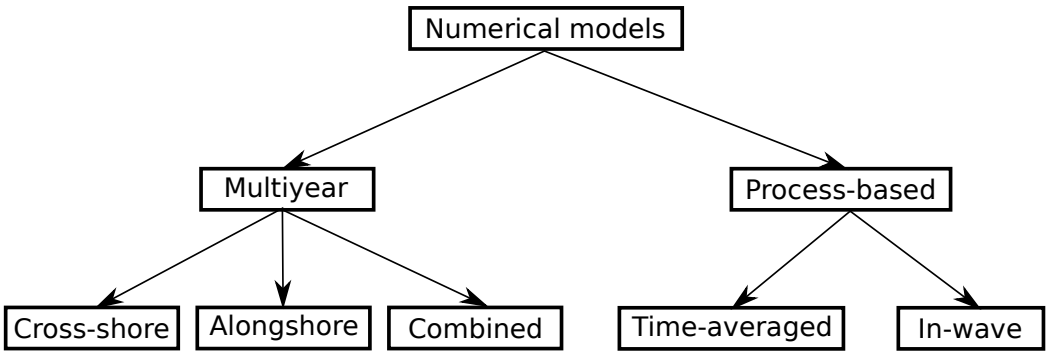

Figure 2.10: Overall classification of numerical models for beach morphodynamics

Focusing on process-based numerical approaches, there is a wide variety that can be used to analyse coastal morphodynamics. They can be classified regarding how they address hydrodynamics and sediment transport.

Concerning the hydrodynamics, two separated groups can be established. Firstly, there are models which calculate the mean flow features without computing in-wave hydrodynamics. Wave effects are considered in these models by including the radiation stress as a source term in their governing equations. Other complex hydrodynamic features due to waves (i.e., eddy viscosity and seabed shear stress

produced by wave breaking) can be also included in the model by using different semi-empirical relations and parameters. The governing equations, used to calculate the mean flow, can vary depending on the particular implementation. The most commonly chosen equations for this purpose are the Generalized Mean Lagrangian (GML) frame Shallow-Water Equations. To compute the wave radiation stress, a specific equation for this variable can be solved, such as the Wave Action Balance Equation (i.e., (Roelvink *et al.* , 2009), (Lesser *et al.* , 2004)).

The second group solve the instantaneous flow rather than its mean value, performing in-wave calculations. Models in this group often solve the Reynolds-Averaged Navier Stokes Equations (RANS). These, among others, are usually referred as Computational Fluid Dynamics (CFD) models. Other type of in-wave solving models which can include sediment transport are the Boussinesq models (Rakha *et al.* , 1997) and Shallow-Water models (i.e., (Zijlema *et al.* , 2011), (Roelvink *et al.* , 2010)). Although most CFD codes use an Eulerian approach to solve the hydrodynamics, the Lagrangian approach of the Smoothed Particle Hydrodynamics (SPH) models, which consists in tracking the position of several integration nodes, has also been applied for Coastal Engineering problems. However, SPH models have not been sufficiently validated and still have a limited applicability for engineering problems in this type of applications. An example of a SPH model applied to sediment transport is given in (Zubeldia *et al.* , 2018).

Models solving the mean flow have a reduced computational cost compared to those solving instantaneous (in-wave) values and, therefore, they are suitable for calculations in relatively large spatial and temporal scales. However, they are less accurate and do not solve some wave transformation (i.e., diffraction, reflection or wave breaking), and hydrodynamics (such as flow separation). Depending on the specific model, more or less of these features are solved. Generally, these models are not precise enough to address the evolution of a cross-shore profile accurately without extensive calibration.

Regarding the sediment transport treatment, numerical models may be divided according to three criteria. The first criterion deals with the different behaviour of cohesive and granular sediments. For cohesive sediment, extra processes must be considered as particles may aggregate into flocs, which can break or aggregate when colliding with others.

The second criterion accounts for the number of phases considered in the hydrodynamic equations. If the sediment effect appears explicitly, for instance as a void fraction or forces induced by sediment particles on the fluid, the model is said to be a Two-Phase model. Otherwise, it is considered as a One-Phase model. One- Phase models usually divide the total sediment transport in bedload and suspended mechanisms, computing each of them separately. In contrast, Two-Phase models consider the water-sediment mixture as a fluid whose characteristics (mainly viscosity and density) depend on the water/sediment ratio and, as particle-particle interactions are accounted for, can avoid treating separately the suspended and bedload mechanisms.

The third criterion regards the sediment transport solving framework, which can be either Eulerian or Lagrangian. Eulerian models focus on static control volumes (cells) and compute sediment transport across its boundaries to determine the variation in sediment concentration inside the control volume. In contrast, Lagrangian models consist in tracking the position of sediment particles by calculating their

trajectories, generally using the Discrete Element Method (DEM). Note that the sediment transport solving approach does not necessarily have to match that of the hydrodynamics.

The classification of in-wave numerical models for sediment transport can be summarized as in Figure 2.11.

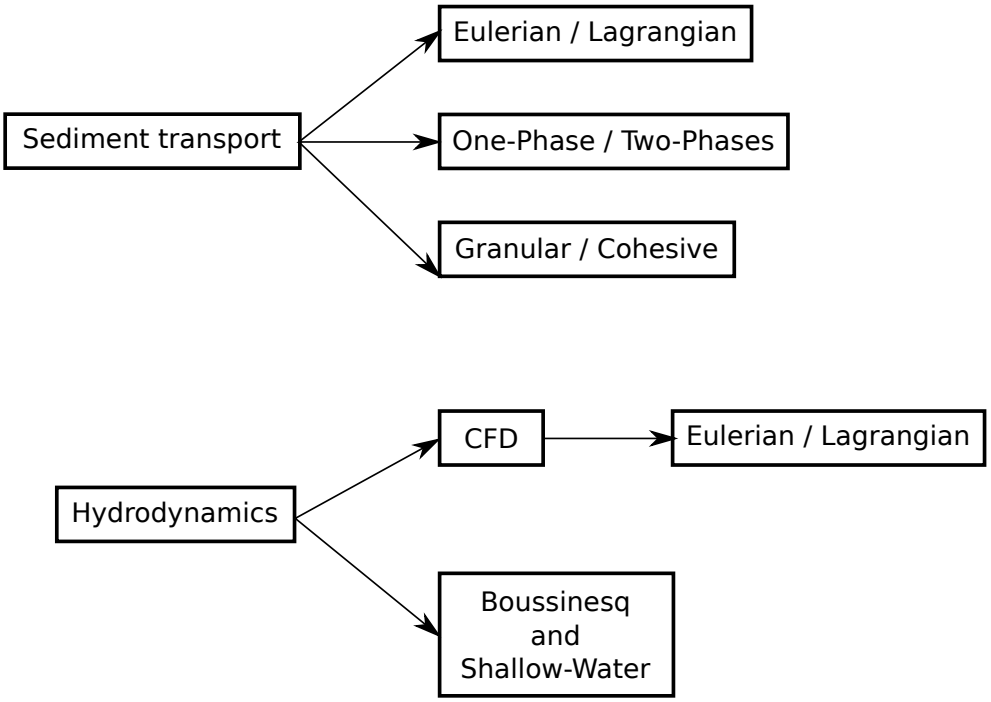

Figure 2.11: Classification of numerical models for sediment transport

Each of the previous types of CFD sediment transport models offers a different balance between computational cost and resolved morphodynamic processes, as summarized in Figure 2.12.

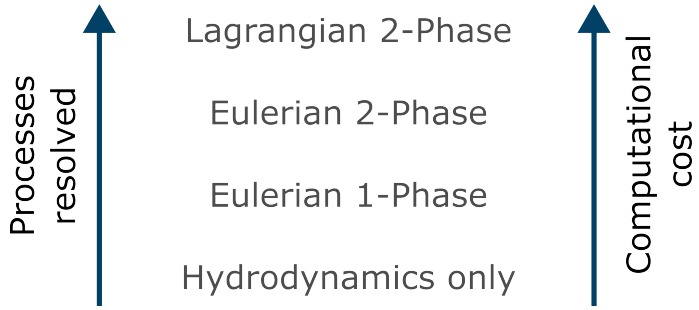

Figure 2.12: CFD sediment transport models and the balance between computational cost and resolved morphodynamic processes.

Overall, CFD models incur in high computational costs, which hinders their application to the research of morphodynamic processes with relatively large temporal scales (i.e., evolution of beach profiles, especially under accretive conditions, and effects of storm sequences). From the previous classification, only One-Phase Eulerian

models are currently suitable for the simulation of a complete beach profile due to the excessive computational cost of the others. Two-Phase Eulerian and Two-Phase Lagrangian models have been applied to investigate smaller scale phenomena, such as the transition from bedload to suspended transport, which are out of the scope of this work.

One of the firsts implementations of One-Phase Eulerian CFD models was given in (Roulund *et al.* , 2005), and it was used to simulate the bed shear stress amplification and scour around a circular pile (see Figure 2.13) . More recently, this implementation was used in (Fuhrman *et al.* , 2014) and (Li *et al.* , 2020), to analyse the scour in submarine pipes (Figure 2.14), in (Larsen *et al.* , 2017) to evaluate tsunami-induced scour around monopile foundations and in (Jacobsen *et al.* , 2014) and (Jacobsen & Fredsoe, 2014) to reproduce the development of a breaker bar in a beach profile. This last simulation has demonstrated the ability of One-Phase Eulerian models to reproduce the relevant cross-shore morphodynamic processes. More recently, in (Zhao *et al.* , 2019), a model using the immersed boundary method for solid treatment was used to predict the scour behind an impermeable seawall produced by a tsunami-like wave (shown in Figure 2.15). In (Peng *et al.* , 2018), a two-dimensional model with partial cell treatment for solid boundaries was used to predict the scour profile in front of a vertical wall, this model considered only the bed-load transport mechanism.

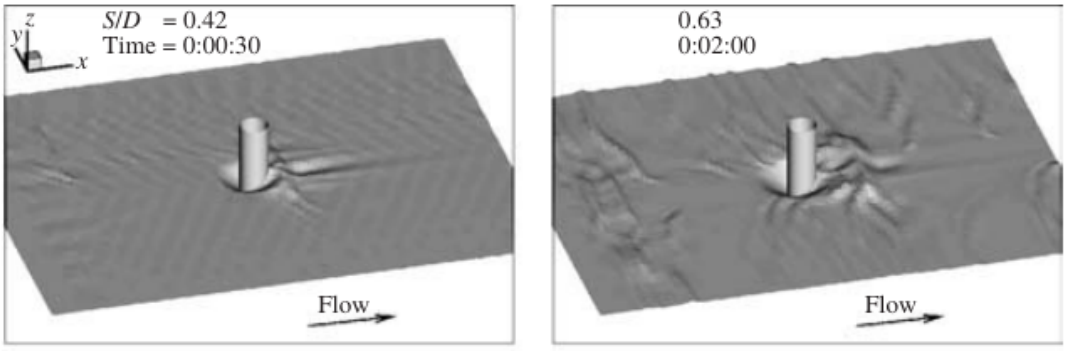

Figure 2.13: Resulting seabed shape from a numerical simulation of scour around a cylinder. Reproduced from (Roulund *et al.* , 2005).

2.5 Conclusions

The mechanisms governing the interaction between hydrodynamics and under given environmental conditions (energy sources, sediment characteristics and morphology) during episodic events are still not fully understood. Such interactions are named morphodynamic processes, according to the framework introduced in Chapter 1. In the existing literature, the main cross-shore hydrodynamic features have been addressed based on field measurements, laboratory and numerical results. Some aspects of the cross-shore sediment transport have been also covered in detail. However, a comprehensive view of the relevant cross-shore morphodynamic processes, caused by the relevant hydrodynamics and sediment transport, and the interactions

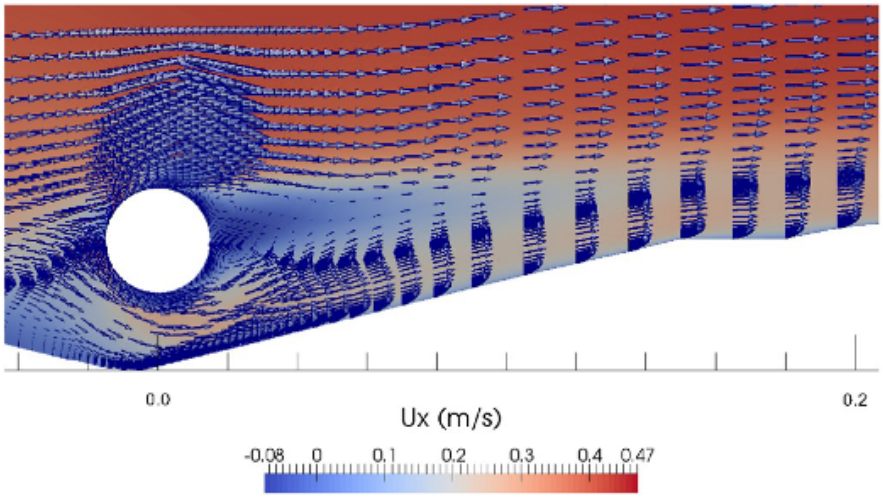

Figure 2.14: Instantaneous velocity field from a numerical simulation of scour beneath a submarine pipeline. Reproduced from (Li *et al.* , 2020).

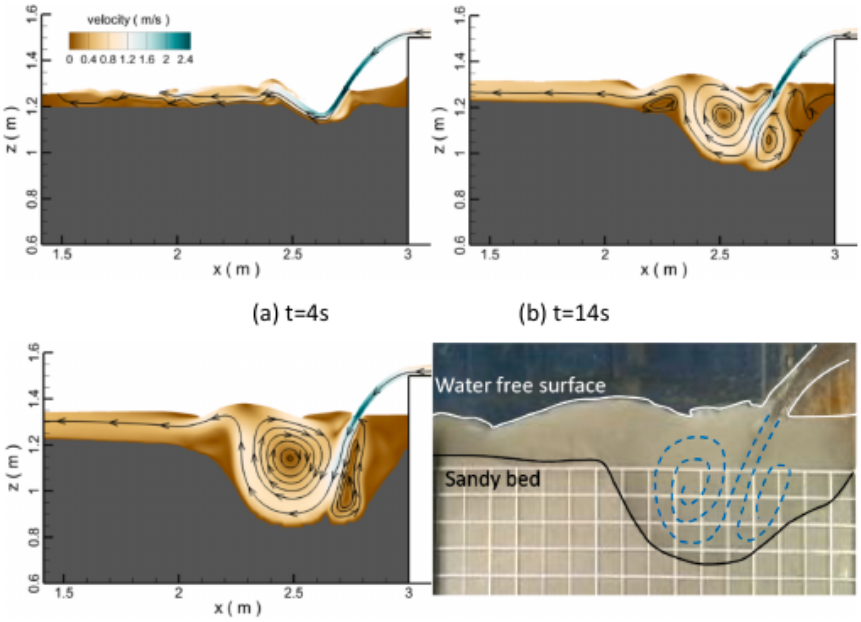

Figure 2.15: Velocity fields and seabed shape caused by a tsunami-like wave overtopping a seawall. Panels a, b and c correspond to different instants along the simulation, while panel d displays experimental results. Reproduced from (Zhao *et al.* , 2019).

between them is lacking. As a result, the morphological evolution of beach profiles is generally addressed in an oversimplified manner.

The limitations of laboratory techniques associated to mobile bed conditions (i.e., as scaling effects) and the simultaneous measurement of fluid and sediment related variables with high spatial and temporal resolution hinder the understanding of the morphodynamic processes that drive beach profile evolution. Field measurements also encounter several difficulties when gathering detailed observations, especially under high energetic wave conditions, (i.e., ensuring the survivability and correct functioning of the instruments or finding the time windows to measure under the desired environmental conditions).

Process-based numerical models are interesting resources that complement the previous techniques when carrying out research on morphodynamic processes. Various types of models offer different balances between resolved processes and computational cost. Among the available types, One-Phase Eulerian models offer an interesting compromise between precision and computational cost, which makes them more suitable for studying coastal morphodynamics at the scale of beach profiles. However, their computational cost is still excessive, and this hinders their applicability for researching morphodynamic processes. Thus, it is desirable to develop new tools with different degrees of precision and computational cost to cover the scales of the morphodynamic processes during episodic events. Particularly, there is a gap between the compromise offered by One-Phase Eulerian and that of non-CFD models (i.e., Boussinesq models) in which many fundamental aspects of the morphodynamic processes in episodic events could be addressed.

A deeper understanding of the morphodynamic processes driving the cross-shore beach profile evolution in episodic events is needed to better establish links between environmental conditions and morphological evolution. Despite the significant advancements in the understanding of morphodynamic processes, the current knowledge is still not enough to provide reliable predictions. A global approach that integrates the existing knowledge on morphodynamic processes involved in the cross-shore beach profile evolution and the interactions between them is of great interest for improving multiyear models, as discussed in (Walstra, 2016).

Chapter 3

Objectives and approach

Contents

3.1 Introduction

In Chapter 2, some knowledge gaps in cross-shore morphodynamics are pointed out. These gaps are:

- The current knowledge in how cross-shore hydrodynamics and sediment transport produce morphodynamic processes and are linked to the morphological evolution is not sufficient.
- A comprehensive understanding of the combined effect of relevant cross-shore morphodynamic processes is lacking.
- The numerical models able to reproduce the relevant morphodynamic processes entail high computational cost, which hinders their application for research purposes.

The objectives of this thesis are set according to these limitations in the understanding of cross-shore morphodynamic processes.

3.2 Main objective

In this thesis. the main objective is to improve our knowledge on the morphodynamic processes that drive the evolution of beach profiles in episodic events. In particular, gaining a global understanding of how the interplay between the relevant hydrodynamic and morphological features brings these processes about and what are their main drivers.

As discussed in Chapter 1, improving the knowledge on cross-shore morphodynamics is a key aspect to better understand how beaches behave and, thus, in designing effective solutions for coastal erosion and management. Particularly, multiyear models, commonly used for coastal erosion analysis, could greatly benefit from a better understanding of morphodynamic processes by reducing the amount of calibration parameters that they require.

3.3 Specific objectives

The main objective is decomposed in a series of specific objectives which are individually tackled in the following chapters.

The specific objectives of this thesis are:

1. Develop a numerical model able to simulate the main morphodynamic processes in cross-shore beach profiles in episodic events at a feasible computational cost.
2. Present a validation of the numerical model.
3. Provide a comprehensive analysis of the morphodynamic processes involved in cross-shore beach profile evolution based on numerical results. Particularly in:
   (a) Morphodynamic processes causing the growth of the breaker bar.
   (b) Morphodynamic processes causing the migration of the breaker bar.
   (c) Morphodynamic processes causing the equilibrium of the breaker bar.

3.4 Methodology

The methodology followed to accomplish these objectives consists of two main parts: the development of the numerical model (specific objectives 1 and 2) and using the model to gain insights into the morphodynamic processes (specific objective 3).

In the first part, the numerical model is developed based on the previously existing hydrodynamic model IH2VOF, which is described in depth in Chapter 4. It is a RANS model which has already been used successfully to simulate surf zone hydrodynamics. A sediment transport model, which is extensively described in Chapter 4, is developed and coupled with IH2VOF to obtain a numerical tool that can be used to analyse the beach profile evolution. The numerical model is extensively validated with experimental data at different geometric scales in order to test its skill to reproduce the main physics under study.

In the second part, the capabilities of the numerical model are exploited to obtain high-definition results, which are useful to understand how the morphodynamic processes occur. Based on these results, observations from experimental works and field measurements, an in-depth description on how the main cross-shore morphodynamic processes occur and their principal drivers is derived.

3.5 Hypotheses

The previous methodology is based on the following hypothesis listed below.

1. The initial 2DV model, IH2VOF, is able to reproduce the main hydrodynamic features in the cross-shore profile with sufficient accuracy despite the simplifications made in exchange for lower computational cost.

2. The numerical error close to solid boundaries due to the cut-cell method does not significantly affect the hydrodynamic features.

3. Eulerian One-Phase models are able to reproduce the main sediment transport features in the cross-shore profile.

4. It is possible to analyse the main cross-shore morphodynamic processes in episodic events using a 2DV model.

Chapter 4

Mathematical model and numerical solution

Contents

4.1 Introduction

In this chapter, Specific Objective 1 is addressed. A non-cohesive One-Phase Eulerian sediment transport model is developed and coupled with the existing 2DV RANS hydrodynamic model IH2VOF. The governing equations of hydrodynamic and sediment transport models are described first in Section 4.2. Later, in Section 4.3, the solving algorithms for these governing equations are presented.

4.2 Mathematical model

The physics of hydrodynamics and sediment transport are represented by a set of Partial Differential Equations (PDEs) and empirical formulae, which comprise the governing equations. These equations are described in this section. Firstly, the governing equations for the hydrodynamic model are discussed. Secondly, those of the sediment transport model are addressed, including the equations for bedload and suspended transport and for the bathymetric evolution.

4.2.1 Hydrodynamic model

The hydrodynamic model used is IH2VOF ((Lara *et al.* , 2011), (Losada *et al.* , 2008)). This model solves the RANS equations in 2DV dimensions by using the Finite Difference Method (FDM) in an orthogonal Cartesian staggered grid. To account for the effect of solid boundaries, the cut-cell method is adopted. The free surface tracking is performed by the Volume of Fluid method (VoF). The model can run in either laminar or turbulent conditions, using a $k-\epsilon$ turbulence model in the latter.

IH2VOF has been extensively validated for different hydrodynamic processes in the surf zone against both laboratory and field data ((Lara *et al.* , 2011), (Torres-Freyermuth *et al.* , 2007), (Ruju *et al.* , 2012)).

Governing equations The governing equations that the hydrodynamic model solves are the RANS equations.

From mass balance in a control volume, the mass conservation equation is

$$\frac{\partial \rho}{\partial t} + \nabla \cdot (\rho \vec{u}) = 0 \tag{4.1}$$

in which $\vec{u}$ is the velocity vector and ρ the density of the fluid. $\nabla \cdot (\ )$ denotes the divergence operator, which for 2DV is

$$\nabla \cdot (\vec{u}) = \frac{\partial (u_x)}{\partial x} + \frac{\partial (u_y)}{\partial y} \tag{4.2}$$

being u_x and u_x the X and Y components of the velocity vector.

For an constant density flow $\frac{\partial \rho}{\partial t} = 0$. Furthermore, if the density is uniform it can be taken out of the divergence, leading to the mass conservation equation commonly used for incompressible flows

$$\nabla \cdot (\vec{u}) = 0 \tag{4.3}$$

Note that Equation 4.3 establishes a restriction on the velocity field. Many velocity fields can match such restriction.

Regarding the momentum conservation equations, starting from the conservation of an arbitrary magnitude per unit of mass (ψ) in a fixed control volume (Eulerian perspective), the following expression results

$$\frac{\partial(\rho\psi)}{\partial t} + \nabla \cdot (\rho\psi\vec{u}) = 0 \tag{4.4}$$

Also, the conservation of this arbitrary magnitude in a moving control volume (Lagrangian perspective) is expressed as a function of the position of the control volume

$$\psi = f(x) = \psi_{(x)} \tag{4.5}$$

The total variation of the magnitude inside the moving control volume is

$$\frac{D\psi}{Dt} = \frac{\partial\psi}{\partial t} + \vec{u}\vec{\nabla}(\psi) \tag{4.6}$$

where $\vec{\nabla}(\ )$ represents the gradient operator, which for 2DV is

$$\vec{\nabla}(\psi) = \frac{\partial(\psi)}{\partial x}\vec{i} + \frac{\partial(\psi)}{\partial y}\vec{j} \tag{4.7}$$

being $\vec{i}$ and $\vec{j}$ the unitary vectors in X and Y directions, respectively.

Expanding the terms of Equation 4.4 using the properties of derivatives

$$\frac{\partial(\rho\psi)}{\partial t} + \nabla \cdot (\rho\psi\vec{u}) = \rho\Big[\frac{\partial\psi}{\partial t} + \vec{u}\vec{\nabla}(\psi)\Big] + \psi\Big[\frac{\partial\rho}{\partial t} + \nabla \cdot (\rho\vec{u})\Big] \tag{4.8}$$

Applying mass conservation, Equation 4.1, the second term on the RHS is eliminated yielding

$$\frac{\partial(\rho\psi)}{\partial t} + \nabla \cdot (\rho\psi\vec{u}) = \rho\Big[\frac{\partial\psi}{\partial t} + \vec{u}\vec{\nabla}(\psi)\Big] \tag{4.9}$$

The remaining RHS term in Equation 4.9 can be identified as the RHS of Equation 4.6 multiplied by the density. Substituting the LHS of Equation 4.9 on the RHS of Equation 4.6 and rearranging

$$\rho\frac{D\psi}{Dt} = \frac{\partial(\rho\psi)}{\partial t} + \nabla \cdot (\rho\psi\vec{u}) \tag{4.10}$$

Equation 4.10 gives a relation between the Eulerian and Lagrangian perspectives on the conservation of momentum. If, instead of the arbitrary magnitude ψ, this expression is applied to the momentum per unit of mass (which is the velocity vector $\vec{u}$ itself), the following expression is obtained

$$\rho\frac{D(\vec{u})}{Dt} = \frac{\partial(\rho\vec{u})}{\partial t} + \nabla \cdot (\rho\vec{u} \otimes \vec{u}) \tag{4.11}$$

in which $\otimes$ denotes the outer product.

Additionally, Newton's Second Law relates the total change in momentum of a particle (moving control volume) with the forces exerted on it.

$$\rho \frac{D\vec{u}}{Dt} = \sum \vec{f_i} \tag{4.12}$$

where $\vec{f_i}$ are the different forces acting on the particle. Among these, the pressure forces (normal stresses) and tangential stresses are of great importance in Fluid Mechanics applications. The sum of forces in Equation 4.12 acting on a fluid particle can be expressed in terms of these as

$$\sum \vec{f_i} = \vec{\nabla} p + \nabla \cdot (\bar{\bar{\tau}}) + \vec{S_m} \tag{4.13}$$

where p is the pressure, $\bar{\bar{\tau}}$ is the Cauchy stress tensor and $\vec{S_m}$ represents other external forces that could be acting on the particle (such as the gravitational force).

Considering Equations 4.11, 4.12 and 4.13, the RHS term in Equation 4.13 can be substituted on the LHS of Equation 4.11. The following results

$$\frac{\partial(\rho\vec{u})}{\partial t} + \nabla \cdot (\rho\vec{u} \otimes \vec{u}) = \vec{\nabla} p + \nabla \cdot (\bar{\bar{\tau}}) + \vec{S_m} \tag{4.14}$$

To continue with the derivation of some useful form of the momentum conservation equation, it is required to reduce the number of variables by establishing relations between them. For this purpose, a model for the calculation of the Cauchy stress tensor is included. This model assumes that the stress tensor is proportional to the deformation rate tensor ($\bar{\bar{S}}$).

$$\bar{\bar{\tau}} = 2\mu\bar{\bar{S}} \tag{4.15}$$

in which μ is the kinematic molecular viscosity, a scalar value for isotropic fluids. This equation fundamentally represents the momentum transfer produced by the molecular viscosity.

Thus, Equation 4.14 can be rewritten as

$$\frac{\partial(\rho\vec{u})}{\partial t} + \nabla \cdot (\rho\vec{u} \otimes \vec{u}) = \vec{\nabla} p + \nabla \cdot (2\mu\bar{\bar{S}}) + \vec{S_m} \tag{4.16}$$

Equations 4.1 and 4.16 are the Navier-Stokes equations, which only include the viscous behaviour assumption (relating the Cauchy stress tensor to the deformation rate).

The deformation rate $\bar{\bar{S}}$ is defined as

$$\bar{\bar{S}} = \frac{1}{2}\Big[\vec{\nabla}\vec{u} + (\vec{\nabla}\vec{u})^T\Big] + \frac{2}{3}\nabla \cdot (\vec{u}) \tag{4.17}$$

The last term in the RHS represents the rate of expansion or compression of the fluid element. For an incompressible flow, this term vanishes due to mass conservation, leading to the following expression for the deformation rate

$$\bar{\bar{S}} = \frac{1}{2}\Big[\vec{\nabla}\vec{u} + (\vec{\nabla}\vec{u})^T\Big] \tag{4.18}$$

These two terms express the linear deformation rate. Inserting them into Equation 4.16 leads to the term

$$\nabla \cdot \Big(\mu\Big[\vec{\nabla}\vec{u} + (\vec{\nabla}\vec{u})^T\Big]\Big) = \nabla \cdot (\mu\vec{\nabla}\vec{u}) + \nabla \cdot \Big[\mu(\vec{\nabla}\vec{u})^T\Big] \tag{4.19}$$

Assuming a uniform kinematic viscosity, the first term on the RHS can be simplified

$$\nabla \cdot (\mu \vec{\nabla} \vec{u}) = \mu \nabla^2 (\vec{u}) \tag{4.20}$$

The second term can be expanded to

$$\nabla \cdot \left[\mu (\vec{\nabla} \vec{u})^T \right] = \vec{\nabla} \mu (\vec{\nabla} \vec{u})^T + \mu \vec{\nabla} (\nabla \cdot \vec{u}) \tag{4.21}$$

In this expansion, it can be noted that the second RHS term in Equation 4.19 is zero assuming a fluid with uniform kinematic viscosity ($\vec{\nabla} \mu = 0$) and incompressible flow ($\nabla \cdot (\vec{u}) = 0$). Thus, Equation 4.16 can be simplified to

$$\frac{\partial (\rho \vec{u})}{\partial t} + \nabla \cdot (\rho \vec{u} \otimes \vec{u}) = \vec{\nabla} p + \mu \nabla^2 \vec{u} + \vec{S_m} \tag{4.22}$$

The resulting equation is commonly used along with Equation 4.3, as the isotropic fluid and incompressible flow assumptions are suitable for many situations. A more general form is Equation 4.16, which only includes the hypothesis of viscous flow. The most general is Equation 4.14, which does not imply a viscous behaviour of the fluid (another types of constitutive model to obtain the stress tensor could be used).

However, Equation 4.22 involves resolving the velocity field which, in turbulent flows, features small scale, high-frequency oscillations. Such oscillations are expensive to model, as the time and spatial discretizations must be fine enough to capture them. Even though these oscillations occur in small scales, they can have an important influence on the macroscopic flow. Thus, it is aimed to find some equations that can capture the macroscopic effects of the small turbulent fluctuations without actually simulating them.

To tackle this, the velocity vector is considered as a random variable resulting from adding an averaged (deterministic) and a fluctuating (random) components. Note that the value of the velocity vector (and thus of the velocity fluctuation) is completely deterministic according to Equation 4.22, although its precise value is hard to compute as the fluctuations are highly dependant on the initial conditions (it has a chaotic behaviour). Thus, the turbulent fluctuations of the velocity field are modelled as a random process.

$$\vec{u} = \vec{U} + \vec{u'} \tag{4.23}$$

where $\vec{U}$ is the averaged velocity vector ($\vec{U} = \bar{\vec{u}}$) and $\vec{u'}$ is its fluctuating component. As $\vec{U}$ is deterministic, its average value is equal to itself ($\bar{\vec{U}} = \vec{U}$). Also, according to Equation 4.23, $\bar{u'} = 0$).

Introducing this decomposition in Equation 4.22 leads to

$$\frac{\partial \left[\rho (\vec{U} + \vec{u'}) \right]}{\partial t} + \nabla \cdot \left[\rho (\vec{U} + \vec{u'}) \otimes (\vec{U} + \vec{u'}) \right] = \vec{\nabla} p + \mu \nabla^2 (\vec{U} + \vec{u'}) + \vec{S_m} \tag{4.24}$$

Averaging both sides and rearranging yields

$$\frac{\partial (\rho \vec{U})}{\partial t} + \nabla \cdot \left(\rho \vec{U} \otimes \vec{U} \right) = \vec{\nabla} p + \nabla \cdot \left(\rho \vec{u'} \otimes \vec{u'} \right) + \mu \nabla^2 (\vec{U}) + \vec{S_m} \tag{4.25}$$

Equations 4.1 and 4.25 are the Reynolds-Averaged Navier-Stokes (RANS) equations, in which only one term including the velocity fluctuations remains ($\nabla \cdot \left(\rho \vec{u'} \otimes \vec{u'}\right)$) known as the Reynolds Stress Tensor. These are the governing equations solved by the different RANS CFD models (although more equations could be added depending on the application). Other types of CFD models use different strategies to deal with the velocity fluctuations, such as LES models (Large Eddy Simulation), which simulate part of the turbulent fluctuations, or DNS models (Direct Numerical Simulation) which directly solve the Navier-Stokes equations.

To compute the Reynolds Stress Tensor, different approaches can be used. Particularly, an analogy with the momentum transport produced by the molecular viscosity (Equation 4.15) can be used to relate the Reynolds Stress Tensor ($\bar{\bar{R}}$) with the deformation rate.

$$\bar{\bar{R}} = 2\mu_t \bar{\bar{S}} \tag{4.26}$$

in which μ_t is the turbulent kinematic viscosity. The deformation rate tensor is obtained from the averaged velocity vector, not including the effect of turbulent fluctuations. This is known as the Boussinesq hypothesis, and allows to isolate the effect of turbulent fluctuations in the turbulent viscosity.

Inserting Equation 4.26 in Equation 4.25 and following an analogous process as in Equation 4.16 results in

$$\frac{\partial(\rho\vec{U})}{\partial t} + \nabla \cdot \left(\rho\vec{U} \otimes \vec{U}\right) = \vec{\nabla} p + (\mu + \mu_t)\nabla^2(\vec{U}) + \vec{S_m} \tag{4.27}$$

At this point, this equation requires a way of computing the turbulent viscosity. For this purpose, a turbulence model is used. There are some turbulence models that attempt to compute this quantity assuming an isotropic effect of the turbulent fluctuations. Other turbulence models directly compute the Reynolds Stress Tensor, which allows to consider the three-dimensional effects of the turbulent fluctuations at the cost of computing the 6 different components of the Reynolds Stress Tensor instead of just one magnitude for the turbulent viscosity.

Assuming incompressible flow, this equation can be further simplified to

$$\frac{\partial(\vec{U})}{\partial t} + \nabla \cdot (\vec{U} \otimes \vec{U}) = -\frac{\vec{\nabla} p}{\rho} + (\nu + \nu_t)\nabla^2\vec{U} + \vec{S_M} \tag{4.28}$$

where p is the pressure, ρ is the fluid density, ν and ν_t are the molecular and turbulent dynamic viscosities and $\vec{S}_M$ represents different body forces acting on the fluid. In this case, the only body force considered is the gravitational force.

Equations 4.28 and 4.3 are suitable for the kind of application for which the model is intended to be used. However, the numerical treatment of solid boundaries used in this model requires a modification of these equations.

Scalar-transport equations To obtain ν_t, a turbulence closure model is needed. In this case, a $k - \epsilon$ model is used, which solves the transport equations for the turbulent kinetic energy (k) and its dissipation rate (ϵ). For each of these scalar fields, its transport equation considers the time variation and advective flux on the left-hand side and the diffusive flux, source and sink terms on the right-hand side. The turbulence model is based on (Hsu *et al.* , 2002), which incorporates a damping

function in order to avoid the overproduction of turbulent kinetic energy addressed in (Larsen & Fuhrman, 2018).

$$\frac{\partial k}{\partial t} + \nabla \cdot (\vec{U}k) = \nabla \cdot \left[\left(\nu + \frac{\nu_t}{\sigma_k} \right) \vec{\nabla} k \right] + (\vec{u'} \otimes \vec{u'}) \vec{\nabla}(\vec{U}) - \epsilon \tag{4.29}$$

$$\frac{\partial \epsilon}{\partial t} + \nabla \cdot (\vec{U}\epsilon) = \nabla \cdot \left[\left(\nu + \frac{\nu_t}{\sigma_\epsilon} \right) \vec{\nabla} \epsilon \right] + C_{1\epsilon} \frac{\epsilon}{k} (\vec{u'} \otimes \vec{u'}) \vec{\nabla}(\vec{U}) - C_{2\epsilon} \frac{\epsilon^2}{k} \tag{4.30}$$

where σ_k and σ_ϵ are the Schmidt numbers for k and ϵ respectively. $C_{1\epsilon}$ and $C_{2\epsilon}$ are empirical coefficients. The values from (Wilcox, 1998) are

$$\sigma_k = 1.0; \sigma_\epsilon = 1.3; C_{1\epsilon} = 1.44; C_{2\epsilon} = 1.92 \tag{4.31}$$

Once k and ϵ are obtained, the turbulent viscosity can be calculated as

$$\nu_t = C_d \frac{k^2}{\epsilon} \tag{4.32}$$

where C_d is another empirical coefficient with a recommended value of $C_d = 0.09$.

The Volume of Fluid (VoF) method for free surface tracking consists in solving the advective transport of a magnitude representing the amount of fluid inside the cell. In contrast with other numerical models using the same strategy, IH2VOF does not solve the velocity, pressure and turbulent fields (k and ϵ) for the air phase. The equation for the advection of the VoF function F is

$$\frac{\partial F}{\partial t} + \nabla \cdot (\vec{U}F) = 0 \tag{4.33}$$

The cut-cell method The cut-cell method, used to account for the effect of solid boundaries, includes the effect of the openness of the cell volume (θ) and of the cell faces (θ_f) to the fluid. The RANS equations are derived for a fully open control volume. Thus, to include the effect of the boundaries, the shape of the corresponding control volume must be inferred from the cell volume and faces openness. This means that in cut-cells the actual control volume in which the fluid equations are solved is not the computational cell.

Two considerations must be observed when discretizing the RANS equations to account for his difference.

Firstly, the volume of the control volume in a cut-cell is smaller than volume of the cell. Thus, when intensive properties (per unit of mass) are computed, it should be considered that the fluid mass contained in the control volume (m_{cv}) is

$$m_{cv} = \rho \theta V_{cell} = \rho_{eq} V_{cell} \tag{4.34}$$

in which ρ_{eq} is the equivalent density of the cell. Notice that this equivalent density is also applied to the calculation of molecular and turbulent kinematic viscosities.

Secondly, when computing fluxes across the bounding surface of the control volume, it must be considered that the faces of cut-cells do not correspond to those of the control volume in which the RANS equations are solved. Rather, the control volume faces are obtained as

$$A_{eq} = \theta_f A \tag{4.35}$$

4.2.2 Sediment transport model

The sediment transport is handled by a One-Phase Eulerian model which accounts for both bedload and suspended transport mechanisms. In addition, landslides are considered as a special type of bedload transport. Once these contributions are calculated, a mass balance is performed to obtain the seabed movement and, finally, the solid boundaries of the hydrodynamic model are updated by modifying the cut-cell parameters.

The overall structure of the model is based on (Roulund *et al.* , 2005), although several aspects of the implementation have been changed to improve its behaviour and adapt it to the specific meshing strategy of the hydrodynamic model.

The inputs required by the sediment transport model are grain size, bulk density and porosity. The sediment fall velocity can be either specified by the user or estimated from the previous parameters using empirical formulae.

Bedload transport

Among the existing empirical methods that provide the instantaneous bedload transport rate (i.e. (Bailard & Inman, 1981), (Stive, 1986)), the one from (Roulund *et al.* , 2005) is selected as it has been previously used in (Jacobsen *et al.* , 2014) to successfully simulate the evolution of a beach profile, as well as in other sediment transport related problems such as (Baykal *et al.* , 2015) and (Larsen *et al.* , 2016). The sediment volumetric flux ($\vec{Q_{bl}}$) is calculated with

$$\vec{Q_{bl}} = \frac{1}{6}\pi d P_{ef} \vec{U_b} \tag{4.36}$$

in which d is the particle diameter, P_{ef} is the proportion of moving particles, which depends on the difference between the Shields number and its critical value, and $\vec{U_b}$ is the velocity of moving particles, obtained from the friction velocity. Equation 4.36 is used for both friction-induced bedload transport and landslides.

The proportion of moving particles (P_{ef}) can be obtained as

$$P_{ef} = \left[1 + \left(\frac{\frac{1}{6}\pi\mu_d}{\phi - \phi_c}\right)^4\right]^{-\frac{1}{4}} \tag{4.37}$$

where μ_d is the dynamic friction coefficient considered as 0.51 in (Roulund *et al.* , 2005), ϕ is the Shields parameter associated to skin friction and ϕ_c the critical Shields value.

The critical value of Shields parameter (ϕ_c) must consider the effect of the slope of the seabed. For this reason, its value is composed by a basic value, for a flat bed, and a coefficient accounting for the effect of the slope. The critical Shields parameter is therefore obtained as

$$\phi_c = \phi_0 k_\beta \tag{4.38}$$

being ϕ_0 the basic value of the critical Shields parameter and k_β a coefficient to include the slope effect, which is computed as

$$k_\beta = \begin{cases} \frac{\sin(\beta_r+\beta)}{\sin\beta_r} & if \quad \beta < 0 \\ \frac{\sin(\beta_r-\beta)}{\sin\beta_r} & if \quad \beta > 0 \end{cases} \tag{4.39}$$

where β is the angle of the slope and β_r is the internal friction angle of the sediment. The friction angle of the sediment has a default value of 30 degrees, it can also be provided as an input if data is available.

To determine the percentage of moving particles using Equation 4.37, the Shields parameter produced by the fluid skin friction is obtained with

$$\phi = \frac{|\vec{U_f}|^2}{(s-1)gd} \tag{4.40}$$

where $\vec{U_f}$ is the friction velocity vector and s is the relative density of the sediment.

Once the bedload transport is calculated, its divergence (representing the increment of sediment volume at each point of the fluid-sediment interface) is obtained. This value is later considered to compute the variation of the seabed position.

Further information about this method can be found in (Roulund *et al.* , 2005)

Suspended transport

The suspended sediment transport can produce erosion or deposition of sediment in different zones along the beach profile. However, the sediment is not necessarily eroded and deposited at the same position, it can be advected by the fluid and settle in completely different zones. For this reason, in order to obtain the sediment interchange between fluid and solid, the evolution of the sediment concentration field in the fluid domain must be computed. This is done by solving the following advective-diffusive transport equation

$$\frac{\partial C}{\partial t} = \nabla \cdot \left[(\vec{U} + \vec{w_s})C\right] + \nabla \cdot \left[\left(\frac{\nu + \nu_t}{\sigma_c}\right)\vec{\nabla}C\right] \tag{4.41}$$

where C is the sediment concentration. $\vec{w_s}$ is the sediment fall velocity and σ_c is the Schmidt number for the sediment which was estimated between 0.5 and 0.7 in (Amoudry *et al.* , 2005). In this case, $\sigma_c = 0.5$ has been considered.

The magnitude of the sediment fall velocity can be provided as an input. In case it is not given, a default value based on the formulae from (Fredsoe & Deigaard, 1992) is used.

$$|\vec{w_s}| = \sqrt{\frac{4(s-1)gd}{3C_d}} \tag{4.42}$$

where C_d is the drag coefficient, obtained from the grain Reynolds number (Re) as

$$C_d = 1.4 + \frac{36}{Re} \tag{4.43}$$

in which grain Reynolds number, calculated with

$$Re = \frac{w_s d}{\nu} \tag{4.44}$$

One of the challenges for the calculation of the sediment concentration field is determining how much sediment is put in suspension from the seabed. The physical processes involved in this interchange between solid and fluid are complex and occur at a small scale in the fluid layers close to the solid boundary, where the distinction between bedload and suspended transport is not clear. The individual sediment

particles are mobilized by the friction velocity and then are lifted by turbulent motions. Furthermore, particle-particle interactions play an important role in this zone, due to the high levels of sediment concentration. The simulation of such a small-scale advective sediment flux is out of the scope of the present model, as it requires a fine mesh discretization close to the seabed, a more detailed treatment of the hydrodynamics of the boundary layer and accounting for the interaction between sediment particles. Such simulations can be found for instance in (Sun & Xiao, 2016) and (Elghannay & Tafti, 2018). To maintain an attractive compromise between computational cost and precision, the turbulent advection of sediment is modelled as a diffusive flux driven by the concentration gradient and turbulent viscosity.

To estimate the sediment concentration gradient, the reference concentration (C_b) is used. It is obtained as proposed in (Smith & McLean, 1977).

$$C_b = \frac{0.65\gamma_0 S_0}{1 + \gamma_0 S_0} \tag{4.45}$$

where $\gamma_0 = 2.4 \times 10^{-3}$ and $S_0 = \frac{\phi - \phi_c}{\phi_c}$

This formulation has been tested in (Garcia & Parker, 1991), providing the best results together with (van Rijn, 1984).

Note that, as the reference concentration is a function of the friction velocity, this strategy for the suspended transport boundary condition provides a connection between the suspended and bedload transport mechanisms.

Seabed displacement

In order to calculate the displacement of the seabed produced by the previous transport mechanisms, a sediment balance is performed for each cell in the fluid-solid interface. This balance computes the variation in the position of the interface (Δh), considering the bedload and suspended transport contributions, (Δh_b and Δh_s respectively). The equations for the sediment balance are

$$\Delta h_b = -\frac{1}{1 - e_d} \frac{\nabla \cdot (\vec{Q_b})}{\vec{e_g}\vec{N}} \Delta t \tag{4.46}$$

$$\Delta h_s = -\frac{1}{1 - e_d} \frac{\left|\vec{E} - \vec{D}\right|}{\vec{e_g}\vec{N}} \Delta t \tag{4.47}$$

$$\Delta h = \Delta h_b + \Delta h_s \tag{4.48}$$

where $\vec{e_g}$ is the unitary vector in vertical direction, e_d is the sediment porosity and $\vec{N}$ is the face normal vector, whose norm is equal to the face area.

Once the seabed movement is determined, the openness function values (θ and θ_n) for the cells must be updated in order to affect the hydrodynamics and achieve the bidirectional interaction with the sediment transport. The new values for θ and θ_n are determined purely by geometrical relations and then used in the next time step for the fluid motion calculation.

4.3 Numerical solution

Once the governing equations for the hydrodynamic and sediment transport models have been addressed, the numerical methods used to solve them are discussed. The resulting numerical model is a combination of different strategies used to compute approximate solutions for each of the previous equations.

4.3.1 Hydrodynamic model

Aiming to solve the coupled velocity and pressure fields, IH2VOF uses the Two-Step Projection method. The FDM is used to obtain the expression of the required spatial derivatives for velocity and pressure fields in each cell. The system of equations which arises from the application of the Poisson Pressure Equation has a pentadiagonal coefficient matrix, in contrast with the system resulting from an unstructured mesh, which allows a more efficient solution of the pressure field. This system of equations is solved by using the Conjugate Gradient method preconditioned with an incomplete Cholesky factorization.

The Two-Step Projection method

The Two-Step Projection method is a segregated algorithm to solve the pressure and velocity fields.

Starting with the RANS equations including the Boussinesq hypothesis (Equations 4.3 and 4.28), the pressure term is removed to obtain an equation for an intermediate velocity field ($\vec{\tilde{U}}$), which carries the right vorticity but does not satisfy the momentum balance.

$$\frac{\partial(\vec{\tilde{U}})}{\partial t} = -\nabla \cdot (\vec{U} \otimes \vec{U}) + (\nu + \nu_t)\nabla^2 \vec{U} + \vec{S_M} \tag{4.49}$$

where $\vec{\tilde{U}}$ is the intermediate velocity field.

Considering a discretization of time-step size Δt, the following relation between intermediate velocities in the current (n) and next $(n+1)$ time-steps can be derived

$$\frac{\vec{\tilde{U}}^{n+1} - \vec{\tilde{U}}^{n}}{\Delta t} = -\nabla \cdot (\vec{U}^n \otimes \vec{U}^n) + (\nu + \nu_t)\nabla^2 \vec{U}^n) + \vec{S_M} \tag{4.50}$$

in which superscripts n and $n+1$ denote values in the current and next time steps, respectively.

The difference between the intermediate velocity field and the actual velocity, intended to be obtained, is the pressure term. Thus, at the time-step $n+1$

$$\frac{\vec{U}^{n+1} - \vec{\tilde{U}}^{n+1}}{\Delta t} = -\frac{\vec{\nabla} p}{\rho}^{n+1} \tag{4.51}$$

This expression directly relates the velocity and pressure fields. However, the velocity fields that satisfy this equation do not necessary fulfil the mass conservation condition (Equation 4.3).

Thus, to find the solution that satisfies both Equations 4.51 and 4.3, the solution for Equation 4.51 must be located into the subspace of velocity fields matching Equation 4.3.

To find this solution, Equation 4.51 is projected onto a hyperplane in which the velocity fields satisfy the mass conservation condition (Equation 4.3). This divergence-free hyperplane matches $\nabla \cdot (\star) = 0$. Restricting Equation 4.51 to this domain, the Poisson Pressure Equation (PPE) is obtained

$$\nabla \cdot \left(\frac{\vec{\nabla} p^{n+1}}{\rho^n} \right) = \frac{1}{\Delta t} \nabla \cdot \left(\vec{\tilde{U}}^{n+1} \right) \tag{4.52}$$

in which $\nabla \cdot (\vec{U}^{n+1}) = 0$ has been applied according to Equation 4.3.

Notice that both the pressure and intermediate velocity fields in this equation are the ones corresponding to time-step $n+1$. By solving Equation 4.52, the correct pressure field can be calculated.

The Two-Step Projection method comprises the following stages. Firstly, Equation 4.50 is applied to obtain $\vec{\tilde{U}}^{n+1}$. Secondly, the PPE (Equation 4.52) is solved to compute the new pressure field p^{n+1}. At this point, the boundary conditions for the pressure field are applied. Then, the new velocity field $\vec{U}^{n+1}$ is calculated with Equation 4.51. Once these two fields are updated, the remaining equations depending on them (such as those of the turbulence model or the VoF advection) can be solved explicitly to obtain the terms in Equation 4.50 for the calculation of the next time-step.

To find a solution for this set of differential equations, they are converted to algebraic expressions by discretizing the pressure velocity fields. For this purpose, the spatial derivatives are approximated with the FDM.

Once discretized, Equations 4.50 and 4.51 can be solved explicitly. In contrast, the PPE is solved implicitly to determine the pressure field. Once discretized, its RHS can be obtained directly from the results of the previous time-step as a vector. The LHS can be expressed as the product of a coefficient matrix times the unknown pressure vector. Thus, the discretized (4.52) can be expressed as a system of equations in matrix form

$$Ax = b \tag{4.53}$$

where A contains the FDM coefficients for the LHS discretization, x is the vector containing the pressure at each cell and b is the RHS of Equation 4.52.

However, at this point, the considerations made to account for the difference between the computational cells and the actual control volumes in which the equations are solved must be applied. In cut-cells, the pressure term must be calculated for the mass in the control volume, thus applying the equivalent density (ρ_{eq}). In the same way, the terms in $\vec{\tilde{U}}^{n+1}$ also have to be calculated using the equivalent density (i.e., adjusting the dynamic viscosity). Furthermore, when computing the divergences, the surface of the control volume should be considered instead of the surface of the cell by using the equivalent area (A_{eq}).

The coefficients for the discretization of the pressure term on the LHS of Equation 4.52, considering the mismatch between cell and control volume in cut-cells, are

$$\nabla \cdot \Big(\frac{\vec{\nabla} p^{\,n+1}}{\rho^n}\Big) \approx \frac{\Big[\theta_f\big(\frac{1}{\rho_{eq}}\big)\vec{\nabla} p^{\,n+1}\Big]_{CR} - \Big[\theta_f\big(\frac{1}{\rho_{eq}}\big)\vec{\nabla} p^{\,n+1}\Big]_{CL}}{\Delta x_C} + \frac{\Big[\theta_f\big(\frac{1}{\rho_{eq}}\big)\vec{\nabla} p^{\,n+1}\Big]_{CT} - \Big[\theta_f\big(\frac{1}{\rho_{eq}}\big)\vec{\nabla} p^{\,n+1}\Big]_{CB}}{\Delta y_C} \tag{4.54}$$

in which subscripts CR, CL, CT and CB represent values on the right, left, top and bottom faces of the cell, respectively. Subscript C denotes values at the cell centre. Including the discretization of the gradient at cell faces

$$\nabla \cdot \Big(\frac{\vec{\nabla} p^{\,n+1}}{\rho^n}\Big) \approx \frac{\Big(\frac{\theta_f}{\rho_{eq}}\Big)_{CR}\Big[\frac{2(P_R - P_C)}{\Delta x_C + \Delta x_R}\Big] - \Big(\frac{\theta_f}{\rho_{eq}}\Big)_{CL}\Big[\frac{2(P_C - P_L)}{\Delta x_C + \Delta x_L}\Big]}{\Delta x_C} + \frac{\Big(\frac{\theta_f}{\rho_{eq}}\Big)_{CT}\Big[\frac{2(P_T - P_C)}{\Delta y_C + \Delta y_T}\Big] - \Big(\frac{\theta_f}{\rho_{eq}}\Big)_{CB}\Big[\frac{2(P_C - P_B)}{\Delta x_C + \Delta y_B}\Big]}{\Delta y_C} \tag{4.55}$$

where subscripts R, L, T and B represent the values at the right, left, top and bottom cell centres, respectively.

From Equation 4.55, the terms of the coefficient matrix for the system of equations can be obtained. These are obtained by isolating the pressure terms from the surrounding cells. For this purpose, it is convenient to group the terms as follows

$$\alpha_R = 2\Big(\frac{\theta_f}{\rho_{eq}}\Big)_{CR}\frac{\Delta x}{\Delta x_C + \Delta x_R} \tag{4.56}$$

$$\alpha_L = 2\Big(\frac{\theta_f}{\rho_{eq}}\Big)_{CL}\frac{\Delta x}{\Delta x_C + \Delta x_L} \tag{4.57}$$

$$\gamma_T = 2\Big(\frac{\theta_f}{\rho_{eq}}\Big)_{CT}\frac{\Delta y}{\Delta y_C + \Delta y_T} \tag{4.58}$$

$$\gamma_B = 2\Big(\frac{\theta_f}{\rho_{eq}}\Big)_{CB}\frac{\Delta y}{\Delta y_C + \Delta y_B} \tag{4.59}$$

With these definitions, Equation 4.55 can be rewritten as

$$\nabla \cdot \Big(\frac{\vec{\nabla} p^{\,n+1}}{\rho^n}\Big) \approx aP_R + bP_L + cP_T + dP_B - (a+b+c+d)P_C \tag{4.60}$$

As can be noted, only the adjacent cells (right, left, top and bottom) are involved in the coefficients for the LHS discretization due to the selected discretization schemes. This relation can be represented by a cell stencil consisting of 5 adjacent cells. This 5-cell stencil is depicted in Figure 4.1.

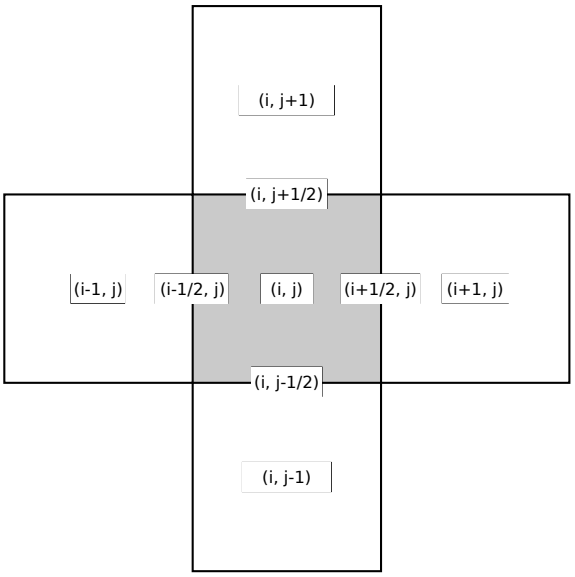

Figure 4.1: 5-cell stencil used to discretize the numerical domain. The indexes of each cell relative to the central cell of the stencil (coloured in grey) are represented.

As can be observed in Figure 4.1, the index of the adjacent cells can be directly obtained from those of the central cell using constant offsets. Thus, Equation 4.60 can be expressed as

$$\nabla\cdot\Big(\frac{\vec{\nabla}p^{\,n+1}}{\rho^n}\Big) \approx \alpha_R P_{(i+1,j)}+\alpha_L P_{(i-1,j)}+\gamma_T P_{(i,j+1)}+\gamma_B P_{(i,j-1)}-(\alpha_R+\alpha_L+\gamma_T+\gamma_B)P_{(i,j)} \tag{4.61}$$

This implies that the 5 elements in each row of the coefficients matrix (A) are always at the same distance from the diagonal element. Therefore, A is a sparse pentadiagonal matrix. Notice that this feature arises from the use of a Cartesian grid along with the two-dimensionality of the equations being solved and the compact stencil resulting from the selected discretization schemes.

Regarding the LHS of Equation 4.52, the divergence of the intermediate velocity field can be obtained as

$$\frac{1}{\Delta t}\nabla\cdot\big(\vec{\tilde{U}}^{n+1}\big) \approx \frac{1}{\Delta t}\Big[\frac{(\tilde{U_R}\theta_R)-(\tilde{U_L}\theta_L)}{\Delta x_C}+\frac{(\tilde{U_T}\theta_T)-(\tilde{U_B}\theta_B)}{\Delta y_C}\Big] \tag{4.62}$$

where $\tilde{U_R}$, $\tilde{U_L}$, $\tilde{U_T}$ and $\tilde{U_B}$ are the intermediate velocities at the right, left, top and bottom faces of the cell, respectively.

To solve the system of equations 4.53, the Preconditioned Conjugate Gradient iterative algorithm is used. The preconditioner is an Incomplete Cholesky Factorization.

Transport equations

Once the pressure and velocity fields are calculated, the transport equations (Equations 4.33 for the VoF function and 4.29 and 4.30 for the turbulence model) are solved explicitly using the FDM. Note that the same considerations in the discretization

of terms for cut-cells introduced in the Two-Step Projection method are applied in the solution of Equations 4.29, 4.30 and 4.33.

For further information about the solving method, the reader is referred to (Lin & Liu, 1998).

4.3.2 Sediment transport model

Bedload transport

To determine the bedload transport, the friction velocity ($\vec{U_f}$) must be obtained from the hydrodynamic model. It is estimated considering a turbulent boundary layer with a logarithmic velocity profile:

$$\vec{U} = \vec{U_f}\frac{1}{\kappa}Ln\Big(\frac{y}{y_0}\Big) \tag{4.63}$$

where $\vec{U}$ is the velocity at a distance y of the solid boundary, κ is the von Karman constant with a value of 0.41 and y_0 represents the shift of the velocity profile due to the boundary roughness. y_0 depends on the flow regime in the boundary layer, which can be divided in smooth, transition and rough regimes. For each regime, y_0 is obtained with a different expression (Equations 4.64, 4.65 and 4.66 for the smooth, transition and rough respectively).

$$y_0 = \begin{cases} \dfrac{0.11\nu}{|\vec{U_f}|}, & \text{if } \frac{k_s|\vec{U}_f|}{\nu} < 5 \quad (4.64) \\ \dfrac{0.11\nu}{|\vec{U_f}|} + \dfrac{k_s}{30}, & \text{if } 5 < \frac{k_s|\vec{U}_f|}{\nu} < 70 \quad (4.65) \\ \dfrac{k_s}{30}, & \text{if } \frac{k_s|\vec{U}_f|}{\nu} > 70 \quad (4.66) \end{cases}$$

where k_s is the Nikuradse roughness of the sediment, considered as 2.5 times the sediment diameter.

To avoid discretization problems inherent to the use of orthogonal grids with non-aligned boundaries, a method based on (Capizzano, 2011) to obtain the velocity vector close to the seabed is implemented. A similar approach was used in (Lin *et al.* , 2016) to interpolate velocities close to boundaries and, later, in (Han & Lin, 2018). The points at which the velocity is obtained are located at a distance of $1.5\Delta y$, where Δy is the vertical discretization of the mesh, in the direction normal to the seabed, passing through the cell centroid (as shown in Figure 4.2). The velocity components at these points are obtained for each seabed segment (u_i, v_i) by a bilinear interpolation weighted with the VoF function.

Once the velocity components are obtained, the velocity vector at the interpolation point is calculated. Then, it is projected on the direction parallel to the seabed. The resulting velocity vector is inserted into Equation 4.63 along with the distance $y = 1.5\Delta y$ to obtain the friction velocity ($\vec{U_f}$). Once the friction velocity is known, the value of the Shields parameter induced by skin friction can be calculated using Equation 4.40.

Notice that for smooth and transition regimes (Equations 4.64 and 4.65) the friction velocity appears also in the expression for y_0, and Equation 4.63 cannot be

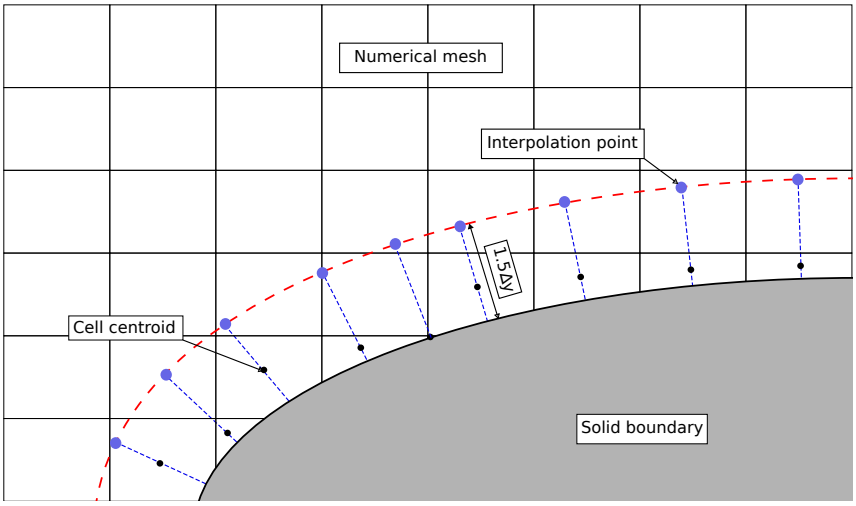

Figure 4.2: Values for different magnitudes are calculated at interpolation points (blue dots). These are positioned at a distance $1.5\Delta y$ from the solid boundary (red line) and in a line normal to the wall surface (blue dashed lines) which passes through the cell centroid of the cell intersected by the wall surface (black dots).

solved directly. Instead, a Newton-Raphson algorithm is implemented to achieve an approximated solution.

To determine the basic value of critical Shields parameter (ϕ_0), the analytical expressions for the Shields abacus curves are used. These expressions depend on the dimensionless particle diameter (d^*)

$$d^* = d\left[\frac{9.81(s-1.0)}{\nu^2}\right]^{\frac{1}{3}} \tag{4.67}$$

The analytical expressions for Shields curves are

$$\phi_0 = \begin{cases} 0.24{d^*}^{-1} & if \quad d^* < 4 \\ 0.14{d^*}^{-0.64} & if \quad 4 < d^* < 10 \\ 0.04{d^*}^{-0.1} & if \quad 10 < d^* < 20 \\ 0.013{d^*}^{0.29} & if \quad 20 < d^* < 150 \\ 0.055 & if \quad d^* > 150 \end{cases} \tag{4.68}$$

Then, the slope effect is added to its basic value according to Equation 4.38. The basic value of the critical Shields parameter is obtained only once, at the beginning of the simulation, while the slope effect is recalculated each iteration to account for the variability of the seabed shape.

Knowing the difference between the Shields number and its critical value, P_{ef} can be calculated directly by Equation 4.37. The sediment transport at the centre of each seabed segment is obtained with the previously calculated P_{ef} and $\vec{U_f}$ with Equation 4.36. Finally, the divergence of bedload transport in each segment of the interface ($\nabla \cdot (\vec{q_{b_i}})$) is obtained as

$$\nabla \cdot (\vec{q_{b_i}}) = |\vec{q}_{b_{i-\frac{1}{2}}}| - |\vec{q}_{b_{i+\frac{1}{2}}}| \tag{4.69}$$

where the bedload transport at the segment sides is obtained from the centre value by linear interpolation.

Suspended transport

The Finite Volume Method (FVM) is used to solve the advective-diffusive transport equation (Equation 4.41) in the spatial domain. The application of this method leads to an Ordinary Differential Equation (ODE) in the time domain for the concentration inside each cell.

Firstly, Equation 4.41 is integrated over the cell volume resulting in

$$\oint_V \frac{\partial C}{\partial t} dV = \oint_V \nabla \cdot [(\vec{U} + \vec{w_s})C] dV + \oint_V \nabla \cdot \Big[\Big(\frac{\nu + \nu_t}{\sigma_c} \Big) \vec{\nabla} C \Big] dV \tag{4.70}$$

Then, the Gauss divergence theorem is invoked to convert the integrals over the cell volume on the RHS to integrals over the bounding surface of the cell

$$\oint_V \frac{\partial C}{\partial t} dV = \oint_S C(\vec{U} + \vec{w_s}) dS + \oint_S \Big(\frac{\nu + \nu_t}{\sigma_c} \Big) \vec{\nabla} C dS \tag{4.71}$$

The sediment concentration is assumed to be uniform inside the cells, therefore

$$\oint_V \frac{\partial C}{\partial t} dV = \frac{\partial C}{\partial t} V_{cell} \tag{4.72}$$

The same Cartesian mesh used to solve the hydrodynamics is adopted for the suspended transport in order to avoid mapping the velocity field to a different mesh. Therefore, the integrals over the bounding surface of each cell can be converted to

$$\oint_S C(\vec{U} + \vec{w_s}) dS = \sum_f C_f (\vec{U} + \vec{w_s})_f A_f \tag{4.73}$$

$$\oint_S \Big(\frac{\nu + \nu_t}{\sigma_c} \Big) \vec{\nabla} C = \sum_f \Big(\frac{\nu + \nu_t}{\sigma_c} \Big)_f \vec{\nabla} C_f A_f \tag{4.74}$$

where subscript f denotes the cell face. The first integral represents the sediment volumetric flux due to advective transport and the second one due to the diffusive transport. The cell face area A_f must consider the openness of the corresponding cell face (θ_f). The cell face area can be obtained as

$$A_{i,j,f} = \begin{cases} \Delta x_i \theta_{f_{i,j}} & \text{(Horizontal face)} \\ \Delta y_j \theta_{f_{i,j}} & \text{(Vertical face)} \end{cases} \tag{4.75}$$

Finally, the discretized advective-diffusive transport equation for the control volume is

$$\Big(\frac{\partial C}{\partial t} \Big)_{i,j} \simeq \Big[\frac{\sum_f C_f (\vec{U} + \vec{w_s})_f A_f + \sum_f (\nu + \nu_{t,f}) \vec{\nabla} C_f A_f}{V_{cell}} \Big]_{i,j} \tag{4.76}$$

The cell volume V_{cell} is computed considering the volumetric openness of the cell as

$$V_{cell\,i,j} = \Delta x_i \Delta y_j \theta_{i,j} \tag{4.77}$$

To compute the time-derivative of sediment concentration in each cell with Equation 4.76, the cell face values of $\vec{U}$, $\vec{w_s}$, C, ν_t and $\vec{\nabla} C$ are needed. However, as the hydrodynamic model uses a staggered grid, some of the involved variables must be interpolated to the cell faces in order to determine the sediment fluxes across the cell faces.

In Figure 4.3, the position at which the involved variables are obtained and the sediment fluxes of Equation 4.41 are represented.

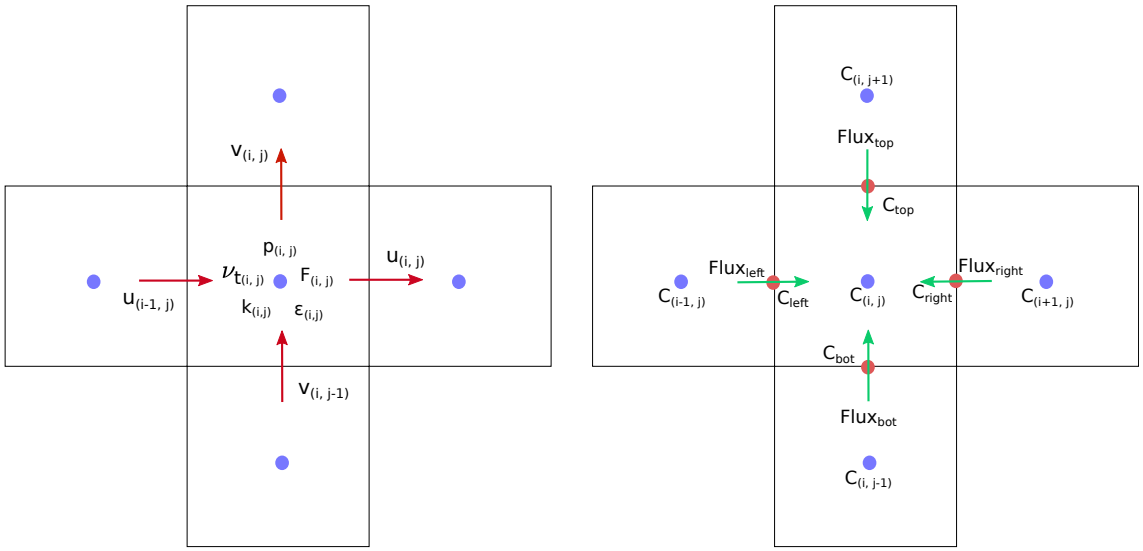

Figure 4.3: Numerical stencil for hydrodynamic (left) and sediment (right) variables used in the model. Variables are calculated in the staggered grid for cell centres (blue dots) and faces (red dots). In the left panel, hydrodynamic variables (velocity, pressure, k, ϵ turbulent viscosity and VoF function), the velocity is represented with red arrows. In the right panel, the sediment module variables (sediment concentration in cell centre and interpolated to cell faces and sediment fluxes). The sediment fluxes are represented with green arrows, note the sign criteria for sediment fluxes (positive if entering the cell).

The interpolation schemes used for each variable are described next.

Interpolation of hydrodynamic magnitudes Regarding the hydrodynamic variables, the fluid velocity components provided by the hydrodynamic model ($u_{i,j}$ and $v_{i,j}$) are already calculated on the faces, therefore no interpolation is needed for them. However, the turbulent viscosity is calculated at the cell centres, and it is interpolated to the cell faces using a central differencing scheme.

Interpolation of sediment fall velocity For the sediment fall velocity, two possible values are considered for the air (represented as void space in the hydrodynamic model) and water phases.

To determine if the cell is full of water, air or on the free surface, the value of the VOF function (F) is used as indicator

$$w_{s,i,j+\frac{1}{2}} = w_{s,i,j-\frac{1}{2}} = \begin{cases} w_{s,water} & if \quad F_{i,j} = 1 \\ w_{s,air} & if \quad F_{i,j} = 0 \end{cases} \tag{4.78}$$

On the free surface, a sharp interface between these two values is prescribed to improve the behaviour of the model when wave breaking occurs and in the swash zone. The face values are obtained with

$$w_{s,i,j+\frac{1}{2}} = \begin{cases} w_{s,water} & if \quad F_{i,j} = 0 \text{ and } F_{i,j+1} > 0 \\ w_{s,air} & if \quad F_{i,j} > 0 \text{ and } F_{i,j+1} = 0 \end{cases} \tag{4.79}$$

$$w_{s,i,j-\frac{1}{2}} = \begin{cases} w_{s,air} & if \quad F_{i,j} > 0 \text{ and } F_{i,j+1} = 0 \\ w_{s,water} & if \quad F_{i,j} = 0 \text{ and } F_{i,j+1} > 0 \end{cases} \tag{4.80}$$

Note that the sediment fall velocity is only needed for the advective fluxes across the top and bottom faces, since they do not produce sediment flux normal to the right and left faces. Thus, the interpolation is only performed for the top and bottom faces,

An example on how the sediment fall velocities are assigned to the cell faces depending on the position of the free surface is provided in Figure 4.4.

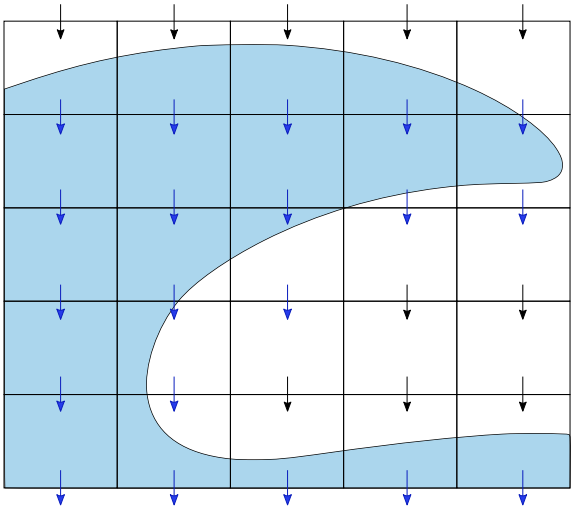

Figure 4.4: Schematic representation of the sediment fall velocity interpolation. The water sediment fall velocity is represented by blue arrows, while that corresponding to the air is represented by black arrows. The blue area represents the real free-surface position.

Interpolation of sediment concentration The sediment concentration has to be interpolated from cell centre to cell face. To ensure the boundedness of the concentration field, an upwind scheme is adopted for this interpolation, in which the concentration value used to compute the sediment transport is the value at the upstream cell. The upstream cell is determined depending on the velocity components, being the concentration on the cell face calculated as

$$C_{i,j+\frac{1}{2}} = \begin{cases} C_{i,j} & if \quad v_{i,j+\frac{1}{2}} > 0 \\ C_{i,j+1} & if \quad v_{i,j+\frac{1}{2}} < 0 \end{cases} \tag{4.81}$$

$$C_{i,j-\frac{1}{2}} = \begin{cases} C_{i,j-1} & if \quad u_{i,j-\frac{1}{2}} > 0 \\ C_{i,j} & if \quad v_{i,j-\frac{1}{2}} < 0 \end{cases} \tag{4.82}$$

$$C_{i+\frac{1}{2},j} = \begin{cases} C_{i,j} & if \quad u_{i+\frac{1}{2},j} > 0 \\ C_{i+1,j} & if \quad u_{i+\frac{1}{2},j} < 0 \end{cases} \tag{4.83}$$

$$C_{i-\frac{1}{2},j} = \begin{cases} C_{i-1,j} & if \quad u_{i-\frac{1}{2},j} > 0 \\ C_{i,j} & if \quad u_{i-\frac{1}{2},j} < 0 \end{cases} \tag{4.84}$$

An example of the application of this interpolation scheme is displayed in Figure 4.5.

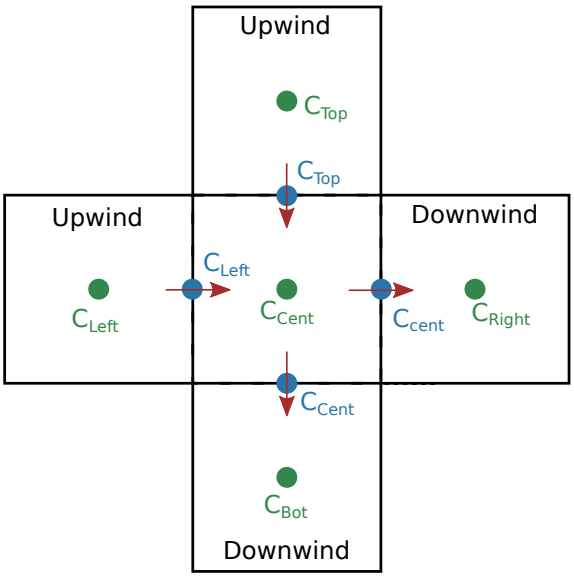

Figure 4.5: Example of cell centre to cell face interpolation using the upwind scheme. The velocity vectors are represented in red. The sediment concentration at the centres of cells in the stencil are represented in green. The magnitudes interpolated to the cell faces, used to compute the advective sediment fluxes, are represented in blue.

Concentration gradient Spatial derivatives of sediment concentration at cell faces are obtained with a first order central differencing scheme. However, for cells on the fluid-sediment interface, a boundary condition for the sediment fluxes must be applied for the gradient on their bottom faces.

The computation of the concentration gradient can be quite expensive, as it requires a very fine mesh discretization close to the seabed. To avoid this, a model for the sediment concentration distribution close to the seabed is adopted. it is assumed that the concentration in a thin layer close to the solid is constant (reference concentration). Its value is calculated using the aforementioned empirical formulae from (Smith & McLean, 1977). Introducing this consideration, the approximation of the concentration gradient for the fluid-seabed interface is computed with

$$(\vec{\nabla} C)_{b,i} = \frac{C_{interp,i} - C_{b,i}}{1.5\Delta y} \tag{4.85}$$

where $(\vec{\nabla}C)_b$ is the value of the concentration gradient for the boundary condition, C_{interp} is the interpolated value of the concentration field and C_b is the reference concentration obtained with (Smith & McLean, 1977). Subscript i^{th} is the cell column index. To determine the reference concentration ($C_{b,i}$), the Shields number obtained by the bedload transport module for the i^{th} seabed segment is used.

The concentration field presents the same discretization problems close to solid boundaries as the velocity vector in the friction velocity equation, due to the use of the cut-cell method. For this reason, the concentration ($C_{i,j}$) used in Equation 4.85 is interpolated with the same method followed to infer the velocity vector close to the wall (see Figure 4.2). Furthermore, this value of sediment concentration close to the seabed is used to compute the advective flux in the lower boundary of the domain, which corresponds to the deposition rate.

Sediment fluxes on the seabed boundary condition The values of sediment fluxes on the seabed boundary constitute the interchange of sediment between fluid (suspended sediment) and solid (seabed). The deposition rate ($\vec{D}$) corresponds to the advective flux and the erosion rate ($\vec{E}$) to the diffusive flux. Thus, the expressions for the deposition and erosion rates are

$$\vec{D} = C_{interp}(\vec{U} + \vec{w_{s,bot}})A_{bot}\theta_{bot} \tag{4.86}$$

$$\vec{E} = (\nu + \nu_t)(\vec{\nabla}C)_b A_{bot}\theta_{bot} \tag{4.87}$$

where subscript *bot* denotes values on the bottom face of the cells.

In Figure 4.6, the sediment fluxes for a cell intersected by the seabed are represented. As can be noted, the cell can interchange sediment with the adjacent cells and with the seabed, the later leading to variations in the seabed position.

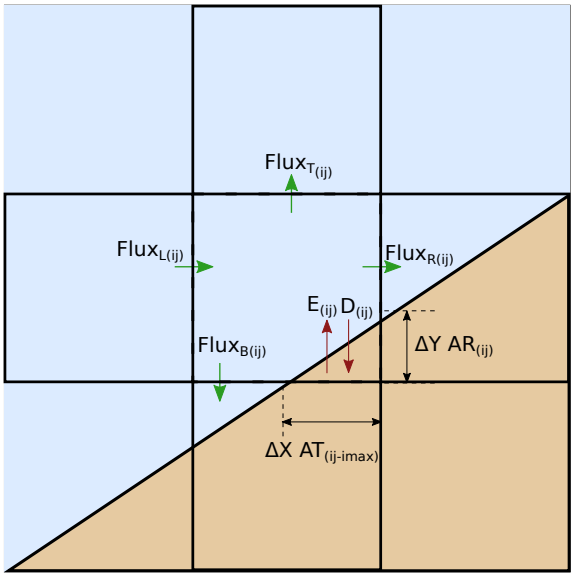

Figure 4.6: Schematic representation of sediment fluxes in a cell intersected by the seabed.

The boundary conditions imposed on the seabed assume that the sediment flux from fluid to solid is fully advective and that the inverse is fully diffusive. This means that sediment particles enter the solid domain by settling due to their own

weight and that they enter the fluid domain due to transport produced by turbulent fluctuations.

In this way, the boundary condition for advective sediment flux depends on the direction of the sediment velocity ($\vec{U} + \vec{w_s}$). If the velocity is negative (sediment flux exits the fluid domain) a zero-gradient condition is prescribed. On the contrary, a fixed value of zero is imposed. This boundary condition models the settlement of sediment due to its own fall velocity and, at the same time, avoids advective sediment flux from solid to fluid domain.

The condition for diffusive transport depends on the direction of the concentration gradient. If the concentration gradient is positive (pointing inwards the fluid domain), a fixed gradient condition calculated with Equation 4.85 is imposed. For a negative concentration gradient, pointing outward the fluid domain, a fixed value of zero is imposed to avoid diffusive flux of sediment towards the solid domain.

Solution of the concentration field Once all the required interpolations are performed, the interpolated variables are inserted in Equation 4.76. This results in an Ordinary Differential Equation which represents the evolution of C in time, and it is solved numerically using the 4^{th} grade Runge-Kutta method for each cell in the domain.

The Runge-Kutta algorithm aims to estimate the time-derivative as the averaged value of a series of intermediate time-derivatives. Particularly, the 4^{th} grade Runge-Kutta algorithm obtains the time-derivative between two times (t_{init} and t_{end}) as the average value of 4 intermediate time-derivatives (K_1 to K_4). Apart from t_{init} and t_{end}, it uses the middle point between them (t_{half}) to compute such derivatives (one at t_{init}, two at t_{half} and one at t_{end}). Each of the intermediate time-derivatives is calculated using Equation 4.76 with an auxiliary concentration field. Note that, according to Equation 4.76, the time-derivative of the concentration only depends on the concentration field itself (the advective and diffusive fluxes are influenced by it and the hydrodynamic magnitudes are considered constant between t_{init} and t_{end}). In Figure 4.7, a graphical representation of the method is provided.

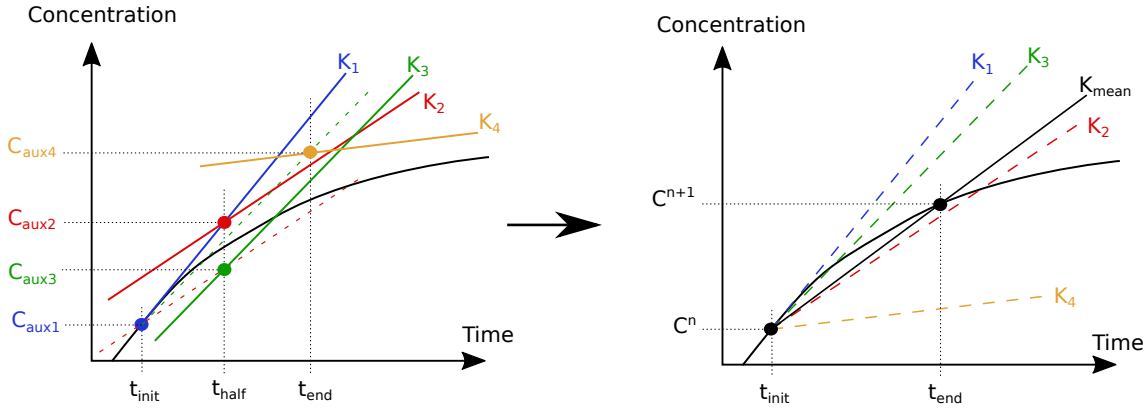

Figure 4.7: Graphical representation of the 4^{th} Grade Runge Kutta method for estimating the time derivative of the sediment concentration. Left panel, intermediate slopes (K_1 to K_4). Right panel, average slope (K_{mean}) considered as the real time-derivative of the concentration inside the cell.

The first derivative (K_1) is obtained considering the concentration field at t_{init} (C_{aux1}), which is the concentration at the current time-step (C^n). Then, the first

intermediate concentration (C_{aux2}) is calculated by projecting C_{aux1} to t_{half} using the slope K_1. The second time-derivative (K_2) is calculated using C_{aux2}. For the third intermediate concentration (C_{aux3}), the initial concentration (C_{aux1}) is projected again to t_{half}, but now using K_2. The third slope (K_3) is computed using C_{aux3}. Finally, the fourth intermediate concentration (C_{aux4}) is calculated by projecting C_{aux1} to t_{end} using K_3. The last intermediate time-derivative (K_4) is calculated using C_{aux4}. These intermediate slopes are averaged to obtain K_{mean}, which is the approximation of the time-derivative of the sediment concentration between t_{init} and t_{end}. By projecting C_n from t_{init} to t_{end} using the time-derivative K_{mean}, the concentration field for the next time-step (C^{n+1}) is obtained.

Thus, the solving algorithm for the suspended transport consists in a main loop in which the time-derivatives of sediment concentration for the Runge-Kutta method are obtained by invoking Equation 4.76. As the concentration field is different for each time-derivative calculation, the involved variables are calculated and interpolated to the cell faces using the previously described schemes prior to solve Equation 4.76. Variables which depend only on the hydrodynamics are interpolated only once per time step outside the main loop since they are independent of the sediment concentration. During the calculations of concentration fields, the advective and diffusive fluxes on the bottom face of the fluid-sediment interface cells are saved and, once the loop finishes, the erosion and deposition rates are obtained from them as the averaged value of them (similarly to the computation of the time-derivative of the sediment concentration). For each of the 4 steps in the RK4 method, the time derivatives of the sediment concentration in each cell, obtained according to Equation 4.76, are stored in an array of 4 times the mesh size. Additionally, another array of the mesh size is required to store the auxiliary sediment concentration, which is calculated by projecting the initial sediment concentration to the corresponding intermediate time-step using the intermediate sediment fluxes. The sediment interchanges between fluid and seabed are stored and computed following a similar approach.

Seabed displacement

The previously described equations for the sediment balance (Equations 4.46, 4.47 and 4.48) must be adapted taking into account the type of mesh that is used by IH2VOF. As it is an orthogonal grid based-on model, the product $\vec{e_g}\vec{N} = \Delta x_i$. Therefore, the sediment balance (Equation 4.48) can be simplified to

$$\Delta h_i = \Delta h_{bi} + \Delta h_{si} = -\frac{1}{1-e_d}\frac{\nabla \cdot (\vec{q_{bi}}) + E_i - D_i}{\Delta x_i}\Delta t \tag{4.88}$$

The seabed displacement is computed at the centre of each seabed segment, while the position of the interface (Y_{inter}) is defined at the sides of seabed segments. Consistently, a simple linear interpolation is used to translate segment-centre to segment-side values.

$$\Delta Y_{inter\,i+\frac{1}{2}} = \frac{\Delta h_i + \Delta h_{i+1}}{2} \tag{4.89}$$

A schematic description of the variables involved in the sediment balance performed for each cell intersected by the seabed, and the interpolation of the seabed displacement to the cell faces is displayed in Figure 4.8.

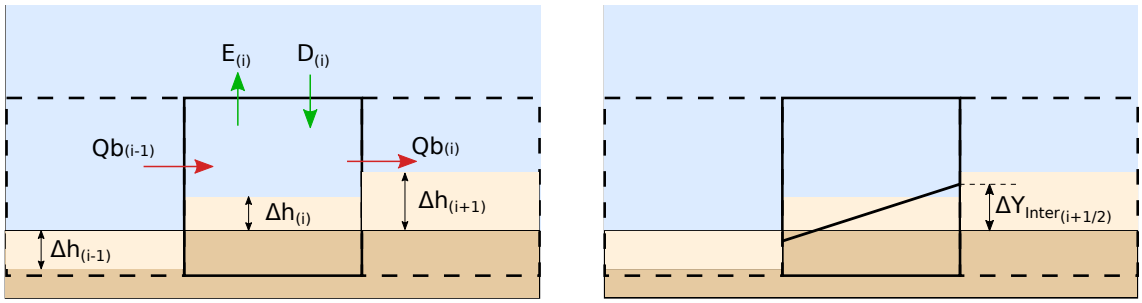

Figure 4.8: Sediment balance (left) and interpolation of the seabed displacement from cell centres to cell faces (right). The initial seabed for the three cells is flat.

To determine the variation of the openness of a cell due to the new interface position, different geometrical relations can be deduced depending on the relative position of the interface and the cell faces. For this reason, a catalogue with all the possible configurations of the interface inside the cell is created. The geometrical relations to obtain the new openness of cell faces (θ_f) and volume (θ) are derived for each of them assuming a linear fluid-solid interface inside the cell. The configurations taken into account are represented in Figure 4.9. Therefore, each cell is classified depending on the values of the cut-cell parameters using the catalogue and, then, the corresponding geometrical relations are applied to determine the openness of cell faces and volume. The cell type is stored in a separate array, and it is updated at the end of the algorithm if the new configuration of the seabed inside the cells results in a different cell type.

The new cut-cell parameters are used in the next time step by the hydrodynamic model when solving the pressure and velocity fields according th the methods described in Section 4.2.1.

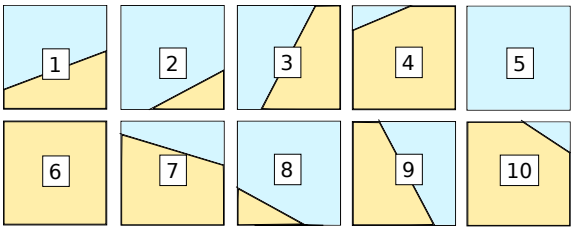

Figure 4.9: Catalogue of considered cell types for the calculation of cell openness. An expression for $\theta_{i,j}$ and $\theta_{f_{ij}}$ is obtained for each type.

A minimum value for the volumetric cell openness (AC) is prescribed to avoid instabilities of the numerical solution for the velocity and concentration fields. When the cell openness falls below this minimum the cell is closed by setting AR, AC and AT to zero without increasing the seabed level. After this,the sediment concentration inside the cell is eliminated and the seabed level is elevated accordingly. In this way, numerical instabilities are avoided while maintaining the sediment mass conservation.

4.4 Parallelization

4.4.1 Purpose

A great portion of the total computational cost of the model is associated to the resolution of the system of equations that provides the pressure values in the Two-Step Projection method. For this reason, the resolution of the system of equations has been parallelized to solve it in multiple CPU cores.

4.4.2 Parallelization strategy

The overall idea for the parallelization consist in solving the system of equations arising from the Two-Step Projection method with multiple cores, while using a single core for the rest of the calculations. Although it would be optimal to parallelize all the calculations, so that all cores are kept working, for this first version only the most expensive part is addressed. Many of the remaining calculations can be easily parallelized in future versions, as they perform the calculations for each cell independently.

The solution of the system of equations consists of two main steps: preconditioning and solving. Additionally, the matrix of the system has to be assembled in parallel so that each core has access to the required cell values. Once the solution for the systems is found, it is gathered in the main processor so it can access the solutions for all the cells in the domain. Then, the remaining calculations can be performed only using the main core. A schematic description of this parallelization strategy is shown in Figure 4.10.

4.4.3 Implementation details

For the implementation of the parallelized solver, the PETSc library ((Balay *et al.* , 2015b), (Balay *et al.* , 2015a), (Balay *et al.* , 1997)) has been selected, as it includes highly optimized algorithms for solving systems of equations. Additionally, the MPI protocol is used to transfer data between processors.

Memory Preallocation

A fundamental aspect to achieve a high efficiency is to avoid performing memory allocations each time the coefficient matrix and vectors are updated. As these have constant sizes (no new cells are created or destroyed along the simulation), this can be done by preallocating the required memory at the beginning of the simulation and then reusing it in every time-step.

For the preallocation, matrix classes from the PETSc library are used, as they are convenient to update the matrix coefficients efficiently and to correctly distribute the memory among the processors. The Compressed Row Format (CSR) is adapted for efficiently storing the entries of the sparse matrix.

By using the versions of vectors and matrices from the PETSc library, their partition among processors is handled automatically.

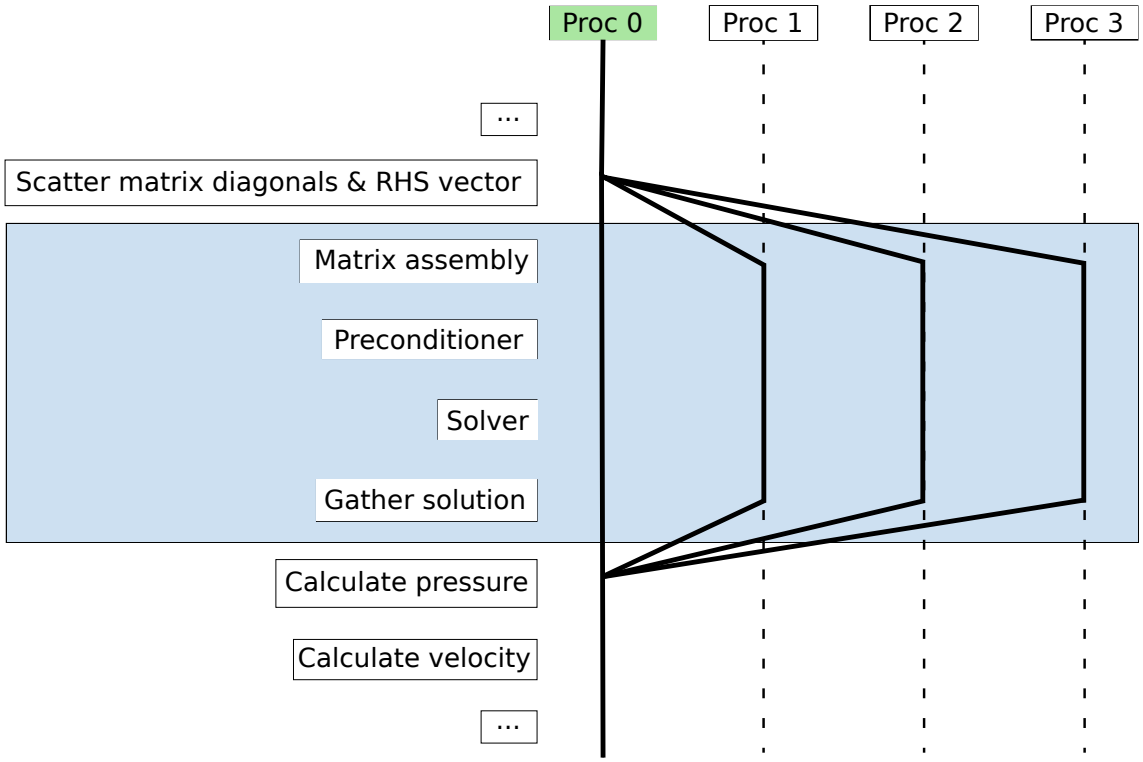

Figure 4.10: Overall view of the parallel version of the code. The functions are listed on the left side. On the right side, the program flow for a simulation running in 4 cores is represented. The functions inside the blue area are performed in parallel, while the rest are run only in the main core (marked in green).

Communication between processors

As the VoF, representing the percentage of water volume inside each cell, changes along the simulation, the density of the fluid and the percentage of the cell occupied by solids appearing in the coefficients matrix of the system must be updated. As the coefficient matrix is pentadiagonal, the new information can be arranged in the form of 5 vectors representing the entries of each diagonal. These 5 vectors are scattered among the processors so that each of them has access to the elements corresponding to the matrix entries that they need.

By organizing the communication between processors in this way, the matrix update can be performed in parallel, as each processor modifies the matrix entries it is responsible for.

After solving the system of equations, each processor has access to a certain partition of the solution vector. All these parts are gathered in the main processor so that it can access the whole solution to keep performing the calculations.

Solving the system of equations

Once the coefficients matrix and RHS vector are updated with the new entries, the system of equations is solved using the functions included in PETSc. The solution process includes a preconditioning stage and the solving algorithm itself. The same preconditioner and solving algorithm as in the serial version of the numerical model are maintained (Incomplete Cholesky Factorization and Preconditioned Conjugate

Gradient, respectively).

4.4.4 Performance

A speed-up factor of approximately 1.75 has been achieved for the simulations, including hydrodynamics and sediment transport, when using an extra CPU core compared with the single-core version.

4.5 Conclusions

A new numerical model capable of solving the cross-shore beach profile evolution, IH2VOF-SED, is developed. The model offers a unique compromise between precision and computational cost. Furthermore, it does not include any calibration parameter or modifications of the empirical formulae used in it.

The parallelization of the hydrodynamic solver represents a noticeable decrease in the computation time. This parallelization can be further extended to other calculations in the hydrodynamic and sediment transport models to improve the scalability and allow for even faster simulations.

Thus, Specific Objective 1 has been accomplished.

Chapter 5

Numerical model validation

Contents

5.1 Introduction

In this chapter, Specific Objective 2 is pursued. The validation strategy starts with assessing the ability of the hydrodynamic model to predict the bed shear stress induced by breaking waves, which is a fundamental magnitude controlling the bedload transport and the amount of sediment put in suspension. Once the shear stress is validated, the skill in predicting the morphological evolution of a beach profile is addressed. Finally, to ensure that the results from the model are suitable for the analysis of morphodynamic processes, relevant hydrodynamic and sediment-related magnitudes, such as currents and suspended sediment concentration profiles, are examined.

Following this strategy, the newly developed model is validated against three laboratory experiments selected from the literature. The first experiment, from (Sumer *et al.* , 2013), consists in determining the shear stresses induced by a solitary wave breaking on a slope, responsible for the bedload transport and the dragging of sediment into suspension. The other two experiments, from (Baldock *et al.* , 2011) and (van der Zanden *et al.* , 2017a), consist in the evolution of a beach profile under regular wave action. While the experimental data from (Baldock *et al.* , 2011) is mainly used to assess the skill of the model in reproducing morphological evolution, the more comprehensive data from (van der Zanden *et al.* , 2017a) are used to compare other relevant magnitudes in addition to the morphological evolution. In all three experiments, several complex processes encountered in the surf zone, such as wave breaking, reflection or the undertow, need to be modelled accurately. They are considered to be representative of the kind of problems for which the model will be applied. In addition, previous efforts to simulate the evolution of a complete beach profile using CFD models resulted in highly expensive computations and numerical instabilities in certain parts of the domain. The benchmark cases for beach profile evolution have been selected in order to have different scales (see Table 5.1).

While the overall objective of this validation is to assess the ability of the model to reproduce the significant hydro-and morphodynamic processes occurring in the surf zone, as well as their interactions, these validations also provide an estimate of the computation costs and robustness of the model.

5.2 Validation of shear stresses on the seabed

The particular aim of the first validation case is to assess the ability of the model to reproduce the friction velocity ($\vec{u_f}$) generated by waves on a beach profile, which is a key variable in sediment transport modelling. With this objective, the experiment presented in (Sumer *et al.* , 2011), performed on a fixed bed, is simulated numerically.

The experiment consisted in a series of 7.1 cm high solitary waves breaking on a 1:14 slope covered with PVC plates to avoid erosion and water entrainment. The PVC plates were instrumented with hot film probes to measure the bottom shear stress. Free surface elevation was recorded using conventional resistive wave gauges. They were synchronized with the shear stress probes. Data from 7 sections are provided in (Sumer *et al.* , 2013) (see locations in Figure 5.1). The first section is located at the toe of the beach and only wave height was measured at that position. Sections 1, 2 and 3 were located inside the shoaling zone, Section 5 at the still water level, separating the swash and surf zones, and Sections 6 and 8 in

the swash zone (dry beach). The breaking point was located between sections 3 and 5. Several repetitions of the experiment were performed, allowing to obtain a statistical description of the solitary wave induced bottom shear stresses. In (Sumer *et al.* , 2013), the solitary wave breaking on the slope is divided in four stages: shoaling and breaking, run-up, run-down, and hydraulic jump and trailing wave. The same experiment is numerically reproduced in (Li *et al.* , 2019) and (Larsen & Fuhrman, 2019), the results from these works are also included in this validation for comparison with the present model.

For the numerical simulation, a solitary wave is generated 1.24 m from the toe of a 1:14 rigid slope, with a wave height equal to the one generated in the experiments and using Boussinesq theory. The mesh has a uniform discretization of $\Delta X = 0.0071\ m$ and $\Delta Z = 0.0035\ m$, corresponding to an aspect ratio of 2, resulting in a total of 384,960 cells. A schematic view of the numerical set-up and the position of the sections used for the validation are given in Figure 5.1.

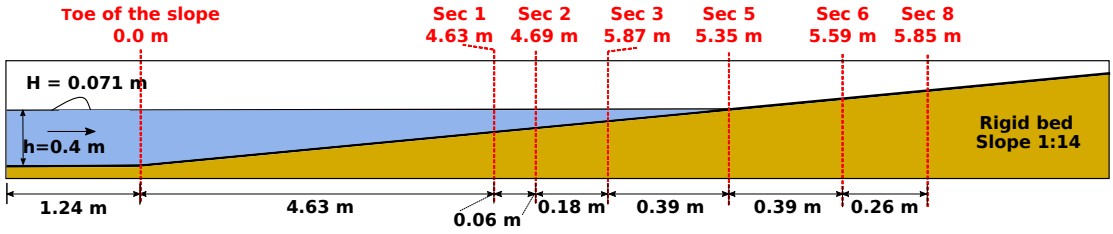

Figure 5.1: Schematic view of the numerical domain and position of the sections where stresses and free surface are measured.

A comparison between the experimental and the numerical results of free-surface evolution is shown in Figure 5.2. As in the experimental results, $t = 0$ is considered as the instant when the wave crest is at the toe of the beach.

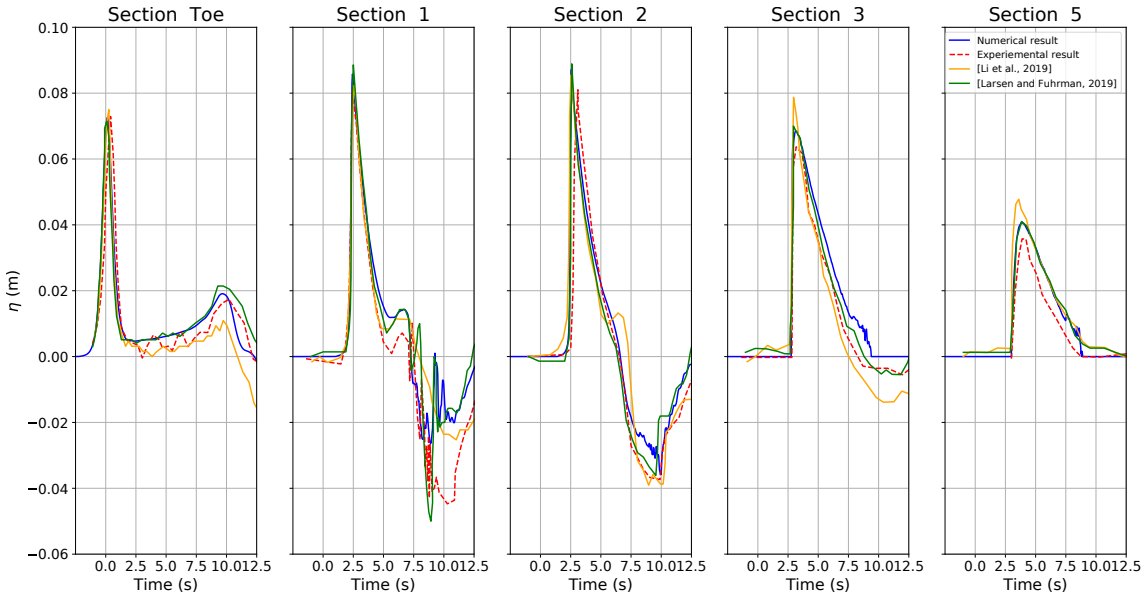

Figure 5.2: Free-surface evolution recorded at the toe, and sections 1, 2, 3 and 5. Blue continuous line: numerical results from IH2VOF-SED. Orange continuous line: results from (Li *et al.* , 2019). Green continuous line: results from (Larsen & Fuhrman, 2019) Red dashed line: experimental results.

It can be observed that the free-surface is overall well predicted for the first two stages (shoaling and wave breaking and run-up, until $t = 3.0$). In the rundown and hydraulic jump stage the differences are more noticeable, particularly during the hydraulic jump (starting at 7.5 s). The trailing wave, which can be observed in the last part of the simulation at the toe section ($t = 10$ s approximately), is well modelled. The reason for the discrepancies in the hydraulic jump can be due to the three-dimensional and air entrainment effects, which are not accounted for in the model.

A comparison between experimental and numerical shear stresses induced on the seabed is presented in Figure 5.3. Numerical bottom shear stresses are compared with the experimental ensemble-averaged stresses. The RMS (Root Mean Squared) of their fluctuations is also represented.

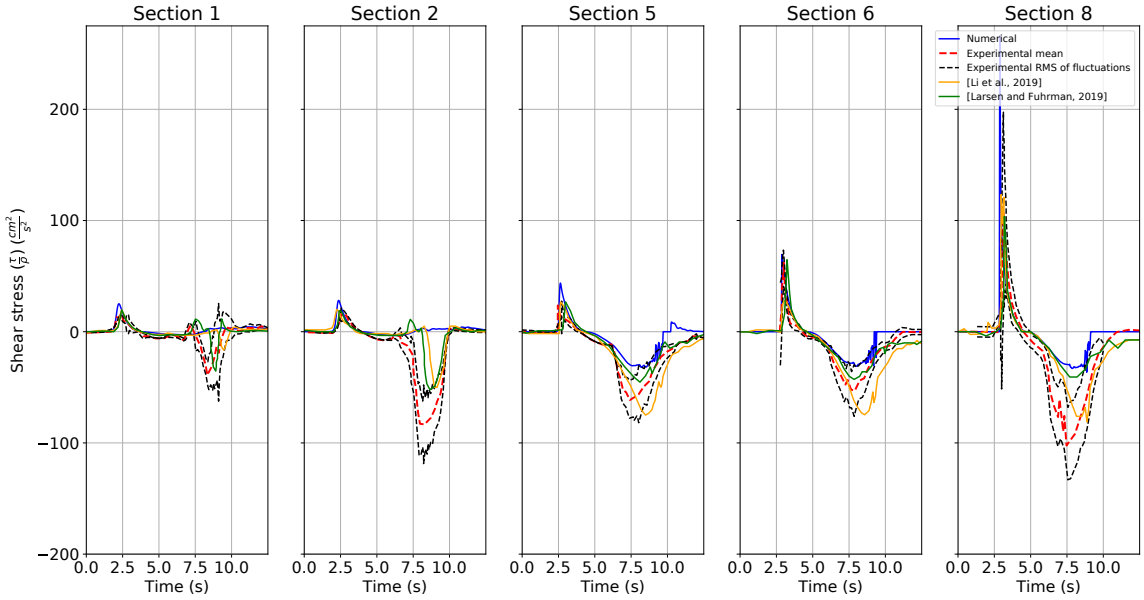

Figure 5.3: Bottom shear stress evolution. Blue solid line: numerical results from IH2VOF-SED. Orange continuous line: results from (Li *et al.* , 2019). Green continuous line: results from (Larsen & Fuhrman, 2019). Red dashed line: mean shear stresses obtained in the experiment. Black dashed lines: RMS of the fluctuations added and subtracted from the experimental mean value.

The results for the bed shear stresses provided by IH2VOF-SED can be compared to those of the aforementioned numerical models. In (Li *et al.* , 2019), a similar order of magnitude in the accuracy is achieved for the wave crest phase. The run-down is predicted also with a similar level of accuracy for sections 5, 6 and 8, while the result for sections 1 and 2 are better than in IH2VOF-SED as the model is able to reproduce the negative (seaward) bed shear stresses. (Larsen & Fuhrman, 2019) provides a more accurate reproduction of the wave crest phase by adjusting the density of the cell in contact with the seabed instead of considering a fixed one and using a finer mesh. Whereas the accuracy of the results in sections 5, 6, and 8 is on the order of magnitude as IH2VOF-SED and (Li *et al.* , 2019), the wave trough phase is clearly better predicted for sections 1 and 2, as (Larsen & Fuhrman, 2019) correctly reproduces the magnitude of the negative bed shear stresses.

It should be noted that the two models used as benchmark for IH2VOF-SED apply a body-fitted meshing strategy in contrast to the partial cell treatment used

here. The former allows for a more accurate description of boundary layer effects but incurring in a higher computational cost, reported between two weeks and two months for (Larsen & Fuhrman, 2019) running in 12 Intel Xeon Processor ES-2680 v2 cores and one day for (Li *et al.* , 2019). With the present model, the simulation lasted for 1 hour 45 minutes running in single-core.

As it was observed for the free surface measurements, the model predicts well the shoaling, wave breaking, initiation of the run-down and trailing wave for both the surf and swash zones. However, the shear stresses generated by the hydraulic jump are underestimated due to the aforementioned aspects. Note that this feature is enhanced in the case of a solitary wave compared to wind waves. Therefore, it is expected to have a reduced effect on the evolution of a beach profile. Thus, for the kind of problems that the model is intended to handle, simplifications made in exchange for faster calculations can be considered to be acceptable.

Recalling that the friction velocity is directly related to the shear stress ($\vec{u_f} = \sqrt{\frac{\tau}{\rho}}$), the model can provide accurate predictions for it, as well as for the associated sediment transport features (bedload transport and amount of sediment put into suspension). It is also remarkable that the accurate prediction of the bottom shear stresses extends to the swash zone, as can be observed in Sections 6 and 8 in Figure 5.3.

5.3 Validation of beach profile evolution

The validation of beach profile evolution experiments specifically aims to confirm that the new model is able to predict the evolution of the seabed, as well as its interaction with the hydrodynamics, independently of scale.

Consequently, the validation of the cross-shore beach profile evolution is performed for two different scales. For the medium-scale validation, the experiment from (Baldock *et al.* , 2011) is selected. This experiment has been used previously as a validation case for the numerical model presented in (Jacobsen & Fredsoe, 2014). In fact, results in (Jacobsen & Fredsoe, 2014) are included as part of this validation since more precise boundary layer and turbulence treatment were implemented in the numerical model. However, at a very high computational cost. For the large-scale, the experiments from (van der Zanden *et al.* , 2017a) are selected, as they provide measurements of other relevant variables, such as velocities and sediment concentration.

The hydrodynamic and sediment conditions of the beach profile validation cases are summarized in Table 5.1. The nondimensional parameters which characterise the beach behaviour are the Iribarren's number (Ir_0) , Dean parameter (Ω), Rouse number (P) and Shields number (ϕ) ((Grasso *et al.* , 2009), (Grasso *et al.* , 2011)). These parameters are also given in Table 5.1 and are obtained as

$$Ir_0 = \frac{\tan\alpha}{\sqrt{\frac{H}{L_0}}} \tag{5.1}$$

$$\Omega = \frac{H}{w_s T} \tag{5.2}$$

$$P = \frac{w_s}{u'} \tag{5.3}$$

$$\phi = \frac{1}{2} f_w \frac{(A\omega)^2}{g\left(\frac{\rho_s}{\rho} - 1\right) d_{50}} \tag{5.4}$$

where α is the angle of the offshore slope of the shoaling zone, H is the wave height on the paddle, L_0 is the wave length in deep water, w_s is the sediment fall velocity, T is the wave period, u' the turbulent fluctuation of the velocity, f_w the friction factor, A is the wave stroke close to the seabed and ω is the angular frequency of the wave

Table 5.1: Nondimensional numbers for the validation cases. Iribarren's number (Ir_0), Dean parameter (Ω), Rouse number (P) and Shields number (ϕ).

Case	**H** (m)	**T** (s)	**h** (m)	$\mathbf{d_{50}}$ (mm)	$\mathbf{w_s}$ (m/s)	$\boldsymbol{\tan\alpha}$	$\boldsymbol{Ir_0}$	$\boldsymbol{\Omega}$	**P**	$\boldsymbol{\phi}$
Medium	0.43	3.7	2.50	0.25	0.034	1:15	0.47	3.42	3.1	0.14
Large	0.85	4.0	2.55	0.29	0.034	1:10	0.54	5.51	1.86	0.42

According to the Iribarren's number, spilling breakers are expected for the medium-scale case and plunging breakers for the large-scale one. Regarding the Dean parameter (Ω), they correspond to intermediate beach states, being the large-scale closer to a dissipative state. In both of them a breaker bar formation is expected. The Rouse number is useful to characterize the surf zone and depends on the turbulence generated by wave breaking. The shoaling zone is driven by the Shields number. Rouse number and Dean parameter characterize the same physical processes (as explained in (Wright & Short, 1984)), as they represent the relation between the advective sediment transport due to turbulent motions and the sediment fall velocity, providing an estimation on the ability of turbulent motions to keep sediment in suspension. As these nondimensional parameters cover a wide range, the validation cases can be considered representative of the ability of the model to handle real beach configurations, despite the scaling of each individual experiment does not match any particular beach. Both validation cases of beach profile evolution are performed under monochromatic wave conditions.

The position along the beach profile (x) is normalized by the position and water depth associated to the breaking point (considered as the point in which the wave height starts decreasing). Therefore, the coordinate along the cross-shore profile is expressed as $\tilde{x} = \frac{x - x_b}{h_b}$ where x_b is the breaking point position and h_b the water depth at that position. To facilitate the analysis and discussion of the results, the beach profile is divided into shoaling ($\tilde{x} < 0$), outer surf ($0 < \tilde{x} < 5$) and inner surf ($\tilde{x} > 5$) zones according to (Ting & Kirby, 1994).

Unfortunately, some sediment properties are not given for the experimental cases in the corresponding literature. They are therefore estimated, although this may lead to some discrepancies between numerical and experimental results.

Medium-scale validation

The experiments from (Baldock *et al.* , 2011) were carried out in a 100 m long, 3 m wide and 5 m high wave flume at the Polytechnic University of Catalunya (UPC, Spain). The set-up consisted of a beach profile starting at 43 m from the wave paddle with a slope of approximately 1:15. Among the different wave conditions tested in the experiments, the case named ME is selected for validation. The wave

conditions were wave height H = 0.43 m, wave period T = 3.7 s, and water depth at the toe of the beach h = 2.50 m. The sediment characteristics were d_{50} = 0.25 mm and w_s = 0.034 m/s. More information about the grain size distribution used in this experiment is given in (Cáceres *et al.* , 2009), where it is reported that 92% of the grain size is between 0.15 and 0.35 mm. The seabed profile was obtained using a mechanical bed profiler after 24 minutes of waves.

The numerical simulations are performed considering 390 waves, consistently with the wave conditions reported by (Baldock *et al.* , 2011). Waves are generated at the left boundary of the numerical domain using Stokes II theory and active wave absorption. The beach slope of the numerical domain starts at 53.28 m from the position of the experimental wave paddle, with a 5.84 m long horizontal area to ensure that the generated waves can adapt to the water depth before getting transformed along the beach profile. The domain also includes part of the dry beach to ensure that the run-up does not reach the end of the domain. The final mesh has a total of 147.823 cells with $\Delta X = 0.038\ m$ and $\Delta Z = 0.019\ m$. A mesh sensitivity analysis for this simulation is provided in Appendix B. Regarding the sediment properties, the nominal diameter and the sediment fall velocity were set according to the experimental data. The density is considered to be 2650 kg/m^3 and the sediment porosity 0.40 (standard values for sand).

A schematic view of the numerical set-up is shown in Figure 5.4.

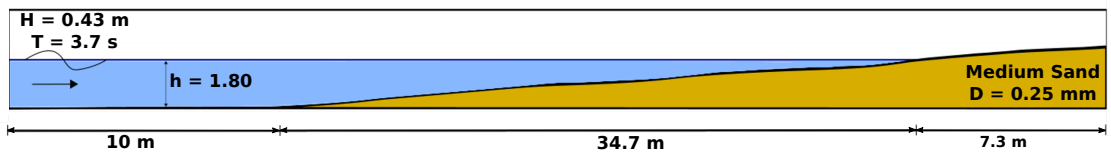

Figure 5.4: Schematic view of the numerical domain.

The simulation, with morphological time of 2880 s (48 min), lasted 143 h (6 days) running on a single core and 93 h (less than 4 days) on two cores, without using any morphological acceleration factor. This represents a great reduction in the computational effort compared to the more complex model used for benchmarking. (Jacobsen & Fredsoe, 2014) reports that, for a case with a similar number of cells, it took one month to simulate 6000 s of morphological time considering a morphological acceleration factor of 5 and running in parallel using 4 cores. Notice that, using a morphological factor of 5, the same simulation using IH2VOF-SED would take 44 hours in a single core or 25 hours using two cores.

In Figure 5.5, the bathymetry after 24 and 48 min of simulation (390 and 780 waves approximately) is compared with results from the experiment, XBeach (using default parameters) and the model from (Jacobsen & Fredsoe, 2014). Only the part of the domain where significant changes in the bathymetry occurred is shown.

Laboratory and numerical results from IH2VOF-SED are displayed in Figure 5.5 corresponding to 24 minutes and 48 minutes of wave action. In both, laboratory and experiment, a breaker bar and trough are generated in the same position initially, and they migrate offshore between minutes 24 and 48. The main differences are in the size of the trough and the secondary breaker bar (at $\tilde{x} = 10$). Regarding the swash zone, the erosion is correctly reproduced.

There are various potential sources for the discrepancies between IH2VOF-SED and the experimental results. Firstly, the three-dimensional nature of the breaking

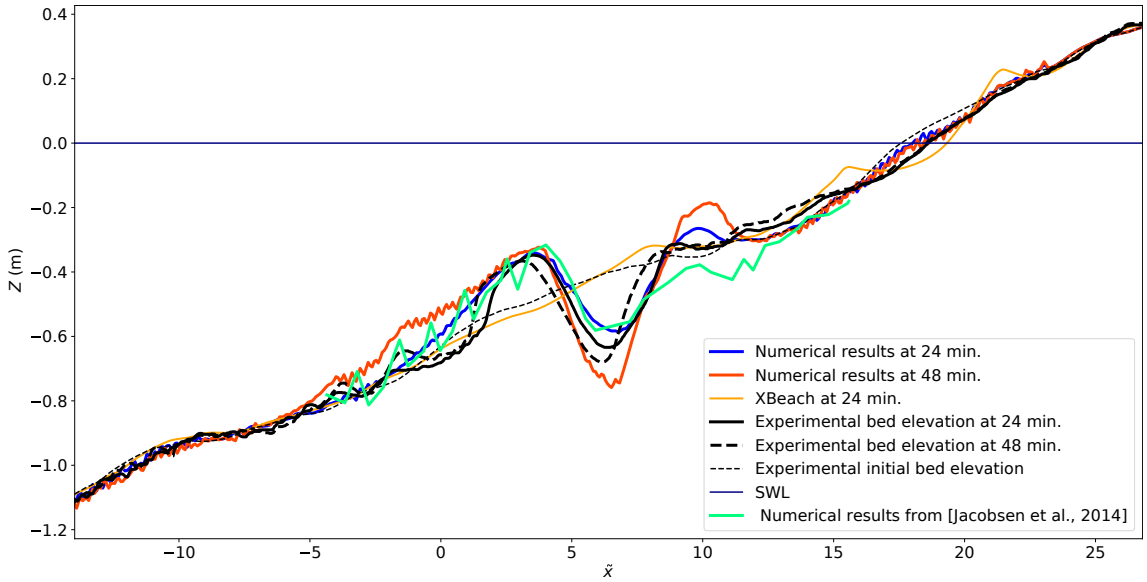

Figure 5.5: Resulting bathymetry after 24 and 48 min of waves. Blue line: IH2VOF-SED after 24 min. Red line: IH2VOF-SED after 48 min. Green line: numerical results from (Jacobsen & Fredsoe, 2014) after 23 minutes. Orange line: XBeach (default parameters) after 24 minutes. Black dashed line: initial bed level.

process and the influence of the air entrainment are not accounted for in the numerical model, neither are the effects of the grain size distribution in sediment transport. Additionally, some non-uniformity of the profile across the wave flume is reported in (Baldock *et al.* , 2011). Furthermore, differences regarding the exact conditions in which the experimental and numerical simulations were performed, such as the wave generation/absorption system and sediment properties, can lead to the aforementioned discrepancies. In particular, the uncertainty in the exact position of the initial and final seabed can be responsible for the differences in the depth of the trough. The mechanical device used to measure the position of the seabed in (Baldock *et al.* , 2011) had a limited precision, and systematically measured the position of the trough of the ripples. By performing a mass balance with the provided experimental results, it can be observed that there is an excess of erosion of around 0.5 m^3 per meter of width. As discussed in (Baldock *et al.* , 2011), this excess of erosion cannot be directly imputed to a certain region of the beach profile. Finally, the precision of the empirical formulae included in the model also limits its overall performance.

A comparison of the cross-shore beach profile results obtained from IH2VOF-SED, XBeach and (Jacobsen & Fredsoe, 2014) for the 24 minutes profile is performed. The numerical model presented in (Jacobsen & Fredsoe, 2014) provides a similar prediction of the position of the breaker bar and trough, and large erosion in the inner surf zone, while in the present model the later does not suffer significant changes. The computational cost in which the model from (Jacobsen & Fredsoe, 2014) incurs to simulate some features of the hydrodynamics is much higher than the present model for the simulation of a significantly smaller domain. The main reason for this is the different types of meshing strategy followed by each model. While IH2VOF-SED uses an orthogonal structured mesh, (Jacobsen & Fredsoe, 2014) uses an unstructured meshing strategy. The former provides substantial

advantages in terms of computational cost, as the system of equations being solved in the Two-step Projection Method has a pentadiagonal matrix in contrast with the sparse matrix arising from the use of unstructured meshes. However, unstructured meshes can easily adapt to the solid shapes while IH2VOF-SED relies on the, less precise, partial cell treatment for this purpose. In addition, as reported in (Jacobsen & Fredsoe, 2014), numerical instabilities due to the combination of air and water in a thin layer required an upper cut-off of the beach profile eliminating the swash zone to be able to run the simulations. The difficulties to numerically simulate the swash zone are also pointed in (van Rijn *et al.* , 2011). The elimination of the swash zone implies that some of the hydrodynamic processes could be affected. For instance, the balance between onshore/offshore-directed mass and linear momentum fluxes, key aspect for the generation of the undertow current in the surf zone, can be altered by this simplification. Furthermore, sediment which can be potentially eroded and transported to the breaker bar (and viceversa) is not accounted for, and the morphological effects that result from this interaction, such as beach accretion, may not be reproduced. Finally, a morphological acceleration factor was used to perform the simulations, which can also affect the resulting bathymetry.

Regarding the results from XBeach, they are clearly deviated from the laboratory results. The breaker bar and trough are not generated. Instead, a general erosion in the shoaling and surf zones is predicted. The main accumulation of sediment occurs in the inner surf zone.

In order to quantify the ability of each model to correctly reproduce the evolution of the beach profile, the Brier Skill Score (BSS) is used. As the BSS uses the difference between initial and final observed profiles, the aforementioned excess of erosion in the final laboratory profile must be compensated. As the excess of erosion cannot be directly imputed to a certain part of the profile, this is done by adding a uniform shift on the final profile of 8 mm. The skill score is calculated for the same domain simulated in (Jacobsen & Fredsoe, 2014) so that the three models can be compared. The obtained values are -0.21 for XBeach, 0.75 for IH2VOF-SED and 0.42 for (Jacobsen & Fredsoe, 2014). According to (van Rijn *et al.* , 2003), the performance of the models can be classified as bad ($BSS < 0$) for XBeach, reasonable for (Jacobsen & Fredsoe, 2014) ($0.30 < BSS < 0.60$) and good for IH2VOF-SED ($0.60 < BSS < 0.80$). If the same comparison is performed for the complete beach profile, including the shoaling and swash zones, the results are -0.23 for XBeach and 0.73 for IH2VOF-SED, results for (Jacobsen & Fredsoe, 2014) cannot be obtained as the simulated domain did not cover these areas. After 48 minutes of simulation, the BSS for IH2VOF-SED is 0.30 (reasonable).

Using IH2VOF-SED only, the evolution of the seabed shape along the simulation is displayed in Figure 5.6.

There is an initial growth of the breaker bar produced by the sedimentation of sand eroded from the shoaling, surf and swash zones. The trough is generated mainly after 9.6 minutes, once the breaker bar has acquired a sufficient size to significantly affect the hydrodynamics. The breaker bar grows in the same place until minute 19.6 approximately. Later, it starts migrating offshore (minutes 19.6 to 38.2). For the last interval (minutes 43.2 to 48), it can be noted that the breaker bar stops migrating and the bar trough does not deepen any further, reaching a pseudo-equilibrium status. This behaviour is observed in both, the experiment (not shown) and the numerical simulation.

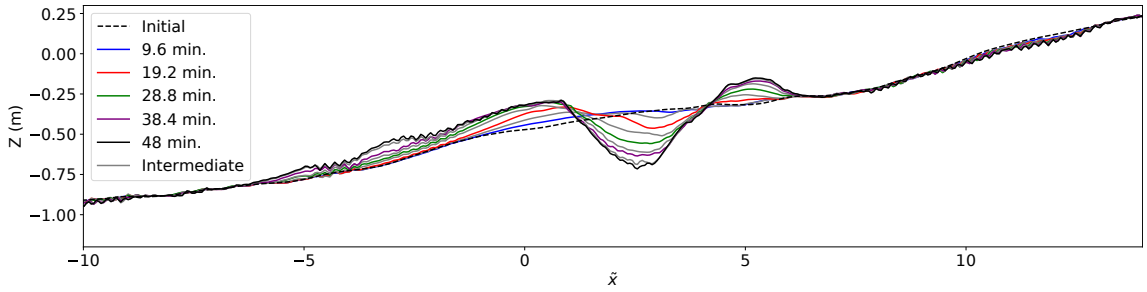

Figure 5.6: Mean seabed shape at different instants along the simulation. Black dashed line: initial seabed. Blue line: after 9.6 minutes (155 waves). Red line: after 19.2 minutes (311 waves). Green line: after 28.8 minutes (467 waves). Purple line: after 38.4 minutes (622 waves). Black line: after 48 minutes (778 waves). Gray lines: intermediate profiles each 4.8 minutes (78 waves)

.

The contribution of each sediment transport mechanism to the bathymetry changes can be also extracted from the model according to Equations 4.46, 4.47 and 4.48. These contributions are shown in Figure 5.7.

As can be noted, both the bedload and suspended contributions tend to erode the position of the bar trough and to accumulate sediment where the breaker bar is generated. At the beginning of the simulation, the zone in which the suspended transport accumulates sediment starts close to the wave breaking point (at $\tilde{x} = -1$) and extends until the plunge point $\tilde{x} = 3$ approximately. The bedload contribution accumulates sediment on a reduced area ($2 < \tilde{x} < 3$), leading to the growth of the onshore side of the breaker bar. As the simulation advances, both transport contributions produce erosion in the bar trough, and the suspended contribution is shifted offshore with respect to the bedload component. It can also be noted that the zones where sediment is accumulated by both mechanisms are displaced offshore as the simulation progresses (more remarkably in the case of the suspended contribution, from $-1 < \tilde{x} < 3$ to $-5 < \tilde{x} < 0$). This results in the migration of the breaker bar shown in the bathymetry evolution of Figure 5.6. Close to the end of the simulation, both time-averaged contributions are smaller, and they compensate each other on top of the breaker bar ($\tilde{x} = 1$) and, partially, in the bar trough ($\tilde{x} = 3$) as the beach profile approaches the pseudo-equilibrium status.

In Figure 5.8, the evolution of wave height, friction velocity, bedload and suspended sediment transports and bathymetry are shown.

Panels A and B in Figure 5.8 show that the net friction velocity is positive seaward of the breaking point and changes its sign in the surf zone, approximately at the breaking point ($\tilde{x} = 0$). This can be explained considering the mean velocity distribution along the beach profile (shown in Figure 5.9). It can be observed that the peak in negative friction velocity occurs at the position where the trough is generated ($\tilde{x} = 2.5$ approximately). The near-bed mean velocity is onshore-directed in the shoaling zone, due to the asymmetry of shoaling waves and steady streaming, and offshore-directed in the surf zone, due to the undertow. This is a well-known feature, on which many simpler numerical models rely to predict the resulting beach profile (i.e. (Hoefel & Elgar, 2003)). However, after the breaker bar is generated, an onshore-directed friction velocity appears in the bar trough, consistent with the high friction velocities induced by the breaking process (when the plunging jet reaches the

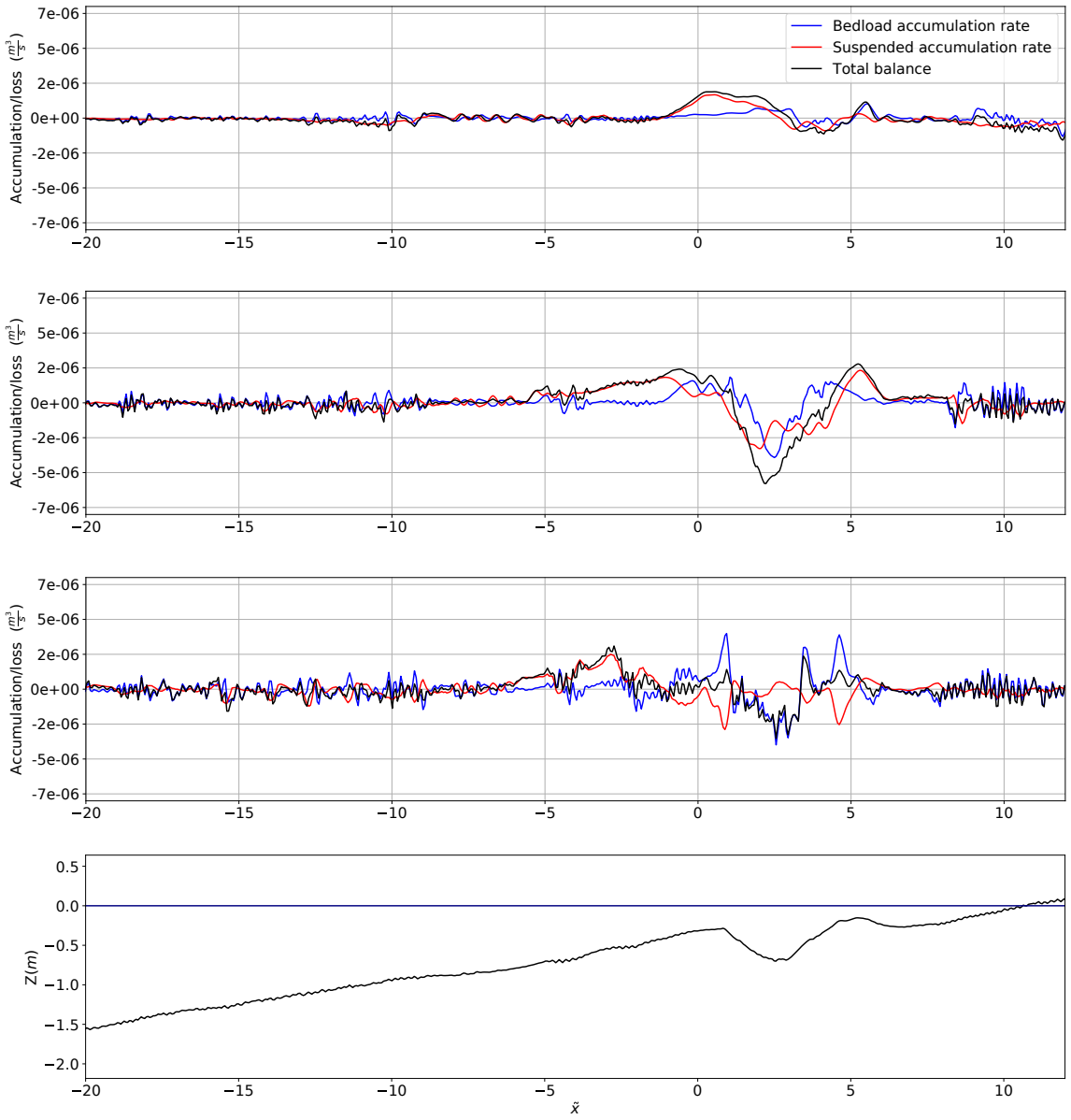

Figure 5.7: Contributions of the bedload and suspended transport mechanisms to the bathymetry changes. Panel A: waves 0 to 100. Panel B: waves 300 to 400. Panel C: waves 600 to 700. Panel D: Bathymetry after 700 waves

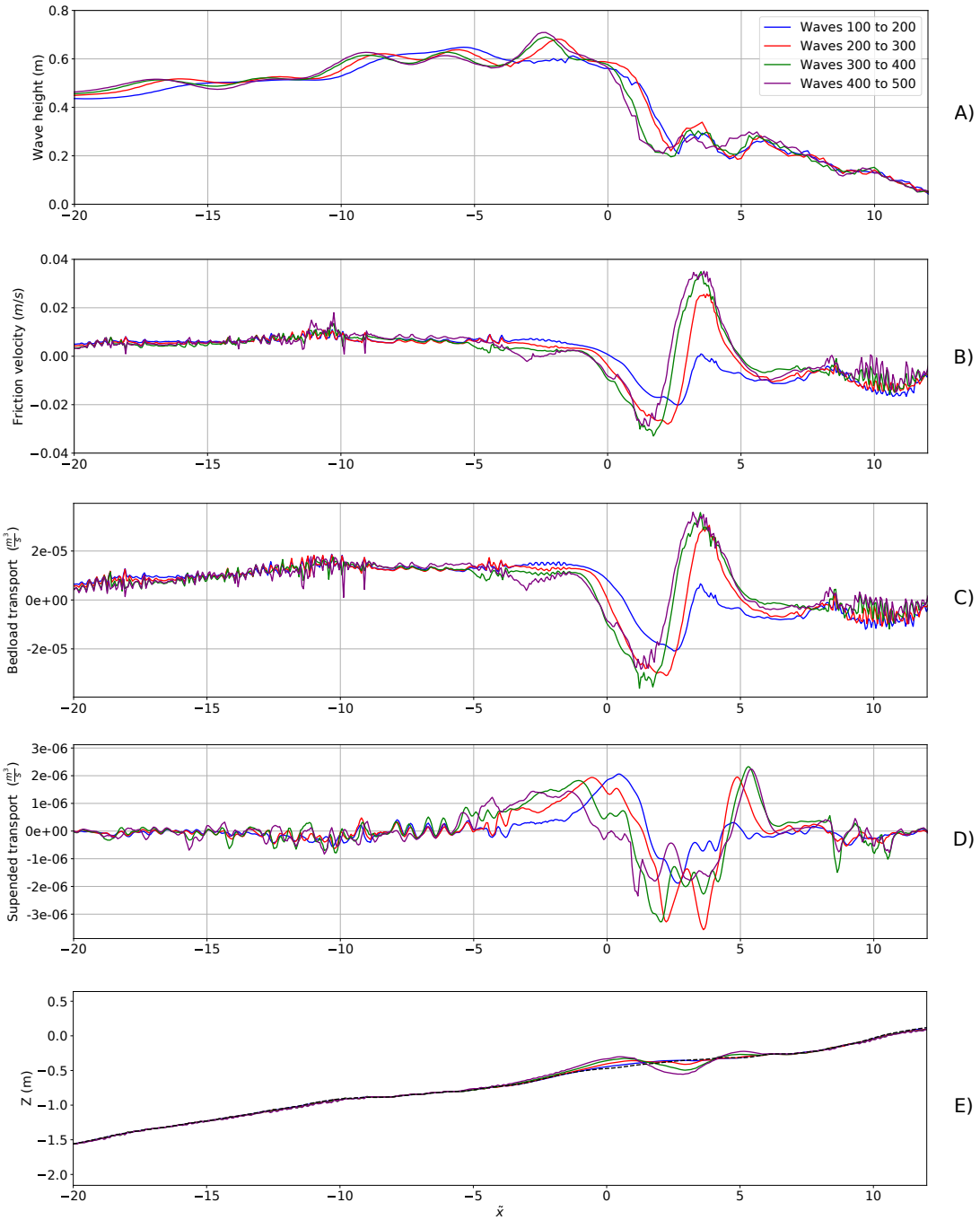

Figure 5.8: Evolution of wave height, friction velocity, bedload and suspended transports and resulting bathymetry. Blue line: waves 100 to 200. Red line: waves 200 to 300. Green line: waves 300 to 400. Purple line: waves 400 to 500. In the bottom panel, the initial bed elevation is displayed in black dashed line.

seabed). The effect of this high instantaneous velocity is also reflected in Figure 5.9 panel D, where a small area of near-bed onshore-directed mean velocity can be spotted between $\tilde{x} = 3$ and $\tilde{x} = 5$. This same feature is shown in some laboratory data (e.g. (Okayasu & Katayama, 1992)). In panel C, the bedload transport follows the same trend as the friction velocity, consistently with Equation 4.36. The suspended transport, shown in panel D, produces erosion in the shoaling zone and part of the surf zone (initially for $\tilde{x} < 5$). The eroded sediment is deposited mainly around the breaking point at the beginning of the simulation, resulting in the generation of the breaker bar. For the last time interval, a significant change in the suspended transport trend can be observed, the sediment is no longer deposited at the breaker bar position but rather on its offshore slope, effectively inhibiting further growth of the breaker bar and producing offshore migration as discussed in Figure 5.7. The mean seabed shape for every interval is represented in panel E for reference.

One of the main drivers of the cross-shore profile evolution is the undertow. To examine its variation along the simulation due to the interaction with the changing seabed, the time-averaged horizontal velocity field is represented in Figure 5.9.

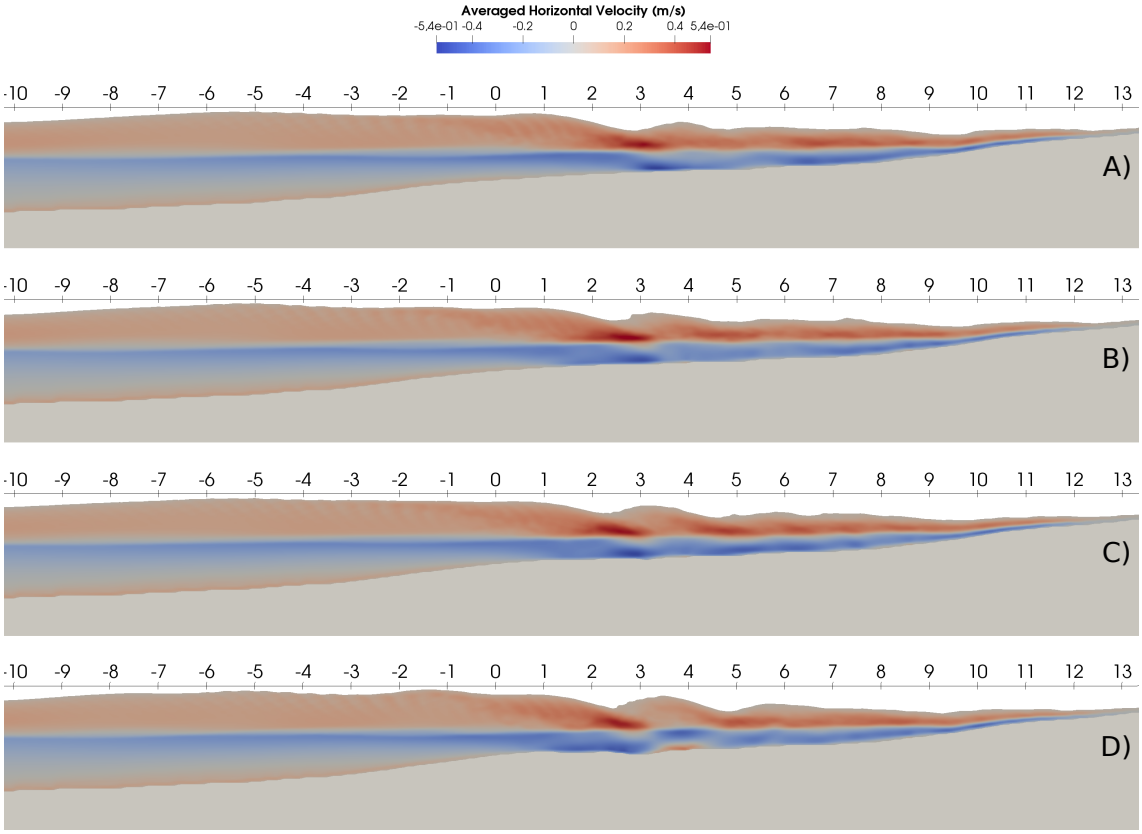

Figure 5.9: Time-averaged horizontal velocities obtained for different wave intervals. Panel A: waves 50 to 60. Panel B: waves 100 to 110. Panel C: waves 150 to 160. Panel D: waves 200 to 210. The wave envelope and seabed shape are represented by white lines. Negative velocities are offshore-directed

The undertow can be clearly identified as the blue areas (offshore-directed velocities in Figure 5.9). The red coloured areas correspond to onshore-directed mean velocities. For the initial situation (panel A) the maximum undertow occurs offshore the plunge point (where the plunge jet impinges the water, at $\tilde{x} = 3.0$ ap-

proximately), coinciding with the maximum onshore-directed mass flux produced by breakers, and weakens as it moves into the shoaling zone. In the subsequent panels, the maximum value occurs at a larger distance seawards of the plunge point, the value right at the plunge point close to the seabed even becomes positive in the last intervals (panels C and D, can also be noted in Figure 5.8 panel B). It can be observed that, seawards of the breaking point, the undertow is being enhanced as the breaker bar develops. Another aspect that can be noted is the undertow detachment from the seabed. The detachment point (where the near-bed velocities change their sign, being offshore directed in the onshore side and onshore directed in the seaward side) is also displaced offshore as moving from panel A to D. This can be quantitatively observed in panel B of Figure 5.8, where the point in which the mean friction velocity changes its sign is displaced offshore for the first 400 waves.

A key aspect in the generation of the breaker bar is the correct simulation of sediment fluxes induced by the breakers. To further analyse this aspect, the instantaneous sediment fluxes and concentration fields for different time instants during wave breaking are represented in Figure 5.10, together with the instantaneous friction velocities.

Panel A shows a shoaling wave approaching the break point. The suspended sediment transports resulting from the wave crest passing (onshore directed) and the undertow current (offshore directed), meet at $\tilde{x} = -2$ approximately. Panel B displays the instant when wave breaking starts ($\tilde{x} = -1.0$). The sediment transported by the previous mechanisms is accumulated in the wave front ($\tilde{x} = -0.5$). The instant when the plunger jet impinges the water is displayed in Panel C. It can be observed that a large eddy is generated at $\tilde{x} = 2.0$. This eddy produces a great mixing of sediment. Finally, panel D displays how the large eddy breaks into several smaller ones (roughly at $\tilde{x} = 2.25,\ 3.25,\ 5.5$), that occupy the available water depth, further mixing the upper and lower layers of the surf zone. The mixing effect of these eddies also enhances the momentum transfer between upper and lower layers, resulting in a reduction of the undertow velocity for the inner surf zone in accordance with (Ting & Kirby, 1995).

The sediment concentration and flux patterns shown in Figure 5.10 are in agreement with qualitative experimental observations, as the ones given in (Sumer *et al.* , 2013).

Large-scale validation

The experiments used for the large-scale validation were conducted in the UPC laboratory, in the same flume used for the medium-scale validation test. In this case, an initial position of the breaker bar was obtained in the first run. Then, several runs tracking the evolution of the breaker bar and measuring hydrodynamic parameters were conducted starting with the same initial profile, which was recovered after each run. Wave conditions in this case were H = 0.75 m at the toe of the beach (reportedly 0.85 m at the generation), T = 4 s and h = 2.55 m at the wave-maker. A total of 450 waves (1800 s) were generated. Sediment grain size was $d_{50} = 0.29\ mm$ with $d_{90} = 0.42\ mm$ and $d_{10} = 0.19\ mm$, and its fall velocity equal to 0.034 m/s. The wave height was measured using resistive wave gauges. For the velocities, ADVs were located at different positions to obtain velocity profiles. Regarding sediment concentration, Transverse Suction System nozzles (TSS)

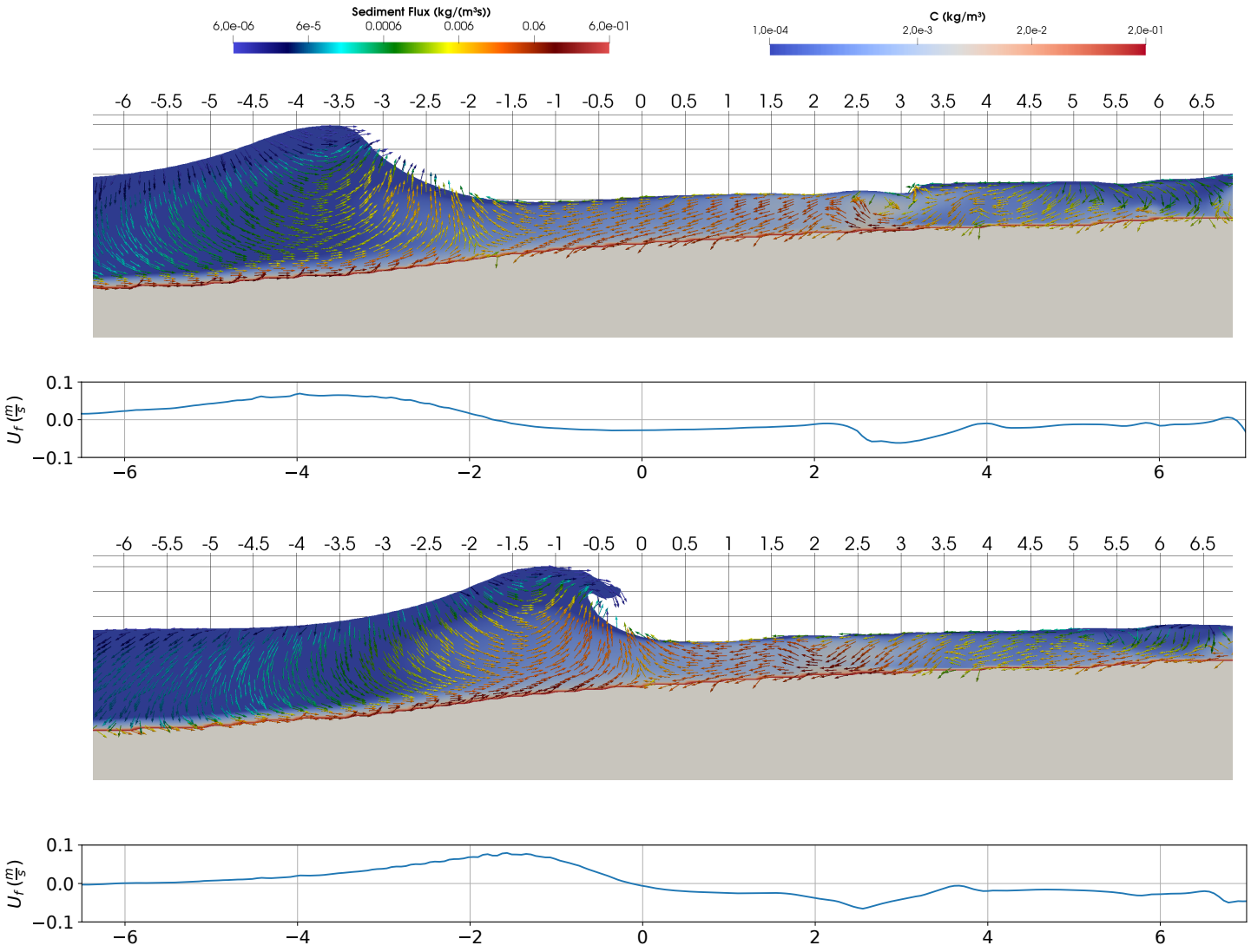

(a) Top panel: prior to break. Lower panel: during wave breaking

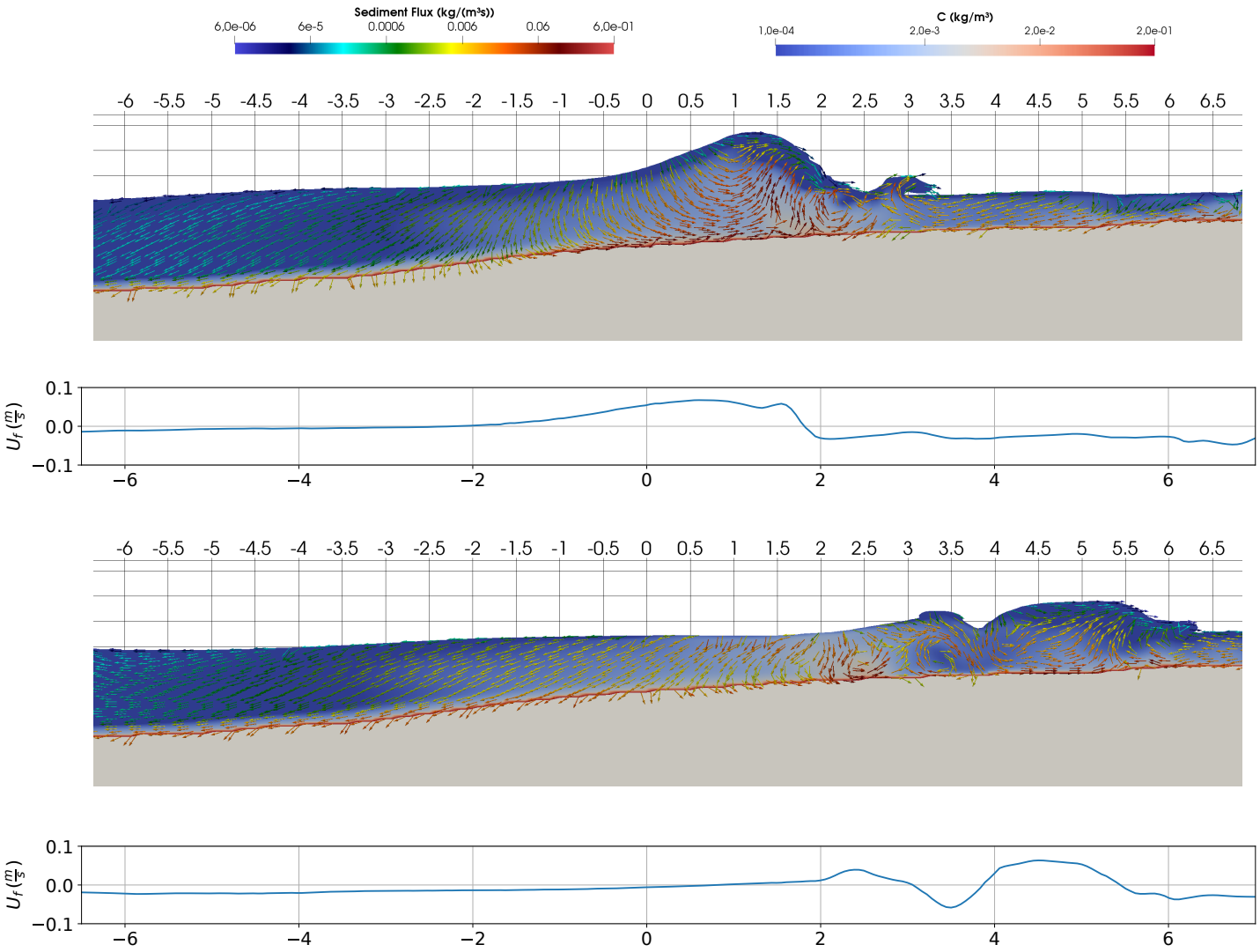

(b) Top panel: plunge. Lower panel: after plunge.

Figure 5.10: Sediment flux and concentration during different stages of wave breaking. The instantaneuos fields are obtained after 50 waves. Below each vector map, the instantaneous friction velocity is represented. Coloured arrows: sediment flux. Colour map: sediment concentration. Blue continuous line: friction velocity.

and Optical Backscatter Sensors (OBS) were used for the outer flow, while Acoustic Concentration and Velocity profilers (ACVP) were used close to the seabed.

For this validation, the evolution of the breaker bar, starting from the same initial profile as the one in the experiments, is numerically reproduced. The averaged beach profile and its top and bottom bounds, obtained by adding and subtracting the standard deviation of the results, are compared with the numerical results.

In the experimental set-up, the foreshore ($\tilde{x} > 13.0$) was protected by a geotextile. This feature is introduced in the numerical simulation as an immobile-bed boundary condition. Waves are generated using Stokes II theory and active wave absorption. The sediment nominal diameter and fall velocity are set according to the experiments. Sediment porosity is set to 0.40 (standard value for a loosely packed bed) and the sediment density is considered to be 2650 m^3/s. The mesh consisted of 127.300 cells considering $\Delta X = 0.058\ m$ and $\Delta Z = 0.029\ m$. The influence of mesh discretization is discussed in Appendix B. A schematic description of the numerical domain, including the position of the different gauges that are used for the validation, is shown in Figure 5.11. The simulation took 57 h running in a single core and 33 h in two cores.

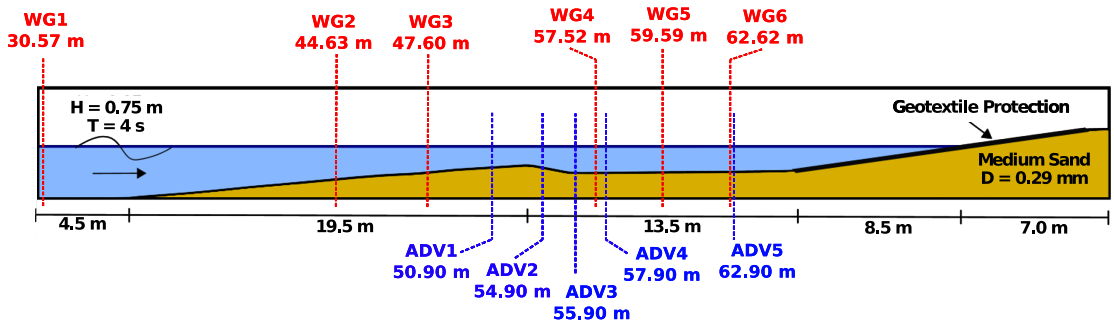

Figure 5.11: Schematic view of the numerical domain and the position of sensors (wave gauges in red, ADVs in blue) which are used for the validation. The x position in the experiment to which they correspond is also indicated on each sensor for reference.

The numerical results are compared to the experimental data. The position and depth of the breaking point provided in (van der Zanden *et al.* , 2017a) are used to normalize the results. Numerical results of wave height along the cross-shore profile, obtained as the mean value between waves 50 and 100, are compared to the experimental data in Figure 5.12.

The evolution of the wave height along the cross-shore profile shows a good agreement with the experimental results, as observed in Figure 5.12. It can be noted that the mean wave height coincides at the generation boundary, shoaling, outer and inner surf zones. Also, the position of the breaking point (where the drop in wave height starts) has been accurately reproduced by the model as it is located at $\tilde{x} = 0$.

The phase-averaged free surface at different positions along the profile is also compared with experimental data, it has been obtained for 50 waves after 200 s of regularization time. Figure 5.13 shows this comparison.

Figure 5.13 shows an overall good agreement between the numerical and the experimental data. Close to the wave generation, the differences are more noticeable (panel A left). The differences vanish close to the breaking point (panels A right

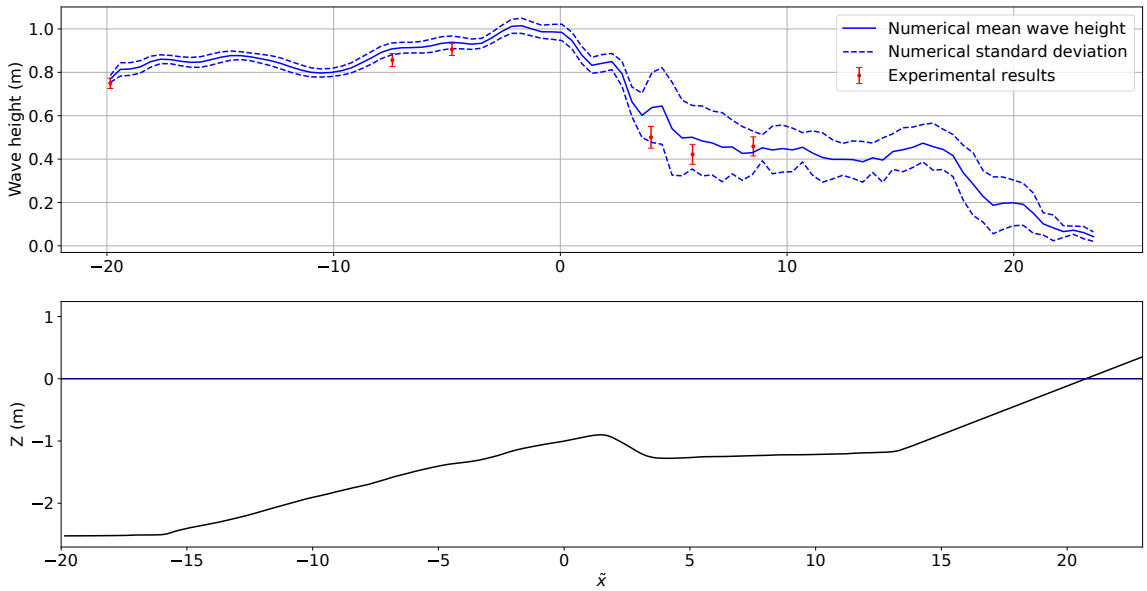

Figure 5.12: Wave height at different locations along the experimental set-up for waves 50 to 100. Upper panel: wave height evolution along the profile. Bottom panel: initial seabed shape. Blue continuous line: numerical mean wave height. Blue dashed lines: standard deviation of numerical wave height. Red dots: experimental mean wave height. Red bars: standard deviation of the experimental wave height.

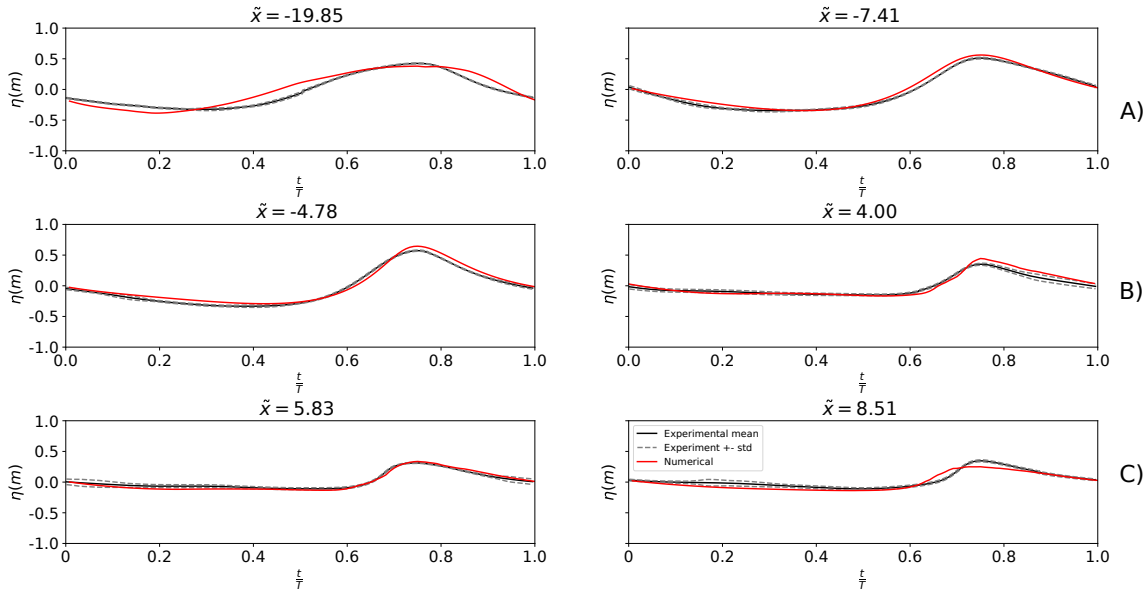

Figure 5.13: Phase-averaged free surface. Red lines: Numerical results. Black continuous lines: experimental phase-averaged free-surface from (van der Zanden *et al.* , 2017a). Grey dashed lines: standard deviation of experimental free-surface.

and B left). Onshore of the breaking point (panels B right, C left and C right) the numerical results are also in good agreement with the experimental ones.

The comparison between numerical and experimental results for phase-averaged velocities at different points in the domain is also performed and shown in Figure 5.14. Five positions along the cross-shore profile are presented. Row A corresponds to the onshore part of the shoaling zone, very close to the breaking point. Rows B, C and D correspond to different positions in the outer surf zone and row E to a position in the inner surf zone. For each position along the profile three points are measured in the vertical. The first column in Figure 5.14 corresponds to measurements close to the seabed. The second column displays results for a position at approximately half of the water depth, and the third column shows results close to the free surface. The coordinate Z represents the distance from the bottom of the channel ($Z = 2.55\ m$ for the still water level). Again, the phase-averaged values are obtained for 50 waves after 200 seconds of simulation.

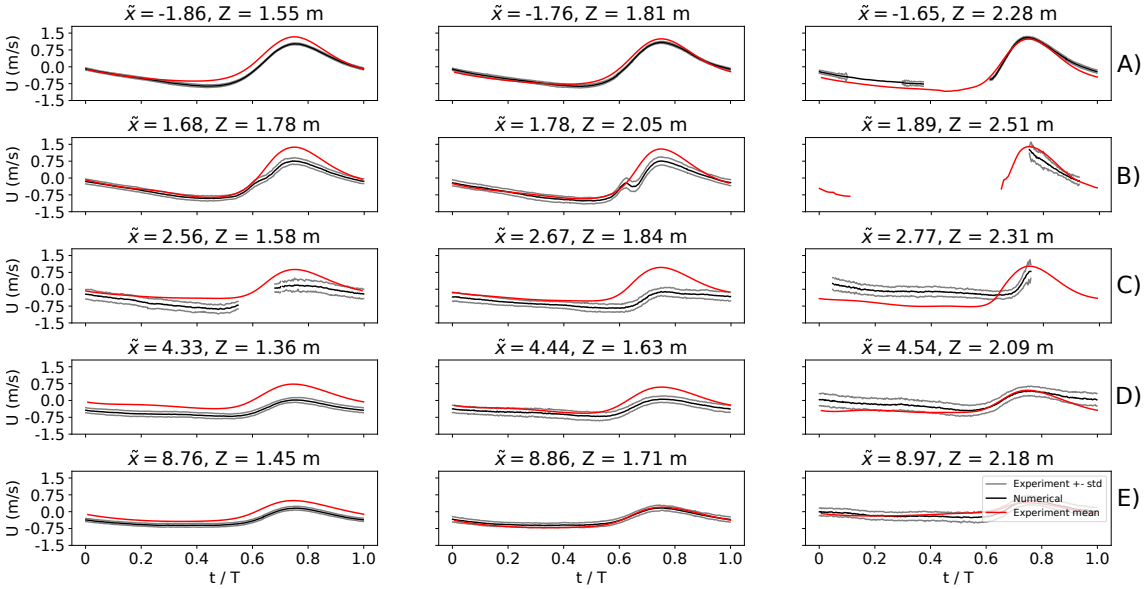

Figure 5.14: Phase-averaged velocities. Red line: numerical model results. Black line: mean experimental results from (van der Zanden *et al.* , 2017a). Grey lines: standard deviation of experimental results.

As can be observed in Figure 5.14, numerically obtained velocities are in good agreement with the experimental results. The outer surf zone (particularly rows B and C) presents the most noticeable differences. The shoaling zone (row A) and inner surf zone (row D) show good agreement between the numerical and the experimental data, although the mean velocity is slightly overestimated. An underprediction of the undertow velocity could be the reason for this deviation.

The numerical and experimental mean sediment concentration profiles at different positions along the beach profile are also compared. Figure 5.15 shows the numerical and experimental averaged concentration profiles, obtained for 50 waves after 400 s of simulation.

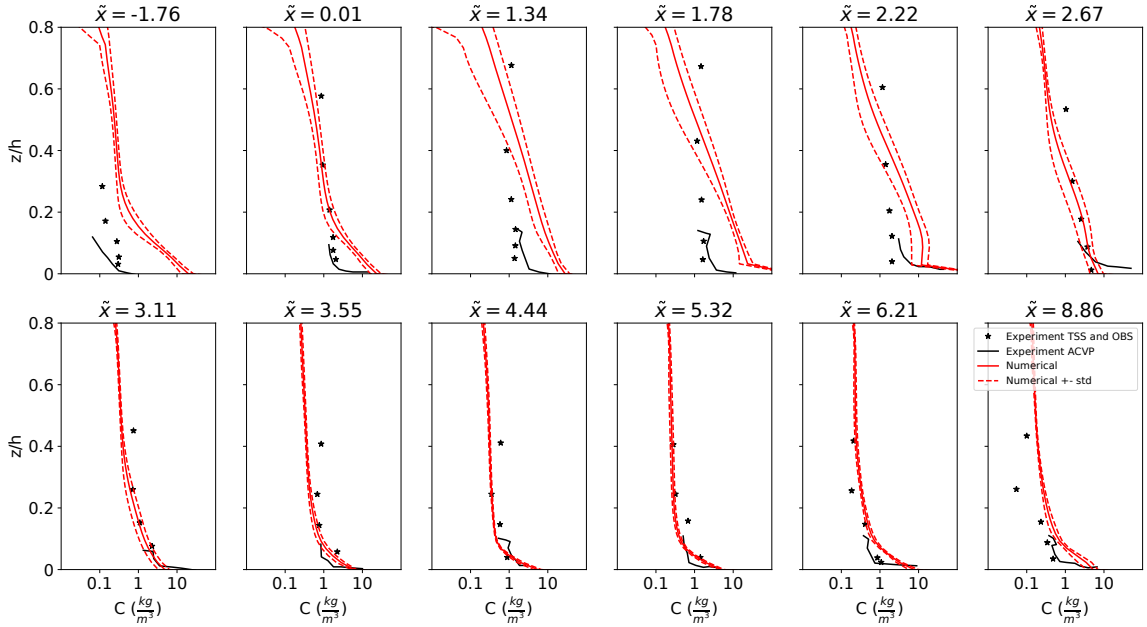

Figure 5.15: Averaged concentration profiles at different positions. Red continuous lines: numerical results. Red dashed lines: standard deviation of the numerical results. Black stars: experimental data obtained from TSS and OBS measurements. Black lines: near-bed data from ACVP measurements.

Figure 5.15 shows a reasonable overall agreement between experimental and numerical results. For the shoaling region, close to the breaking point, and initial part of the outer surf zones (until $\tilde{x} = 2.7$ approximately) the differences are more noticeable as the model over-predicts the sediment concentration, with a Root Mean Square Error (RMSE) between 6.2 and 9.8 kg/m^3, while for the rest of the outer surf zone and inner surf zone the results are very close to the experimental measurements, with a RMSE of 0.17 to 1.9 kg/m^3.

The differences between experimental and numerical results in the surf zone are of the same order of magnitude as the results provided by the empirical formulae used to compute the entrainment of sediment into suspension (see (Garcia & Parker, 1991)). Therefore, the accuracy of the formulae could be responsible for a significant part of the differences between experimental and numerical concentration profiles in the surf zone. For the shoaling zone and the beginning of the outer surf zone, a low concentration gradient close to the seabed is responsible for the poor agreement. This low concentration gradient can be due to an overestimation of the near-bed mixing processes (vertical velocities and turbulence) produced in the initiation of the wave breaking. Additionally, it should be kept in mind that the near-bed concentration measurements have a high level of uncertainty, according to (van der Zanden *et al.* , 2017b). The aforementioned underprediction of the undertow velocities, which results in larger velocities during the crest phase (as shown in Figure 5.14), also leads to a larger volume of sediment put into suspension in the inner surf zone.

Finally, the resulting beach profile after 30 minutes of simulation (450 waves) is compared with the experimental measurements in Figure 5.16.

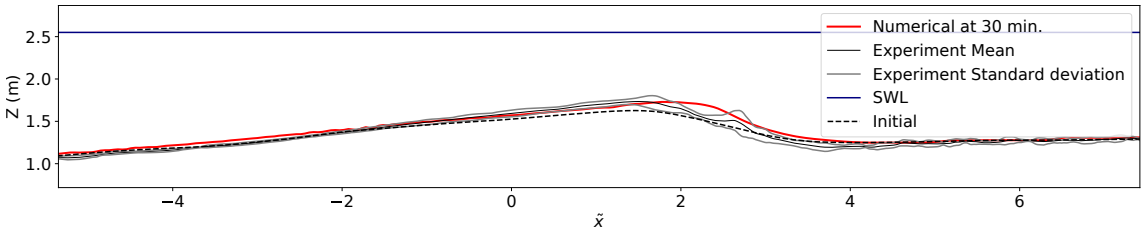

Figure 5.16: Beach profile at after 30 minutes. Red line: numerical results. Black line: averaged experimental beach profile. Grey dashed lines: standard deviation of the experimental beach profile

Figure 5.16 shows that the experimental and numerical results are close to each other. The main difference is the excessive growth of the breaker bar obtained with the numerical model in comparison with the experimental data. This discrepancy can be explained by the excessive concentration put in suspension shown in Figure 5.15, which results in more rapid variations of the seabed. There is also a small landwards shift in the bar position which is associated to the underestimation of undertow velocities commented in Figure 5.14, leading to an increase in the onshore sediment transport. However, the quantitative evaluation of the performance of the numerical model for the region around the breaker bar ($\tilde{x} = -2$ to $\tilde{x} = 6$), gives a Brier Skill Score (BSS) of 0.07 for the numerical results, which is classified as "poor" (slightly better than the null hypothesis) according to (van Rijn *et al.* , 2003). Comparing this value to that of the medium-scale validation case, also obtained in the breaker bar region, (0.75 for IH2VOF-SED) this seems to be a low value. In this regard, it should be kept in mind that in the large-scale validation case the small variations of the initial bathymetry, in which the breaker bar is already present, make the comparison with numerical results more unfavourable. If compared to a null hypothesis of an unbarred initial profile (as in the medium scale validation), the difference between experimental results and null hypothesis would be larger, and the BSS for the numerical model better. Unfortunately, the author does not have access to the shape of the experimental beach profile before the breaker bar was generated to compute this quantity.

5.4 Conclusions

Validations show that the model is able to predict the morphological evolution of a complete beach profile under regular waves and erosive conditions, including the shoaling, surf and swash zones, in a satisfying manner.

The first validation case consists in comparing the tangential stresses induced by a solitary wave during its breaking process. Laboratory and numerical model provide similar results, being the largest differences in the run-down stage due to the difficulties in the simulation of the hydraulic jump.

Another two validation cases, in which the evolution of the beach profile is numerically reproduced, show consistent agreement between experimental and numerical results. In the large-scale validation, the hydrodynamic magnitudes (wave height, shape and velocities) and the resulting seabed shape are well predicted by the model, a reasonable approximation of the concentration profiles has also been achieved. Overall discrepancies between experimental and numerical results can be due to

the three-dimensional and air entrainment effects in the wave breaking process, the simplifications introduced by the empirical formulae, and differences between the exact conditions in which the tests were run regarding sediment properties, wave characteristics, and wave generation and absorption.

A remarkable reduction in the computational cost, which is approximately 10 times less than in previous RANS models, is attained. Additionally, the parallel version allows to run the simulations in even shorter times.

The comparisons with experimental data also show some limitations of the model. Particularly, the model tends to under-predict the strength of the undertow and to over-predict the near-bed sediment concentration in the outer surf zone. Such limitations can be related to the use of the cut-cell method for solid walls, the relatively simple turbulence model, the accuracy of empirical formulae introduced in the sediment transport model or physical processes not accounted for in the governing equations, i.e., three-dimensional effects and effect of air entrainment. The simplifications from which these limitations arise are made in exchange for a significant reduction in the computational cost. Regardless, the validations show that the model is capable of reproducing the main morphodynamic processes that control the evolution of a beach profile under the erosive conditions associated to episodic events.

Therefore, Specific Objective 2 has been attained in this chapter.

Chapter 6

Analysis of cross-shore beach morphodynamics

Contents

6.1 Introduction

In this chapter, Specific Objective 3 is addressed. It is aimed to provide new insights in morphodynamic processes and a global view of the interactions between them. As stated before, the focus is on morphodynamic processes during episodic events. To achieve this objective, the numerical model developed and validated in Chapters 4 and 5 is used to simulate the evolution of a beach profile in the erosive conditions associated to episodic events. Data extracted from this simulation and observations made in physical models and field campaigns by other authors are used to support the hypotheses proposed in this work. Specific Objective 3 is divided in three parts, 3.a, 3.b and 3.c, which correspond to different stages of the evolution of a cross-shore beach profile. Sections 6.3, 6.4 and 6.5 undertake each of these three parts. Finally, Section 6.6 compares different wave conditions to look at how the basic ideas proposed mechanisms change under different energy sources. This section is mainly focused on the concepts given in Section 6.3, since they constitute the basis supporting the ideas of Sections 6.4 and 6.5. All the wave conditions analysed are erosive.

In this chapter, the underlying physical processes leading to the generation, migration and equilibrium of a breaker bar in a beach profile are studied in conjunction. The main objective is to explain how different components of the hydrodynamics-morphology interaction produce morphodynamic processes. The analysis is based on data obtained from the newly developed numerical model presented in Chapter 4.

6.2 Methodology

6.2.1 Introduction

Some initial reflections are needed to make a rational application of the numerical approach developed in this thesis. The various processes involved in coastal hydrodynamics occur at different time scales. Firstly, there are processes with temporal scales larger than the wave period ($T > T_w$), this is the case of currents such as the undertow and the steady streaming. Secondly, processes with a time-scale similar to that of the wave period ($T \approx T_w$), known as intra-wave variations, such as the changes in flow velocity and sediment concentration along the wave phase. Finally, there are other processes with a time scale smaller than the wave period ($T < T_w$), like turbulent fluctuations produced by breaking waves. In this work, the two first time scales are addressed while the latter one is not considered, as RANS models do not resolve the turbulent fluctuations, but rather consider their effect via a turbulence closure model on the other scales. Additionally, as the numerical model used in this work is two-dimensional, processes such as rip currents, longshore variability or 3D effects of wave breaking are not accounted for. Although numerical modelling requires introducing certain simplifications of the real phenomena, RANS models do not rely on calibrations and need a reduced number of assumptions to tackle the relevant processes in surf zone hydrodynamics as compared with other standard approaches. These models solve the hydrodynamic processes (i.e., wave breaking or the generation of undertow) based on the RANS equations. They offer the right balance between relevant physical processes simulated, accuracy and required com-

putational effort. Furthermore, the particular model used in this work has been already validated against laboratory data for the evolution of the cross-shore beach profile under erosive conditions in the previous chapter. Therefore, despite a certain level of empiricism in the sediment transport equations, the results obtained with the numerical model will be assumed to be suitable for the analysis of the underlying phenomena and will contribute to complete potential efforts based on observations. In addition, data and knowledge currently available in the literature will be used to back up the numerical results and the conclusions deriving from them.

6.2.2 Case set-up

The study case is based on the experiments from (Baldock *et al.* , 2011), already modelled with IH2VOF-SED in Chapter 5 resulting in a good agreement between numerical and experimental results (Brier Skill Score 0.75). Regular wave conditions were used with wave height (H) equal to 43 cm and a wave period (T) of 3.7 s over a water depth (h) at the wave paddle equal to 2.50 m. The nominal diameter of the sediment (d_{50}) was 0.25 mm, and the slope of the initial beach profile was 1:15 approximately. The numerical domain is designed in accordance with the experimental set-up. It is 41 m long and 2.58 m high. The initial profile has a fully plain 1:15 slope, as this simplifies the analysis of the fundamental processes compared to an irregular initial profile. It starts at 5.82 m from the wave generation boundary in order to accommodate the waves to the water depth before reaching the slope. Regular waves with the same height and period as the experimental set up are generated on the left boundary, at which the water depth is 2.00 m, using Stokes II theory and active wave absorption. The sediment diameter is set to 0.25 mm consistently with the experimental value. The bulk density of the sediment is assumed to be of 2650 kg/m^3 and the sediment porosity equal to 0.40. The computational mesh consists of 146,608 cells (1078x136) with a constant spatial discretization of $\Delta x = 0.038m$ and $\Delta z = 0.019m$ in the horizontal and vertical directions, respectively. A total of 800 waves (2960 seconds) are simulated to achieve the equilibrium profile without using any morphological acceleration factor. The simulation took approximately 109 hours (4.5 days) running in a single Intel i7-7700K CPU core. The parameters of the model are set as in Chapter 5, without performing any calibration.

The non-dimensional numbers characterizing the beach profile evolution, i.e.: the Iribarren's number (Ir_0), Dean parameter (Ω), Rouse number (P) and Shields number (ϕ), are given in Table 6.1 and are calculated according to Equations 6.1 to 6.4.

$$Ir_0 = \frac{\tan\alpha}{\sqrt{\frac{H}{L_0}}} \tag{6.1}$$

$$\Omega = \frac{H}{\omega_s T} \tag{6.2}$$

$$P = \frac{\omega_s}{u'} \tag{6.3}$$

$$\phi = \frac{1}{2} f_\omega \frac{(A\omega)^2}{g\left(\frac{\rho_s}{\rho} - 1\right) d_{50}} \tag{6.4}$$

where α is the slope of the initial beach profile, H is the wave height at the numerical wave paddle, L_0 is the wave length in deep water, ω_s is the sediment fall velocity, T is the wave period, u' is the turbulent fluctuation of the velocity, f_ω is the friction factor, A is the wave stroke close to the seabed, ρ and ρ_S are the water and solid bulk densities, and ω is the angular frequency.

A schematic description of the set-up is given in Figure 6.1.

Table 6.1: Nondimensional numbers characterizing the beach profile.

Parameter	$\boldsymbol{Ir_0}$	$\boldsymbol{\Omega}$	**P**	$\boldsymbol{\phi}$
Value	0.47	3.42	3.1	0.14

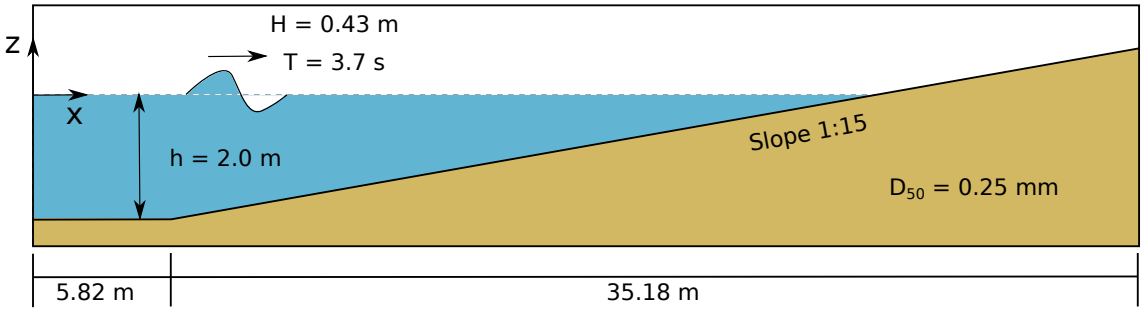

Figure 6.1: Schematic description of the numerical set-up for the analysis of beach profile evolution under erosive conditions.

According to the Iribarren's number, spilling breakers are expected for the initial configuration ($Ir_0 < 0.50$). However, as it is very close to the spilling breakers limit, the generation of the breaker bar is likely to increase the slope at the breaking point, leading to plunging breakers. Regarding the beach profile, Ω indicates an intermediate state in which a breaker bar is generated. Furthermore, the relatively large scale of this configuration along with the use of natural sand provides realistic conditions that can be expected in nature. Therefore, the configuration of the study case is considered to be adequate for the investigation of the processes leading to the generation of a breaker bar in a cross-shore beach profile.

In the coordinate system used in the following, Z refers to as the vertical distance from the still water level and X to as the horizontal distance from the numerical wave-maker, as shown in Figure 6.1. For the discussion of the results, the horizontal coordinate is normalized with the initial wave breaking point position, X_b, and the water depth at that point, h_b ($X_b = 27.01m$, $h_b = 0.745m$). The breaking point is considered as the position at which the wave height starts decreasing after shoaling. The non-dimensional horizontal coordinate (x) is obtained as:

$$\tilde{x} = \frac{X - X_b}{h_b} \tag{6.5}$$

In this case, X_b and h_b are obtained considering the breaking point position for the first 150 waves. Figure 6.2 shows the time-averaged wave height evolution along the cross-shore profile for the first 200 waves, in 50 waves intervals. The time-averaged wave height for each interval is obtained as the difference between the maximum and minimum of the phase-averaged free surface position. As can be

noted, the drop in wave height associated to wave breaking occurs at the nondimensional position $\tilde{x} = 0$. Additionally, the plunge point can be identified approximately at $\tilde{x} = 5$, where the drop in wave height stops with a small increase in wave height due to the water mass displaced by the impinging jet.

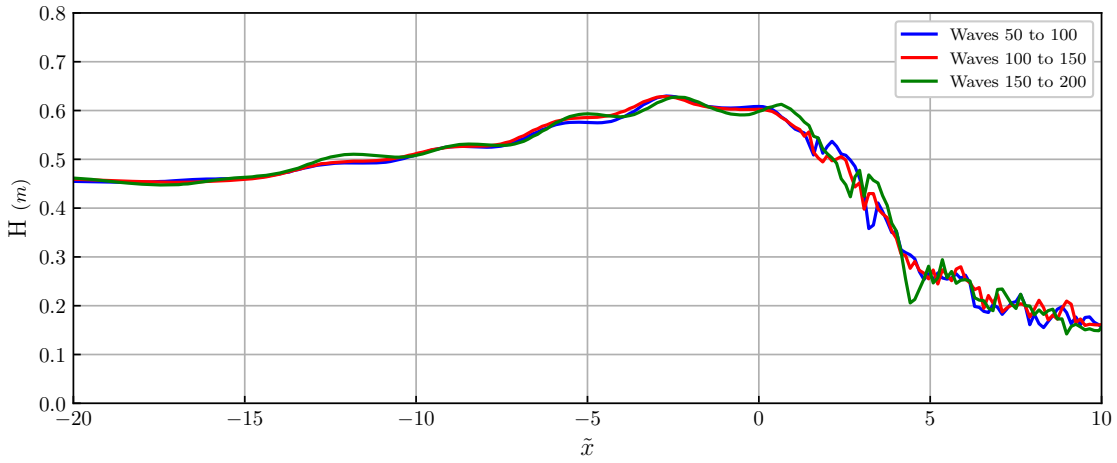

Figure 6.2: Distribution of wave height along the cross-shore profile for the first waves of the simulation. Blue line, waves 50 to 100. Red line, 100 to 150. Green line, waves 150, 200.

Note that, since this is a 2D analysis, the volumetric fluxes of sediment are given per meter of domain width ($\frac{m^3}{s \cdot m}$).

6.2.3 Identification of the stages of beach profile evolution

For this analysis, the evolution of the beach profile in an episodic event (considered as the occurrence of highly energetic conditions leading to significant changes of the cross-shore profile in relatively short periods of time) is conceptualized in three stages attending to the displacement of the breaker bar. Firstly, in the growth stage, the breaker bar increases in size while maintaining its position. Then, in the migration stage, the breaker bar starts displacing offshore while it keeps increasing its size. Finally, in the equilibrium stage the breaker bar stops displacing and maintains its size if the wave conditions do not change; this stage is only achieved if the duration of the event is large enough.

The first step in this analysis of the results is to identify the aforementioned stages for the study case. For this purpose, the seabed shapes obtained every 50 waves during the simulation are represented in Figure 6.3.

As can be noted in Figure 6.3, at the beginning of the simulation (first 200 waves) the height of the breaker bar increases nearly maintaining its position. From waves 200 to 700, the bar keeps growing, and the front of the bar starts migrating offshore. After 700 waves, the migration of the bar front stops and the breaker bar is close to its equilibrium status. Sediment is still being accumulated in the offshore face, at a reducing rate, and the height of the breaker bar crest remains constant. Notice that, even though the bar front migrates offshore, the toe of the bar (on the offshore side) does not move significantly after the first 200 waves.

To establish a qualitative criterion for the identification of the bar growth, migration and equilibrium stages in this study case, the position of the onshore face

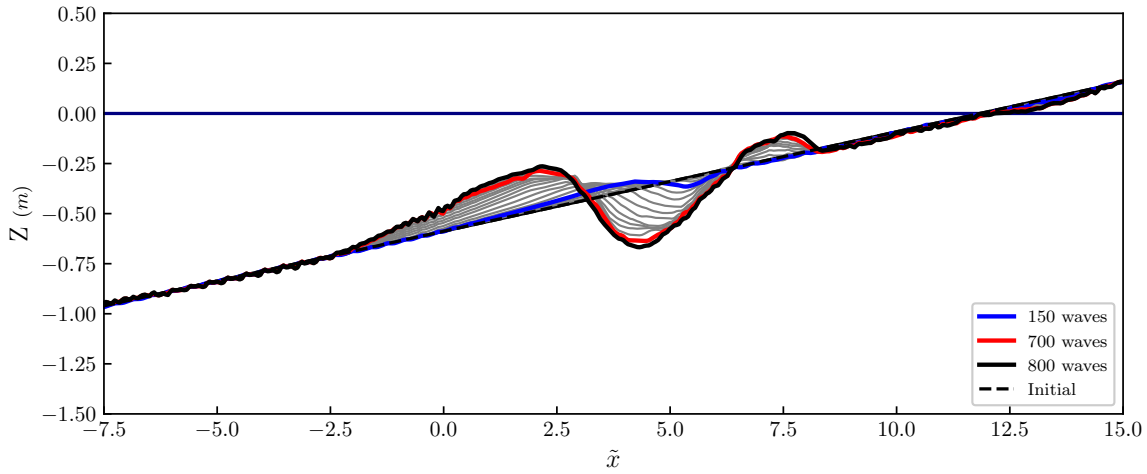

Figure 6.3: Bathymetry evolution along the simulation. Black dotted line, initial profile. Blue line, end of the growth stage. Red line, end of the migration stage. Black line, equilibrium stage. Gray lines, intermediate profiles, every 50 waves.

of the breaker bar along the simulation, considered as the intersection between the onshore-facing slope at a certain time and the initial profile, is used as a reference. Its evolution is represented in Figure 6.4.

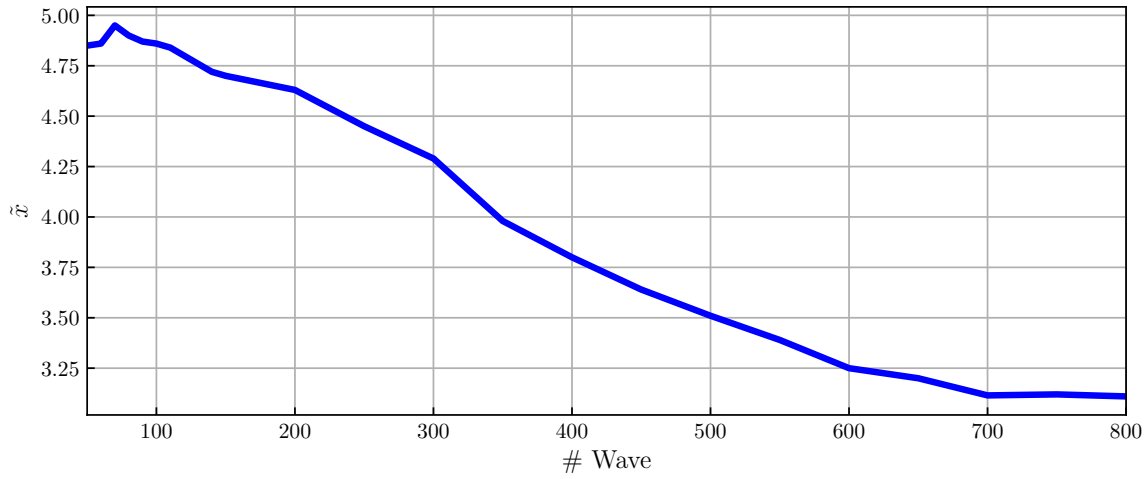

Figure 6.4: Evolution of the position of the onshore face of the breaker bar. Obtained as the intersection between the initial profile and the onshore face of the breaker bar at different time steps along the simulation.

During the first waves of the simulation, initial transient effects associated to the initiation of the hydrodynamic conditions (roughly for the first 50 waves) take place. Due to these transient effects, the position of the onshore face of the breaker bar is displaced onshore, and then, approximately after the next 50 waves, it moves back roughly to the same initial position, as can be observed in Figure 6.4. Therefore, the initial transient effects for the hydrodynamics and bathymetry are damped out after the first 100 waves, approximately. It can also be noted that the wave height does not suffer important variations from waves 50 to 100 to waves 100 to 150 (see Figure 6.2), showing that the wave conditions are stabilized. After 200 waves, the speed at which the breaker bar migrates starts to increase, indicating the initiation of the migration stage. Considering these aspects, the growth stage is identified

in the first 200 waves. The migration stage can be identified in Figure 6.4 from waves 200 to 700, and the equilibrium stage from 700 in advance. There are still some bathymetric changes in the last 100 waves of the simulation but, at the end of the equilibrium step, these variations are significantly smaller than the ones of the migration step.

In the following sections, the three stages of the beach profile evolution are analysed. For the growth stage, the accumulation or loss of sediment in the seabed that led to the bathymetric changes (differentiating the bedload and suspended contributions) is addressed first. The sediment transport processes that cause such accumulations or losses are examined next. Finally, the hydrodynamic processes involved in each of the different mechanisms are investigated. For this assessment, the wave interval 100 to 150 is considered, as the hydrodynamics and sediment transport can be considered to have reached stabilization, and it is representative of the growth stage (identified for waves 0 to 200).

Regarding the migration stage, the reasons for the displacement of the breaker bar are examined. Based on the results of the growth stage, the variations of the influencing factors in the accumulation and loss patterns dxue to bathymetry changes are examined. In this way, the two-way interaction between hydrodynamics and morphology is addressed.

Finally, for the equilibrium stage, the conditions in which it is attained are discussed based on the conclusions extracted from the growth and migration stages analyses.

6.3 Growth stage

In this section, it is aimed to determine the reasons behind the generation of the breaker bar, accomplishing Specific Objective 3.a. For this purpose, the contribution of the two sediment transport mechanisms (suspended and bedload) must be examined separately. Each transport mechanism leads to a particular pattern of accumulation and loss of sediment along the cross-shore profile. These two patterns are responsible for the bathymetric changes. The two rates of accumulation or loss of sediment for each portion of the seabed, which represent the volume of sediment that is being accumulated or lost per unit of time inside it, are calculated as the divergence of the bedload transport (Equation 6.6) and the difference between deposition and erosion rates (Equation 6.7).

$$\left(\frac{\partial Vol}{\partial t}\right)_b = \nabla \cdot (\vec{Q_{bl}}) \tag{6.6}$$

$$\left(\frac{\partial Vol}{\partial t}\right)_s = \vec{D} - \vec{E} \tag{6.7}$$

where $\left(\frac{\partial Vol}{\partial t}\right)_b$ and $\left(\frac{\partial Vol}{\partial t}\right)_s$ are the rate of accumulation or loss of sediment volume in a given portion of the seabed produced by the bedload and suspended mechanisms respectively, $\vec{Q_{bl}}$ is the bedload transport, and $\vec{E}$ and $\vec{D}$ are the erosion and deposition rates, obtained as the diffusive and advective fluxes of sediment across the seabed boundary. The total rate of accumulation $\left(\frac{\partial Vol}{\partial t}\right)_t$ is calculated by adding the two contributions. More information on how these variables are computed can

be found in (García-Maribona *et al.* , 2021). The time-averaged rate of accumulation or loss of sediment along the beach profile produced by each mechanism, obtained for waves 100 to 150, is depicted in Figure 6.5.A .

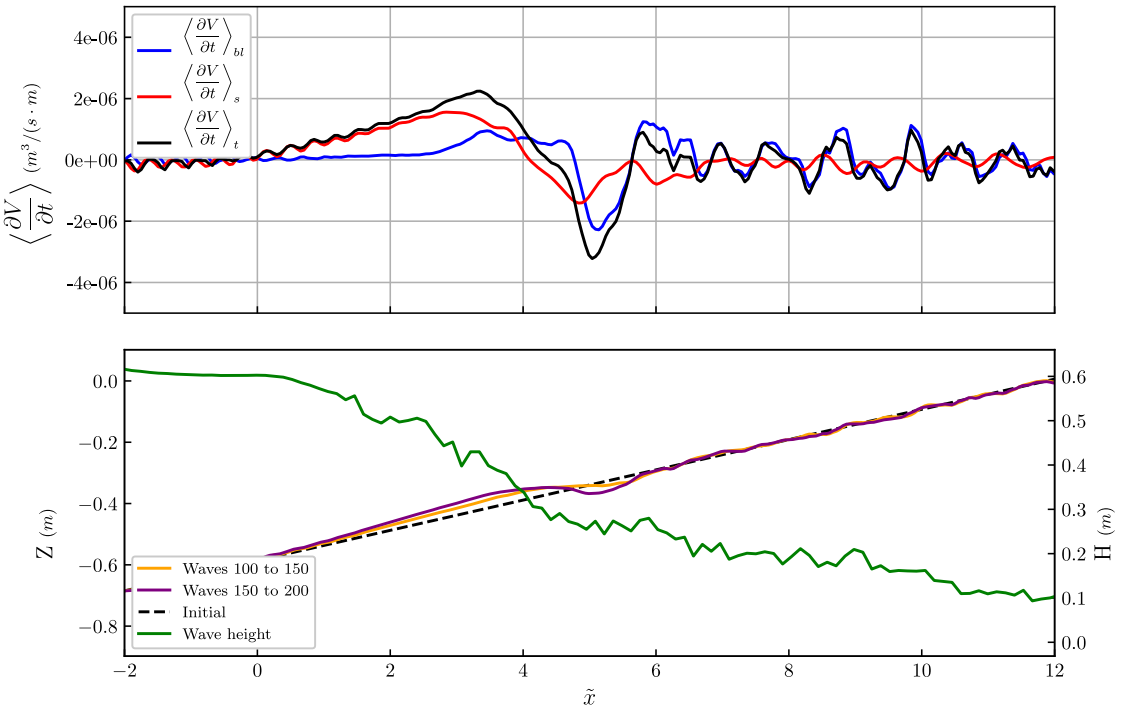

Figure 6.5: Top panel (A), time-averaged bedload and suspended accumulation rates for waves 100 to 150. Bottom panel (B), seabed position after 100 and 150 waves and time-averaged wave height from waves 150 to 200.

As can be noted, the evolution of the bathymetry in Figure 6.5.B follows the accumulation or loss rates shown in Figure 6.5.A, generating the breaker bar in the outer surf zone and a trough at the beginning of the inner surf zone, around the plunge point ($\tilde{x} = 5$). Both suspended and bedload transport tend to accumulate sediment in the outer surf zone (considered as $\tilde{x} = 0$ to $\tilde{x} = 5$), eroding sediment mainly from the inner surf zone ($\tilde{x} > 5$) and, in less amount, from the shoaling zone ($\tilde{x} < 0$). However, there are differences in the accumulation patterns of each contribution. The suspended transport tends to accumulate sediment along most of the outer surf zone ($\tilde{x} = 0$ to $\tilde{x} = 4$), while the bedload transport accumulates sediment just on the onshore side of it ($\tilde{x} = 3$ to $\tilde{x} = 4.5$). This shows that the bedload contribution is the main responsible for the generation of the crest of the breaker bar (onshore face) and the suspended contribution is more relevant for the growth of the tail of the breaker bar (offshore face).

Different approaches have been used to explain these sediment transport mechanisms. Generally, the accumulation of sediment that leads to the generation of the breaker bar is associated to the convergence of an onshore and an offshore sediment transports (Fredsoe & Deigaard, 1992), commonly related to the skewness and asymmetry of shoaling waves and to the influence of the undertow in the surf zone, respectively ((Hoefel & Elgar, 2003), (Henderson *et al.* , 2004) , (Dubarbier *et al.* , 2015)). However, the processes driving the patterns of accumulation or loss of sediment are more complicated. Understanding such processes and the factors that

can produce changes in them is fundamental in order to predict the bathymetric variations of a beach profile accurately. In the next sections, the bedload and suspended contributions are analysed separately to gain more insight in the processes that drive them.

6.3.1 Bedload transport

The main hydrodynamic magnitude driving the bedload transport mechanism is the friction velocity (U_f). Formulae such as (Meyer-Peter & Müller, 1978), (Bailard & Inman, 1981) or (Stive, 1986) estimate the bedload transport as a function of the cubed friction velocity. In the numerical model, this relation is maintained by using the empirical formulae from (Engelund & Fredsoe, 1976).

In this section, the relation between bedload transport and friction velocity is further examined to gain more insight into how the accumulation pattern produced by the bedload contribution, shown in Figure 6.5.A, is produced. Firstly, a time-averaged analysis of the cubed friction velocity and bedload transport distributions along the beach profile is performed. In this way, the influence of hydrodynamic features (currents and wave skewness) in the bedload transport distribution is reflected. Secondly, the remaining factors, related to the interaction between hydrodynamics and sediment transport, are examined in a phase-averaged analysis.

Time-averaged analysis The time-averaged friction velocity ($\langle U_f \rangle$), cubed friction velocity ($\langle U_f^3 \rangle$) and bedload transport ($\langle Q_{bl} \rangle$) along the beach profile, obtained for waves 100 to 150, are represented in Figure 6.6.

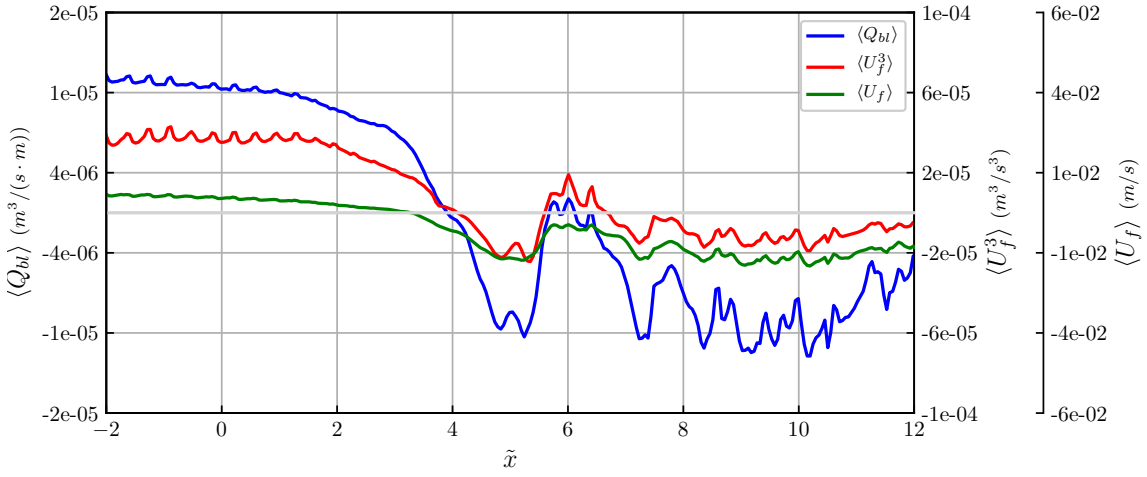

Figure 6.6: Distribution of time-averaged bedload transport, friction velocity and cubed friction velocity along the cross-shore profile. Blue line, time-averaged bedload transport. Red line, time-averaged cubed friction velocity. Green line, time-averaged friction velocity. Obtained for waves 100 to 150.

For the three variables, maxima, minima and zero-pass occur at roughly the same positions, as can be noted in Figure 6.6. The zero-pass of $\langle Q_b l \rangle$ in the outer surf zone is an important feature, at which the offshore- and onshore-directed transports converge, leading to an accumulation of sediment. The zero-pass of $\langle U_f^3 \rangle$ occurs at the onshore side of that of the friction velocity. This is due to the larger onshore-directed values as a result of the wave skewness. Additionally, some important

differences in the slope of the three variables can be noted for $2.5 < \tilde{x} < 4.5$ which, according to Equation 6.6, influence the accumulation of sediment due to bedload transport. The slope of $\langle Q_b l \rangle$ increases moderately from $\tilde{x} = 0$ to $\tilde{x} = 2.5$, where it increases sharply until $\tilde{x} = 3.5$, and then decreases again until it changes its sign at $\tilde{x} < 4.5$ approximately. These different slopes in the bedload transport result in a sediment accumulation pattern observed in Figure 6.5.A, in which the accumulation of sediment increases quickly in $2.5 < \tilde{x} < 3.5$, decreases at a slower rate in $3.5 < \tilde{x} < 4.5$ and then becomes negative (loss of sediment) for $\tilde{x} > 4.5$. Notice that $\langle U_f^3 \rangle$ has a much smoother slope between $\tilde{x} = 0$ and $\tilde{x} = 4.5$. The reasons explaining this pattern are linked to the relation between the friction velocity and bedload transport, as will be explained in the phase-averaged analysis.

Phase-averaged analysis A phase average analysis is performed to investigate how the differences between the slopes of $\langle U_f^3 \rangle$ and $\langle Q_{bl} \rangle$ in the interval $0 < \tilde{x} < 4.5$ are related to the varying relation between these magnitudes. The phase-averaged values of friction velocity ($\overline{U_f}$), bedload transport ($\overline{Q_{bl}}$) and free surface ($\overline{\eta}$), obtained for waves 100 to 150 at different positions along the outer surf zone, are shown in Figure 6.7.

As can be noted in Figure 6.7.A, the maximum onshore-directed $\overline{U_f}$, corresponding to the wave crest phase, is reduced as the waves propagate along the outer surf zone because of the wave breaking process. This can also be noted in the wave height, which also decreases along the outer surf zone. Consistently, $\overline{Q_{bl}}$ is also reduced in the wave crest phase. Regarding the wave trough, the maximum offshore directed $\overline{U_f}$ is nearly the same for $\tilde{x} = 1.5$ and $\tilde{x} = 2.5$, and it increases notably at $\tilde{x} = 3.5$. $\overline{Q_b l}$ follows this same trend during the trough phase.

In the wave crest phase, the reduction in $\overline{Q_{bl}}$ and $\overline{U_f}$ as the wave breaking progresses are proportional (linearly related). However, in the wave trough, relatively small increases in $\overline{U_f}$ lead to large variations of $\overline{Q_{bl}}$ (see Figure 6.7.B). This difference in the relation between friction velocity and bedload transport during the crest and trough phases comes from the separate treatment of the effects of friction velocity in Equation 4.36: the friction velocity influences linearly the velocity at which the moving particles are displaced (U_p) and quadratically the proportion of moving particles (P_{ef}). This aspect is discussed and supported by empirical data in (Engelund & Fredsoe, 1976). For the sediment characteristics of this study case, the relation between friction velocity and bedload transport given by this formula is depicted in Figure 6.7.B. The relation shown in Figure 6.7.B can be divided in two regimes: cubic and linear. They are defined based on the relation between friction velocity and bedload transport, which is conditioned by the critical Shields number. For small values of friction velocities that exceed the critical Shields number, the bedload transport scales roughly with the cube of the friction velocity, as it affects both the velocity at which the sediment particles move (linearly) and the proportion of moving particles (quadratically). For large values of the friction velocity, the proportion of moving particles reaches a maximum value of 1, and further increases in the friction velocity only affect the velocity at which the particles move, thus being linearly related to the bedload transport.

The maximum friction velocities corresponding to the wave crest phase shown in Figure 6.7.A are in the linear range, while the velocities of the trough are in the cubic range, as can be noted in Figure 6.7.B. As the friction velocity during the trough

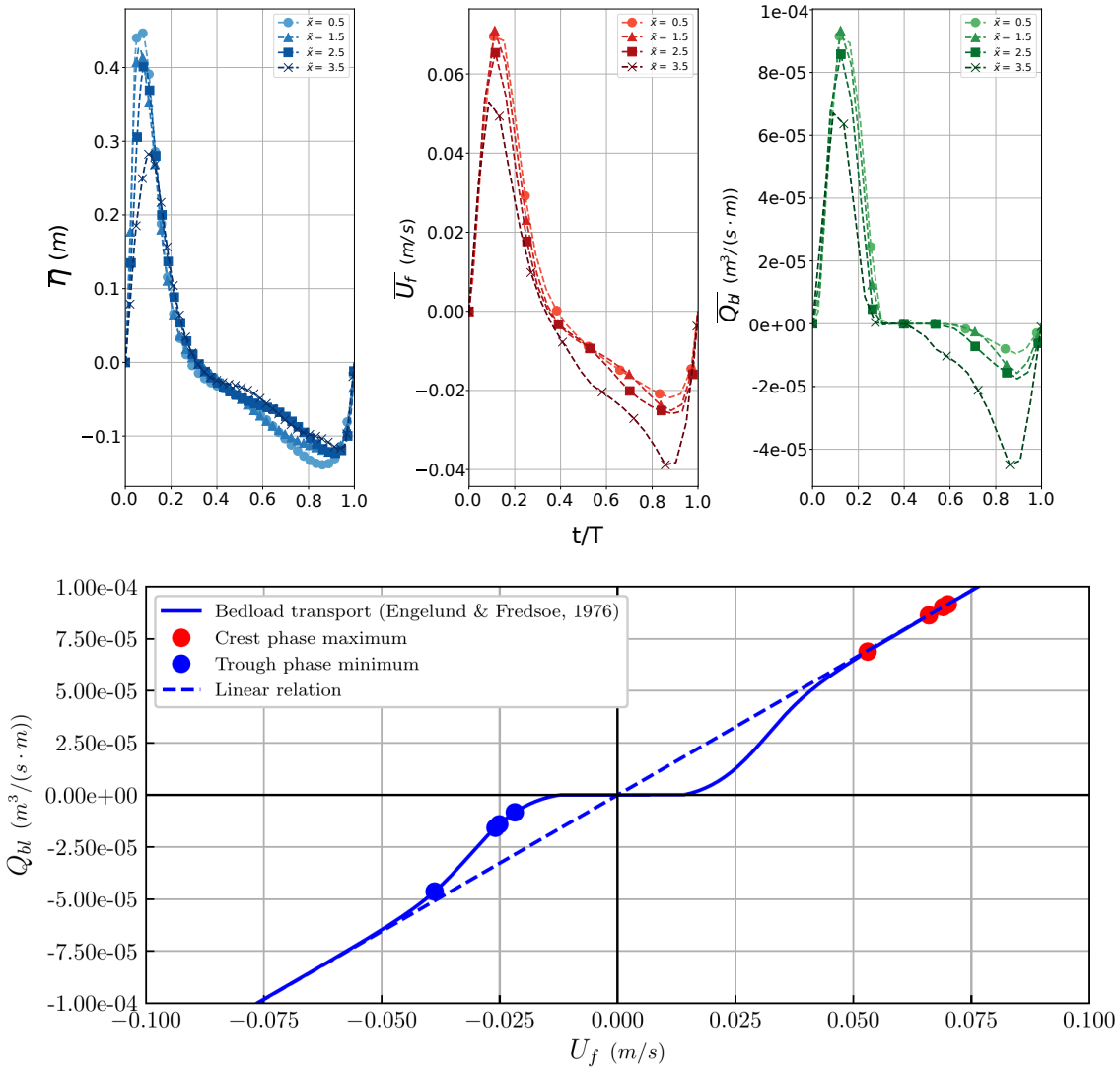

Figure 6.7: Top panel (A): phase-averaged free surface, friction velocity and bedload transport obtained at different positions along the outer surf zone. Blue lines, free surface. Red lines, friction velocity. Green lines, bedload transport. Bottom panel (B): relation between friction velocity and bedload transport. The sediment characteristics are the ones of the numerical setup. Blue line, bedload transport (Engelund & Fredsoe, 1976). Blue dashed line, linear relation between bedload transport and friction velocity. Red dots, bedload transport corresponding to the wave crest. Blue dots, corresponding to the wave trough. Obtained for waves 100 to 150.

phase does not start to increase until $\tilde{x} = 2.5$, the relation between time-averaged bedload transport and friction velocity is essentially linear for $\tilde{x} < 2.5$. Therefore, the bedload transport slope is similar to that of the time-averaged cubic friction velocity as observed in Figure 6.6 for $0 < \tilde{x} < 2.5$. When the friction velocities at the trough start to increase, the relation between time-averaged bedload transport and friction velocity is in the cubic range until $\tilde{x} = 3.5$, approximately. This explains the sharp variation in the time-averaged bedload transport shown in Figure 6.6 in the interval $2.5 < \tilde{x} < 3.5$. Once the friction velocity during the trough phase is large enough to reach the linear range as well, the slope of the bedload transport decreases again, as can be observed for $3.5 < \tilde{x} < 4.5$.

Therefore, the analysis of the bedload transport shows that the skewness of the friction velocity combined with the different relation between friction velocity and sediment transport during the crest and trough wave phases, which can vary from linear to cubic, leads to a delay in the sharp decay of $\langle Q_{bl} \rangle$ with respect to that of $\langle U_f \rangle$. Firstly, due to the skewness of the friction velocity, the point at which the onshore- and offshore-directed $\langle U_f \rangle$ meet is displaced onshore with respect to that of $\langle U_f \rangle$. Secondly, the decrease in the friction velocity associated to the wave crest, at the onset of wave breaking, has a moderate effect on the bedload transport, as the relation between them is linear. However, increasing the friction velocity of the wave trough, which occurs further onshore, has a greater effect, as the relation between friction velocity and bedload transport during the trough phase is cubic. For this reason, $\langle Q_{bl} \rangle$ decreases sharply once the friction velocity of the trough phase starts to increase significantly. These two effects lead to an accumulation pattern that produces the growth of the onshore face of the breaker bar on the onshore side of the point where $\langle U_f \rangle$ changes its direction from onshore to offshore.

6.3.2 Suspended transport

The suspended sediment transport depends fundamentally on the relation between velocity and sediment concentration. In a 2D cross-shore profile, these two variables change along the profile and water depth. To examine the overall distribution of suspended transport, $\langle U_f \rangle$, the depth- and time-averaged sediment concentration ($\langle C_{depth} \rangle$) and the depth-integrated and time-averaged suspended transport ($\langle Q_s \rangle$), obtained for waves 100 to 150, are shown in Figure 6.8.

$\langle Q_s \rangle$ can be interpreted in a similar way to $\langle Q_{bl} \rangle$: its divergence is the rate of accumulation that it produces. Its negative slope between $\tilde{x} = 0$ and $\tilde{x} = 4$ corresponds to the accumulation zone of suspended transport shown in Figure 6.5.A which is obtained from the erosion and deposition rates. Notice that it follows a different trend than $\langle U_f \rangle$ due to the variability of the velocity and sediment concentration along the water depth. Regarding the distribution of $\langle C_{depth} \rangle$ along the cross-shore profile, it can be noted that its maximum ($\tilde{x} = 3$, approximately) does not correspond to those of $\langle U_f \rangle$ or $\langle Q_s \rangle$, and that, overall, it is not directly related to the other two variables due to the variability of sediment concentration distribution along the water depth.

A detailed analysis of the processes involved in the suspended transport mechanism requires a 2DV approach to account for the variability of velocity and sediment concentration over the water depth. Thus, the suspended sediment flux field must be examined. In the following, the main features of these fields are studied in time-

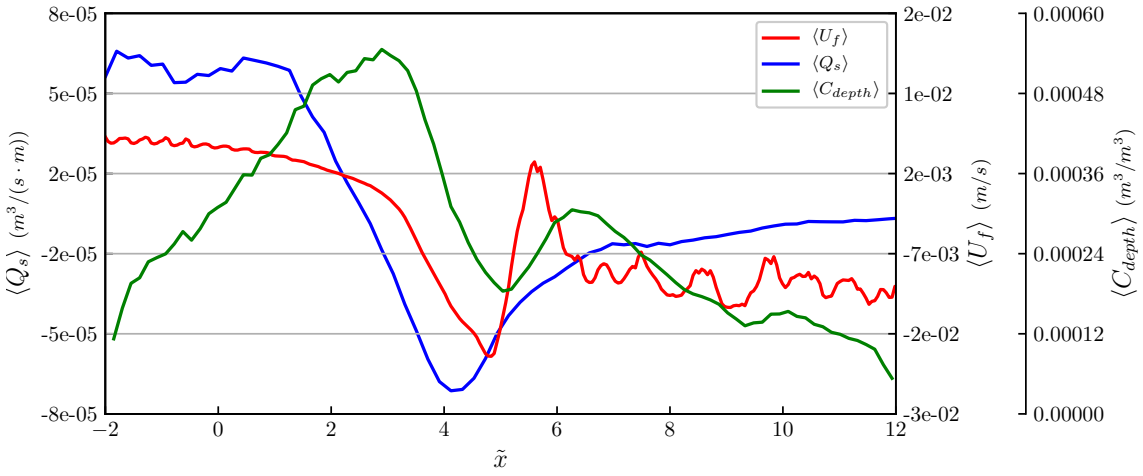

Figure 6.8: Distribution of the time-averaged suspended transport and friction velocity along the cross-shore profile. Obtained for waves 100 to 150.

averaged terms. However, the time-averaged sediment transport field ($\langle F_{sed} \rangle$) is not directly obtained as the product of the time-averaged velocity and concentration fields ($\langle U \rangle$ and $\langle C \rangle$); intra-wave effects (such as the correlation between velocity and concentration) must be also considered. The importance of these intra-wave effects is highlighted by (Aagaard & Jensen, 2013). The analysis of $\langle U \rangle$ and $\langle C \rangle$ captures processes with time scales larger than the wave period, therefore neglecting the intra-wave effects. In contrast, a phase-averaged analysis gives insight into the intra-wave variability. In the following, these two analyses are addressed separately to investigate their effects on the suspended sediment transport.

Time-averaged analysis of the velocity field Time-averaging the velocity field allows to analyse the currents present in the cross-shore profile. Figure 6.9.A shows the time-averaged velocity field ($\langle U \rangle$). Similar time-averaged velocity fields were obtained from laboratory experiments (Okayasu *et al.* , 1986) and (Tajima & Madsen, 2006)).

Two types of near-bed currents are identified in Figure 6.9.A: a steady streaming in the shoaling and outer surf zones (onshore-directed, red coloured) and an undertow in the inner surf zone (offshore-directed, blue coloured). The steady streaming is produced by two competing effects according to (Holmedal & Myrhaug, 2009). On the one hand, the progressive wave steady streaming, due to the non-zero vertical near-bed velocities, enhances onshore transport and increases when the water depth is reduced. On the other hand, the wave skewness effect on turbulent viscosity, produced by the difference in turbulent viscosity between crest and trough wave phases, enhances the offshore sediment transport and increases with wave skewness. The relative wave amplitude (a/h) also influences the magnitude of the steady streaming, with higher steady streaming being produced by larger relative wave amplitude (Kranenburg *et al.* , 2013). Then, the steady streaming is expected to be maximum along the shoaling zone, close to the break point, due to the increase in relative wave amplitude and reduced water depth, although the high wave skewness of the waves close to breaking can partially compensate these effects.

The analysis of the distribution of the steady streaming along the shoaling and outer surf zones can be performed by looking at $\langle U_f \rangle$, which is representative of

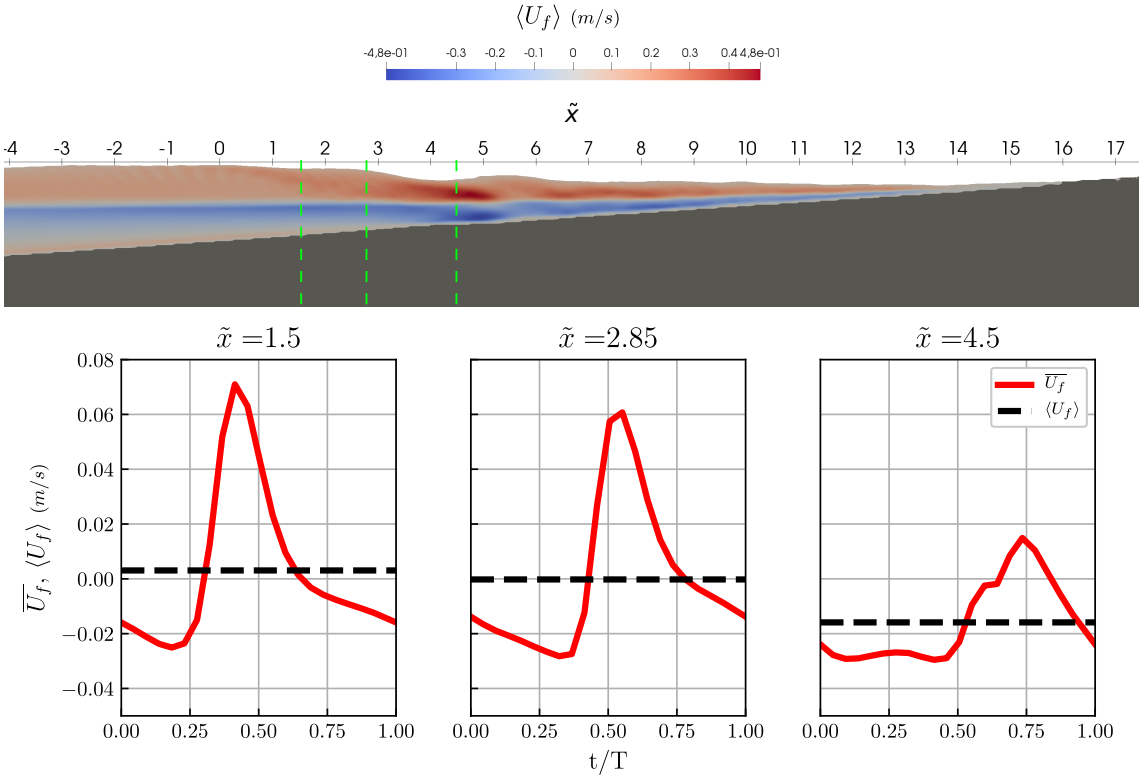

Figure 6.9: Phase- and time-averaged velocity around the undertow detachment point. Top panel (A), time-averaged velocity field. Bottom panel (B), phase-averaged friction velocity at different locations around the undertow detachment. The velocity fields are obtained for waves 100 to 120, the phase-averaged values for waves 100 to 150. Red curves: phase-averaged friction velocity. Black dashed curves: time-averaged friction velocity.

the strength of the near-bed current. As waves are highly non-linear when they approach the breaking point, the relative wave height (H/h) is used in this analysis instead of the relative wave amplitude used in previous studies. Figure 6.10 shows $\langle U_f \rangle$ and H/h along the cross-shore profile, both obtained for waves 100 to 150.

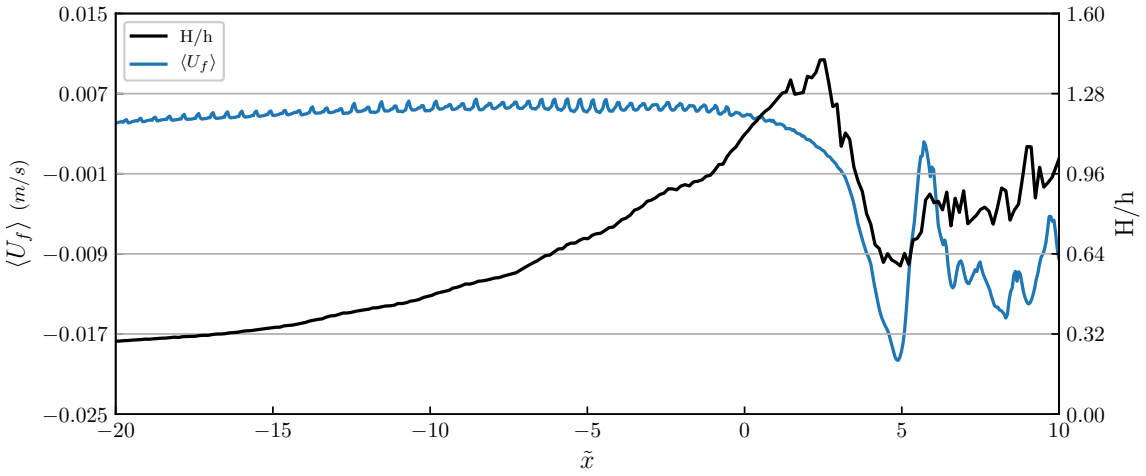

Figure 6.10: Distribution of time-averaged friction velocity along the cross-shore profile, reflecting the effect of the steady streaming. Blue line, time-averaged friction velocity obtained for waves 100 to 150. Black line, time-averaged relative wave height obtained for waves 100 to 150.

The increasing $\langle U_f \rangle$ along the shoaling zone ($\tilde{x} < 0$), reflects the enhancement of the steady streaming due to the increase in H/h. The maximum onshore-directed current occurs at $\tilde{x} = -3$ approximately. Further onshore, the undertow and increasing wave skewness partially compensate the steady streaming, and $\langle U_f \rangle$ remains nearly constant. Once the waves start to break (at $\tilde{x} = 0$), the steady streaming decreases rapidly, although H/h keeps increasing along the outer surf zone until $\tilde{x} = 3$, approximately (see Figure 6.2). This is due to the further reduction in water depth, which decreases faster than the wave height right after the wave breaking process starts, so that H/h increases despite the wave height being smaller. The increase of $\langle U_f \rangle$ along the shoaling zone explains why the accumulation zone of suspended transport starts at $\tilde{x} = 0$ (as shown in Figure 6.5.A): the increasingly strong steady streaming does not let the sediment eroded by the shoaling waves settle, but rather advects it towards the surf zone. Once the steady streaming starts decreasing, part of the sediment advected by it settles, contributing to the growth of the breaker bar. Finally, it can be noted that the time-averaged friction velocity is onshore-directed in a small portion of the surf zone, approximately at $\tilde{x} = 6$. This can be related to the plunging jet reaching the seabed, which results in high, onshore-directed friction velocities.

Regarding the second type of near-bed current identified in Figure 6.9.A, the undertow, it compensates the onshore-directed mass flow rate induced by the crests of breaking waves and steady streaming, so that the mean water flux across each section of the cross-shore profile is zero (if the mean water level already reached its equilibrium configuration). Therefore, its mass flux is determined by that induced by the breaking waves crests and the steady streaming. Also, for a given mass flux and due to mass conservation, the mean (time- and depth averaged) velocity of the undertow depends on the cross-sectional area it flows across. Additionally, for

the same mean velocity, the velocity profile might change its shape depending on the distribution of the stresses along the water depth, resulting in larger or smaller velocities close to the seabed (Svendsen, 1984).

At a certain point in the outer surf zone, these two near-bed currents (undertow and steady streaming) meet and compensate each other in time-averaged terms. This point is named undertow detachment, and it was experimentally observed by (Longuet-Higgins, 1983). As discussed by (Longuet-Higgins, 1983), the undertow detachment is an important feature for the suspended sediment transport as the convergence of the two main near-bed currents, carrying suspended sediment, may result in an accumulation of sediment at that point. It also corresponds to the zero pass of $\langle U_f \rangle$, as the friction velocity and the near-bed velocity are linearly related according to the velocity profile of a boundary layer. In this case, the undertow detachment can be identified in the distribution of $\langle U_f \rangle$, presented in Figure 6.8, at $\tilde{x} = 2.85$. An important caveat that should be considered regarding the undertow detachment is that the value of the instantaneous near-bed velocities at it can be quite high despite the time-averaged value being zero. To illustrate this feature, the phase-averaged friction velocities ($\overline{U_f}$) at the undertow detachment point and on the onshore and offshore sides of it are analysed and represented in Figure 6.9.B along with the corresponding $\langle U_f \rangle$.

Figure 6.9.B shows high values of $\overline{U_f}$ at and near the undertow detachment point. At $\tilde{x} = 1.5$ during the wave trough phase, $\overline{U_f}$ is high and offshore directed despite $\langle U_f \rangle$ being onshore-directed (the undertow is already detached from the seabed). At the undertow detachment point ($\tilde{x} = 2.85$), $\overline{U_f}$ in the wave crest and in the wave trough phases is quite large, even though $\langle U_f \rangle$ is zero. On the onshore side of the undertow detachment ($\tilde{x} = 4.5$) $\langle U_f \rangle$ is offshore-directed, while the maximum $\overline{U_f}$ is positive (onshore-directed) corresponding to the wave crest phase. These high instantaneous friction velocities generated during the crest and trough phases are quite relevant, as they put a significant amount of sediment in suspension.

To further analyse the currents in the cross-shore profile, $\langle U \rangle$ profiles at different positions are shown in Figure 6.11.

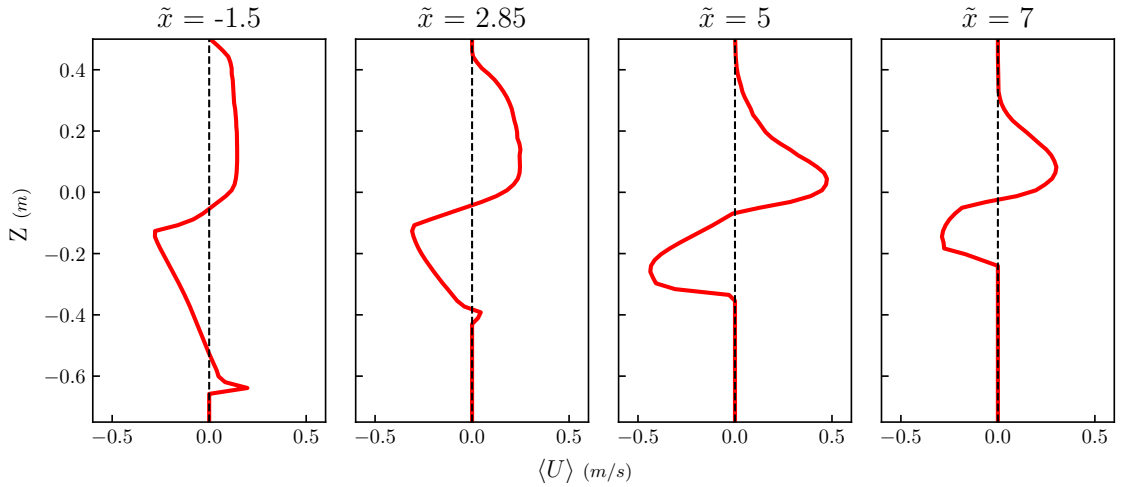

Figure 6.11: Time-averaged velocity profiles at different cross-shore positions. Obtained for waves 100 to 150.

The undertow and steady streaming can be clearly observed in Figure 6.11. On

the offshore side of the undertow detachment point, the influence of the steady streaming is stronger than the undertow near bed. This leads to onshore directed $\langle U \rangle$ close to the seabed. However, the undertow is still present far from it (detached undertow). In contrast, on the onshore side of the undertow detachment, the undertow produces offshore directed $\langle U \rangle$ close to the seabed. The balance between the onshore-directed water mass flux produced by the wave crests and steady streaming, and the offshore-directed due to the undertow can be also noted. According to this idea of compensation between onshore- and offshore-directed fluxes, the maximum mean undertow velocity occurs on the onshore side of the plunge point (at $\tilde{x} = 5.8$ in this case), as the mass flux produced by the breaking waves is also maximum at this position. In Figure 6.11, it can be noted that the undertow velocity is higher close to the plunge point at $\tilde{x} = 5$, also in the $\langle U \rangle$ field of Figure 6.9.A.

The aforementioned influencing factors on the undertow and steady streaming (mass flux produced by the wave crests, water depth, distribution of Reynold's stresses, wave height and wave skewness) can enhance or weaken them, effectively displacing the position of the undertow detachment and the zone where the sediment is accumulated. For instance, a variation of the undertow velocity profile resulting in larger near-bed velocities caused by a redistribution of the Reynold's stresses along the water depth would displace the undertow detachment seawards, and the sediment would start to accumulate at this new position. Therefore, variation of these factors, such as the ones produced by changes in the bathymetry, wave conditions, mean water level and others, modify the way in which the evolution of the beach profile occurs.

Additionally, the reasons for the location of the breaker bar inside the outer surf zone can be derived from the analysis of these influencing factors. In a plane bathymetry with a certain slope, the undertow has a maximum velocity close to the plunge point and decreases as moving offshore due to the increase in water depth (as can be observed in Figure 6.9.A and Figure 6.11). Additionally, the steady streaming has its maximum velocity at the break point and decreases quickly in the outer surf zone (see Figure 6.10). From these observations, it can be concluded that the position at which the undertow is compensated by the steady streaming (the undertow detachment point) is located between the break and plunge points (as shown in Figure 6.9). Consistently, the main accumulation of sediment leading to the growth of the breaker bar is produced at that position (Figure 6.5).

Time-averaged analysis of the concentration field To examine the distribution of the sediment concentration in the cross-shore profile, the time-averaged sediment concentration field ($\langle C \rangle$) is obtained and depicted in Figure 6.12.A. $\langle C \rangle$ profiles at different locations along the cross-shore profile are also given in Figure 6.12.B.

In the shoaling zone, the sediment concentration is present only close to the seabed, as can be noted in Figure 6.12.B at $\tilde{x} = -3$. In contrast, in the inner surf zone, the vortices generated during the wave breaking process produce a strong mixing of sediment and keep it in suspension ($\tilde{x} = 5$ and $\tilde{x} = 7$), as suggested by (Ting & Kirby, 1995). Despite the limitations of RANS models to provide detailed results of the turbulent fluctuations, the mixing effect of the vortices resulting from wave breaking in the inner surf zone is captured by the numerical model (see Chapter 5). Regardless of the strong mixing in the inner surf zone, the $\langle C \rangle$ profile is still far

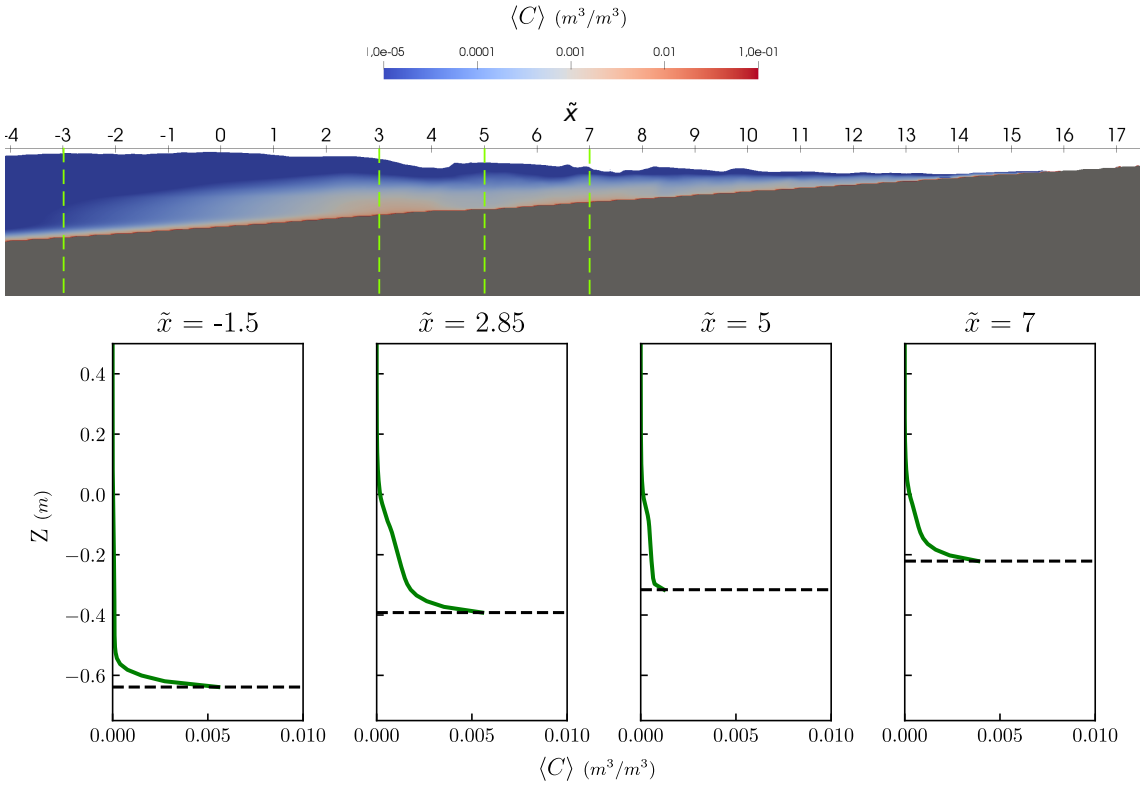

Figure 6.12: Top panel (A), time-averaged concentration field. Bottom panel (B), time-averaged concentration profiles at different positions along the cross-shore profile. The concentration field is obtained for waves 100 to 120, the time-averaged profiles for waves 100 to 150.

from uniform, being $\langle C \rangle$ much higher close to the seabed than in the upper layers. In the outer surf zone ($0 < \tilde{x} < 5$), there is also a high mixing of sediment, although the breaking-induced eddies do not affect this zone. This feature was reported in previous studies such as the experimental study performed by (Wang *et al.* , 2002), and it can be related to the strong vertical velocities generated during the breaking process. Also, in (Bagnold, 1947) it was observed that dye injected in the steady streaming was advected towards the upper layers close to the break point. This explains the influence of the type of wave breaking mechanism (spilling or plunging) in the sediment concentration distribution, observed by (Wang *et al.* , 2002) for the outer surf zone. The large amount of sediment put in suspension in the outer surf zone, close to the seabed, together with the mixing effect of the vertical velocities of the wave breaking process, results in a high $\langle C \rangle$ along the water column in the outer surf zone, as can be noted in Figure 6.12.B at $\tilde{x} = 3$.

Therefore, the distribution of $\langle C \rangle$ is a consequence of the different mixing mechanisms acting in each part of the cross-shore profile. In the shoaling zone, the weak diffusive mixing due to near-bed turbulence, which decreases as moving far from the seabed, is not enough to overcome the sediment fall velocity, and the sediment stays in a thin layer close to the seabed. In the outer surf zone, the vertical velocities produced by the breaking process lift sediment from the lower layers to the upper ones. Finally, in the inner surf zone, a strong mixing is produced by the wave breaking induced vortices leading to a more uniform concentration distribution in the water column. These differences in $\langle C \rangle$ distribution on the water column for breaking and non-breaking waves (corresponding to the shoaling and inner surf zones, respectively) are in agreement with previous laboratory studies (e.g., (Nielsen *et al.* , 1978)) and with field data (e.g., (Ogston & Sternberg, 2002)). The distribution of $\langle C \rangle$ along the water column has important implications in the suspended sediment transport, as will be discussed in the analysis of time-averaged sediment fluxes. Depending on the shape of the $\langle C \rangle$ profiles, more or less sediment concentration is subjected to the effect of the currents described in the analysis of $\langle U \rangle$.

Intra-wave analysis of the velocity and concentration fields The key aspect regarding intra-wave variability is the correlation between velocity and concentration. Highly correlated velocity and concentration results in a large suspended transport, as the peak values of velocity and concentration occur at the same time. To analyse this aspect, the phase-averaged free-surface ($\overline{\eta}$), friction velocity ($\overline{U_f}$) and sediment concentration ($\overline{C}$) for different points close to the seabed (5 cm form it) and at half depth, obtained for waves 100 to 150, are shown in Figure 6.13. Similar results were obtained in previous studies carried out in the field (e.g., (Aagaard & Jensen, 2013)).

Figure 6.13 shows that $\overline{\eta}$ and $\overline{U_f}$ are highly correlated along the shoaling and outer surf zones ($\tilde{x} < 0$ and $0 < \tilde{x} < 5$, respectively) and their high correlation still holds at the plunge point ($\tilde{x} = 5$) during the crest-phase. In the outer surf zone, $\overline{C}$ close to the seabed (continuous green line) is correlated with $\overline{\eta}$ and $\overline{U_f}$, while it is uncorrelated or even negatively correlated for half-depth (dashed green line). At half-depth, for $\tilde{x} < 3$, $\overline{C}$ is negatively correlated to $\overline{\eta}$ and $\overline{U_f}$ (high concentrations occur at the wave trough instead of wave crest phase). This implies that $\langle F_{sed} \rangle$ is offshore directed in the upper layers of the outer surf zone while it is onshore directed in the lower ones. As will be shown in the next section, this has important

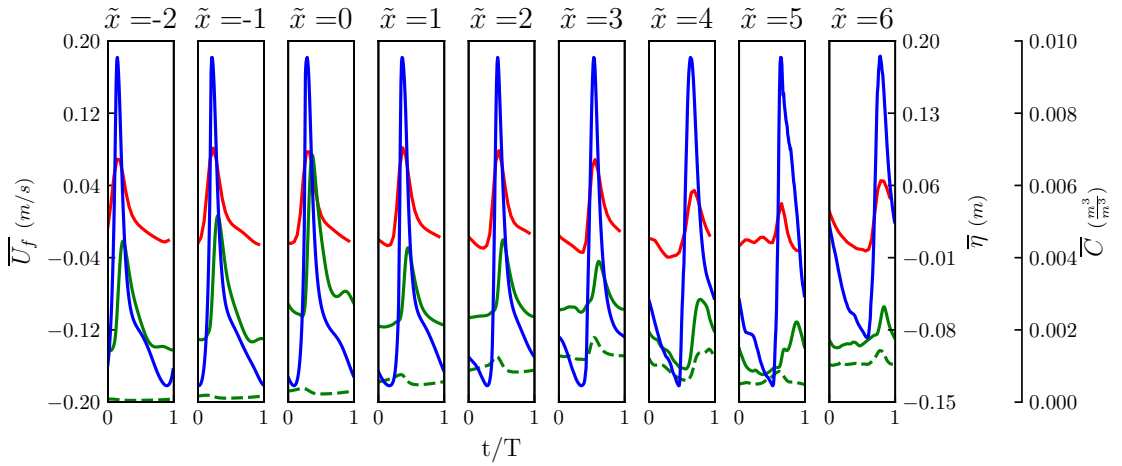

Figure 6.13: Phase-averaged concentration, free-surface and friction velocity. Green line, near-bed concentration (continuous line) and half-depth concentration (dashed line). Blue line, free surface. Red line, friction velocity. Obtained for waves 100 to 150, the near-bed concentrations are obtained at 5 cm from the seabed.

implications on the circulation of suspended sediment in the outer surf zone.

Considering the relation between the mean of a product of two variables and the product of the means of the variables

$$\langle AB \rangle = \langle A \rangle \langle B \rangle + cov\big(A, B\big) \tag{6.8}$$

Likewise, the intra-wave effects in $\langle F_{sed} \rangle$ can be represented by the covariance of the instantaneous velocity and concentration ($cov\big(U, C\big)$). This offers a more quantitative description of the intra-wave effects, accounting for the variance of velocity and concentration as well as for the correlation between them. The vertical profiles of $cov\big(U, C\big)$ are given in Figure 6.14.

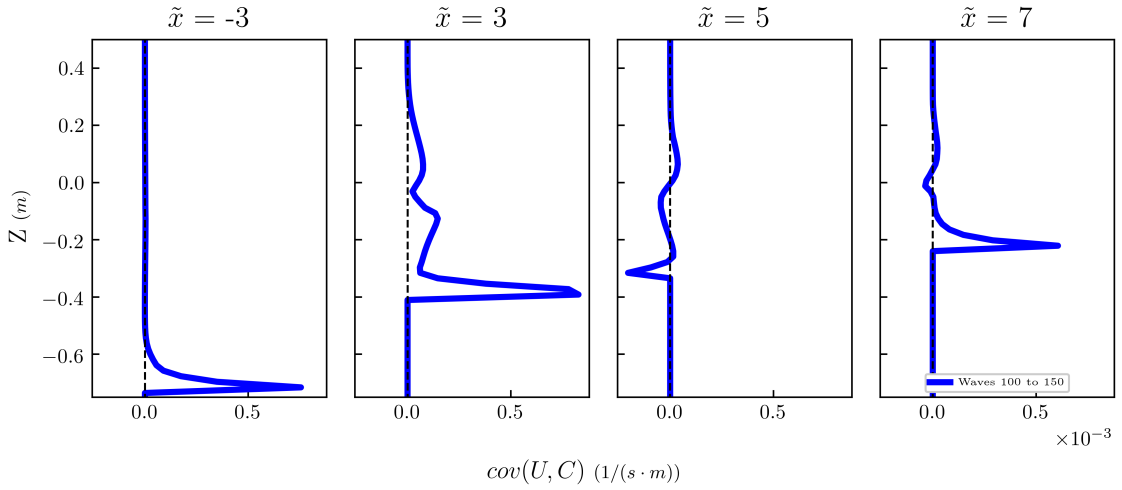

Figure 6.14: Vertical profiles of the covariance between horizontal velocity and sediment concentration at different positions along the beach profile. Obtained for waves 100 to 150.

In Figure 6.14, it can be noted that the intra-wave effects are of great importance

in the shoaling and outer surf zones close to the seabed, as stated in the analysis of phase-averaged magnitudes. However, far from the seabed, the intra-wave effects are much smaller due to the small $cov(U, C)$. Therefore, the sediment fluxes at such positions can be expected to be almost completely driven by the aforementioned system of currents (undertow and steady streaming). Note that the intra-wave effects are onshore-directed except for the plunge point position ($\tilde{x} = 5$).

Considering the previously described $\langle U \rangle$ and $\langle C \rangle$ fields, some important aspects concerning the numerical modelling of sediment transport for beach morphodynamics can be extracted. In the shoaling zone, the suspended sediment concentration far from the seabed is very low due to the absence of strong mixing processes. Thus, assuming the suspended transport to be fully contained in a thin layer close to the seabed in which it has a constant value (behaving like a one-dimensional feature) is not too far from reality. Additionally, the velocity and concentration are highly correlated close to the seabed, so assuming that they are perfectly correlated does not introduce great errors in the results. For these two reasons, the suspended transport in the shoaling zone behaves similarly to the bedload transport, and some of the 1D numerical models using averaged transport rates can predict the evolution of the shoaling zone with suitable accuracy by introducing calibration factors, even if they do not have a separated treatment of the bedload and suspended contributions. However, in the surf zone these two simplifications (assume 1D and perfectly correlated velocity and concentration) are no longer valid, which explains the limited skill that these models present in the predictions of surf zone morphodynamics (e.g. (Kalligeris *et al.* , 2020), (Ruffini *et al.* , 2020)).

Time-averaged analysis of suspended sediment flux To investigate how the suspended sediment circulates in the cross-shore profile as a result of the velocity and concentration distributions and intra-wave effects, the $\langle F_{sed} \rangle$ field is obtained by first calculating its instantaneous value (as the product of instantaneous velocity and concentration fields) and then, performing the time-averaging of the result. The horizontal component of the total $\langle F_{sed} \rangle$ ($\langle F_{sed} \rangle_t$) and that produced only by currents ($\langle F_{sed} \rangle_c$) are presented in Figure 6.15.

In the shoaling zone ($\tilde{x} < 0$), close to the break point, there is a strong, near-bed, onshore-directed $\langle F_{sed} \rangle_t$ ($0.002 \frac{m^3}{m^3 \cdot s}$ approximately at $\tilde{x} = -3$). This is consistent with the combination of the steady streaming and high near-bed concentrations (shown in Figure 6.9 and Figure 6.12, respectively), and with the highly correlated concentration and velocity fields (shown in Figure 6.13). As moving offshore, $\langle F_{sed} \rangle_t$ decreases due to the smaller wave height and near-bed concentrations (see $\tilde{x} = -4$ in Figure 6.15.B).

Another interesting aspect is that, comparing the value of total sediment flux compared to that induced by in wave effects (see Figure 6.14), intra-wave effects are responsible for nearly 40% of the total near-bed sediment flux in the shoaling zone, being the rest due to the steady streaming.

For the outer surf zone ($0 < \tilde{x} < 5$), the near-bed current advecting the sediment depends on whether the undertow is attached (therefore it is advected offshore) or detached (advected onshore by the steady streaming). These two near-bed suspended transports meet at the undertow detachment producing an accumulation of sediment in accordance with what was suggested by (Longuet-Higgins, 1983). However, the high correlation between velocity and concentration close to the seabed

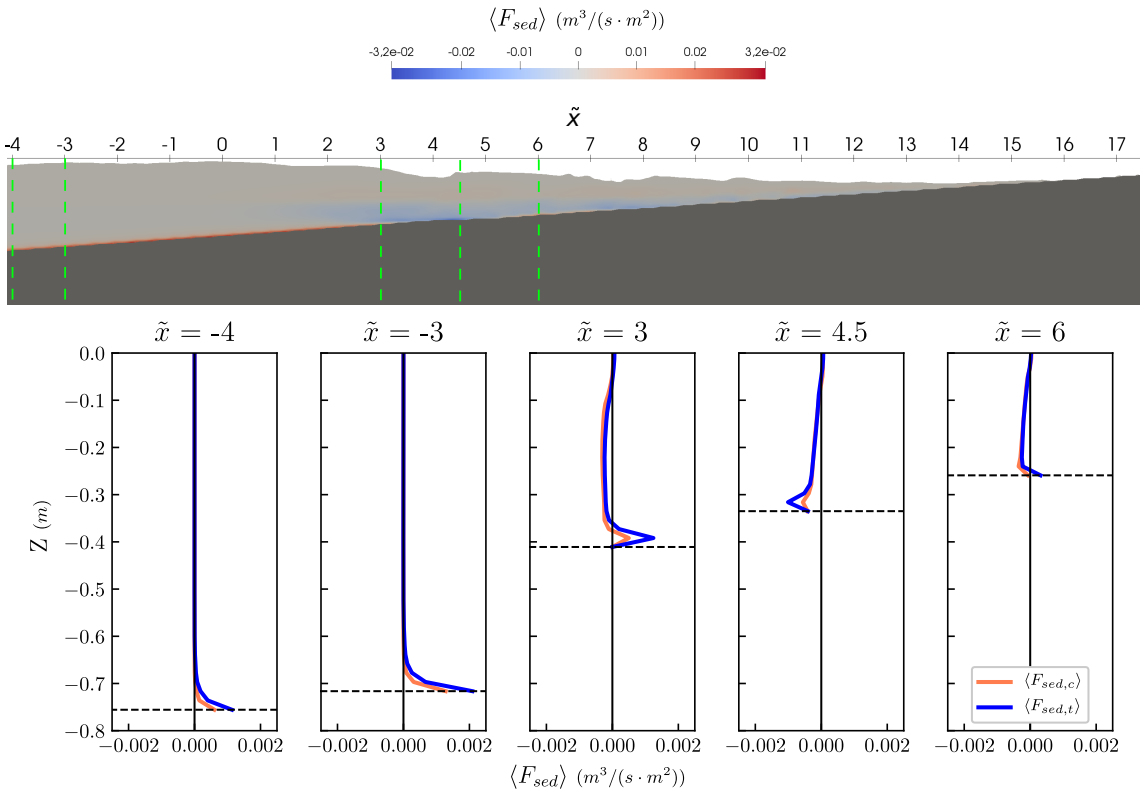

Figure 6.15: Top panel (A): Time-averaged horizontal sediment flux field. Bottom panel (B): time-averaged horizontal sediment flux profiles at different positions. Blue line, total sediment flux. Orange line, sediment flux due to currents. The sediment flux field is obtained for waves 100 to 120, the time-averaged profiles for waves 100 to 150.

favours the onshore transport produced by the steady streaming (as shown in Figure 6.14), pushing this point to the onshore side of the undertow detachment (at $\tilde{x} = 3$ there is still onshore-directed transport close to the seabed). Additionally, along the outer surf zone, the sediment concentration far from the seabed is advected offshore by the detached undertow, towards the shoaling zone. The existence of a significant offshore-directed sediment flux far from the seabed at the break point was also observed in the laboratory, especially under plunging breakers (e.g., (Wang *et al.* , 2002) and (Wang *et al.* , 2003)). This sediment flux increases with larger sediment concentration in the upper layers of the outer surf zone (more uniform concentration profiles) and with higher velocity of the detached undertow. This sediment flux increases the extent of the suspended transport accumulation zone to the offshore side of the undertow detachment point, therefore contributing to the growth of the offshore face of the breaker bar.

In the inner surf zone, there is an offshore-directed sediment flux close to the seabed for $5 < \tilde{x} < 7.5$ approximately, which can be observed in the $\langle F_{sed} \rangle_t$ profile at $\tilde{x} = 6$. $\langle U \rangle$ is only positive in a small portion of this area, as can be noted in the distribution of $\langle U_f \rangle$ depicted in Figure 6.10. The intra-wave effects are responsible for this difference: the sediment concentration and velocity close to the seabed are highly correlated during the wave crest-phase, but not during the wave trough phase for this zone (as shown in Figure 6.13). Thus, the onshore-directed velocities carry more sediment than the offshore-directed ones resulting in a net onshore-directed transport on a larger area than that affected by onshore-directed $\langle U \rangle$. For the rest of the inner surf zone ($\tilde{x} > 7.5$), there is an high near-bed, offshore-directed transport due to the presence of the undertow and a low onshore-directed transport in the upper layer produced by the crests of broken waves. The offshore-directed $\langle F_{sed} \rangle_t$ is relatively small ($-0.001 \frac{m^3}{m^2 \cdot s}$, approximately) compared to the onshore-directed one obseved in the shoaling zone close to the breaking point, as $\langle C \rangle$ is smaller and less correlated to the velocity during the wave trough phase (see Figure 6.13).

Finally, regarding the difference between $\langle F_{sed} \rangle_t$ and $\langle F_{sed} \rangle_c$, it can be noted that intra-wave effects are more significant close to the seabed, where the correlation between sediment concentration and velocity is higher. Note that in the shoaling zone ($\tilde{x} < 0$), the contribution of intra-wave effects is almost as much as that of the currents. Consistently with the previous discussion, at $\tilde{x} = 6$ the intra-wave effects change the direction of $\langle F_{sed} \rangle_t$ from offshore- to onshore-directed.

Considering the $\langle F_{sed} \rangle$ field, shown in Figure 6.15.A, the circulation of sediment in the outer surf zone can be summarized as follows. The high friction velocity produced by breaking waves puts sediment in suspension, which is lifted by the strong vertical velocity occurring during the wave breaking process to the upper layers of the outer surf zone. Then, the detached undertow advects this sediment towards the shoaling zone. Once this sediment settles by gravity, it can be either captured by the steady streaming (for sediment falling on the offshore side of the breaking point) and advected back to the outer surf zone, or it can directly settle in the outer surf zone. In both cases, the sediment transport produced by the detached undertow contributes to the accumulation of sediment along the offshore face of the breaker bar, as observed in Figure 6.5.A.

6.4 Migration stage

In this section, the migration stage of the beach profile evolution is addressed, undertaking Specific Objective 3.b. The previously extracted conclusions on the processes driving the growth of the breaker bar are the starting point of this analysis. These are summarized in the following.

Firstly, a cause-effect relation between the position of the undertow detachment and those at which the bedload and suspended contributions trend to accumulate sediment has been established. As discussed, the suspended contribution mainly accumulates sediment on the offshore side of it due to the offshore-directed sediment flux produced by the undertow detachment. In contrast, the bedload contribution accumulates sediment on its onshore side, due to the effect of wave skewness and the changing relation between friction velocity and the resulting bedload transport.

Secondly, the drivers that determine the position of the undertow detachment were discussed. It occurs where steady streaming and undertow compensate each other near-bed, in time-averaged terms. Thus, the relative strength of these two currents close to the seabed determines the position of the undertow detachment.

Thirdly, the suspended transport circulates in the surf zone following a pattern in which the sediment is initially eroded by the shoaling waves and carried onshore by the steady streaming. Afterwards, it is lifted by the vertical velocities induced by the wave breaking process. Then, the sediment is advected offshore by the detached undertow towards the shoaling zone. Finally, it settles due to gravity and falls back into the steady streaming, closing the loop. Part of the sediment carried onshore by the steady streaming settles between the breaking and undertow detachment points, leading to the growth of the breaker bar, as the steady streaming weakens between them.

According to the identification of the beach profile evolution stages, performed in Section 6.2.3, the migration stage analysis considers the time interval from 200 to 700 waves. Attending to the bathymetric evolution, the breaker bar displaces offshore as the migration stage advances. This can be observed in the evolution of the beach profile shown in Figure 6.16

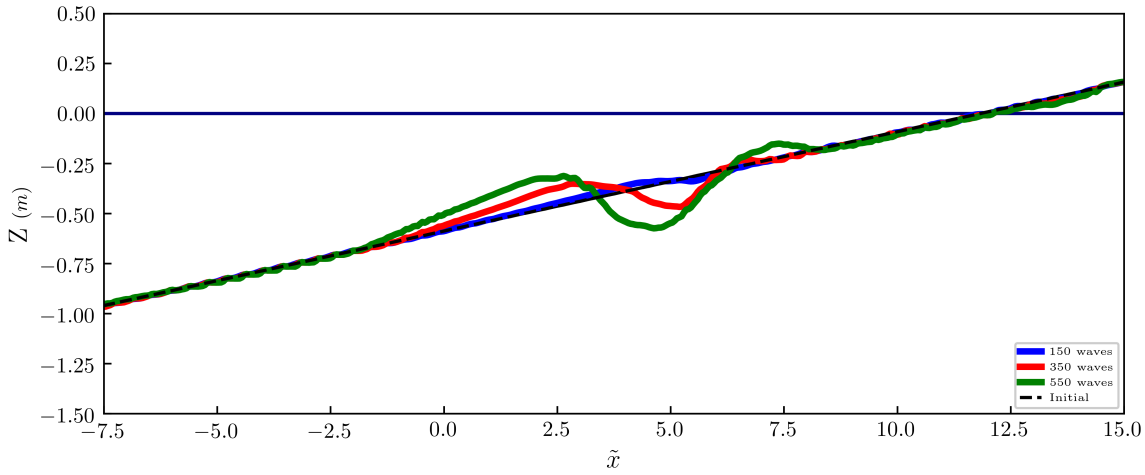

Figure 6.16: Bathymetric evolution along the migration stage obtained at different instants. Blue line, after 150 waves. Red line, after 350 waves. Green line, after 550 waves.

As can be noted in Figure 6.16, the breaker bar keeps growing during the migration stage, and its onshore face displaces offshore as the simulation advances increasing its slope. The bar trough also increases its depth and size. Regarding the offshore face, it does not migrate significantly after the first 350 waves, and its slope increases. Consequently, the length of the breaker bar is reduced and its height increases as it migrates offshore.

The reasons for the migration of the breaker bar can be analysed by looking at how the sediment transport rates change respect to the growth stage. The transport rates for the migration stage are shown in Figure 6.17. As previously indicated, this accumulation rate represents the volume of sediment that is gained or loss in each segment of the seabed per unit of time.

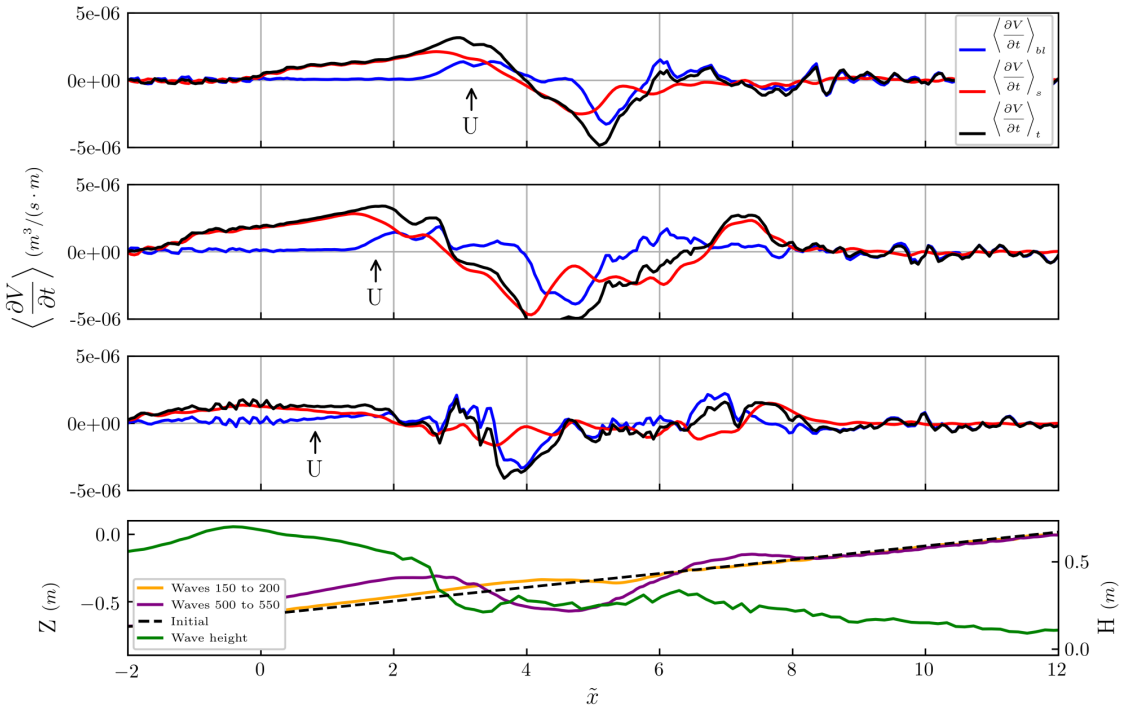

Figure 6.17: Contributions from the bedload and suspended transport mechanisms to the bathymetric evolution. Top panel, waves 100 to 150. Centre-top panel, waves 300 to 350. Centre-bottom panel, waves 500 to 550. Bottom panel, seabed positions and wave height during the migration stage. Black arrows represent the position of the undertow detachment point

As shown in Figure 6.17, both bedload and suspended transport accumulation zones are displaced offshore, leading to the migration of the breaker bar. The amount of sediment being eroded from the inner surf zone and deposited in the outer surf zone increases at the beginning of the migration stage, and then decreases as approaching the equilibrium stage.

Also, the position of the undertow detachment is related to those of the accumulation zones produced by each transport mechanism (positive $\left\langle \frac{\partial V ol}{\partial t} \right\rangle_t$). As can be noted in Figure 6.17, the relation between the position of the undertow detachment and those accumulation zones holds along the migration and equilibrium stages.

The main reason behind the modification of the sediment accumulation patterns (and the consequent migration of the breaker bar) is the displacement of the un-

dertow detachment, based on the cause-effect relationship discussed in Section 6.3. Furthermore, modifications in other hydrodynamic drivers which influence the relation between the undertow detachment position and the accumulation zones, such as the sediment flux produced by the detached undertow, can have additional effects in the resulting accumulation patterns.

In the following, it is intended to examine the reasons for the displacement of the undertow detachment under constant environmental conditions, as it is the main responsible for the offshore displacement of the accumulation zones that brings about the offshore migration of the breaker bar. Note that varying the environmental conditions (i.e., wave height, period, mean sea level) can also produce a displacement of the undertow detachment point and consequent migration of the breaker bar. In addition, the effect of the sediment flux produced by the detached undertow, reported in (Wang *et al.* , 2002), is analysed. As will be explained, this sediment flux has a great significance in achieving a dynamic equilibrium of sediment fluxes resulting in the stabilization of the breaker bar at the end of the migration stage.

6.4.1 Bedload transport

As discussed in Section 6.3.1, the bedload transport accumulation zone, in which $\left\langle \frac{\partial Vol}{\partial t} \right\rangle_b > 0$, is on the onshore side of the undertow detachment point. This situation remains the same as the undertow detachment migrates offshore, as shown in Figure 6.17: the bedload transport accumulation zone follows its displacement until, after 550 waves, the position of the undertow detachment point remains nearly constant and so does that of the bedload transport accumulation zone.

The relation between bedload transport accumulation zone and undertow detachment position has been addressed in Section 6.3. Essentially, the onshore- and offshore-directed near-bed currents converge at the undertow detachment point, and the bedload transports produced by such currents converge on the onshore side of it. The distance between the convergence of bedload transports and undertow detachment point depends on the wave skewness and sediment characteristics. Consistently, as the undertow detachment point displaces offshore, so does the accumulation of sediment caused by the bedload mechanism.

The variation of the near-bed currents, which leads to the offshore migration of the undertow detachment point, can be observed by looking at the distribution of $\langle U_f \rangle$ along the beach profile shown in Figure 6.18.

As can be observed in Figure 6.18, the $\langle U_f \rangle$ distribution is displaced offshore due to the changes in the main currents of the surf zone (steady streaming and undertow), caused by the bathymetric evolution . As the simulation advances, the undertow is enhanced close to the seabed resulting in a high, offshore-directed $\langle U_f \rangle$ in the outer surf zone. At the end of the migration stage, $\langle U_f \rangle$ is reduced again. In the shoaling and and inner surf zones, $\langle U_f \rangle$ does not undergo important modifications.

One of the features that can be noted in Figure 6.18 is that the positive $\langle U_f \rangle$ at $\tilde{x} = 5$ associated to the impact of the plunging jet, discussed in Section 6.3, reaches a constant value after 300 waves. This can be explained by the deepening of the trough, which results in a higher dampening of the plunging jet before reaching the seabed, as will be discussed. Also, in Figure 6.18, the undertow is enhanced at the position of the breaker bar trough (at $\tilde{x} = 4$, approximately) from waves 100-150 to waves 300-350. It seems counter-intuitive that the undertow becomes stronger

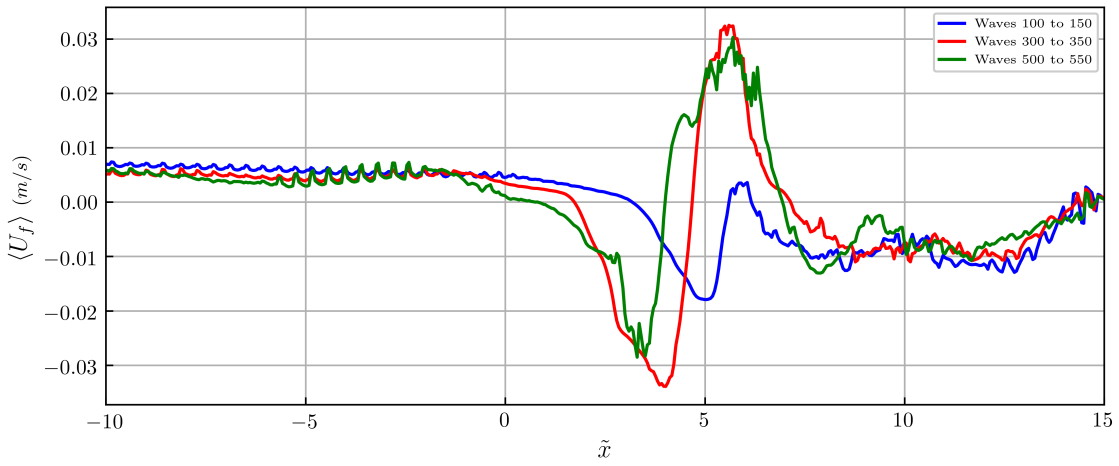

Figure 6.18: Time-averaged friction velocity obtained for different intervals in the migration stage. Blue line, waves 100 to 150. Red line, waves 300 to 350. Green line, waves 500 to 550.

as the bar trough deepens, as there is more cross-sectional area across which the mass flux, which must equilibrate that produced by the wave crests, can exit the surf zone (Svendsen, 1984). To further analyse the reasons behind this change in the strength of the undertow current, and the consequent offshore migration of the undertow detachment, the main currents present in the outer surf zone must be examined. For this purpose, $\langle U \rangle$ profiles are shown in Figure 6.19.

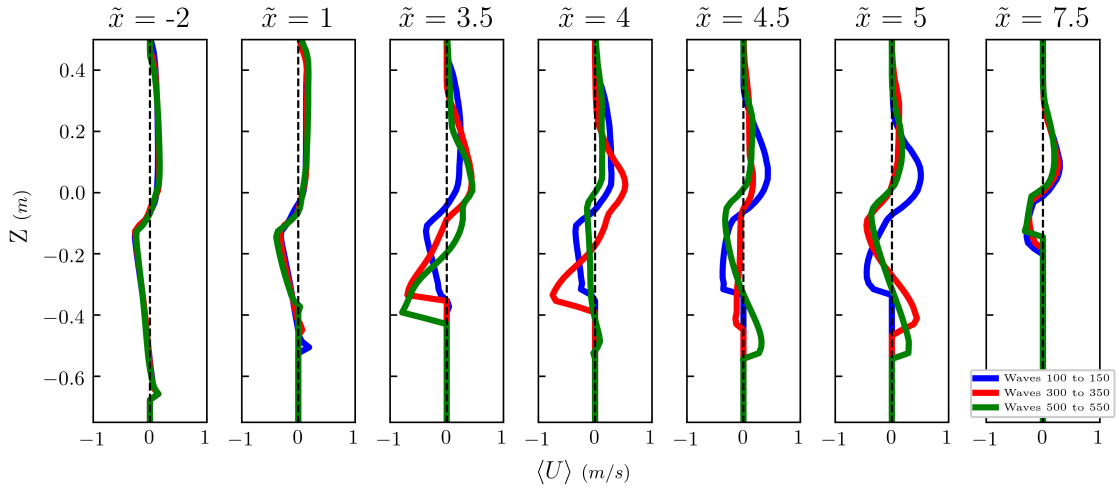

Figure 6.19: Time-averaged velocity profiles obtained for different intervals along the migration stage. Blue line, waves 100 to 150. Red line, 300 to 350. Green line, waves 500 to 550.

Figure 6.19 shows that $\langle U \rangle$ profiles in the shoaling, inner and part of the surf zones do not undergo great variations. In contrast, important transformations of the $\langle U \rangle$ profiles can be noted in the trough region (see $3.5 < \tilde{x} < 5$ in Figures 6.16 and 6.19). The steady streaming remains nearly constant in the shoaling zone, and its velocity decreases in the outer surf zone (see $\tilde{x} = -2$ and $\tilde{x} = 1$). In contrast, the undertow is significantly modified by the deepening of the trough (for instance, at

$\tilde{x} = 3.5$), leading to higher near-bed, offshore-directed $\langle U \rangle$ and contributing to the seaward displacement of the undertow detachment point. At $\tilde{x} = 4$, the $\langle U \rangle$ profile at the end of the migration stage is almost uniform, evidencing a high momentum mixing inside the trough. Similarly, for waves 300 to 350 the $\langle U \rangle$ profile inside the trough ($\tilde{x} = 5$) is more uniform. In contrast, this effect is not observed for waves 100 to 150 as the trough is not developed yet. At $\tilde{x} = 5$ after 300 waves, the near-bed $\langle U \rangle$ is onshore directed. This is caused by the effect of the plunging jet as state before.

Overall, during the migration stage, the $\langle U \rangle$ profile close to the plunge point becomes more uniform as the bar trough develops, and the near-bed $\langle U \rangle$ increases moving from the bar trough towards the shoaling zone, leading to the offshore displacement of the undertow detachment point.

The remaining question is how do the appearance of the trough produces such variations in the velocity profiles. Considering the horizontal momentum balance for a fluid element in the surf zone at a certain depth, the undertow velocity profile must acquire a shape so that the resulting time-averaged turbulent stresses compensate the horizontal gradients of horizontal momentum advection and pressure at each position along the water column. Note that the time-averaged turbulent stresses in the fluid are not fully determined by the time-averaged velocity profile, other factors like the time-averaged turbulent viscosity profile, coherent structures and intra-wave effects (velocity - turbulent viscosity covariance) can affect it. Also, the usual depth-averaging approach for surf zone hydrodynamics (e.g., (Svendsen, 1984)) is not suitable for this analysis, since the vertical distribution of variables involved is fundamental. Determining the effects that the development of the breaker bar and trough has in the redistribution of Reynolds stresses, which lead to the modification of the undertow profile in the aforementioned way, is left for future research. Studies in detailed hydrodynamic aspects of wave breaking (i.e., (Watanabe *et al.* , 2005), (Ting & Nelson, 2011)) and recent advancements in our ability to simulate them ((Larsen & Fuhrman, 2018), (Larsen *et al.* , 2020))) are useful for determining the exact mechanisms behind the redistribution of shear stresses along the water column which, as previously discussed in this work, is the cause of breaker bar migration under constant environmental conditions.

6.4.2 Suspended transport

As commented in Section 6.3.2, the accumulation of sediment due to the suspended transport contribution, areas with $\left\langle \frac{\partial Vol}{\partial t} \right\rangle_s > 0$, occurs mainly on the offshore side of the undertow detachment. Thus, as with the bedload contribution, the offshore displacement of the undertow detachment entails an offshore displacement of the suspended transport accumulation zone. This can be, indeed, observed in Figure 6.17.

However, the main accumulation of sediment due to suspended transport occurs at a certain distance from the undertow detachment. This offshore shift of the suspended transport accumulation respect to the undertow detachment increases as the beach profile evolves, as can be noted in Figure 6.17. Since this offshore shift is produced by the sediment flux of the detached undertow, according to the conclusions extracted from Figure 6.3, the $\langle F_{sed} \rangle_t$ profiles must be examined to determine the reasons for this increase in the offshore-shift. $\langle F_{sed} \rangle_t$ profiles at different positions

along the beach are represented in Figure 6.20.

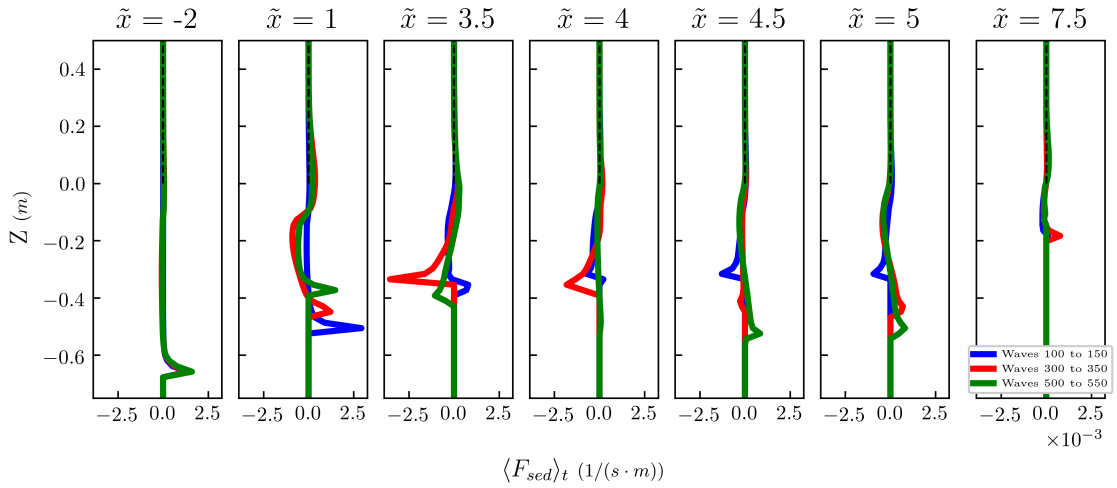

Figure 6.20: Evolution of the time-averaged horizontal advective sediment flux at different positions along the shoaling and surf zones. Blue line, obtained for waves 100 to 150. Red line, waves 300 to 350. Green line, 500 to 550.

As can be noted, the most remarkable changes in $\langle F_{sed} \rangle_t$ occur in the outer surf zone as well. There are no significant variations of $\langle F_{sed} \rangle_t$ in the shoaling zone. In the outer surf zone, the flux produced by the steady streaming right after the break point is reduced at the beginning of the migration stage (waves 300 to 350), consistently with the weakening of the steady streaming observed in Figure 6.19 at $\tilde{x} = 1$. However, this sediment flux is enhanced at the end of the migration stage (waves 500 to 550) due to intra-wave effects, as will be explained later. At $\tilde{x} = 3.5$, the direction of $\langle F_{sed} \rangle_t$ is reverted due to the offshore migration of the undertow detachment, which leads to a displacement of the point in which the near-bed $\langle F_{sed} \rangle_t$ changes its direction, note that this position is on the onshore side of the undertow detachment for waves 100 to 150. In the upper layers of the outer surf zone, at $\tilde{x} = 1$, $\langle F_{sed} \rangle_t$ produced by the detached undertow increases significantly from waves 100-150 to waves 300-350, and then it is reduced as the beach profile is closer to the equilibrium status (waves 500 to 550). This last aspect, regarding the sediment flux of the detached undertow, is of great importance as it partially compensates the onshore-directed flux in the lower layers caused by the steady streaming, contributing to equilibrating the net suspended sediment transport. As the $\langle U \rangle_t$ profiles do not change significantly in this zone (see Figure 6.19 at $\tilde{x} = 1$), the main reason for this variation can potentially be explained by changes in the $\langle C \rangle$ profiles or by intra-wave effects. At $\tilde{x} = 4$, for waves 500 to 550, $\langle F_{sed} \rangle_t$ is nearly zero at the position of the bar trough, which is consistent with the relatively low $\langle U \rangle$ and, as will be shown, with uniformly distributed, low $\langle C \rangle$. Interestingly, at $\tilde{x} = 4.5$ and $\tilde{x} = 5$ for waves 500 to 550, $\langle F_{sed} \rangle_t$ is onshore-directed close to the seabed and offshore-directed far from it. This is consistent with the $\langle U \rangle$ profiles shown in Figure 6.19. In the inner surf zone $\tilde{x} = 7.5$, $\langle F_{sed} \rangle_t$ for waves 500 to 550 is nearly zero.

The previously described variations of $\langle F_{sed} \rangle_t$ profiles can be due to the changes in the time-averaged velocity, concentration or in the covariance of them. To determine the reasons behind these changes, these variables are investigated in the following.

$\langle C \rangle$ profiles at different positions along the beach are shown in Figure 6.21.

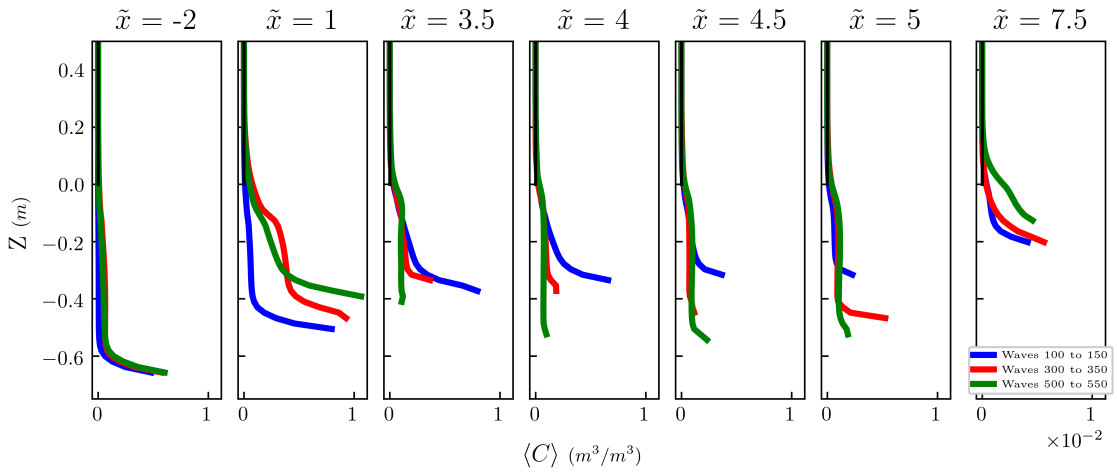

Figure 6.21: Evolution of the time-averaged concentration profiles at different positions along the shoaling and surf zones. Blue lines, waves 100 to 150. Red line, waves 300 to 350. Green line, 500 to 550.

Examining the $\langle C \rangle$ profiles, the shoaling zone does not present remarkable changes, apart from a slight increase in the concentration far from the seabed, consistent with the larger sediment flux of the detached undertow. In the outer surf zone, at $\tilde{x} = 1$, it can be noted that $\langle C \rangle$ is overall higher than in the growth stage. There is also an increase in the near-bed $\langle C \rangle$, which is caused by the higher instantaneous U_f that occurs on top of the breaker bar as it increases its size (as will be shown later). As the simulation advances, the vertical sediment flux from near-bed to the upper layers of the outer surf zone, caused by the vertical velocity induced by the wave breaking process, keeps increasing $\langle C \rangle$ far from the seabed until it reaches an equilibrium. At this point, the amount of sediment advected seaward by the detached undertow is equal to that transported upwards during wave breaking, reaching an equilibrium value for $\langle C \rangle$. This aspect will be further discussed in the analysis of the equilibrium stage. At the bar trough ($\tilde{x} = 3.5$ to $\tilde{x} = 5$, depending on the wave interval), the $\langle C \rangle$ becomes almost uniform for waves 300 to 350 and 500 to 550, with very low sediment concentration levels. This lower $\langle C \rangle$ implies lower $\langle F_{sed} \rangle_t$ in the trough region, as observed in Figure 6.20. Finally, $\langle C \rangle$ increases at $\tilde{x} = 7.5$ due to the higher friction velocity induced by breakers propagating on top of the secondary breaker bar.

To explain the variations of near-bed $\langle C \rangle$ in the outer surf zone, the maxima (onshore-directed) and minima (offshore-directed) friction velocities, $U_{f,max}$ and $U_{f,min}$, along the wave phase are analysed. These are presented in Figure 6.22

As can be noted, there is an increase in $U_{f,max}$ on top of the breaker bar ($\tilde{x} = 0$ to $\tilde{x} = 3.5$, approximately). Also, there is an increase in $U_{f,min}$ in the bar trough in accordance with the previous discussion on the evolution of the $\langle U \rangle$ profiles. An important aspect that can be observed in Figure 6.22 is that $U_{f,max}$ in the trough ($\tilde{x} = 4$) is reduced from waves 300-350 to waves 500-500, which explains the lower $\langle C \rangle$ observed in the trough region for waves 500 to 550 in Figure 6.21. This is consistent with the increase in water depth resulting from the deepening of the trough, which leads to smaller $U_{f,max}$ produced on the seabed during wave breaking. At the position of the secondary breaker bar (around $\tilde{x} = 7.5$), $U_{f,max}$ increases as

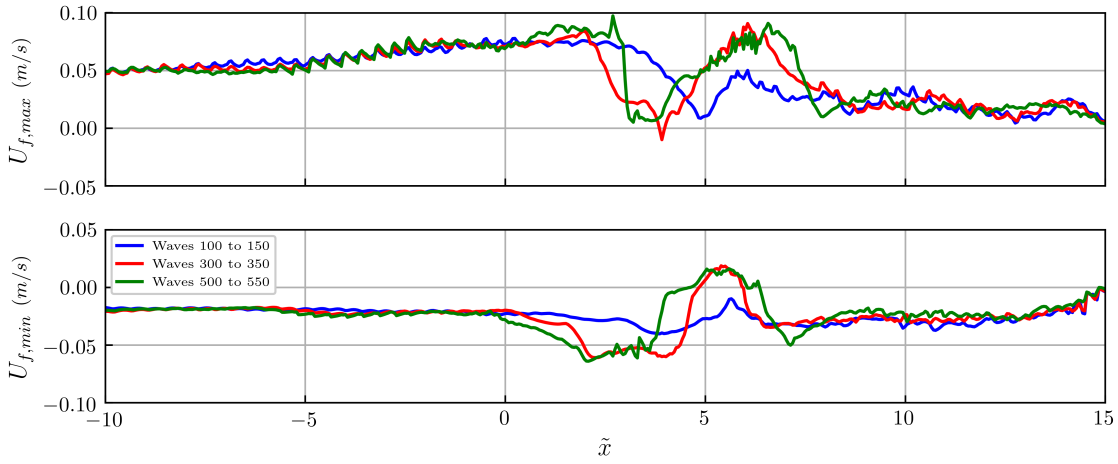

Figure 6.22: Evolution of the maxima and minima friction velocities along the cross-shore profile. Blue line, waves 100 to 150. Red line, waves 300 to 350. Green line, 500 to 550.

the secondary bar grows.

The increase of $U_{f,max}$ on top of the breaker bar along the migration stage is consistent with the waves propagating in reduced water depth, due to the growth of the breaker bar. This increase in friction velocity inhibits further growth of the bar, as it would result in larger erosion leading to a reduction of the bar size. From this, it can be concluded that the growth of the bar is limited by a maximum friction velocity or, for given wave conditions, to the decrease in water depth that leads to such limiting friction velocity. Once the breaker bar acquires its equilibrium size, $U_{f,max}$ on top of it remains nearly constant (as will be shown in the equilibrium stage analysis). Note that this also applies to the size of the secondary breaker bar, which is similarly limited by the friction velocity induced by rollers.

As done before, intra-wave effects must be accounted for in the analysis of sediment fluxes apart from time-averaged magnitudes. For this purpose, the covariance profiles ($cov(U, C)$) during the migration stage are given in Figure 6.23.

In Figure 6.23, it can be noted that the intra-wave effects do not change significantly in the shoaling zone. However, as commented in Section 6.3, the intra-wave effects are more important in the outer surf zone. They are responsible for some features observed in the $\langle F_{sed} \rangle_t$ profiles which are not explained by the variations of $\langle U \rangle$ and $\langle C \rangle$ profiles. At $\tilde{x} = 1$, the covariance increases at the end of the migration stage, resulting in enhanced onshore-directed $\langle F_{sed} \rangle_t$ despite the weaker steady streaming (shown in Figure 6.19). As the breaker bar trough develops, intra-wave effects are less noticeable in the trough region (see $\tilde{x} = 3.5$ to $\tilde{x} = 5$ in Figure 6.23), in which the sediment transport is mainly driven by currents. Finally, for the inner surf zone ($\tilde{x} = 7.5$), the intra-wave effects are enhanced as the bathymetry evolves. Their onshore-directed contribution to $\langle F_{sed} \rangle_t$ compensates that induced by currents (offshore-directed, as can be noted in Figure 6.19) resulting in nearly zero net sediment transport at the end of the migration stage (see Figure 6.20 waves 500 to 550).

Once the observed sediment flux patterns and the reasons behind their evolution along the migration stage have been commented, some conclusions on the reasons

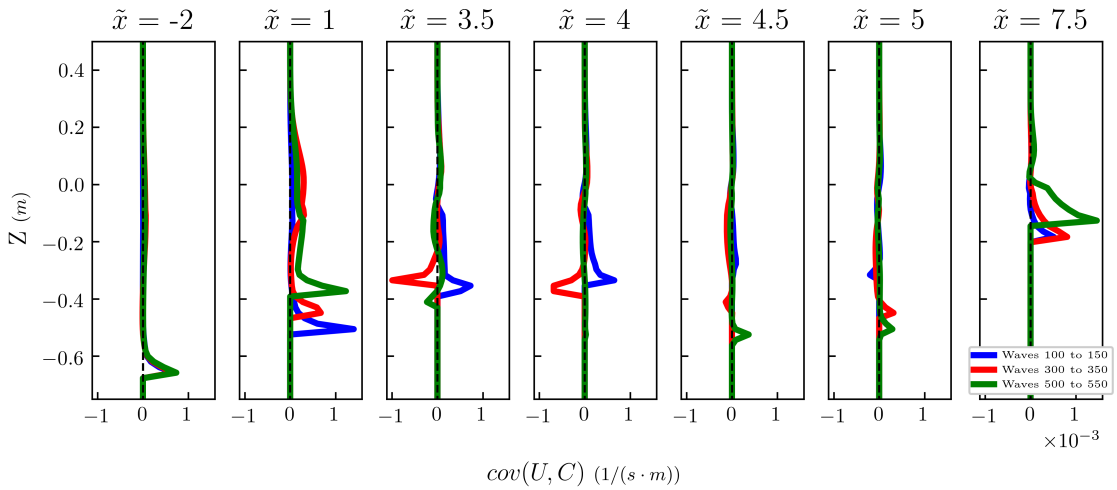

Figure 6.23: Evolution of the covariance of horizontal velocity and sediment concentration at different positions along the shoaling and surf zones. Blue line, waves 100 to 150. Red line, 300 to 350. Green lines, 500 to 550.

behind the suspended transport contribution to the migration of the breaker bar can be extracted.

Firstly, the migration of the undertow detachment leads to a seaward displacement of the accumulation zone. Secondly, the accumulation zone extends further offshore due to the increase in the sediment flux of the detached undertow, which in enhanced due to an increase in the sediment concentration present in the upper layers of the outer surf zone. Thirdly, the suspended sediment concentration in the trough region is reduced, leading to a smaller sediment flux of the (still attached) undertow and to the stabilization of the trough. In the inner surf zone, the sediment flux is nearly zero, as the intra-wave effects compensate the small flux produced by the undertow. Also, this implies that the additional sediment concentration found in the detached undertow comes from the steady streaming and not from erosion in the inner surf zone.

Note that other effects apart from the morphological evolution of the beach can lead to displacements of the undertow detachment point. Following the morphodynamic framework (from (Wright & Thom, 1977), discussed in Chapter 1), variations in the environmental conditions must have an effect in its position. For instance, increasing wave steepness leads to an offshore displacement of the break and plunge points and, consequently, of the undertow detachment and breaker bar. On the contrary, decreasing wave steepness would result in onshore migration of the breaker bar. This is in agreement with field observations ((Bruun, 1954)). Considering this, available knowledge on wave breaking conditions (i.e., (Robertson *et al.* , 2013)) can be used to delimit the position of the undertow detachment point and area in which the breaker bar is generated, and also to predict the consequences of variations of the environmental conditions in a given morphological state.

Additionally, some of the stabilizing features that lead to the equilibrium of the beach profile arise during the migration stage. The maximum size that the breaker bar can achieve is limited by the reduction in water depth (with the consistent increase of the maximum friction velocity on top of it) that it produces. Also, as the bar trough deepens, the friction velocities inside it are smaller, and the amount of

sediment put in suspension is also reduced. The large momentum mixing occurring inside the trough as a result of wave breaking, leading to an almost uniform velocity profile, is another stabilizing feature.

6.5 Equilibrium stage

In this section, Specific Objective 3.c is tackled. As commented in Section 6.4, in the last waves of the migration stage the beach profile starts to acquire an equilibrium configuration. The net sediment fluxes in the trough region and in the inner surf zone are close to zero. Also, the hydrodynamics and sediment transport in the shoaling zone did not undergo important variations. Most of the changes in the variables involved in the evolution of the beach profile are observed in the outer surf zone. In this section, it is intended to examine how the equilibrium of the beach profile is achieved, including the outer surf zone.

As a first step, the bathymetric evolution along the equilibrium stage is displayed in Figure 6.24.

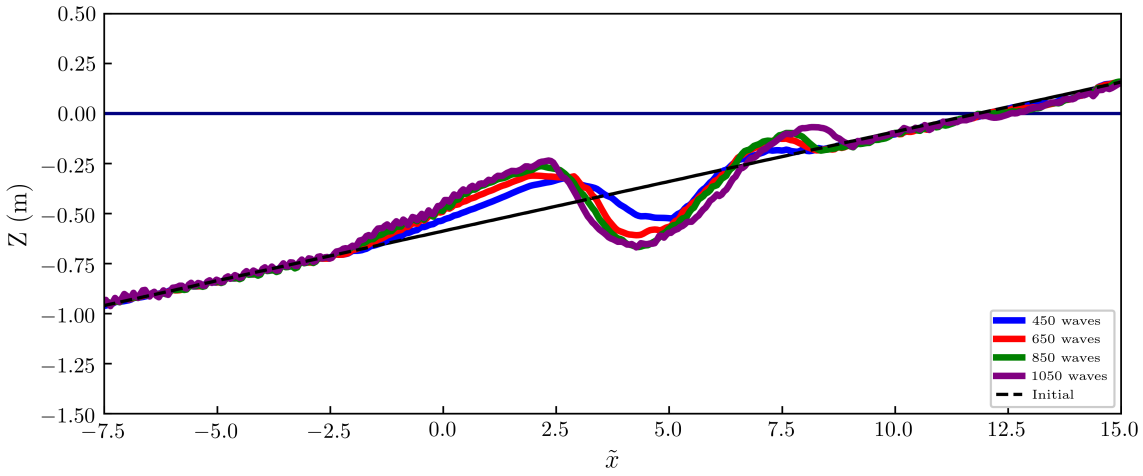

Figure 6.24: Evolution of the bathymetry during the equilibrium stage. Blue line, waves 600 to 650. Red line, 800 to 850. Green lines, 1000 to 1050.

In Figure 6.24, the breaker bar and trough acquire an equilibrium configuration after approximately 850 waves. There are still some variations of the beach profile between waves 850 an 1050, but the bar and trough do not evolve significantly. It can be noted that the accumulation of sediment on the onshore side of the trough results in another breaker bar that migrates towards the coastline. However, the processes involved in the evolution of this secondary bar are not discussed in this work.

The stabilization of the beach profile can also be noted by looking at the accumulation of sediment produced by each sediment transport mechanism, given in Figure 6.25.

As can be observed in Figure 6.25, the transport rates tend to zero as the simulation advances. After 1000 waves, the net accumulation rate in the breaker bar and trough zones ($\left\langle \frac{\partial Vol}{\partial t} \right\rangle_t$) is nearly zero, which confirms that the bar and trough are in equilibrium. On top of the breaker bar ($\tilde{x} = 0$ to $\tilde{x} = 2.5$), $\left\langle \frac{\partial Vol}{\partial t} \right\rangle_b$ accumulates

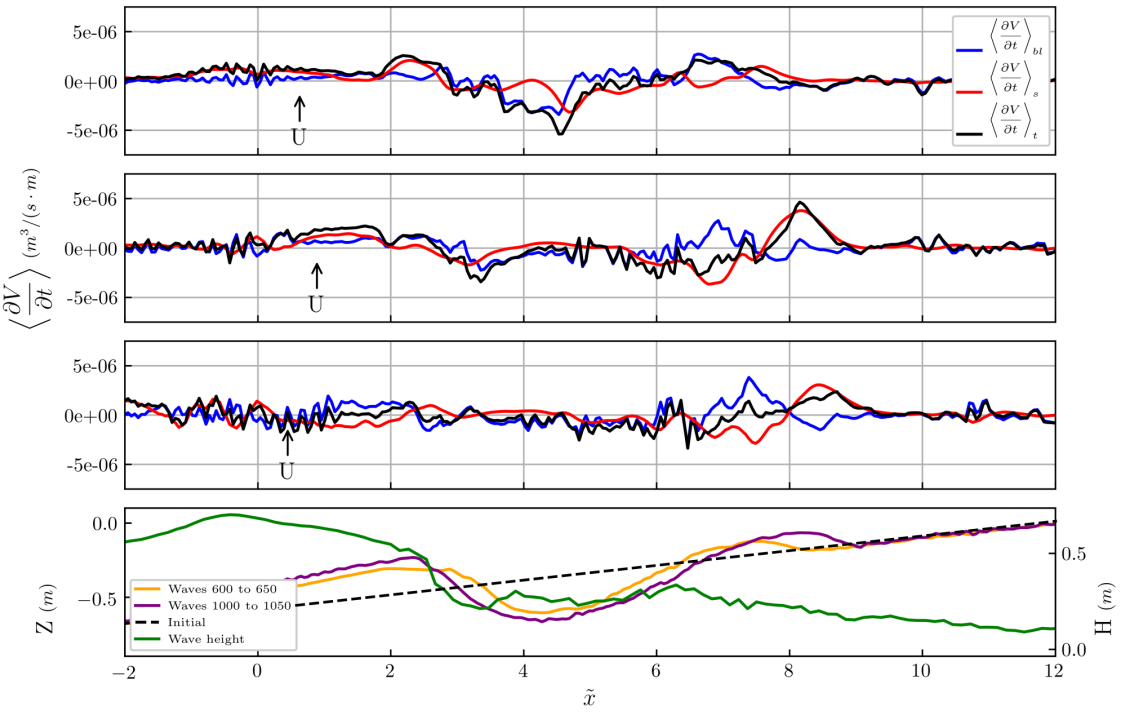

Figure 6.25: Contributions from the bedload and suspended transport mechanisms to the bathymetric evolution. Top panel, waves 600 to 650. Centre-top panel, waves 800 to 850. Centre-bottom panel, waves 1000 to 1050. Bottom panel, seabed positions and wave height during the equilibrium stage. Black arrows represent the position of the undertow detachment.

sediment while $\left\langle \frac{\partial Vol}{\partial t} \right\rangle_s$ produces a loss of sediment. This dynamic equilibrium is consistent with the explanation for the maximum size that the breaker bar can have given in Section 6.4: the sediment accumulated by the bedload mechanism results in an excessive reduction in water depth, increasing the friction velocity produced by shoaling waves and the associated erosion. Also, the accumulation of sediment leading to the formation of the secondary breaker bar, mainly caused by the suspended transport, can be noted at $\tilde{x} = 7.5$ approximately. Note also that the migration of the undertow detachment stops at roughly $\tilde{x} = 0.7$.

In the following analysis, it is intended to determine how the modification of the morphodynamic processes and their drivers result in the $\left\langle \frac{\partial Vol}{\partial t} \right\rangle_t$ being nearly zero.

6.5.1 Bedload transport

Regarding the bedload transport mechanism, as observed in Figure 6.25, it contributes to further deepening of the trough and to increasing the size of the breaker bar for waves 600 to 850. After 1000 waves, the bedload transport only contributes to increasing the size of the breaker bar. As has been done before, the time-averaged friction velocities ($\langle U_f \rangle$) are examined first to investigate the reasons for this change of trend. They are shown in Figure 6.26.

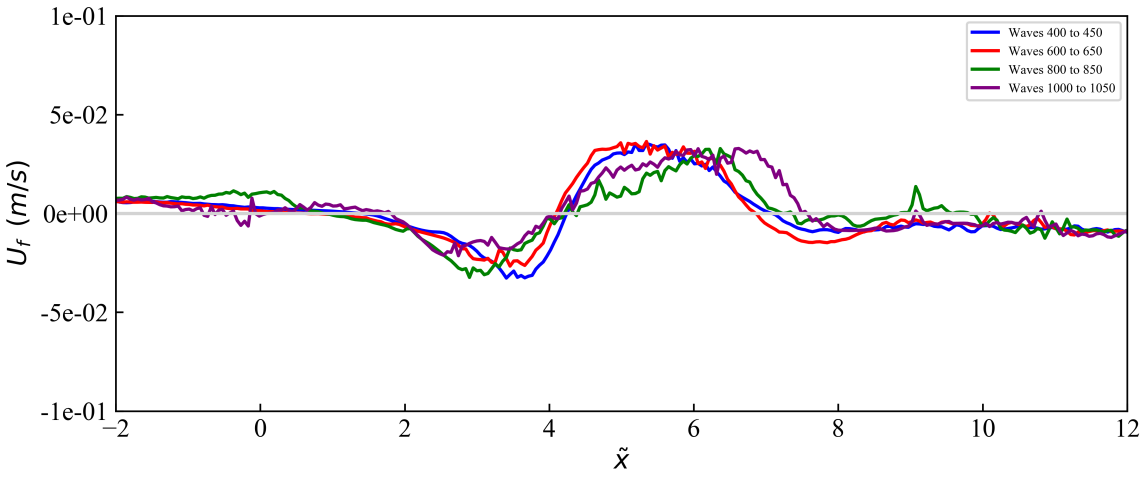

Figure 6.26: Time-averaged friction velocity obtained for different intervals in the migration stage. Blue line, waves 400 to 450. Red line, waves 600 to 650. Green line, waves 800 to 850. Purple line, waves 1000 to 1050.

As can be observed in Figure 6.26, the distribution of $\langle U_f \rangle$ does not undergo great variations in the shoaling zone ($\tilde{x} < 0$). In the outer surf zone ($0 < \tilde{x} < 5$), $\langle U_f \rangle$ has a local minimum at $\tilde{x} = 2.1$, and another local minimum at $\tilde{x} = 3.7$ approximately. The second minimum corresponds to the accumulation at the crest of the breaker bar observed in Figure 6.25. In the breaker bar trough ($\tilde{x} = 3$ to $\tilde{x} = 6$, approximately), the horizontal gradient of $\langle U_f \rangle$ becomes smaller as the profile acquires its equilibrium status, resulting in the reduction of loss of sediment observed in Figure 6.25 and in the stabilization of the wave trough, as commented before. The maximum $\langle U_f \rangle$ occurs in the inner surf zone (roughly at $\tilde{x} = 7$), and it is responsible for the formation of a secondary breaker bar.

Thus, the main features of the bedload transport contribution to the dynamic equilibrium of the beach profile (mainly, a tendency to increase the breaker bar size and no further deepening the trough) can be explained from the $\langle U_f \rangle$ distribution. Moreover, the reasons behind the variations of $\langle U_f \rangle$ can be found in $\langle U \rangle$ profiles. These are displayed in Figure 6.27.

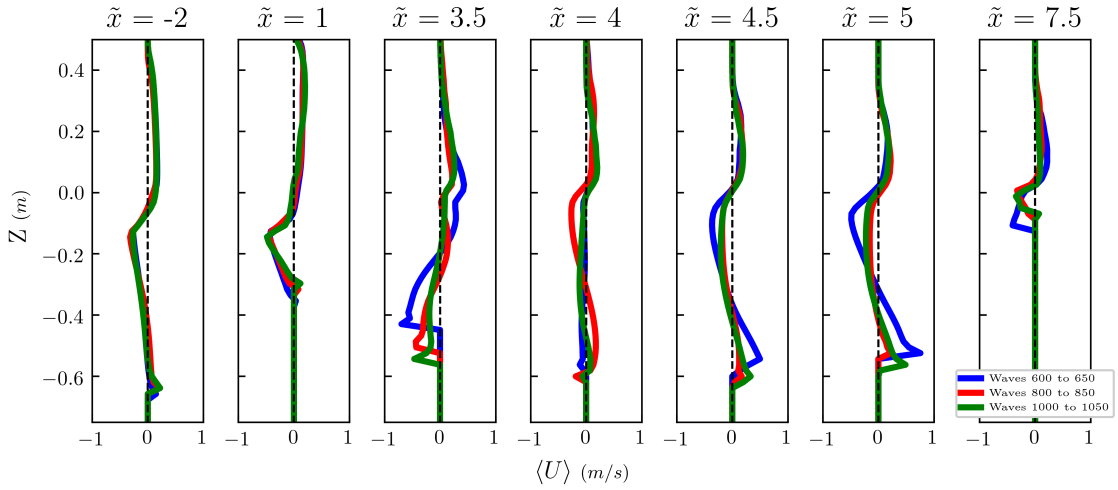

Figure 6.27: Time-averaged velocity profiles obtained for different intervals along the migration stage. Blue line, waves 600 to 650. Red line, 800 to 850. Green line, waves 1000 to 1050.

As can be noted in Figure 6.27, the velocity profiles in the shoaling zone are fundamentally the same. In the bar trough ($\tilde{x} = 3$ to $\tilde{x} = 6$ approximately) the velocity profiles change on the sides ($\tilde{x} = 3.5$ and $\tilde{x} = 5$), showing a smaller undertow velocity. In the centre of the trough ($\tilde{x} = 4$ and $\tilde{x} = 4.5$), $\langle U \rangle$ profiles remain nearly constant, consistently with the bathymetric changes observed in Figure 6.24. Note that after 850 waves the $\langle U \rangle$ profiles in the bar trough do not change significantly. In the inner surf zone, $\langle U \rangle$ profiles are modified by the onshore-migration of the secondary breaker bar. A reversal in the near-bed $\langle U \rangle$ direction can be observed at $\tilde{x} = 7.5$ for waves 1000 to 1050.

The reduction of undertow strength inside the trough implies a smaller cross-shore gradient of $\langle U_f \rangle$ in the outer surf zone. This smaller cross-shore gradient is reflected also in $\langle Q_s \rangle$. According to Equation 6.6, and interchanging operators $\nabla(\cdot)$ and $\langle \cdot \rangle$, $\left\langle \frac{\partial Vol}{\partial t} \right\rangle_b$ is the divergence of $\langle Q_s \rangle$. Considering this, the observed reduction of the cross-shore gradient of $\langle U_f \rangle$ explains the smaller accumulation of sediment due to bedload transport observed in Figure 6.25. However, after the trough is nearly stabilized, there is still some cross-shore gradient of $\langle U_f \rangle$ in the outer surf zone, resulting in a residual accumulation of sediment on top of the breaker bar, also observed in Figure 6.25. Notice that in order to completely eliminate the contribution of bedload transport to the growth of the breaker bar $\langle Q_{bl} \rangle$ must be constant along the whole beach profile. In the case of sediment with relatively low critical shear stress for the initiation of motion, this would imply a nearly constant near-bed $\langle U \rangle$ along the beach profile, which is not the case. Therefore, under such situation the suspended contribution must compensate the accumulation due to bedload transport. In the case of sediment with high critical shear stress (i.e., gravel

beaches), the interplay between friction velocity and bedload transport described in Section 6.3 would have a significant effect in this equilibrium condition, which may achieve a constant $\langle Q_{bl} \rangle$ (necessarily equal to zero) even in presence of $\langle U_f \rangle$ cross-shore gradients, allowing the beach profile to acquire its equilibrium status despite a small or inexistent suspended transport. This type of situation is, however, out of the scope of this thesis.

6.5.2 Suspended transport

In the analysis of the accumulation rates (Figure 6.25), it can be noted that the suspended contribution compensates the accumulation produced by the bedload transport on top of the breaker bar. Also, the accumulation of sediment inside the wave trough disappears after 1000 waves. The reasons for these features can be derived from the $\langle C \rangle$ concentration profiles along with the previously discussed $\langle U \rangle$. Apart from their time-averaged magnitudes, intra-wave effects must be accounted for by looking at the covariance between velocity and concentration ($cov(U, C)$). Firstly, $\langle C \rangle$ profiles are displayed in Figure 6.28.

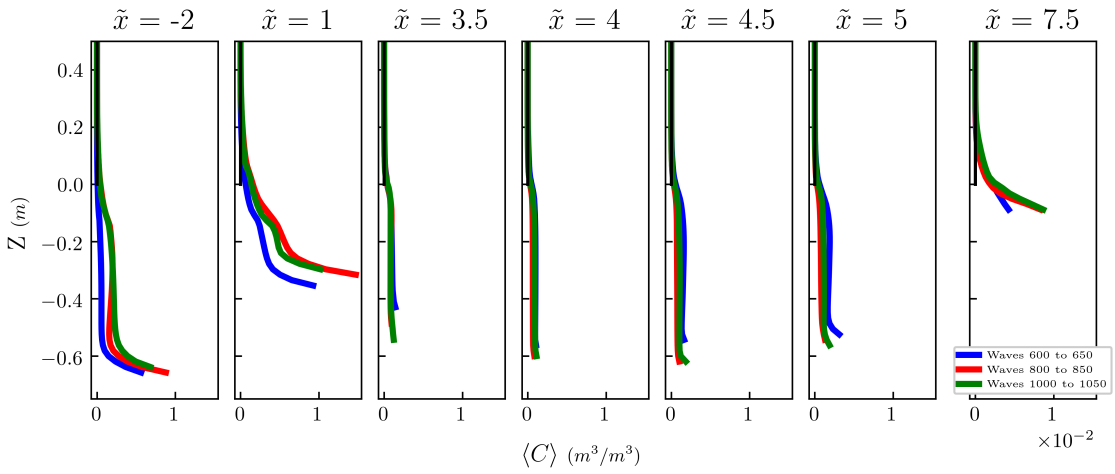

Figure 6.28: Evolution of the time-averaged concentration profiles at different positions along the shoaling and surf zones. Blue lines, waves 400 to 450. Red line, waves 800 to 850. Green line, 1000 to 1050.

In Figure 6.28, it can be noted that $\langle C \rangle$ profiles do not undergo significant changes after 850 waves. In general, $\langle C \rangle$ in the region of the trough ($3 < \tilde{x} < 6$) is very small, On top of the breaker bar and in the inner surf zone ($\tilde{x} = 1$ and $\tilde{x} = -2$, respectively), $\langle C \rangle$ is larger and, as discussed in Section 6.4, the sediment flux induced by wave breaking is compensated by that of the detached undertow, leading to nearly constant $\langle C \rangle$ profiles in the upper layers of these zones. In the inner surf zone, at $\tilde{x} = 7.5$, the near-bed $\langle C \rangle$ increases due to the growth of the secondary bar, which results in a reduction in water depth and, thus, higher friction velocities induced by the rollers resulting from wave breaking.

Therefore, there is an overall reduction of the suspended sediment concentration in the trough region, which leads to a smaller contribution of the suspended transport to the evolution of the beach profile, as observed in Figure 6.25. The reason for this is an overall decrement in the friction velocities in this zone. However, there is still a

significant amount of suspended sediment in the breaker bar region, which increases at the beginning of the equilibrium stage and then decreases again. To examine the reasons for these two aspects, the maximum and minimum friction velocities, given in Figure 6.29, are investigated.

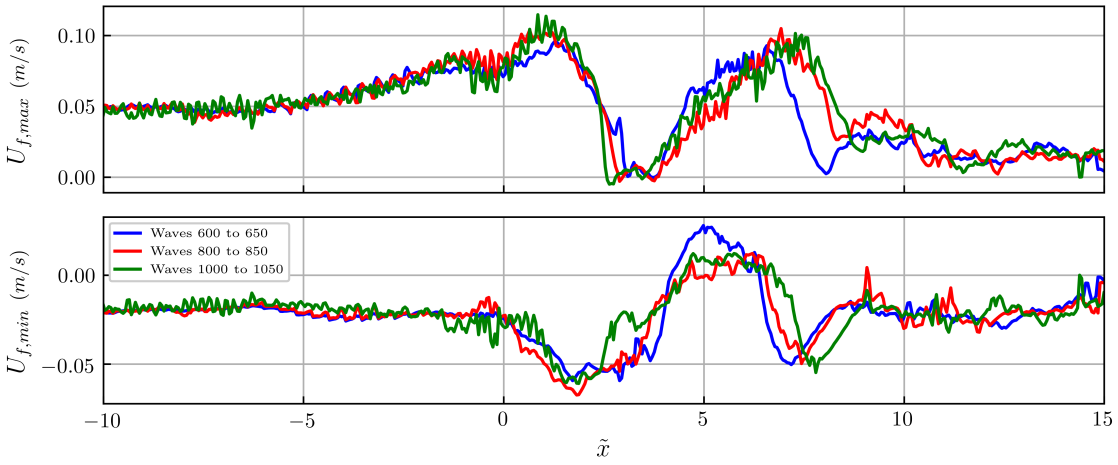

Figure 6.29: Evolution of the maxima and minima friction velocities along the cross-shore profile. Blue line, waves 600 to 650. Red line, waves 800 to 850. Green line, 1000 to 1050.

As can be noted in Figure 6.29, the distributions of $U_{f,max}$ and $U_{f,min}$ are also very similar for the three time intervals. On the breaker bar crest, $U_{f,max}$ does not change significantly between waves 800 and 1050, as the breaker bar already acquired its equilibrium size. However, $U_{f,max}$ is slightly higher for waves 800 to 850, which explains the larger sediment concentration carried by the steady streaming in this wave interval (as seen in Figure 6.28 at $\tilde{x} = 1$). In this zone, $U_{f,max}$ associated to the wave crest phase increase between waves 600 and 800, which is consistent with the increase of the breaker bar size in this interval (see Figure 6.24 at $\tilde{x} = 2.5$ approximately). In the trough region ($3 < \tilde{x} < 6$) $U_{f,min}$ is reduced, as the deepening of the trough increases the cross-sectional area across which the mass flux of the undertow can flow. This is specially noticeable on the onshore side of the trough, in which there are still some bathymetric changes (as can be noted in Figure 6.24). In the inner surf zone, an increase in $U_{f,max}$ right after the plunge point can be noted between waves 800 and 1000 (roughly at $\tilde{x} = 6$), consistent with the reduced water depth due to the appearance of the secondary breaker bar.

The reduction of $U_{f,max}$ on the onshore face of the breaker bar trough, caused by the larger water depth resulting from bathymetric changes, contrasts with the previous increase in $U_{f,min}$ observed in Section 6.4 due to a redistribution of the Reynolds stresses.

Finally, to complete the analysis of the suspended transport components, the intra-wave effects must be examined. These are represented by the ce between velocity and sediment concentration ($cov(U, C)$), shown in Figure 6.30.

As can be noted in Figure 6.30, the $cov(U, C)$ is of great importance on top of the main and secondary breaker bars ($\tilde{x} = 1$ and $\tilde{x} = 7.5$, respectively), and it is less significant in the breaker bar trough region ($\tilde{x} = 3$ to $\tilde{x} = 6$). This tendency increases as the breaker bar acquires its equilibrium status. These two aspects are in

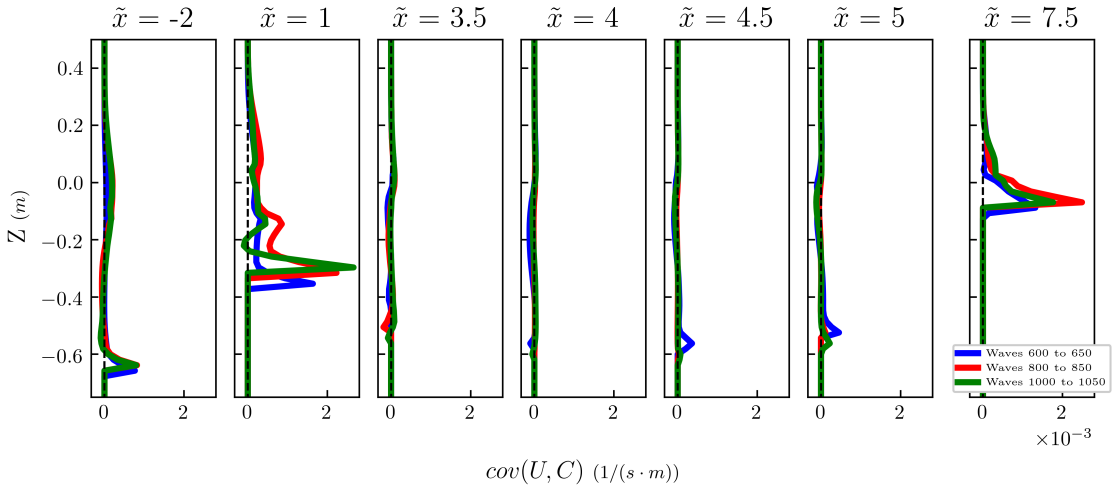

Figure 6.30: Evolution of the covariance of velocity and sediment concentrations at different positions along the shoaling and surf zones. Blue line, obtained for waves 600 to 650. Red line, waves 800 to 850. Green line, 1000 to 1050.

agreement with the previously discussed mechanisms for acquiring the equilibrium status. Firstly, the large intra-wave effects contribution to the onshore suspended transport on top of the breaker bar, associated to the wave crest phase, inhibit any further growth of the breaker bar. Secondly, the intra-wave effects associated to the high friction velocities, resulting from the impact of the plunging jet, are inhibited once the breaker bar trough acquires enough depth.

The joint effects of the variations of $\langle C \rangle$, $\langle U \rangle$ and $cov(U, C)$ profiles in the suspended transport can be examined by looking at the $\langle F_{sed} \rangle_t$ profiles, displayed in Figure 6.31.

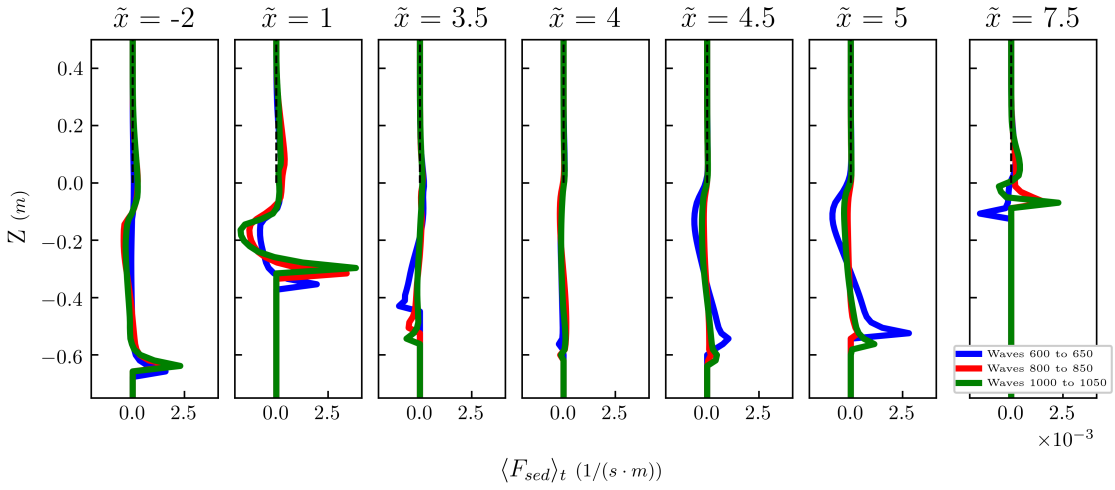

Figure 6.31: Evolution of the time-averaged horizontal advective sediment flux at different positions along the shoaling and surf zones. Blue line, obtained for waves 600 to 650. Red line, waves 800 to 850. Green line, 1000 to 1050.

In Figure 6.31, it can be observed that $\langle F_{sed} \rangle_t$ does not change greatly for waves 800 to 1000, which is consistent with the moderate changes of $\langle U \rangle$ (Figure 6.27), $\langle C \rangle$ (Figure 6.28) and $cov(U, C)$ (Figure 6.30) shown before. In the shoaling zone,

the near-bed $\langle F_{sed} \rangle_t$ is nearly constant after 800 waves, and that associated to the sediment carried by the detached undertow increases slightly, leading to a net suspended sediment flux closer to zero. Also, consistently with the discussion on $\langle C \rangle$ profiles and intra-wave effects, $\langle F_{sed} \rangle_t$ in the trough area is very small, while it is significantly higher on top of the breaker bar. Note that, comparing these $\langle F_{sed} \rangle_t$ profiles with the $cov(U, C)$ profiles given in Figure 6.23, most of the near-bed $\langle F_{sed} \rangle_t$ on top of the breaker bar arises from intra-wave effects (nearly 80%), while far from the seabed it is mainly due to time-averaged effects (detached undertow). In the shoaling zone, the onshore directed transport is mainly due to the steady streaming current, although intra-wave effects have a significant contribution (around 30%). Therefore, there is a transition from current-induced to wave-induced suspended transport as moving from the shoaling zone to the outer surf zone (in the breaker bar region). The reason for this transition is that the intra-wave effects are enhanced due to the reduction in water depth produced by the growth of the breaker bar,

It is clear by looking at Figure 6.31 that there are significant sediment fluxes even when the beach profile acquired the equilibrium status, concretely on top of the breaker bar. Thus, the equilibrium of the breaker bar is a dynamic condition in which high suspended sediment concentration is present in the outer surf zone, with the associated high sediment fluxes. In order to reach this equilibrium configuration, the offshore-directed $\langle F_{sed} \rangle_t$ produced by the detached undertow (observed by (Wang *et al.* , 2002) in large-scale laboratory experiments) must compensate the onshore-directed ones from the steady streaming and intra-wave effects, in such a way that the depth-integrated horizontal sediment flux ($\langle Q_s \rangle$) tends to zero as approaching the equilibrium status.

In Figure 6.32, the evolution of $\langle Q_s \rangle$ at different positions in the shoaling and outer surf zones are represented to illustrate how the suspended sediment transport approaches a dynamic equilibrium.

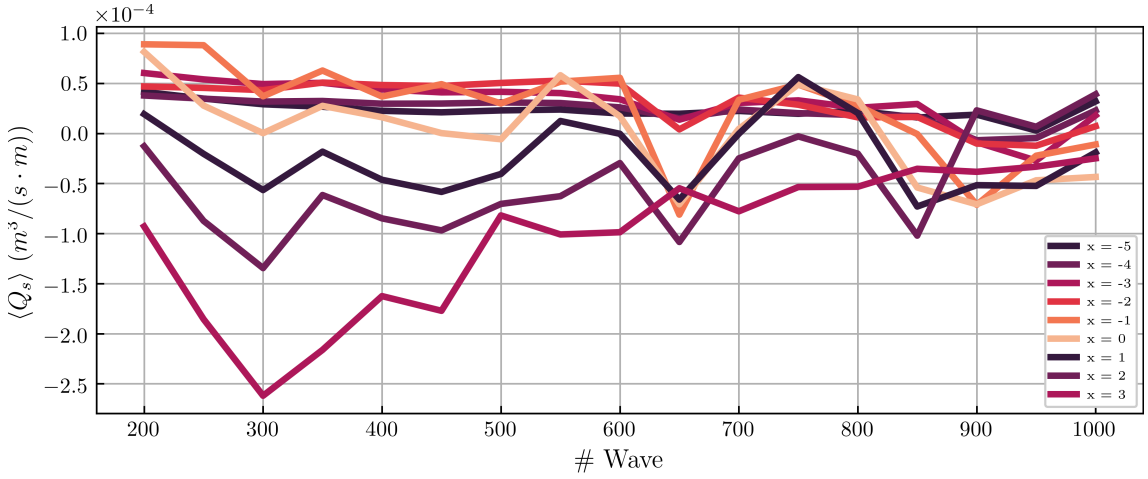

Figure 6.32: Evolution of the depth-integrated horizontal sediment fluxes along the simulation at several positions in the shoaling and outer surf zones.

As can be noted in Figure 6.32, $\langle Q_s \rangle$ tend to zero along the shoaling and outer surf zones as the beach profile reaches the dynamic equilibrium. According to the circulation pattern of suspended sediment proposed before, this trend in the fluxes means that, once the equilibrium is attained, the sediment is circulating in a closed loop on top of the breaker bar. All the sediment carried from the shoaling zone

towards the front face of the breaker bar by the steady streaming and, closer to the outer surf zone, by intra-wave effects is lifted by the high vertical velocities induced by the wave breaking process and then advected back to the shoaling zone by the detached undertow, where it falls into the lower layers due to gravity and it is captured again by the steady streaming.

Therefore, the equilibrium of the breaker bar is achieved when the onshore-directed sediment flux produced by the steady streaming and intra-wave effects is compensated by the offshore-directed one of the detached undertow. At this point, the net suspended transport along the water column is nearly zero. This, combined with the previously described equilibrium condition for the breaker bar size (related to the maximum reduction in water depth that can result from its growth), and trough (once the depth is large enough to avoid the erosion associated to the plunging jet) leads to the complete equilibrium of the breaker bar.

The proposed equilibrium condition for the breaker bar size can also be extended to the shoaling zone: in the equilibrium configuration, the sediment lifted by the friction velocity associated to the wave crest is compensated by that sediment that deposits from the detached undertow. This implies that an increase in the mean sea level results in a seabed rise in the shoaling and outer surf zones. The sediment required to produce this seabed rise comes from the new area of swash zone exposed to wave action and is carried along the inner surf zone by the attached undertow towards offshore. This is in accordance with the widely used Bruun's Rule (see (Bruun, 1962)). However, this reasoning based on morphodynamic processes also considers the effect of wave action: if there are no waves, an increase in sea level does not produce a rise of the seabed. Note also that a sea level rise not only modifies the friction velocity, but also the position of the undertow detachment. The break point would displace onshore due to the larger water depth, and so happens with the plunge point. Therefore, this would result in an onshore displacement of the detached undertow and a consequent onshore migration of the breaker bar, even maintaining highly energetic wave conditions.

6.6 Influence of Iribarren's number

The wave conditions (height and period) clearly influence the aforementioned hydrodynamic processes driving the sediment transport mechanisms. To analyse their influence on the sediment transport rates, a comparison between three different wave conditions is presented. The three test cases are set maintaining the same wave height and changing the wave period to achieve different Iribarren's numbers, aiming to provide a representation of plunging and spilling breakers. The results for the three test cases are also obtained for waves 100 to 150, so that the three wave conditions can be compared despite the different wave periods. Additionally, the normalized position along the cross-shore profile is obtained using the position and water depth of the break point corresponding to the case with wave period equal to 3.7 s. The test conditions and the position of relevant points are given in Table 6.2.

Table 6.2: Nondimensional numbers characterizing the beach profile.

Test case	**Wave height** (m)	**Wave period** (m)	$\boldsymbol{Ir_0}$ (m)	**Plunge** (-)	**Undertow detachment** (-)	**Break** (-)
1	0.43	2.7	0.34	6.81	4.96	1.01
2	0.43	3.7	0.47	5.85	2.87	0.00
3	0.43	4.7	0.60	5.19	2.18	-1.16

The distribution of the wave height along the cross-shore profile for the three tests is shown in Figure 6.33.

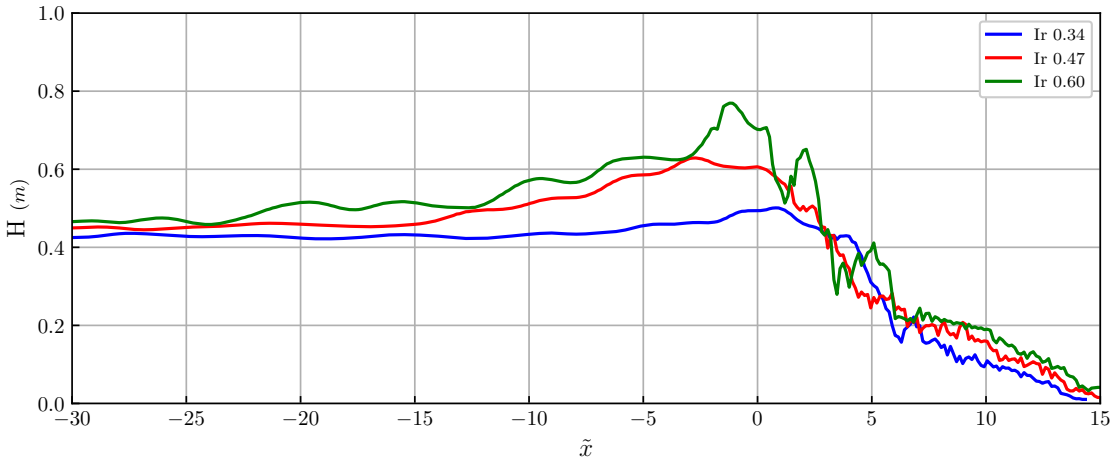

Figure 6.33: Distribution of wave height along the beach profile for the three test cases. Obtained for 100 to 150.

The results in Figure 6.33 show that higher Iribarren's numbers result in a larger wave height at the break point, which is displaced offshore. In addition, for plunger breakers the wave height starts decreasing smoothly, but then it drops sharply (green line in Figure 6.33). At the plunge point, high Iribarren's numbers produce a second peak in the wave height distribution (at $\tilde{x} = 5$,approximately), whereas it does not appear in spilling breakers.

Bathymetric evolution The first step for the comparison of the three Iribarren's numbers is to examine the differences in the resulting bathymetry. For this purpose, the bathymetric evolution of the three test cases is represented in Figure 6.34.

As can be noted, there are some similarities in the bathymetric evolution of the three cases. Consistently with the previous discussion on the sediment accumulation patterns, in all of them the breaker bar is generated around the undertow detachment point, being limited by the break point on the offshore side and by the plunge point on the onshore side. As the Iribarren's number increases, the break, plunge and undertow detachment points are displaced seawards, and the breaker bar is generated further offshore. Additionally, a larger Iribarren's number leads to a quicker development of the breaker bar and trough.

The evolution of the position of the breaker bar front presents important differences among the three test cases. In Figure 6.35, the evolution of the position of

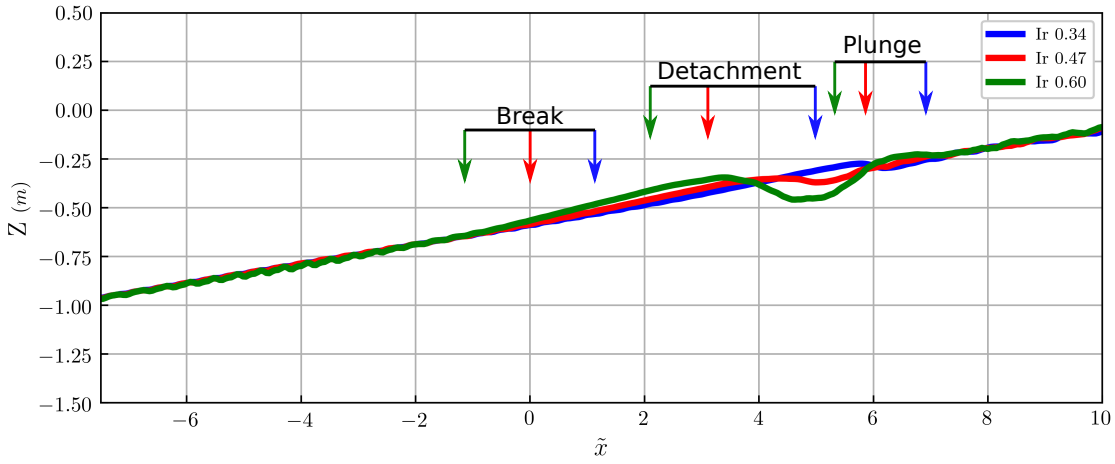

Figure 6.34: Bathymetry after 150 waves for the three test cases. The arrows show the location of the break, undertow detachment and plunge points for the three cases.

the breaker bar front along each simulation, obtained as the intersection between the bathymetry and the initial profile, is displayed.

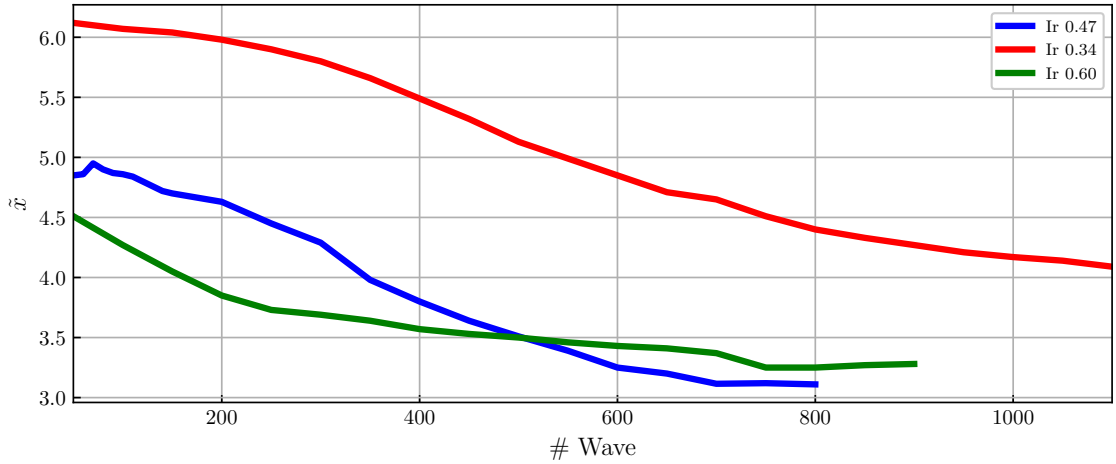

Figure 6.35: Bathymetry after 150 waves for the three test cases. The arrows show the location of the break, undertow detachment and plunge points for the three cases.

Figure 6.35 shows different migration speeds of the breaker bar. For low Iribarren's numbers, the breaker bar migrates slower and has an initial stage in which the breaker bar grows but stays at roughly the same position. In contrast, the plunging breakers quickly lead to the migration of the breaker bar, without a previous growth stage. Additionally, the equilibrium profile is reached after less waves for higher Iribarren's numbers. Overall, the evolution of the cross-shore profile occurs faster for plunging than for spilling breakers, which is to be expected, and the duration of the growth stage is smaller (non-existing for the test case with Iribarren's number 0.60).

In the following analysis, the differences between these three test cases are addressed using the previously discussed processes. Firstly, the time-averaged sediment transport rates corresponding to them are represented in Figure 6.36.

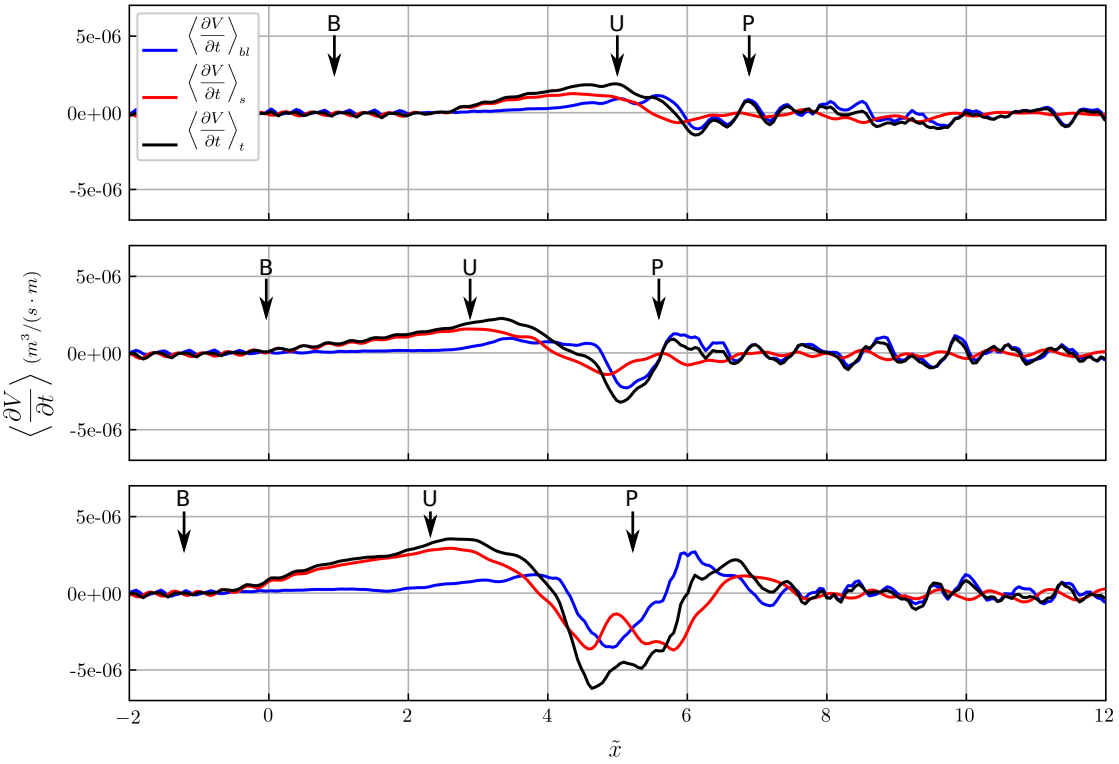

Figure 6.36: Accumulation rates for the three wave conditions obtained from waves 100 to 150. Top panel, Iribarren's number 0.34. Centre panel, Iribarren's number 0.47. Bottom panel, Iribarren's number 0.60. The break (B), undertow detachment (U) and plunge (P) points are also represented with arrows.

As can be observed in Figure 6.36, both the suspended and bedload transport contributions accumulate sediment in the outer surf zone in all the cases, which leads to the generation of the breaker bar. As the Iribarren's number increases, the total sediment transport increases as well, and the accumulation zone moves offshore. The bedload transport accumulates sediment mainly on the onshore side of the undertow detachment, while the suspended contribution accumulates sediment on the offshore side, which is in accordance with the previous discussion. Additionally, the suspended transport produces erosion at the plunge point for the intermediate and plunging breakers, while this does not happen under spilling breakers.

Bedload transport Figure 6.36 shows that the magnitude of the accumulation produced by the bedload transport is similar in all three test cases, and it occurs farther offshore as the Iribarren's number increases. To further investigate this aspect, the distribution of $\langle Q_{bl} \rangle$ is shown in Figure 6.37.

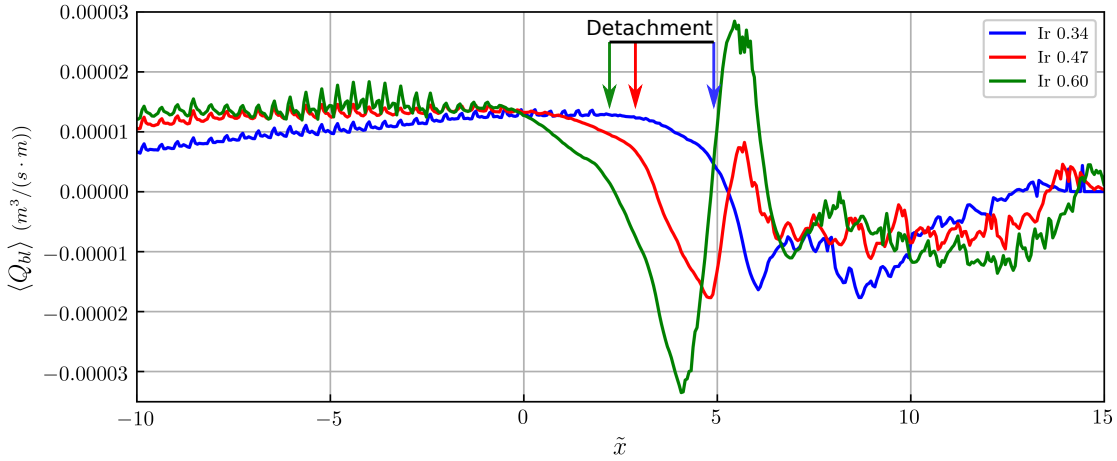

Figure 6.37: Distribution of time-averaged bedload transport along the cross-shore profile for the three test cases. Obtained for waves 100 to 150.

Figure 6.37 shows that the horizontal gradient of $\langle Q_{bl} \rangle$ which leads to the main accumulation of sediment is present in the three cases. It starts approximately at the position of the undertow detachment, producing the main accumulation of sediment at its onshore side. It can be also observed that the offshore-directed transport in the outer surf zone is higher for plunging breakers due to an increase in $\langle U \rangle$ close to the seabed. These higher velocities are responsible for the faster growth of the bar trough at higher Iribarren's numbers. Another aspect enhanced in plunging breakers is the onshore-directed transport produced landwards the plunge point ($\tilde{x} = 6$, approximately), which is to be expected as the plunging jet produces high velocities when it reaches the seabed. Notice that this does not occur for spilling breakers (blue line in Figure 4.46). For the inner surf zone, $\langle Q_{bl} \rangle$ is lower at high Iribarren's numbers, as the undertow is reduced due to the higher momentum mixing produced by the eddies (Ting & Kirby, 1995), (Ting & Nelson, 2011). In the swash zone, $\langle Q_{bl} \rangle$ induced by the spilling breakers becomes the smallest of the three cases. This is consistent with the higher energy dissipation that results in smaller wave height in this zone (as shown in Figure 6.33), leading to a weaker undertow.

These observations in $\langle Q_{bl} \rangle$ can be explained from the variations of the $\langle U \rangle$ profiles close to the seabed; these are shown in Figure 6.38.

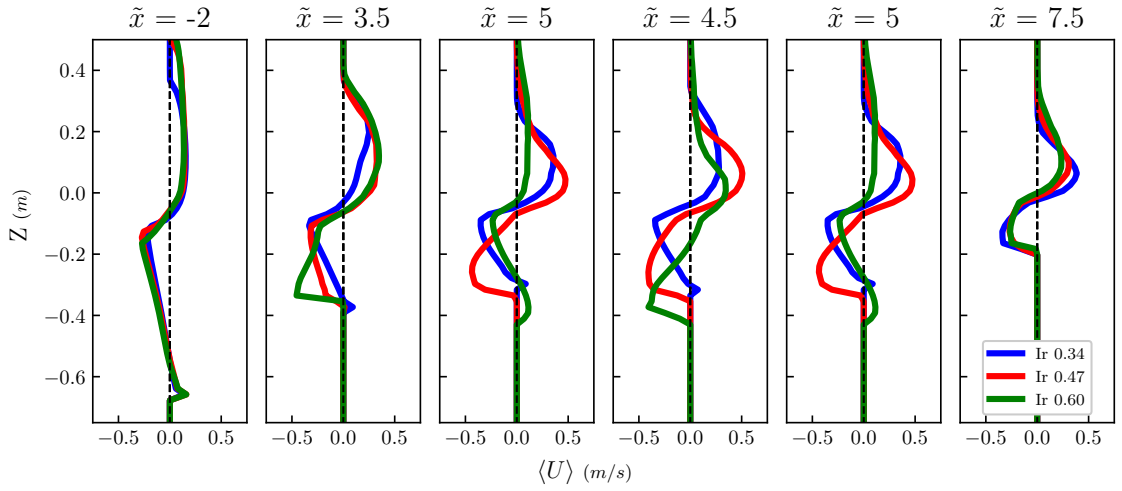

Figure 6.38: Time-averaged velocity profiles at different positions along the beach profile. Obtained for waves 100 to 150.

The increase of $\langle U \rangle$ with the Iribarren's number in the outer surf zone can be clearly observed at $\tilde{x} = 3.5$ and $\tilde{x} = 4$. The velocity profile is shifted downwards under the plunging breakers (green line), so that $\langle U \rangle$ decreases in the upper layers of the outer surf zone and increases closer to the seabed. This change in the shape of the undertow profile can be related to the breaker type and to the bathymetry shape. Under plunging breakers, the undertow is forced to flow in the lower layers of the flow, as the upper ones are highly mixed and subjected to high onshore-directed velocities during the wave-crest phase due to the plunging jet (which loses energy as it penetrates in the lower layers). In contrast, for spilling breakers, the momentum mixing along the water depth is much smaller, and the onshore-directed velocities of the wave crests occur only close to the mean water level. Additionally, as the bar trough is already developed and has a significant depth, the lower layers of the outer surf zone (closer to the seabed) are less influenced by the impinging jet, thus the water flux exiting the surf zone flows at higher velocities close to the seabed. Finally, the reduction in undertow velocity in the inner surf zone for the high Iribarren's numbers can be observed at $\tilde{x} = 7.5$, the undertow produced by the spilling breakers is stronger than those of the intermediate and plunging cases due to the lower momentum mixing along the water column, as explained in (Ting & Kirby, 1994).

Suspended transport The suspended transport undergoes important modifications as the Iribarren's number increases. As previously observed in Figure 6.36, the accumulation in the outer surf zone is higher and occurs farther offshore for plunging breakers. Furthermore, the suspended contribution produces a loss of sediment at the plunge point for high Iribarren's numbers, while for spilling breakers this does not occur.

In order to examine the reasons for these differences, $\langle F_{sed} \rangle_t$ profiles are shown in Figure 6.39.

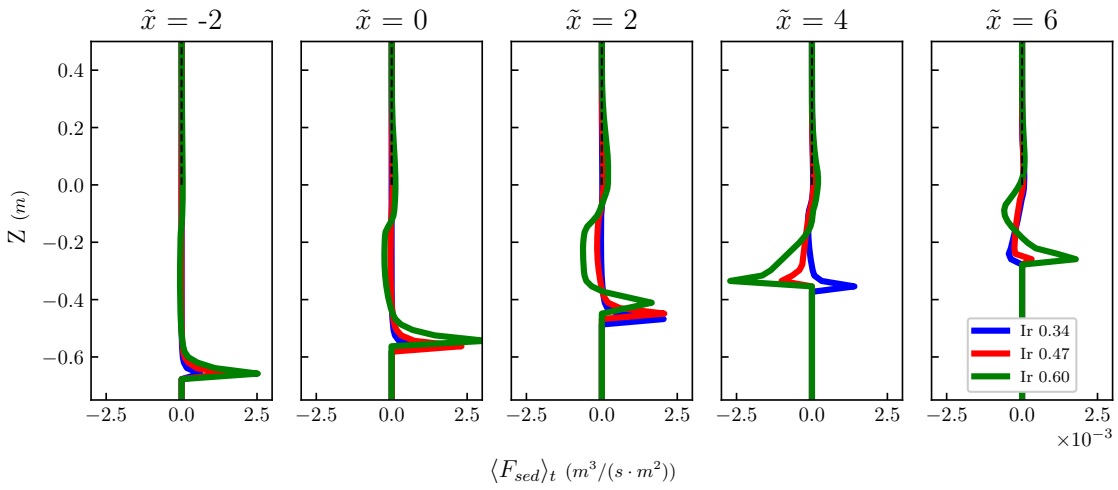

Figure 6.39: Time-averaged horizontal sediment flux profiles. Obtained for waves 100 to 150.

The $\langle F_{sed} \rangle_t$ profiles in Figure 6.39 show a clear increase in the sediment fluxes for higher Iribarren's numbers, which implies that the beach profile evolves faster under plunging breakers than under spilling ones. In the shoaling zone ($\tilde{x} = -2$), the sediment flux produced by the steady streaming increases with the Iribarren's number, consistently with the larger wave height that is expected to produce higher instantaneous friction velocities, stronger steady streaming and to put more sediment in suspension. In the outer surf zone ($\tilde{x} = 2$), the offshore-directed $\langle F_{sed} \rangle_t$ produced by the detached undertow is also higher for plunging breakers, which leads to a higher accumulation of sediment on the offshore face of the breaker bar and also to the higher migration speed observed in Figure 6.35. This is caused by a high sediment concentration present in the upper layers of the outer surf zone. At $\tilde{x} = 4$, the undertow is still detached from the seabed in the case of spilling breakers, while for the others the undertow is attached and produces an offshore-directed $\langle F_{sed} \rangle_t$, which is higher for large Iribarren's numbers. As observed in Figure 6.38, the $\langle U \rangle$ profile for an Iribarren's number of 0.60 has a maximum close to the seabed, which is responsible for this high offshore-directed $\langle F_{sed} \rangle_t$. At ($\tilde{x} = 6$), the higher Iribarren's numbers produce a near-bed onshore-directed $\langle F_{sed} \rangle_t$, which is consistent with the onshore-directed $\langle U \rangle$ observed in Figure 6.38. Moreover, the plunging breaker produces higher instantaneous friction velocities when the plunging jet reaches the seabed, therefore higher sediment concentrations are expected at this position. However, this near-bed onshore-directed $\langle F_{sed} \rangle_t$ is partially compensated by an offshore-directed one produced by the undertow, which depends on the amount of sediment concentration present far from the seabed, so that the net onshore-directed $\langle F_{sed} \rangle_t$is reduced.

In addition to the previous results of $\langle U \rangle$ profiles, these patterns of the sediment flux profiles are explained based on the $\langle C \rangle$ profiles depicted in Figure 6.40.

In Figure 6.40, it can be noted that $\langle C \rangle$ is higher close to the seabed for larger Iribarren's numbers in the shoaling zone (see $\tilde{x} = -2$), this is caused by the higher instantaneous friction velocities produced by the larger wave height (displayed in Figure 6.33). Additionally, the larger accumulation of sediment in the outer surf zone for large Iribarren's numbers can be related to the higher $\langle C \rangle$ present in it, shown in

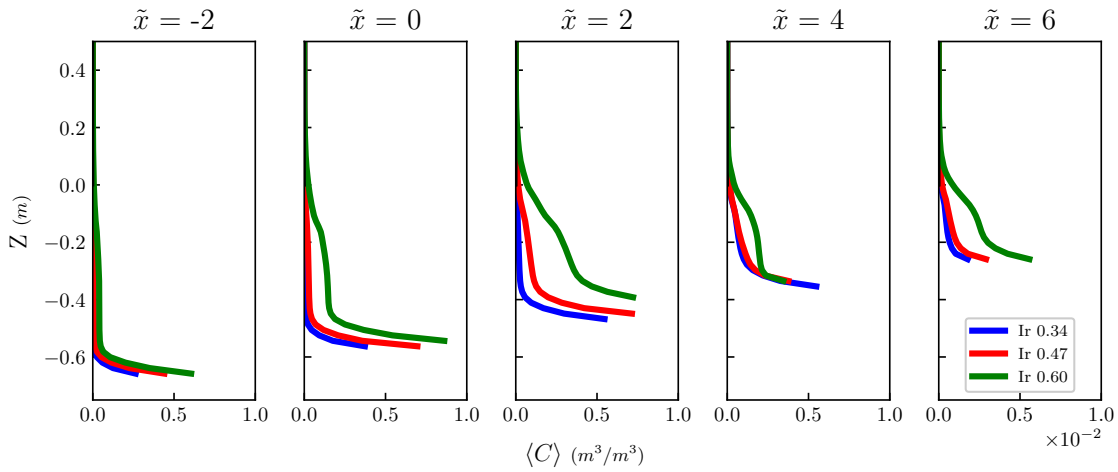

Figure 6.40: Time-averaged concentration profiles for the three test cases at different positions along the beach profile. Obtained for waves 100 to 150.

Figure 6.40 for $0 < \tilde{x} < 4$, which leads to a higher $\langle F_{sed} \rangle_t$. The reason for this is the higher instantaneous friction velocity produced by the plunging breakers in the outer surf zone, which results in a higher near-bed $\langle C \rangle$. The vertical velocities produced by the breakers advect the sediment from the lower layers to the upper ones, increasing $\langle C \rangle$ far from the seabed and enhancing the offshore-directed $\langle F_{sed} \rangle$ of the detached undertow. Thus, more suspended sediment is transported towards the offshore face of the breaker bar. In contrast, at $\tilde{x} = 4$ $\langle C \rangle$ is higher close to the seabed for the spilling breakers. Notice that the undertow is attached at this position for the spilling breakers while being detached for the other two test cases. This difference explains the larger $\langle C \rangle$ for the lowest Iribarren's number: the concentration is advected to this position by the steady streaming. Additionally, the plunging breakers have a more uniform $\langle C \rangle$ profile at this position. This is explained by the high advection of sediment produced by the primary vortex generated in plunging breakers (named M vortex in (Sumer *et al.* , 2013)) which distributes sediment over the water column at the breaking point. At $\tilde{x} = 6$, $\langle C \rangle$ is much higher close to the seabed for the plunging breakers than for the other two configurations, which is consistent with the high friction velocities produced by the plunging jet where it reaches the seabed. This high near-bed $\langle C \rangle$ close to the seabed, together with the onshore-directed $\langle U \rangle$ shown in Figure 6.38, are responsible for the onshore-directed $\langle F_{sed} \rangle$ at the plunge point observed in Figure 6.39, as explained before.

Finally, there is an interesting feature appearing for Iribarren's number 0.60 at $\tilde{x} = -2$. It can be observed that there is sediment concentration in the upper layers of the shoaling zone, regardless of the absence of mixing mechanisms that could advect the sediment from the lower layers. This feature does not appear for the other two cases, and it is consistent with the sediment flux pattern proposed in this work. This concentration far from the seabed comes from the outer surf zone, advected by the detached undertow, and falls due to gravity to the lower layers as the detached undertow loses its velocity.

As commented before, one of the main sources for the differences in the accumulation rates for different types of breakers is the maximum value of the friction velocity produced by them at different positions along the cross-shore profile. To

examine this, the maximum (onshore-directed) and minimum (offshore-directed) friction velocities ($U_{f,max}$ and $U_{f,min}$) produced in each of the test cases are shown in Figure 6.41.

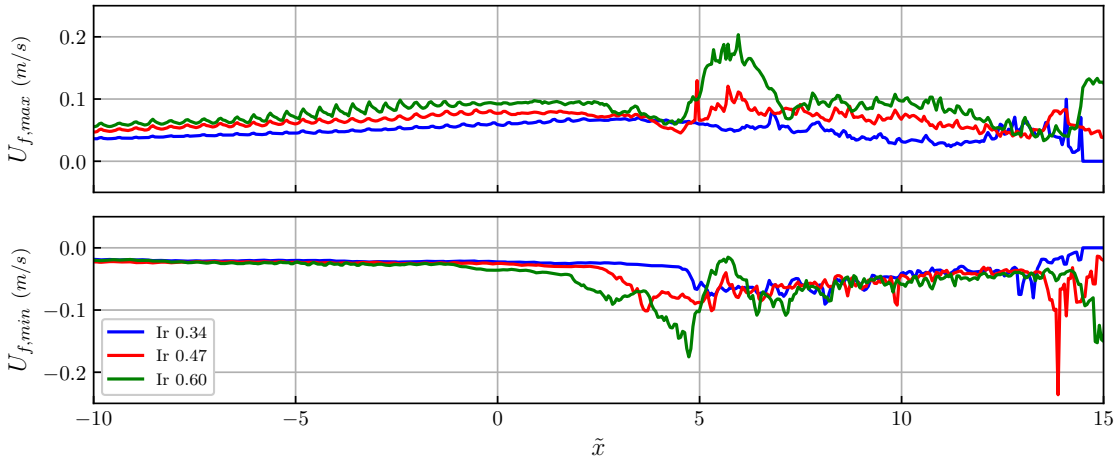

Figure 6.41: Distribution of maximum and minimum friction velocity along the cross-shore profile. Obtained as the maximum value of onshore- and offshore-directed friction velocities for waves 100 to 150.

As can be observed in Figure 6.41, $U_{f,max}$ of shoaling waves around the break point ($\tilde{x} < 2.5$) is higher for the larger Iribarren's numbers, which is to be expected considering their larger wave height in this zone (shown in Figure 6.33). St the plunge point, $U_{f,max}$ is higher for plunging breakers than for spilling breakers (see $\tilde{x} = 6$), which supports the previous reasoning on the origin for the onshore-directed near-bed sediment flux at this position being caused by the impinging jet; notice that the peak in $U_{f,max}$ does not occur under spilling breakers, as the impinging jet is not present. $U_{f,min}$ is larger for higher Iribarren's numbers at the bar trough, which agrees with the idea of the offshore-directed flux of water exiting the outer surf zone being forced to flow close to the seabed, where the onshore-directed velocities and high mixing produced by the plunging jet are smaller. Also, for the plunging breakers, there is another peak in $U_{f,min}$ located at the top of the breaker bar, which can be explained by the larger size of it reducing the section across which the undertow can flow. $U_{f,max}$ produced by the spilling breakers at $\tilde{x} = 4$ are smaller than for the other cases, therefore the higher near-bed $\langle C \rangle$ observed in Figure 6.40 is indeed advected by the steady streaming to this position rather than eroded at it.

Overall, plunging breakers generate higher friction velocities during the crest and trough phases, putting more sediment in suspension. This is the reason why the growth of the breaker bar occurs much faster in such a situation. In addition, the loss of sediment at the plunge point that appears under higher Iribarren's number conditions is explained by the large friction velocities produced by the impinging jet, at the point where it reaches the seabed.

6.7 Discussion

6.7.1 Limitations of the study approach

The approach used in this study takes advantage of a newly developed numerical model which allows to access highly detailed data on the variables influencing the evolution of a cross-shore beach profile. The ability to examine morphodynamic processes with this approach is limited to the assumptions of the model. Firstly, empirical formulae are used to avoid computing some of the morphodynamic processes (i.e., bedload transport, reference concentration). This implies relying on their ability to accurately represent specific morphodynamic processes. In the case of bedload transport, the choice of empirical formulae can partially affect the analysis of the bedload transport distribution, as they consider different relationships between bedload transport and friction velocity. (Engelund & Fredsoe, 1976) considers a varying relation between friction velocity and bedload transport, which produces an additional onshore shift for the position of the onshore face of the breaker bar respect that of the undertow detachment (adding to the shift produced by wave skewness). Secondly, there are limitations in terms of the simplifications in the governing equations of the model for the processes that are numerically resolved. Particularly, these affect the turbulence treatment, boundary layer approximations and the effect of alongshore features (which are not accounted for since the model is 2D). Regardless of these limitations, the model can reproduce the evolution of the beach profile and gives an overall view of how morphodynamic processes interact with each other (including those approximated by empirical formulae) to bring about the evolution of a beach profile, as demonstrated in previous validations. Additionally, this study focuses on erosive conditions. The base case (Iribarren's number 0.43) is analysed in depth, and other two erosive cases are added to verify that the different cross-shore profile evolutions are consistent with the findings of this work. In spite, most of the findings can be useful for future analysis of accretive conditions, since the underlying phenomena described in this work should be also present in milder wave conditions (although with different relative importance).

6.7.2 Implications of the findings

This work provides an integral view of the main drivers of cross-shore beach profile evolution, aggregating previous knowledge and new insights into the individual morphodynamic processes and establishing relationships between them. This new knowledge can be useful to better represent these processes in models suitable for simulations of larger temporal and spatial scales, resulting in improved accuracy and a reduction of the number of calibration parameters. Simpler models incorporating these aspects can be fast enough to be used in the usual design process of coastal infrastructures at larger spatial and temporal scales. Particularly, 2D and intra-wave effects in the surf zone have been highlighted in this work as a potential source of errors in such models,and their treatment could be improved based on the new insights provided in this work. Furthermore, this knowledge can serve as a basis for future research on beach morphodynamics as the main drivers for the morphodynamic processes have been pointed.

6.8 Conclusions

In this chapter, a solid basis for the analysis of beach cross-shore morphodynamics has been provided, and the processes leading to the generation, migration and equilibrium of the breaker bar have been discussed in depth. An integral analysis of the different morphodynamic processes involved in the evolution of cross-shore beach profiles, analysing the contribution of each one of them to the evolution of the profile, the factors that influence this contribution and how they interact with each other, has been given. Conclusions are based on the results of a numerical analysis and previous observations in experiments and field campaigns available in the literature. Additionally, a comparison between the transport rates produced by plunging and spilling breakers has been carried out. A schematic representation of the main findings of this chapter is given in Figure 6.42.

Breaker bar growth. The breaker bar is generated in the outer surf zone around the undertow detachment point and limited on its offshore side by the breaking point and on its onshore side by the plunging point. While the suspended transport contributes to the growth of the breaker bar along the whole outer surf zone, especially on its offshore side, the bedload mechanism only contributes to the growth mainly on the onshore side of the undertow detachment.

The onshore shift between the zone in which the bedload transport mechanism tends to accumulate sediment and the undertow detachment depends on the wave skewness and the sediment transport regime in the wave-trough phase (linear or cubic).

The suspended contribution requires a 2D analysis of the time-averaged velocity and concentration field and intra-wave effects arising from the covariance of them.

The time-averaged velocity field reveals two main near-bed currents: undertow and steady streaming. The undertow detachment is a result of the compensation of these opposed currents, and its position position varies depending on the relative strength of these near-bed currents. The main influencing variables that can enhance or weaken each of them have been discussed (wave skewness, wave height, mass flux produced by breaking waves, distribution of fluid stresses along the water column and water depth). From their analysis, it can be concluded that the undertow detachment is located between the plunging and breaking point in a plane beach profile.

Regarding the concentration field, the different vertical mixing mechanisms in the shoaling, outer and inner surf zones and the way in which they condition the sediment transport distribution along the water depth have been discussed. In the shoaling zone, the absence of significant mixing effects results in high sediment concentration close to the seabed and low far form it. In the outer surf zone, the vertical velocities produced during the wave breaking process lift sediment from the seabed. In the inner surf zone, the breaking-induced vortices are responsible for high vertical mixing.

Regarding intra-wave effects, they have been studied by looking at the covariance between velocity and concentration. This covariance is larger close to the seabed in the shoaling and outer surf zones due to the high correlation between velocity and concentration. In contrast, intra-wave effects are less significant far from the seabed and in the inner surf zone, where the sediment flux is rather current-induced.

The sediment flux field resulting from the aforementioned velocity and concentration features and intra-wave effects have been discussed. A circulation pattern for suspended sediment which leads to accumulation along the outer surf zone (generating the breaker bar) has been identified. It is represented in the top panel of Figure 6.42. The relative importance of current- and wave-induced transport has been also addressed. The sediment flux produced by the detached undertow has been identified as the reason behind the suspended contribution tending to accumulate sediment mainly on the offshore side of the undertow detachment.

Breaker bar migration. A cause-effect relation between the migration of the undertow detachment point and the migration of the breaker bar has been established, based on the previous conclusions. The main reason behind the migration of the undertow detachment is an increase in near-bed time-averaged velocity caused by a variation of the undertow velocity profile in the trough region. This variation is produced by a redistribution of the time-averaged tangential stresses along the water column resulting from the deepening of the trough. The exact physics connecting the redistribution of shear stresses with the deepening of the trough will be researched in the future.

During the migration of the breaker bar, the bedload contribution is displaced offshore due to the variations of the time-averaged friction velocity distribution along the cross-shore profile resulting from the migration of the undertow detachment. As approaching the equilibrium of the beach profile, the time-averaged friction velocity distribution is stabilized.

Regarding the suspended transport contribution, a weakening of the near-bed, onshore-directed flux in the outer surf zone, due to steady streaming and intra-wave effects, has been observed. Also, an increase in the sediment flux produced by the detached undertow has been observed, which partially equilibrates this onshore-directed transport. Additionally, the point at which onshore and offshore directed suspended fluxes converge near-bed is displaced offshore, following the migration of the undertow detachment. In the sediment flux patterns, it has been observed that the sediment flux of the undertow in the inner surf zone and trough is nearly zero. Thus, the increased amount of sediment in the detached undertow must come from the shoaling zone and breaker bar, not form the trough and inner surf zone. This situation is depicted in the centre panel of Figure 6.42.

The concentration profiles undergo significant changes due to the bathymetric evolution. The sediment concentration increases in the upper layers of the outer surf zone, which explains the larger sediment flux of the detached undertow. As the beach profile approaches its equilibrium configuration, the concentration profiles are nearly constant. In the trough, the time-averaged sediment concentration is nearly zero.

To examine the way in which the seabed changes affect the sediment concentration distribution in such way, the maxima and minima friction velocities are examined. On top of the breaker bar, the maximum friction velocity is higher due to the smaller water depth. This increase limits the growth of the breaker bar, as excessive reduction of water depth would result in high erosion. The maximum friction velocity in the trough, associated to the plunging, is smaller due to the increased water depth. The minimum is higher, consistently with the aforementioned enhancement of the undertow close to the seabed.

Regarding the evolution of intra-wave effects, they are stronger in the outer surf zone, increasing the near-bed onshore-directed flux despite the steady streaming being weaker in this zone. In the trough, the intra-wave effects are reduced to nearly zero. In the inner surf zone, they compensate the offshore-directed flux of the undertow.

Breaker bar equilibrium. Once the cross-shore profile reaches the equilibrium configuration, the total contribution from the bedload and suspended transports is nearly zero. On top of the breaker bar, both transport mechanisms compensate each other, with the bedload contribution tending to increase the breaker bar size and the suspended contribution eroding it. In the trough region, both transport contributions are nearly zero. Additionally, the undertow detachment stops migrating.

Concerning the bedload contribution, a lower horizontal gradient of the time-averaged friction velocity distribution has been observed, consistent with the smaller accumulation rate. This is caused by a smaller undertow velocity in the trough region. However, the horizontal gradient of time-averaged friction velocity cannot completely disappear in the outer surf zone, there will be always be a certain negative gradient leading to accumulation (as long as the friction velocities are large enough to mobilize sediment). This small accumulation in the outer surf zone is compensated by the suspended contribution.

Regarding the suspended transport contribution, the concentration profiles show small time-averaged sediment concentration in the trough and increasing concentration on top of the breaker bar. This higher concentration is caused by an increase in the maximum friction velocity produced in the wave-crest phase. The lower concentration in the trough is caused by a further reduction of the friction velocity produced by the impinging jet due to the larger water depth. The sediment fluxes continue evolving as described in the migration stage. The net depth-integrated sediment fluxes tend to zero as the beach profile acquires its equilibrium configuration, being nearly zero along the shoaling and outer surf zones at the equilibrium. In the shoaling zone and breaker bar region this situation is achieved by the onshore and offshore fluxes occurring at different positions along the water depth compensating each other. In the trough region, the sediment fluxes are nearly zero along the whole water column. Thus, the way in which the equilibrium configuration is achieved in the shoaling zone and breaker bar region is different from that of the trough region. In the formers, the equilibrium of suspended sediment flux is due to a closed circulation pattern; in the later, due to the small friction velocities induced by breaking waves as a result of the increase in water depth. This circulation pattern is represented in the bottom panel of Figure 6.42.

Intra-wave effects are more important on top of the breaker bar, where they are responsible for most of the suspended transport once the equilibrium si achieved. In the trough region, the intra-wave effects produce almost zero transport, consistently with the low sediment concentration present in it.

Concerning the bathymetry shape at equilibrium. The height of the breaker bar depends on the maximum water depth reduction that can be sustained, which can be expected to be higher for larger critical shields number of the sediment. The depth of the trough at equilibrium is achieved once the impinging jet does not produce friction velocities large enough to mobilize sediment. As the migration of the breaker bar is linked to the deepening of the trough, the breaker bar remains nearly at the

same position once the trough stabilizes. Finally, the complete equilibrium of the breaker bar is achieved once the sediment fluxes produced by steady streaming and intra-wave effects are compensated by that of the detached undertow.

The comparison between accumulation rates under different types of breakers shows differences in the spatial distribution of the accumulation and loss of sediment and in the speed at which the breaker bar and trough are generated and migrate towards offshore. As the Iribarren's number increases, the break, undertow detachment and plunge points are displaced offshore, and so do the resulting breaker bar and trough. Additionally, the growth and migration of the breaker bar and trough are faster in plunging breakers, as the larger instantaneous friction velocities acting on the seabed result in higher erosion and a higher amount of suspended sediment in the surf zone, making it evolve faster. Such differences are explained by the hydrodynamic and sediment transport features described in this work.

In conclusion, a comprehensive view of the morphodynamic processes that drive the evolution of beach profiles under the erosive conditions associated to episodic events has been provided, including the growth, migration and equilibrium stages. Even if direct observation in the field or in the lab would be the most appropriate way to disentangle the complex interplay between the different processes contributing to the generation of breaker bars, the simultaneous measurement of all the different components is still a challenge. Numerical modelling based on advanced and well-tested RANS models offer, combined with the state of the art fragmented know-how based on observations, a suitable approach to set the base for new experimental work that can help to provide a full disclosure of the mechanisms behind breaker bar generation. Therefore, Specific Objective 3 has been achieved.

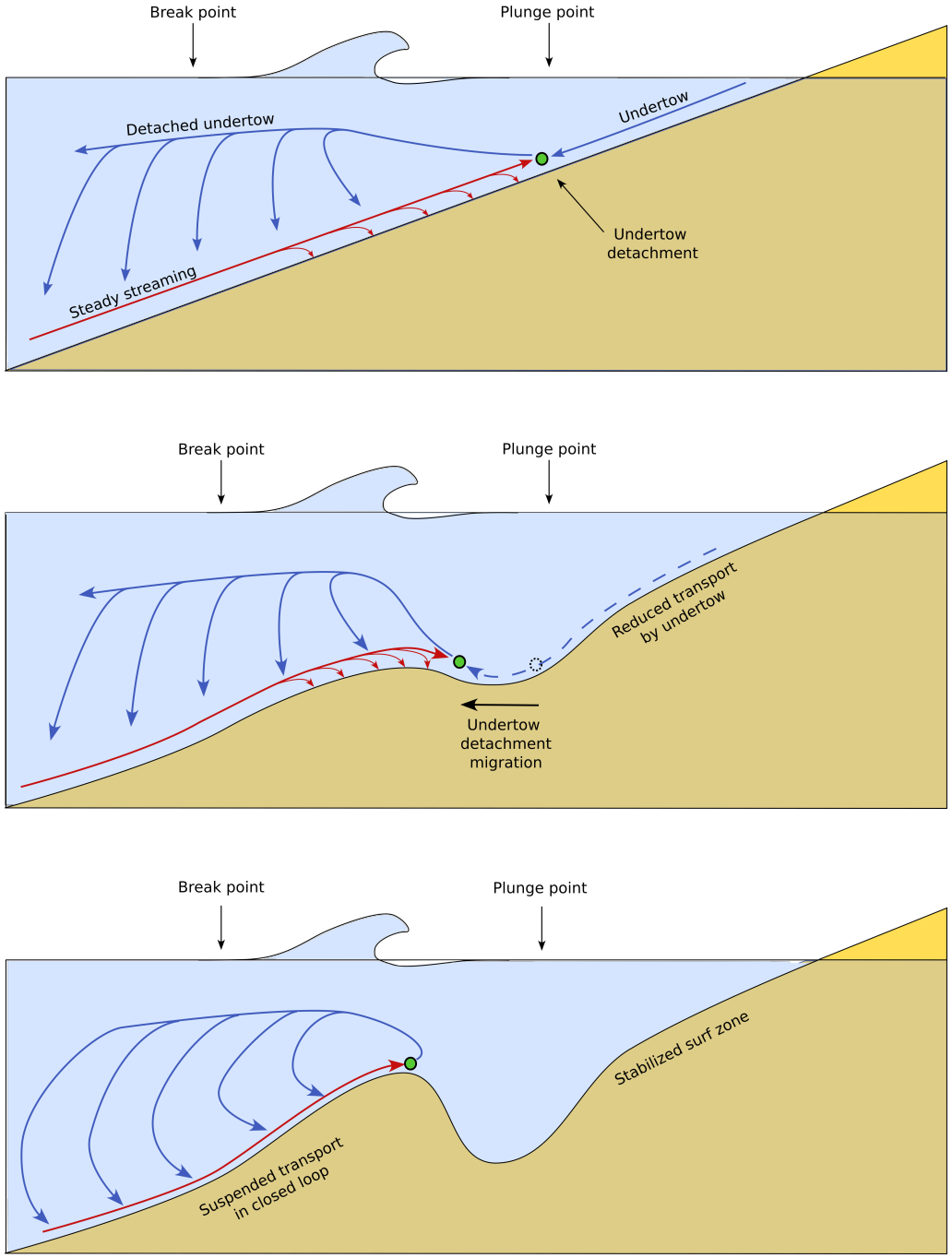

Figure 6.42: Schematic description of the main morphodynamic processes during the growth, migration and equilibrium of the breaker bar. Top panel, growth stage. Centre panel, migration stage. Bottom panel, equilibrium stage.

Chapter 7

Conclusions

The main and specific objectives posed in this thesis have been covered. Based on the results presented in previous chapters, the following conclusions can be extracted in relation to each objective.

Specific Objective 1: development of a numerical model for cross-shore morphodynamic processes. Upon analysis of the available types of models to simulate sediment transport, Eulerian One-Phase models have been deemed more suitable for the analysis of cross-shore beach morphodynamics, as they combine enough simulated processes and reasonable computational cost to address the time and spatial scales aimed to reproduce. According to the selected type, a sediment transport module has been developed for the previously existing RANS hydrodynamic code IH2VOF. Additional improvements, such as enhanced treatment of solid boundaries and parallelization of the Poisson Pressure Equation solving algorithm, have been included in the hydrodynamic module. The resulting numerical model has a significantly reduced computational cost compared to other RANS models used for cross-shore morphodynamics. This new version of the model has been named IH2VOF-SED. With this, Specific Objective 1 has been achieved.

Specific Objective 2: validation of the numerical model. An extensive validation against laboratory results has been provided. The validation covers different spatial and temporal scales. Apart from the bathymetric evolution, several key magnitudes involved in the beach profile evolution, such as free-surface position, friction velocity, velocity and sediment concentration have been considered. No calibration parameters have been used to adjust the model in each validation case. Overall, the numerical model resulting from the previously existing hydrodynamic model and the developments included in this work, IH2VOF-SED, has been proven to be able to reproduced the morphodynamic processes leading to the evolution of the cross-shore beach profile in 2D. Moreover, several hydrodynamic and sediment transport features observed in laboratory experiments and in nature have been also reproduced. These have been discussed in the analysis of the morphodynamic processes.

Consequently, the numerical model accomplishes the objective of providing results that are in qualitative and quantitative agreement with those obtained by physical modelling. Furthermore, the computational cost of simulating the validation cases resulted around 10 times smaller than other RANS models. Therefore, Specific Objective 2 has been achieved.

Specific Objective 3: comprehensive analysis of cross-shore morphodynamics. The numerical model developed in this work has been used to study the morphodynamic processes driving the evolution of a beach profile under erosive conditions, associated with episodic events, taking advantage of the high spatial and temporal definition of the data provided by the model. The way in which environmental conditions (energy sources, sediment properties and morphologic state) affect the morphodynamic processes has been investigated. Moreover, the modifications that the morphodynamic processes produce in the morphologic state of the beach have been examined. This resulted in an in-depth analysis of the morphodynamic processes driving the evolutionary sequence of the beach.

The main drivers in the generation of a breaker bar have been identified. The key role of the undertow detachment, around which the breaker bar grows, has

been highlighted. The fundamental aspects that affect the bedload and suspended contributions have been discussed, stating how the hydrodynamics influence each of them. Also, the circulation of suspended sediment has been described in detail. This accomplishes Specific Objective 3.a

Regarding the offshore migration of the breaker bar, it has been found that it is a consequence of the offshore displacement of the undertow detachment. The way in which this affects the bedload transport gradients and the circulation patterns of suspended sediment have been examined. With this analysis, Specific Objective 3.b is fulfilled.

Finally, the equilibrium of the cross-shore beach profile has been analysed. A description on how the bathymetric equilibrium is achieved due to a compensation between the bedload and suspended contributions is provided. Once the equilibrium is reached, the bedload contribution still produces further growth of the breaker bar. However, the suspended contribution tends to erode it. In the trough, both contributions tend to zero on time-averaged terms. The pattern of suspended sediment circulation in the shoaling and outer surf zone has been found to evolve towards a configuration in which the depth-integrated suspended transport is nearly zero. Therefore, Specific Objective 3.c has been attained.

Main Objective: improving the knowledge in coastal morphodynamics. With the aforementioned findings, this work contributes to a better understanding of the morphodynamic processes that drive the evolutionary sequence of cross-shore beach profiles, which is fundamental for correctly assessing, preventing and mitigating coastal erosion arising from natural and human factors. Furthermore, the numerical model developed in this work is a contribution to the available tools for researchers and practitioners when facing coastal morphodynamic problems. Thus, the Main Objective of this thesis has been achieved.

Chapter 8

Future lines of research

There are several potential lines of work to extend the current research. They can be divided into: a) research related to the numerical model and b) development of knowledge on beach morphodynamics.

8.1 Numerical model

8.1.1 Further developments

Subsequent improvements of the numerical model can include new physics, such as the effect of impermeable and porous structures and vegetation. Moreover, the efficiency of the model may be improved by extending the parallelization to other functions and, overall, optimizing the hydrodynamic and sediment functions.

An important aspect of the development of the numerical model is to extend the range of conditions and physics for which the model is validated. This is of great importance in order to keep exploiting the model in research and consultancy. Accretive conditions should be one of the first candidates for validation, as the most required physics are already included in the model. Of course, the aforementioned new physics to be implemented should be validated as well.

8.1.2 Numerical investigation of morphodynamic processes

In its current state, the model offers plenty of possibilities to further research important aspects of beach morphodynamics. For example, the behaviour under accretive conditions and irregular waves. Extending the available knowledge in these topics can result in important findings that help to better understand and manage coastal areas.

8.1.3 Methodologies for designing coastal infrastructure

The newly developed numerical model can be included in the design process of coastal infrastructures, as is being done with CFD codes for other purposes. Furthermore, due to its ability to produce accurate results without calibration, it can be used as a data augmentation strategy, generating data to adjust the parameters of simpler numerical models. This strategy can be used in conjunction with experimental and field data.

8.1.4 New features and physics

The numerical model can be further extended with new functionality. The implementation of non-erodible elements would allow for the simulation of scour in 2D marine structures such as vertical and rubble mound breakwaters. Furthermore, such model could be used in the assessment of coastal defence strategies aiming to mitigate beach erosion and prevent flooding.

Other aspects that can be included in the model are vegetation, porous media, empirical formulae appropriate for other types of sediments (i.e., gravel, clay).

Thus, the model presented in this work comprises a solid basis on top of which several features can be implemented, resulting in a greatly useful tool for both researchers and practitioners.

8.2 Knowledge on beach morphodynamics

8.2.1 Improvements of simpler numerical models

The main conclusions on how beach morphodynamics work under erosive conditions can be transferred to simpler process-based morphodynamic models to improve their predicting ability by reducing the number of parameters that they depend on.

Developing analytic and empirical models for some of the identified hydrodynamic and sediment transport features influencing the morphodynamic processes may result in a reduction of the required calibration parameters (decreasing the risk of over fitting) and improvements of the accuracy, once the relationships between them are known.

8.2.2 Further research on the morphodynamic processes

The ideas proposed in this work may be used as an starting point in explaining the morphodynamic processes under different conditions. Notice that, despite being obtained based on data for erosive conditions, the conclusions on the morphodynamic processes extracted from them might well be directly applied in the research of accretive conditions, as they are based on the analysis underlying physics rather than empirical formulae with a limited application range.

In addition, backing these findings with data from laboratory experiments would increase the validity of the results of this research. Such experiments can be specifically designed to measure the significant variables at the right positions (i.e., tracking the position of the undertow detachment, measuring the sediment concentration in the detached undertow, etc.).

Finally, after the research performed in this work, it has been highlighted that the redistribution of current-induced Reynolds stresses due to bathymetric changes is the reason behind the offshore migration of the breaker bar. However, the reasons for this redistribution have not been analysed. Potential reasons for this interaction are: variations due to bathymetric changes of the turbulent viscosity distribution, horizontal momentum transfer and dynamic pressure. These aspects might be investigated in the future by means of numerical and physical modelling.

Appendix A

Mass conservation analysis

To check whether a proper mass conservation is achieved or not, the total volume of sediment inside the domain is monitored.

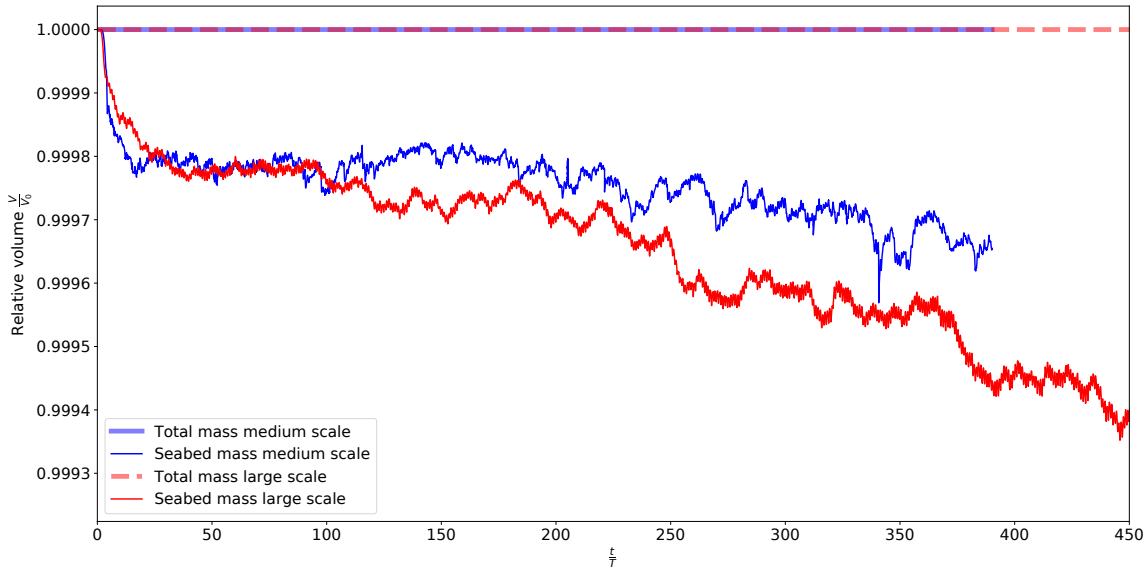

Figure A.1: Evolution of total and suspended mass of sediment in the numerical domain.

Figure A.1 shows the total and suspended sediment volumes inside the numerical domain normalized with the initial total volume of sediment. The volumes have been obtained by integrating the sediment contained on each cell over the whole domain, also considering the amount that exits the domain through the wave generation boundary. As only a small part of the total sediment volume in the domain is mobilized by the hydrodynamics, the mass conservation is shown relative to the amount of sediment put into suspension. Accordingly, the vertical axis does not start at 0.

It can be observed that the total volume of sediment is constant along the simulation, therefore, a proper mass conservation has been achieved. The difference between total sediment and the sediment contained in the seabed is the suspended sediment. During the first seconds of simulation, a large erosion is generated increasing the total suspended volume in the domain. Oscillations in the total suspended sediment due to the wave breaking and other phenomena with larger time scales than the wave period can be noted.

Appendix B

Mesh convergence analysis

To analyse the influence of mesh discretization on the results, a mesh sensitivity analysis is performed for the medium-scale validation case. This case is selected for the sensitivity analysis as the seabed displacements are more noticeable than in the large-scale case. The characteristics of the three meshes considered for this analysis are given in Table B.1, an aspect ratio of 2 is maintained for all of them.

Table B.1: Characteristics of meshes tested in the sensitivity analysis.

Case	ΔY	ΔX	Cells	Computing time (1 core)
H/20	0.022	0.044	110212	42h
H/22.5	0.019	0.038	147823	60h
H/25	0.017	0.034	184564	123h

The effect of mesh discretization on wave evolution along the profile is analysed. Figure B.1 shows the results obtained for meshes described in Table B.1. The mean wave height has been obtained for waves 50 to 100.

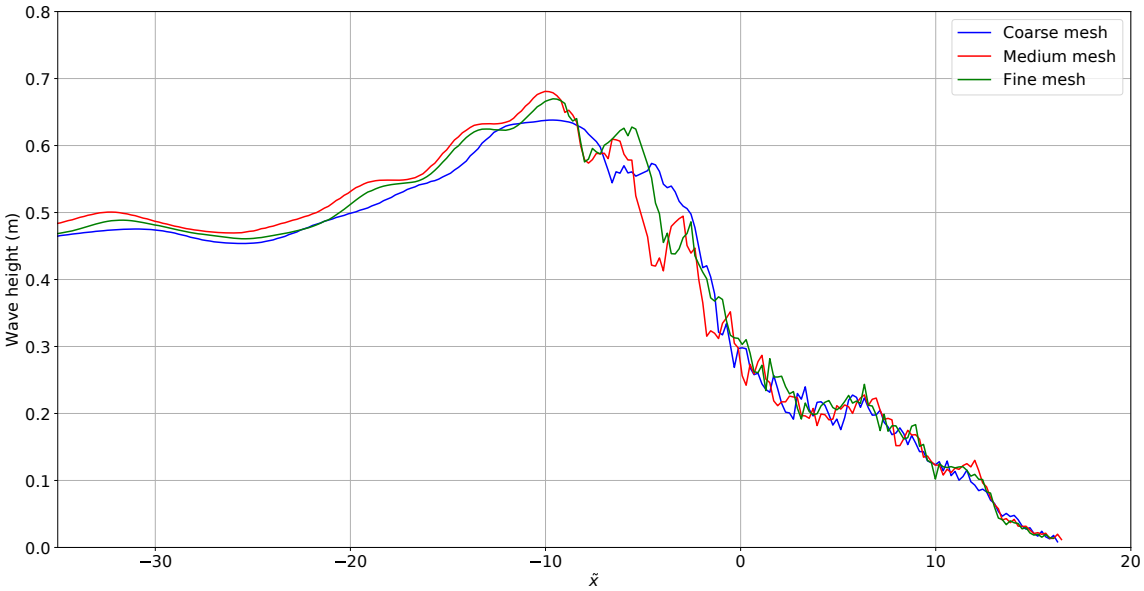

Figure B.1: Sensitivity analysis for the wave height.

Figure B.1 reveals a small mesh dependency for the wave height evolution along the beach profile. In the shoaling and swash zones the results are very similar, while in the proximity of the breaking point and surf zone the differences are more noticeable. The sudden drop in wave height is produced at the same position in all cases. However, there are differences in the evolution of wave height seawards this point, especially for the coarse mesh.

The mesh discretization influence on friction velocity is shown in Figure B.2. The time-averaged friction velocity has been obtained for waves 50 to 100.

Friction velocities are more sensitive to mesh discretization than wave height evolution, especially in the outer surf zone. The medium and fine meshes provide similar results for the shoaling and swash zones and the landwards part of the inner surf zone. Although the distribution of friction velocity obtained with the medium and fine meshes are similar in shape, the finer mesh gives smaller time-averaged friction velocities in the surf zone.

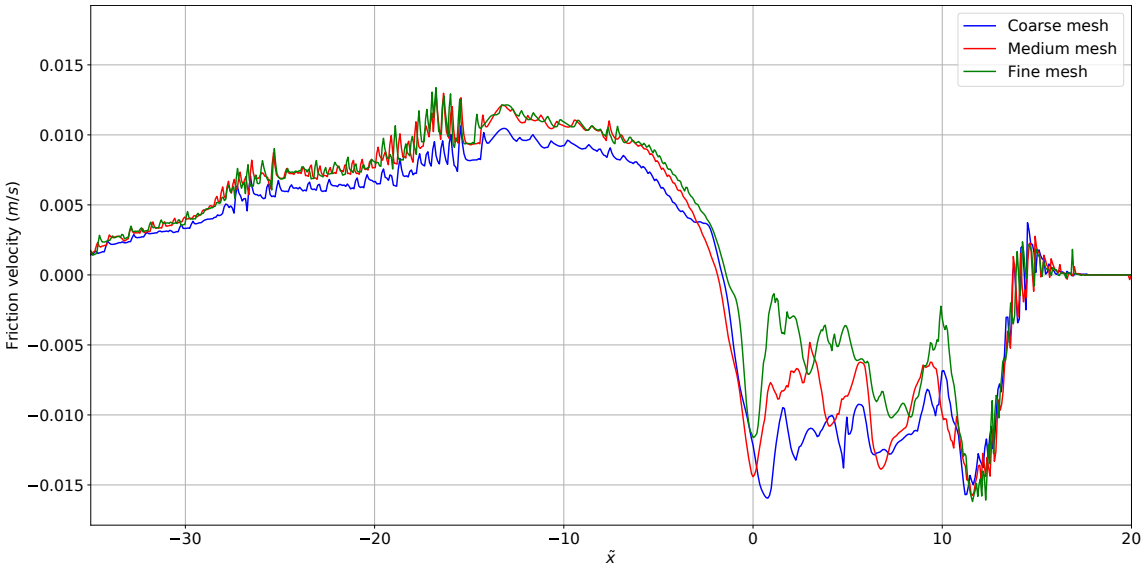

Figure B.2: Sensitivity analysis for the wave height.

The friction velocity is more sensitive to the mesh discretization as not only the outer flow has to be resolved with sufficient resolution, but also the distance between the first non-solid cell and the seabed has to be small enough so that the assumed logarithmic profile for the boundary layer is applicable.

The successive reduction in mesh size results in a similar friction velocity distribution. The medium mesh (H/22.5) is used in the validation cases as it provides a good overall agreement with the experimental results at low computational cost, being therefore the one that better matches the objectives of this work.

Bibliography

Aagaard, T., & Jensen, S. G. 2013. Sediment concentration and vertical mixing under breaking waves. *Marine Geology*, **336**, 146 – 159.

Alexandrakis, George, Manasakis, Constantine, & Kampanis, Nikolaos A. 2015. Valuating the effects of beach erosion to tourism revenue. A management perspective. *Ocean and Coastal Management*, **111**, 1–11.

Amoudry, L. O., Hsu, T. J., & Liu, P. L.F. 2005. Schmidt number and near-bed boundary condition effects on a two-phase dilute sediment transport model. *Journal of Geophysical Research C: Oceans*, **110**(9), 1–12.

Bagnold, R A. 1940. Beach formation by waves: some model experiments in a wave tank. *Journal of the Institution of Civil Engineers*, **15**(1), 27–52.

Bagnold, R A. 1947. Sand movement by waves : some small-scale experiments with sand of very low density. *Journal of the Institution of Civil Engineers*, **27**(4), 447–469.

Bailard, James A., & Inman, Douglas L. 1981. An energetics bedload model for a plane sloping beach: Local transport. *Journal of Geophysical Research: Oceans*, **86**(C3), 2035–2043.

Balay, S., Gropp, W. D., McInnes, L. C., & Smith, B. F. 1997. Efficient Management of Parallelism in Object Oriented Numerical Software Libraries. *Pages 163–202 of:* Arge, E., Bruaset, A. M., & Langtangen, H. P. (eds), *Modern Software Tools in Scientific Computing*. Birkhäuser Press.

Balay, S., Abhyankar, S., Adams, M F., Brown, J., Brune, P., Buschelman, K., Dalcin, L., Eijkhout, V., Gropp, W D., Kaushik, D., Knepley, M G., McInnes, L. C., Rupp, K., Smith, B F., Zampini, S., & Zhang, H. 2015a. *PETSc Users Manual*. Tech. rept. ANL-95/11 - Revision 3.6. Argonne National Laboratory.

Balay, S., Abhyankar, S., Adams, M F., Brown, J., Brune, P., Buschelman, K., Dalcin, L., Eijkhout, V., Gropp, W D., Kaushik, Dinesh, Knepley, Matthew G., McInnes, Lois Curfman, Rupp, Karl, Smith, Barry F., Zampini, Stefano, & Zhang, Hong. 2015b. *PETSc Web page*. `http://www.mcs.anl.gov/petsc`.

Baldock, T. E., Alsina, J. A., Caceres, I., Vicinanza, D., Contestabile, P., Power, H., & Sanchez-Arcilla, A. 2011. Large-scale experiments on beach profile evolution and surf and swash zone sediment transport induced by long waves, wave groups and random waves. *Coastal Engineering*, **58**(2), 214–227.

Baykal, C., Sumer, B. M., Fuhrman, D. R., Jacobsen, N. G., & Fredsøe, J. 2015. Numerical investigation of flow and scour around a vertical circular cylinder. *Philosophical Transactions of the Royal Society A: Mathematical, Physical and Engineering Sciences*, **373**(2033), 20140104.

Berry, Ashton J., Fahey, Shireen, & Meyers, Noel. 2014. Boulderdash and beachwalls – The erosion of sandy beach ecosystem resilience. *Ocean and Coastal Management*, **96**, 104–111.

Blondeaux, P., Vittori, G., Bruschi, A., Lalli, F., & Pesarino, V. 2012. Steady streaming and sediment transport at the bottom of sea waves. *Journal of Fluid Mechanics*, **697**, 115–149.

Bruun, Per. 1954. Coast Erosion and the Development of Beach Profiles. United States Beach Erosion Board. Washington, United States.

Bruun, Per. 1962. Sea-level rise as a cause of shore erosion. *Journal of the Waterways and Harbors division*, **88**(1), 117–132.

Bruun, Per. 1988. The Bruun Rule of Erosion by Sea-Level Rise: A Discussion on Large-Scale Two- and Three-Dimensional Usages. *Journal of Coastal Research*, **4**(4), 627–648.

Butt, T., & Russell, P. 2000. Hydrodynamics and Cross-Shore Sediment Transport in the Swash-Zone of Natural Beaches: A Review. *Journal of Coastal Research*, **16**(2), 255–268.

Cáceres, I., Alsina, J.M., & Sánchez-Arcilla, A. 2009. Mobile bed experiments focused to study the swash zone evolution. *Journal of Coastal Research*, **2009**(SPEC. ISSUE 56), 1736–1740.

Capizzano, F. 2011. Turbulent Wall Model for Immersed Boundary Methods. *AIAA Journal*, **49**(11), 2367–2381.

Cáceres, I., & Alsina, J.M. 2016. Suspended sediment transport and beach dynamics induced by monochromatic conditions, long waves and wave groups. *Coastal Engineering*, **108**, 36 – 55.

Davidson, M.A., Splinter, K.D., & Turner, I.L. 2013. A simple equilibrium model for predicting shoreline change. *Coastal Engineering*, **73**, 191–202.

Dean, R.G. 1977. *Equilibrium Beach Profiles: U.S. Atlantic and Gulf Coasts*. Ocean Engineering Report. Department of Civil Engineering and College of Marine Studies, University of Delaware.

Deigaard, Rolf, Justesen, Peter Dueholm, & Fredsøe, Jørgen. 1991. Modelling of undertow by a one-equation turbulence model. *Coastal Engineering*, **15**, 431–458.

Dubarbier, B., Castelle, B., Marieu, V., & Ruessink, G. 2015. Process-based modeling of cross-shore sandbar behavior. *Coastal Engineering*, **95**, 35 – 50.

Eichentopf, Sonja, Karunarathna, Harshinie, & Alsina, José M. 2019. Morphodynamics of sandy beaches under the influence of storm sequences: Current research status and future needs. *Water Science and Engineering*, **12**(3), 221–234.

Elfrink, B., & Baldock, T. 2002. Hydrodynamics and sediment transport in the swash zone: a review and perspectives. *Coastal Engineering*, **45**(3), 149 – 167. Surface and Swash Zone Mechanics.

Elghannay, Husam, & Tafti, Danesh. 2018. LES-DEM simulations of sediment transport. *International Journal of Sediment Research*, **33**(2), 137 – 148.

Engelund, F., & Fredsoe, J. 1976. A Sediment Transport Model for Straight Alluvial Channels. *Nord Hydrol*, **7**(10).

Europa Press. 2020. El Gobierno destina casi 20 millones a reparar los daños de la borrasca 'Gloria'. *20minutos*. Available at `https://www.20minutos.es/noticia/4153749/0/el-gobierno-destina-9-6-millones-a-reparar-los-danos-en-la-costa-de-la-comunitat-provocados-por-gloria/` (in Spanish).

European Commission, & Directorate-General for Maritime Affairs and Fisheries. 2009. *The economics of climate change adaptation in EU coastal areas summary report*. Publications Office.

European Commission, Directorate-General for Maritime Affairs and Fisheries, Addamo, A, Calvo Santos, A, Carvalho, N, Guillén, J, Magagna, D, Neehus, S, Peralta Baptista, A, Quatrini, S, & Schinasi Romeu, Y. 2021. *The EU blue economy report 2021*. Publications Office.

Faria, A., Thornton, Ed, Lippmann, T., & Stanton, Tim. 2000. Undertow over a barred beach. *Journal of Geophysical Research*, **105**(06), 16999–17010.

Fredsoe, J., & Deigaard, R. 1992. *Mechanics Of Coastal Sediment Transport*. Advanced Series On Ocean Engineering. World Scientific Publishing Company.

Fuhrman, David R., Baykal, Cüneyt, Sumer, B. Mutlu, Jacobsen, Niels G., & Fredsøe, Jørgen. 2014. Numerical simulation of wave-induced scour and backfilling processes beneath submarine pipelines. *Coastal Engineering*, **94**, 10 – 22.

Gallagher, E., Elgar, S., & Guza, R. 1998. Observations of sand bar evolution on a natural beach. *Journal of Geophysical Research*, **103**(02), 3203–3216.

Garcia, M., & Parker, G. 1991. Entrainment of Bed Sediment into Suspension. *Journal of Hydraulic Engineering*, **117**(4), 414–435.

García-Maribona, J., Lara, J.L., Maza, M., & Losada, I.J. 2021. An efficient RANS numerical model for cross-shore beach processes under erosive conditions. *Coastal Engineering*, **170**, 103975.

Gislason, K., Fredsøe, J., & Sumer, B.M. 2009. Flow under standing waves. Part 2. Scour and deposition in front of breakwaters. *Coastal Engineering*, **56**(3), 363–370.

Gopalakrishnan, Sathya, Smith, Martin D., Slott, Jordan M., & Murray, A. Brad. 2011. The value of disappearing beaches: A hedonic pricing model with endogenous beach width. *Journal of Environmental Economics and Management*, **61**(3), 297–310.

Grasso, F., Michallet, H., Barthélemy, E., & Certain, R. 2009. Physical modeling of intermediate cross-shore beach morphology: Transients and equilibrium states. *Journal of Geophysical Research: Oceans*, **114**(9), 1–15.

Grasso, F., Michallet, H., & Barthélemy, E. 2011. Experimental simulation of shoreface nourishments under storm events: A morphological, hydrodynamic, and sediment grain size analysis. *Coastal Engineering*, **58**(2), 184–193.

Han, X., & Lin, P. 2018. 3D Numerical Study of the Flow Properties in a Double-Spur Dikes Field during a Flood Process. *Water*, **10**, 1574.

Henderson, S. M., Allen, J. S., & Newberger, P. A. 2004. Nearshore sandbar migration predicted by an eddy-diffusive boundary layer model. *Journal of Geophysical Research: Oceans*, **109**(C6).

Hoefel, F., & Elgar, S. 2003. Wave-induced sediment transport and sandbar migration. *Science*, **299**(5614), 1885–1887.

Holmedal, L. E., & Myrhaug, D. 2009. Wave-induced steady streaming, mass transport and net sediment transport in rough turbulent ocean bottom boundary layers. *Continental Shelf Research*, **29**(7), 911 – 926.

Howe, Blenkinsopp, Turner, Baldock, T., & Puleo. 2019. Direct Measurements of Bed Shear Stress under Swash Flows on Steep Laboratory Slopes at Medium to Prototype Scales. *Journal of Marine Science and Engineering*, **7**(10), 358.

Hsu, T.J., Sakakiyama, T., & Liu, P. L.F. 2002. A numerical model for wave motions and turbulence flows in front of a composite breakwater. *Coastal Engineering*, **46**(1), 25 – 50.

Hughes, Michael G., Masselink, Gerhard, & Brander, Robert W. 1997. Flow velocity and sediment transport in the swash zone of a steep beach. *Marine Geology*, **138**(1), 91–103.

Jackson, Derek, & Short, Andrew. 2020. *Sandy Beach Morphodynamics*. Elsevier.

Jacobsen, N. G., Fredsoe, J., & Jensen, J. H. 2014. Formation and development of a breaker bar under regular waves. Part 1: Model description and hydrodynamics. *Coastal Engineering*, **88**, 182 – 193.

Jacobsen, Niels, & Fredsoe, Jorgen. 2014. Formation and development of a breaker bar under regular waves. Part 2: Sediment transport and morphology. *Coastal Engineering*, **88**(06), 55–68.

Kalligeris, N., Smit, P.B., Ludka, B.C., Guza, R.T., & Gallien, T.W. 2020. Calibration and assessment of process-based numerical models for beach profile evolution in southern California. *Coastal Engineering*, **158**, 103650.

Kim, Tae-Kon, Lim, Changbin, & Lee, Jung-Lyul. 2021. Vulnerability Analysis of Episodic Beach Erosion by Applying Storm Wave Scenarios to a Shoreline Response Model. *Frontiers in Marine Science*, **8**, 1586.

Kranenburg, W. M., Ribberink, J. S., Schretlen, J. J. L. M., & Uittenbogaard, R. E. 2013. Sand transport beneath waves: The role of progressive wave streaming and other free surface effects. *Journal of Geophysical Research: Earth Surface*, **118**(1), 122–139.

Lara, J. L., Ruju, A., & Losada, I. J. 2011. Reynolds averaged Navier-Stokes modelling of long waves induced by a transient wave group on a beach. *Proceedings of the Royal Society A: Mathematical, Physical and Engineering Sciences*, **467**(2129), 1215–1242.

Larsen, B. E., & Fuhrman, D. R. 2018. On the over-production of turbulence beneath surface waves in Reynolds-Averaged Navier–Stokes models. *Journal of Fluid Mechanics*, **853**, 419–460.

Larsen, B. E., Fuhrman, D. R., B., C., & Sumer, B. M. 2017. Tsunami-induced scour around monopile foundations. *Coastal Engineering*, **129**, 36 – 49.

Larsen, B. E., van der A, D. A., van der Zanden, J., Ruessink, G., & Fuhrman, D. R. 2020. Stabilized RANS simulation of surf zone kinematics and boundary layer processes beneath large-scale plunging waves over a breaker bar. *Ocean Modelling*, **155**, 101705.

Larsen, Bjarke Eltard, & Fuhrman, David R. 2019. Full-scale CFD simulation of tsunamis. Part 1: Model validation and run-up. *Coastal Engineering*, **151**, 22–41.

Larsen, Bjarke Eltard, Fuhrman, David R., & Sumer, B. Mutlu. 2016. Simulation of Wave-Plus-Current Scour beneath Submarine Pipelines. *Journal of Waterway, Port, Coastal, and Ocean Engineering*, **142**(5), 04016003.

Larson, Magnus, & Kraus, Nicholas. 1994. Temporal and spatial scales of beach profile change, Duck, North Carolina. *Marine Geology*, **117**(03), 75–94.

Larson, Magnus, & Sunamura, Tsuguo. 1993. Laboratory experiment on flow characteristics at a beach step. *Journal of Sedimentary Research*, **63**(3), 495–500.

Lee, Guan-Hong, Nicholls, Robert J., & Birkemeier, William A. 1998. Storm-driven variability of the beach-nearshore profile at Duck, North Carolina, USA, 1981–1991. *Marine Geology*, **148**(3), 163–177.

Lesser, G.R., Roelvink, J.A., van Kester, J.A.T.M., & Stelling, G.S. 2004. Development and validation of a three-dimensional morphological model. *Coastal Engineering*, **51**(8-9), 883–915.

Li, Jinzhao, Qi, Meilan, & Fuhrman, David R. 2019. Numerical modeling of flow and morphology induced by a solitary wave on a sloping beach. *Applied Ocean Research*, **82**, 259–273.

Li, Yuzhu, Ong, Muk Chen, & Fuhrman, David R. 2020. CFD investigations of scour beneath a submarine pipeline with the effect of upward seepage. *Coastal Engineering*, **156**(December 2019), 103624.

Lin, P., Cheng, L., & Liu, D. 2016. A two-phase flow model for wave–structure interaction using a virtual boundary force method. *Computers and Fluids*, **129**, 101 – 110.

Lin, Pengzhi, & Liu, Philip L-F. 1998. A numerical study of breaking waves in the surf zone. *Journal of Fluid Mechanics*, **359**, 239–264.

Longuet-Higgins, M. S. 1983. Wave set-up, percolation and undertow in the surf zone. *Proceedings of the Royal Society of London. A. Mathematical and Physical Sciences*, **390**(1799), 283–291.

Longuet-Higgins, M. S., & Stoneley, R. 1953. Mass transport in water waves. *Philosophical Transactions of the Royal Society of London. Series A, Mathematical and Physical Sciences*, **245**(903), 535–581.

Losada, I. J., Lara, J. L., Guanche, R., & Gonzalez-Ondina, J. M. 2008. Numerical analysis of wave overtopping of rubble mound breakwaters. *Coastal Engineering*, **55**(1), 47 – 62.

Lubin, P., Vincent, S., Abadie, S., & Caltagirone, JP. 2006. Three-dimensional Large Eddy Simulation of air entrainment under plunging breaking waves. *Coastal Engineering*, **53**(8), 631 – 655.

Mares Nasarre, Patricia. 2021. *Overtopping flow on mound breakwaters under depth-limited breaking wave conditions*. Ph.D. thesis, Universitat Politècnica de València.

Matsunaga, N., & Honji, H. 1980. The backwash vortex. *Journal of Fluid Mechanics*, **99**(4), 813–815.

Meyer-Peter, E., & Müller, R. 1978. Formulas for bed-load transport. *Proceedings of the 2nd Meeting of the International Association for Hydraulic Structures Research. Stockholm, Sweden*, **1**, 87.

Morton, Robert A., Paine, Jeffrey G., & Gibeaut, James C. 1994. Stages and Durations of Post-Storm Beach Recovery, Southeastern Texas Coast, U.S.A. *Journal of Coastal Research*, **10**(4), 884–908.

Nadaoka, Kazuo, Hino, Mikio, & Koyano, Yoshiji. 1989. Structure of the turbulent flow field under breaking waves in the surf zone. *Journal of Fluid Mechanics*, **204**, 359–387.

Nielsen, P., Svensen, I.A., & Staub, C. 1978. Onshore-offshore sediment movement on a beach. *Coastal Engineering Proceedings*, **1**(16), 87.

Ogston, A.s, & Sternberg, R.W. 2002. Effect of wave breaking on sediment eddy diffusivity, suspended-sediment and longshore sediment flux profiles in the surf zone. *Continental Shelf Research*, **22**(03), 633–655.

Okayasu, Akio, & Katayama, Hiroyuki. 1992. Distribution of Undertow and Long-wave Component Velocity due to Random Waves. *Coastal Engineering Proceedings*, **1**(23).

Okayasu, Akio, Shibayama, Tomoya, & Mimura, Nobuo. 1986. Velocity Field Under Plunging Waves. *Coastal Engineering Proceedings*, **1**(20), 50.

Otsuka, Junichi, Saruwatari, Ayumi, & Watanabe, Yasunori. 2017. Vortex-induced suspension of sediment in the surf zone. *Advances in Water Resources*, **110**, 59–76.

Oumeraci, Hocine, Allsop, William, Groot, M., Crouch, R., & Vrijling, J. 2001. *Proverbs: Probabilistic design tools for vertical breakwaters*. CRC Press.

Peng, Zhong, Zou, Qing-Ping, & Lin, Pengzhi. 2018. A partial cell technique for modeling the morphological change and scour. *Coastal Engineering*, **131**, 88 – 105.

Rakha, K.A., Deigaard, R., & Brøker, I. 1997. A phase-resolving cross-shore sediment transport model for beach profile evolution. *Coastal Engineering*, **31**(1-4), 231–261.

Rattanapitikon, Winyu, & Shibayama, Tomoya. 2000. Simple Model for Undertow Profile. *Coastal Engineering Journal*, **42**(1), 1–30.

Robertson, Bryson, Hall, Kevin, Zytner, Richard, & Nistor, Ioan. 2013. Breaking Waves: Review of Characteristic Relationships. *Coastal Engineering Journal*, **55**(1), 1350002–1–1350002–40.

Roelvink, D., Reniers, A., van Dongeren, A., van Thiel de Vries, J., McCall, R., & Lescinski, J. 2009. Modelling storm impacts on beaches, dunes and barrier islands. *Coastal Engineering*, **56**(11-12), 1133–1152.

Roelvink, Dano J.A., Reniers, Ad, van Dongeren, Ap, Thiel de Vries, Jaap, Lescinski, Jamie, & McCall, Robert. 2010 (01). *XBeach Model – Description and Manual*. Available at `https://svn.oss.deltares.nl/repos/openearthtools/sandbox/DSD_2014/XBeachExecutable/xbeach_manual.pdf`.

Roulund, A., Sumer, B. M., Fredsøe, J., & Michelsen, J. 2005. Numerical and experimental investigation of flow and scour around a circular pile. *Journal of Fluid Mechanics*, **534**, 351–401.

Ruessink, B.G., Michallet, H., Abreu, T., Sancho, F., van der A, D.A., van der Werf, J.J., & Silva, P.A. 2011. Observations of velocities, sand concentrations, and fluxes under velocity-asymmetric oscillatory flows. *Journal of geophysical research : Oceans*, **116**(C3).

Ruffini, G., Briganti, R., Alsina, J. M., Brocchini, M., Dodd, N., & McCall, R. 2020. Numerical Modeling of Flow and Bed Evolution of Bichromatic Wave Groups on an Intermediate Beach Using Nonhydrostatic XBeach. *Journal of Waterway, Port, Coastal, and Ocean Engineering*, **146**(1), 04019034.

Ruju, A., Lara, J. L., & Losada, I. J. 2012. Radiation stress and low-frequency energy balance within the surf zone: A numerical approach. *Coastal Engineering*, **68**, 44 – 55.

Schlacher, Thomas A., Dugan, Jenifer, Schoeman, Dave S., Lastra, Mariano, Jones, Alan, Scapini, Felicita, McLachlan, Anton, & Defeo, Omar. 2007. Sandy beaches at the brink. *Diversity and Distributions*, **13**(5), 556–560.

Schwartz, Maurice L. 1967. The Bruun Theory of Sea-Level Rise as a Cause of Shore Erosion. *The Journal of Geology*, **75**(1), 76–92.

Smith, J. D., & McLean, S. R. 1977. Spatially averaged flow over a wavy surface. *Journal of Geophysical Research*, **82**(12), 1735–1746.

Splinter, Kristen D., Turner, Ian L., Davidson, Mark A., Barnard, Patrick, Castelle, Bruno, & Oltman-Shay, Joan. 2014. A generalized equilibrium model for predicting daily to interannual shoreline response. *Journal of Geophysical Research: Earth Surface*, **119**(9), 1936–1958.

Stive, Marcel JF, Aarninkhof, Stefan GJ, Hamm, Luc, Hanson, Hans, Larson, Magnus, Wijnberg, Kathelijne M, Nicholls, Robert J, & Capobianco, Michele. 2002. Variability of shore and shoreline evolution. *Coastal engineering*, **47**(2), 211–235.

Stive, M.J.F. 1986. A MODEL FOR CROSS-SHORE SEDIMENT TRANSPORT. *Coastal Engineering Proceedings*, **1**(20), 114.

Sumer, B. M., Sen, M. B., Karagali, I., Ceren, B., Fredsøe, J., Sottile, M., Zilioli, L., & Fuhrman, D. R. 2011. Flow and sediment transport induced by a plunging solitary wave. *Journal of Geophysical Research: Oceans*, **116**(1), 1–15.

Sumer, B. M., Guner, H.A.A., Hansen, N.M., Fuhrman, D.R., & Fredsøe, J. 2013. Laboratory observations of flow and sediment transport induced by plunging regular waves. *Journal of Geophysical Research: Oceans*, **118**(11), 6161–6182.

Sun, R., & Xiao, H. 2016. SediFoam: A general-purpose, open-source CFD–DEM solver for particle-laden flow with emphasis on sediment transport. *Computers and Geosciences*, **89**, 207 – 219.

Svendsen, I.A. 1984. Mass flux and undertow in a surf zone. *Coastal Engineering*, **8**(4), 347–365.

Svendsen, Ib A. 2006. *Introduction to Nearshore Hydrodynamics*.

Tajima, Yoshimitsu, & Madsen, Ole Secher. 2006. Modeling Near-Shore Waves, Surface Rollers, and Undertow Velocity Profiles. *Journal of Waterway, Port, Coastal, and Ocean Engineering*, **132**(6), 429–438.

Ting, F. C.K., & Kirby, J. T. 1994. Observation of undertow and turbulence in a laboratory surf zone. *Coastal Engineering*, **24**(1), 51 – 80.

Ting, F. C.K., & Kirby, J. T. 1995. Dynamics of surf-zone turbulence in a strong plunging breaker. *Coastal Engineering*, **24**(3), 177 – 204.

Ting, F. C.K., & Nelson, J. R. 2011. Laboratory measurements of large-scale near-bed turbulent flow structures under spilling regular waves. *Coastal Engineering*, **58**(2), 151–172.

Toimil, Alexandra, Losada, Iñigo J., Nicholls, Robert J., Dalrymple, Robert A., & Stive, Marcel J.F. 2020. Addressing the challenges of climate change risks and adaptation in coastal areas: A review. *Coastal Engineering*, **156**, 103611.

Torres-Freyermuth, A., Losada, I. J., & Lara, J. L. 2007. Modeling of surf zone processes on a natural beach using Reynolds-Averaged Navier-Stokes equations. *Journal of Geophysical Research: Oceans*, **112**(C9).

Tsoukala, Vasiliki, Katsardi, Vanessa, Adjibiros, K., & Moutzouris, C. 2015. Beach Erosion and Consequential Impacts Due to the Presence of Harbours in Sandy Beaches in Greece and Cyprus. *Environmental Processes*, **2**(08), 55–71.

van der A, D. A., van der Zanden, J., O'Donoghue, T., Hurther, D., Cáceres, I., McLelland, S. J., & Ribberink, J. S. 2017. Large-scale laboratory study of breaking wave hydrodynamics over a fixed bar. *Journal of Geophysical Research: Oceans*, **122**(4), 3287–3310.

van der Werf, J. J., Doucette, J. S., O'Donoghue, T., & Ribberink, J. S. 2007. Detailed measurements of velocities and suspended sand concentrations over full-scale ripples in regular oscillatory flow. *Journal of Geophysical Research: Earth Surface*, **112**(F2).

van der Werf, J.J., Magar, V., Malarkey, J., Guizien, K., & O'Donoghue, T. 2008. 2DV modelling of sediment transport processes over full-scale ripples in regular asymmetric oscillatory flow. *Continental Shelf Research*, **28**(8), 1040–1056.

van der Zanden, J., van der A, D. A., Hurther, D., Cáceres, I., O'Donoghue, T., Hulscher, S. J.M.H., & Ribberink, J. S. 2017a. Bedload and suspended load contributions to breaker bar morphodynamics. *Coastal Engineering*, **129**(April), 74–92.

van der Zanden, J., van der A, D.A., Hurther, D., Cáceres, I., O'Donoghue, T., & Ribberink, J.S. 2017b. Suspended sediment transport around a large-scale laboratory breaker bar. *Coastal Engineering*, **125**, 51 – 69.

van Rijn, L., Ribberink, J., van der Werf, J., & Walstra, DJ. 2013. Coastal sediment dynamics: Recent advances and future research needs. *Journal of Hydraulic Research*, **51**(10).

van Rijn, L. C. 1984. Sediment Transport, Part II: Suspended Load Transport. *Journal of Hydraulic Engineering*, **110**(11), 1613–1641.

van Rijn, L.C, Walstra, D.J.R, Grasmeijer, B, Sutherland, J, Pan, S, & Sierra, J.P. 2003. The predictability of cross-shore bed evolution of sandy beaches at the time scale of storms and seasons using process-based Profile models. *Coastal Engineering*, **47**(3), 295 – 327.

van Rijn, L.C., Tonnon, P.K., & Walstra, D.J.R. 2011. Numerical modelling of erosion and accretion of plane sloping beaches at different scales. *Coastal Engineering*, **58**(7), 637 – 655.

Wang, Ping, Smith, Ernest, & Ebersole, Bruce. 2002. Large-Scale Measurements of Longshore Sediment Transport Under Spilling and Plunging Breakers. *Journal of Coastal Research*, 12.

Wang, Ping, Ebersole, Bruce, & Smith, Ernest. 2003. Beach Profile Evolution under Spilling and Plunging Breakers. *Journal of Waterway Port Coastal and Ocean Engineering*, 01.

Watanabe, Yasunori, Saeki, Hiroshi, & Hosking, Roger J. 2005. Three-dimensional vortex structures under breaking waves. *Journal of Fluid Mechanics*, **545**, 291–328.

Wilcox, D. C. 1998. *Turbulence Modelling for CFD*. DCW Industries.

Wright, L. D., & Short, A. D. 1984. Morphodynamic variability of surf zones and beaches: A synthesis. *Marine Geology*, **56**(1), 93–118.

Wright, L.D., & Thom, B.G. 1977. Coastal depositional landforms: a morphodynamic approach. *Progress in Physical Geography: Earth and Environment*, **1**(3), 412–459.

Wright, L.D, Short, A.D, & Green, M.O. 1985. Short-term changes in the morphodynamic states of beaches and surf zones: An empirical predictive model. *Marine Geology*, **62**(3), 339 – 364.

Yates, M. L., Guza, R. T., & O'Reilly, W. C. 2009. Equilibrium shoreline response: Observations and modeling. *Journal of Geophysical Research: Oceans*, **114**(C9).

Yoon, Hyun-Doug, & Cox, Daniel T. 2012. Cross-shore variation of intermittent sediment suspension and turbulence induced by depth-limited wave breaking. *Continental Shelf Research*, **47**, 93–106.

Zhao, Enjin, Qu, Ke, & Mu, Lin. 2019. Numerical study of morphological response of the sandy bed after tsunami-like wave overtopping an impermeable seawall. *Ocean Engineering*, **186**, 106076.

Zijlema, Marcel, Stelling, Guus, & Smit, Pieter. 2011. SWASH: An operational public domain code for simulating wave fields and rapidly varied flows in coastal waters. *Coastal Engineering*, **58**(10), 992–1012.

Zubeldia, Elizabeth H., Fourtakas, Georgios, Rogers, Benedict D., & Farias, Márcio M. 2018. Multi-phase SPH model for simulation of erosion and scouring by means of the shields and Drucker–Prager criteria. *Advances in Water Resources*, **117**(May 2018), 98–114.